Optical Studies on Dirac and Weyl Semimetals

Von der Fakultät Mathematik und Physik
der Universität Stuttgart zur Erlangung der Würde eines Doktors
der Naturwissenschaften (Dr. rer. nat.) genehmigte Abhandlung

vorgelegt von
Micha Benjamin Schilling
aus Günzburg

Hauptberichter: Prof. Dr. Martin Dressel
Mitberichter: Dr. Jurgen Smet

Tag der mündlichen Prüfung: 19.11.2018
Prüfungsvorsitzende: Prof. Dr. Maria Daghofer

1. Physikalisches Institut der Universität Stuttgart
2018

Wer die Grenzen akzeptiert,
der ist grenzenlos beschränkt!

Paul Hartmut Würdig (Sido) in 'Grenzenlos' - Sido feat. Marius Müller-Westernhagen (2013)

To God and all creation

Abstract

This thesis presents the results of optical spectroscopy measurements on various Dirac materials, including the nodal line semimetal ZrSiS, the topologically non-trivial half-Heusler compounds YbPtBi and GdPtBi, and the anisotropic Dirac semimetals $CaMnBi_2$ and $SrMnBi_2$. Generally, optical studies of this kind access the low-energy excitation spectra of the materials. In case of Dirac materials, optics probes the dynamics of Dirac and Weyl fermions, as well as other exotic quasiparticles emerging in these quantum materials. The major results, obtained in this work can be summarized as follows.

In ZrSiS, the response of the nodal line Dirac fermions is revealed by a frequency-independent optical conductivity $\sigma_1(\omega)$, which arises from the effectively reduced dimensionality of the linearly dispersing bands [1, 2]. This is consistent with band structure calculations [3] and verified by a theoretical model for the optical response of nodal line semimetals [2]. From our optical fits, we derive the length k_0 of the nodal line in the reciprocal space and an upper limit for the energy gap Δ induced by spin-orbit coupling. Additionally, we discuss the origin of two low-energy excitation modes in the optical spectrum and compare our interband results to theoretical calculations of Ref. [4].

For the half-Heusler compound YbPtBi, we provide a two-channel conduction model containing highly mobile (Dirac-like) electrons and conventional holes [5]. This model is verified by magneto-transport and Hall measurements, as well as by a double-Drude fit for the intraband optical conductivity. The mobility of the electrons is found to be record high for half-Heusler compounds. This is a strong indication for Dirac-like states, which are usually associated with high charge carrier mobilities [6, 7]. The interband spectrum of YbPtBi is compared to the results obtained on the sister compound GdPtBi. For both, we find strong evidence for the recently predicted triple point fermions, which emerge when a doubly degenerate and a non-degenerate band cross [8]. Namely, we find that the frequency depen-

dence of the interband conductivity is linear [9, 10]. From the slope of $\sigma_1(\omega)$ we derive the Fermi velocity of the relevant linear dispersing bands. We compare these results to band structure calculations and find excellent agreement.

Finally, we trace the fingerprints of the anisotropic Dirac states in $CaMnBi_2$ and $SrMnBi_2$. In the low-frequency range, the interband conductivity of both compounds disperses linearly with frequency. This is caused by linear dispersions of the bands in all three dimensions. From the slope of $\sigma_1(\omega)$, we calculate the Fermi velocity and obtain values in good agreement with theory and angle-resolved photoemission spectroscopy measurements [11]. At higher frequencies, the effective band dimensionality is reduced due to the strong anisotropy. This is observed as a $\sigma_1(\omega) \propto \omega^{-1}$ decay in the optical conductivity. In $CaMnBi_2$, we identify an anomaly at 50 K, present in both, dc conductivity and our optical spectrum, and narrow down the origin of this anomaly to a density wave scenario. This is further verified by magnetic susceptibility measurements and the presence of Fermi surface nesting in $CaMnBi_2$ [12].

Overall, the results of this thesis confirm the relevance of Dirac physics for all studied materials and reveal that the low-energy electrodynamics of these compounds are governed by the quasiparticles possessing Dirac(-like) dispersion relations.

dt. Zusammenfassung

Diese Arbeit fasst die Ergebnisse von optischen Spektroskopie-Messungen an verschiedenen Dirac Materialien, unter anderem am *nodal line* Halbmetall ZrSiS, an den topologisch nicht-trivialen half-Heusler Materialien YbPtBi und GdPtBi und an den anisotropischen Dirac Halbmetallen $CaMnBi_2$ und $SrMnBi_2$. Im Allgemeinen bieten optische Untersuchungen dieser Art einen Zugang zu den Anregungsspektren der Materialien im Bereich kleiner Energien. Bezüglich Dirac Materialien untersuchen solche optischen Messungen die Dynamik der Dirac und Weyl Fermionen, ebenso von anderen Quasiteilchen welche in dieser Art von Quantenmaterialien vorkommen können. Die wichtigsten Ergebnisse dieser Arbeit können folgendermaßen zusammengefasst werden:

In ZrSiS wird die Antwort der *nodal line* Dirac Fermionen durch eine Frequenzunabhängige optische Leitfähigkeit $\sigma_1(\omega)$ enthüllt, welche von der effektiv reduzierten Dimensionionalität der linear verlaufenden Bänder verursacht wird [1, 2]. Dies stimmt mit Bandstruktur-Berechnungen überein [3] und wird durch ein theoretisches Modell für die optische Antwort sogenannter *nodal line* Halbmetallen verifiziert [2]. Aus unseren optischen Modellierungen leiten wir sowohl die Länge k_0 der *nodal line* im reziproken Raum, als auch ein Maximalwert für die Energielücke Δ, welche durch die Spin-Orbital-Wechselwirkung entsteht, ab. Zusätzlich diskutieren wir mögliche Ursachen für zwei Anregungsmoden im Bereich kleiner Energien und vergleichen unsere Interband-Ergebnisse mit theoretischen Berechnungen aus Ref. [4].

Für das half-Heusler Material YbPtBi entwickeln wir ein zwei-Kanal Leitungsmodell, welches sehr bewegliche (Dirac-ähnliche) Elektronen und normale Löcher enthält [5]. Dieses Modell bestätigen wir durch magnetische Transportmessungen, Hall Messungen und ein zwei-Drude Modell für die intraband optische Leitfähigkeit. Die Beweglichkeit der Elektronen stellt einen neuen Rekord für half-Heusler Materialien auf und liefert einen starken Hinweis auf Dirac-ähnliche Zustände, wel-

che üblicherweise mit einer sehr hohen Beweglichkeit der Ladungsträger in Verbindung gebracht werden [6, 7]. Das Interband-Spektrum von YbPtBi wird zudem mit den Ergebnissen des verwandten Materials GdPtBi verglichen. Für beide finden wir deutliche Anzeichen für die erst kürzlich vorhergesagten Triple-Punkt Fermionen, welche auftreten wenn ein zweifach entartetes Band und ein nicht entartetes Band sich schneiden [8]. Dies zeigt sich in einer linearen Frequenzabhängigkeit der Interband-Leitfähigkeit [9, 10]. Aus der Steigung der Leitfähigkeit leiten wir die Fermi Geschwindigkeit der involvierten linear verlaufenden Bänder ab. Die Ergebnisse liefern eine ausgezeichnete Übereinstimmung mit Bandstruktur-Berechnungen.
Abschließend spüren wir die Charakteristiken der anisotropischen Dirac Zustände in $CaMnBi_2$ und $SrMnBi_2$ auf. Im Bereich kleiner Frequenzen steigt die Interband-Leitfähigkeit linear mit der Frequenz an. Dies wird durch linear verlaufende Bänder in drei Dimensionen verursacht. Aus der Steigung der Leitfähigkeit berechnen wir die Fermi Geschwindigkeit und finden eine gute Übereinstimmung mit theoretischen Werten und winkelaufgelösten Photoemissionsspektroskopie Messungens [11]. Bei höheren Frequenzen wird die effektive Banddimensionalität auf Grund der starken Anisotropie reduziert, welches durch eine ω^{-1} Abhängigkeit der optischen Leitfähigkeit bestätigt wird. In $CaMnBi_2$ beobachten wir sowohl in der DC als auch in der optischen Leitfähigkeit eine Anomalie bei 50 K und schränken die Ursache der Anomalie auf eine Zustandsdichte-Welle ein. Dies wird durch die Messung der magnetischen Suszeptibilität und die Realisierung von Fermi Oberflächen *nesting* weiter bekräftigt [12].
Insgesamt bestätigen die Ergebnisse dieser Arbeit die Bedeutsamkeit der Dirac Physik für alle untersuchten Materialien und enthüllen, dass die Elektrodynamik im Bereich kleiner Energien von Quasiteilchen mit Dirac(-ähnlicher) Dispersionsrelation bestimmt wird.

Struktur der Arbeit

Nach einer kurzen Einführung und Motivation in **Kapitel 1**, ist die Arbeit folgendermaßen gegliedert:

Kapitel 2 liefert einen theoretischen Einstieg in das Feld der Dirac Physik in Festkörpern. Dies beinhaltet sowohl einen Vergleich verschiedener Messmethoden,

welche für die Enthüllung der Spuren der Dirac Physik verwendet werden können als auch eine ausführliche Diskussion der Antwort von Dirac Materialien in der frequenzabhängigen optischen Leitfähigkeit.

Kapitel 3 bietet einen Überblick über das Prinzip der Fourier-Transform Infrarotspektroskopie, die verwendeten experimentellen Aufbauten und die Datenauswertung, inklusive des Verfahrens zur Datenextrapolation und der Kramers-Kronig Transformation.

Kapitel 4-6 beinhalten die experimentellen Ergebnisse dieser Arbeit. Jedes Kapitel beginnt mit einer kurzen Beschreibung des untersuchten Materials, gefolgt von einer allgemeinen Darstellung der optischen Ergebnisse und endet mit einer Interpretation unter Berücksichtigung der speziellen Bandstruktur jedes Materials.

Kapitel 4 diskutiert die optische Antwort des *nodal line* Halbmetalls **ZrSiS** und seine frequenzunabhängige optische Leitfähigkeit, welche einen direkten Zugang zur Länge der *nodal line* im reziproken Raum liefert.

Kapitel 5 behandelt das half-Heusler Material **YbPtBi** mit seinem zwei-Kanal Leitungsmodell und der möglichen Beteiligung der Dirac Physik. Letzteres wird durch den Vergleich zum verwandten Material GdPtBi bestärkt.

Kapitel 6 beschreibt die optische Antwort der Dirac Halbmetalle $\mathbf{CaMnBi_2}$ und $\mathbf{SrMnBi_2}$ und vergleicht zwei mögliche Szenarien für die Leitfähigkeit im mittleren Infrarot-Bereich: die Formation einer Zustandsdichte-Welle und die Kennzeichen der anisotropischen Dirac *cones*.

Publications

Some results from this thesis are published:

- **M. B. Schilling**, L. M. Schoop, B. V. Lotsch, M. Dressel, and A. V. Pronin, "Flat Optical Conductivity in ZrSiS due to Two-Dimensional Dirac Bands" In: *Phys. Rev. Lett.*, Vol. 119, Iss. 18, 187401 (2017).

- **M. B. Schilling**, A. Löhle, D. Neubauer, C. Shekhar, C. Felser, M. Dressel, and A. V. Pronin, "Two-channel conduction in YbPtBi" In: *Phys. Rev. B*, Vol. 95, Iss. 15, 155201 (2017).

- F. Hütt, A. Yaresko, **M. B. Schilling**, C. Shekhar, C. Felser, M. Dressel, and A. V. Pronin, "Linear-in-Frequency Optical Conductivity in GdPtBi due to Transitions near the Triple Points" In: *Phys. Rev. Lett.*, Vol. 121, Iss. 17, 176601 (2018).

Other scientific publications:

- **M. B. Schilling**, A. Baumgartner, B. Gorshunov, E. S. Zhukova, V. A. Dravin, K. V. Mitsen, D. V. Efremov, O. V. Dolgov, K. Iida, M. Dressel, and S. Zapf, "Tracing the $s_{\pm}$ symmetry in iron pnictides by controlled disorder" In: *Phys. Rev. B*, Vol. 93, Iss. 17, 174515 (2016).

- D. Neubauer, A. Yaresko, W. Li, A. Löhle, R. Hübner, **M. B. Schilling**, C. Shekhar, C. Felser, M. Dressel, and A. V. Pronin, "Optical conductivity of the Weyl semimetal NbP" In: *Phys. Rev. B*, Vol. 98, Iss. 19, 195203 (2018).

- F. Berkmann, L. Augel, **M. B. Schilling**, A. Berrier, D. Schwarz, D. Weißhaupt, M. Oehme, J. Schulze, I. A. Fischer,
  "Optical characterization of highly n-type doped $Ge_{0.95}Sn_{0.05}$ rod antennas on Si(001) substrates"
  In: *mipro 2018 conference proceedings*, meet 06, p. 0032 (2018)

Contents

1. Introduction

The ability to design and manufacture materials with required properties is one of the main goals of today's condensed matter physics research. Recently, it has been shown that many exotic and less exotic particles, theoretically predicted in high-energy physics, may emerge as quasiparticles in solids. In particular interest are the Dirac and Weyl equations and the massless, relativistic fermions [13, 14], described by these equations. At certain circumstances, quasiparticles with properties similar to relativistic Dirac and Weyl fermions can be found in condensed matter: If conduction and valence bands cross each other, the dispersion of the bands in the vicinity of the crossing point can be linear [15]. Thus, the quasiparticles living in these linearly dispersing bands can only be described by the relativistic Dirac/Weyl equation with the speed of light being replaced by the Fermi velocity v_F. Important is, however, that the Fermi level is situated near the crossing point, otherwise the observation of such quasiparticles is problematic. These quasiparticles come with fascinating properties, such as the suppressed back scattering, which leads to ultra-high carrier mobilities (in the order of 10^4 to $10^5\,\mathrm{cm}^2/\mathrm{Vs}$), or negative longitudinal magneto-resistance induced by the chiral anomaly [6, 7, 16, 17]. These make the so-called Dirac materials[1] an attractive material class for future applications. By now, many different types of Dirac materials confirmed by theory and experiment, e.g., two dimensional graphene, three dimensional Dirac and Weyl semimetals, topological insulators, d-wave superconductors, and nodal line semimetals.

[1] I.e., the materials, which low-energy electronic bands can be described by the Dirac or Weyl equations.

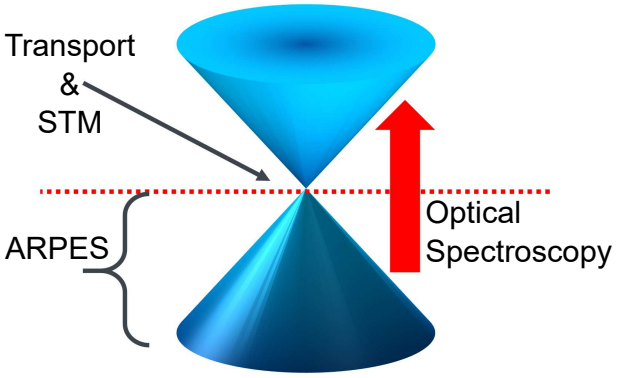

Figure 1.1.: Various experimental techniques address different parts of Dirac bands: ARPES detects occupied states, hence can only be used to map the bands below the Fermi level; transport and tunneling experiments probe the physics directly at the Fermi level, hence, are able to map the Fermi surface; optical probes excite electrons from the valence band into the conduction band and, thus, map transitions from the lower half of the Dirac cone to the upper one.

1.1. Motivation

To utilize Dirac materials, the understanding of their (low-energy) electrodynamic response is essential. Thus, a lot of attention is drawn to the investigations by means of band structure calculations and various experimental techniques, such as angle-resolved photoemission spectroscopy (ARPES), (magneto-)transport measurements, tunneling microscopy (STM), and optical spectroscopy. Each method addresses the Dirac physics in a different energy range, leading to complementing results, as sketched in Figure 1.1. Among the commonly applied experimental techniques, optical spectroscopy is the only one which excites charge carriers across the Fermi level and, hence, is able to probe the complete Dirac cone.

The goal of this work is to apply mainly optical spectroscopy to probe the linearly dispersing bands across the Fermi level. Theoretical models show that this technique is sensitive to the dimensionality of the Dirac states [9, 10], it provides access to the slope of the linear dispersion, i.e., to the Fermi velocity v_F, it probes a possible energy gap Δ at the crossing point, and the distance between the crossing point and the Fermi level, i.e., the position of the chemical potential μ [9, 18, 19].

In this thesis, we investigate materials with different dimensionality d of the Dirac bands and detect the frequency behavior of the optical conductivity, which has been predicted to be directly related to d and to the power z of the band dispersion,

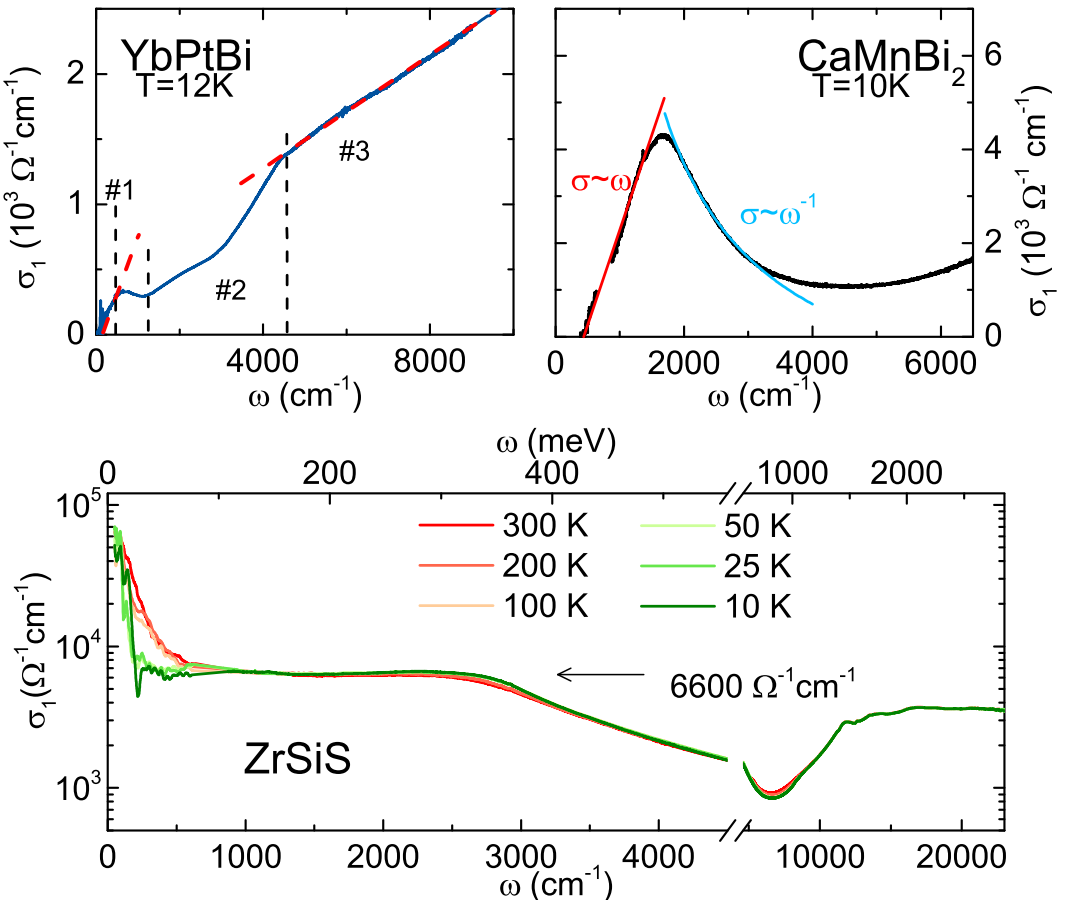

Figure 1.2.: The (interband) optical conductivity of the investigated compounds YbPtBi, $CaMnBi_2$, and ZrSiS. Their frequency dependence reveals the fingerprints of Dirac states of different dimensionality. The interband conductivity of $SrMnBi_2$ is similar to the one of $CaMnBi_2$ and, hence, not shown here.

$E(k) = k^z$ [9, 10]. We show that the proposed simple relation, $\sigma_1(\omega) \propto \omega^{(d-2)/z}$, nicely holds for many different materials, possessing linear bands. The materials studied in this thesis contain Dirac (i.e., linearly dispersing) bands in:

- three dimensions (YbPtBi, $CaMnBi_2$, $SrMnBi_2$), leading to a linear dispersion of $\sigma_1(\omega)$,
- two dimensions (ZrSiS) with a frequency-independent optical conductivity,
- one dimension ($CaMnBi_2$, $SrMnBi_2$), which results in a ω^{-1}-decay of $\sigma_1(\omega)$,

as shown in Figure 1.2. Additionally, we apply more advanced models to each of the mentioned compounds to obtain in-depth information about the electrodynamics in the Dirac bands.

1.2. Structure of the thesis

After the above presented introduction (**chapter 1**), the thesis is organized as follows.

chapter 2 provides an introduction to the field of Dirac physics in condensed matter. This includes a comparison of various experimental techniques which can be applied to unveil the fingerprints of Dirac physics and a detailed discussion of the Dirac response in the frequency-dependent optical conductivity.

chapter 3 gives an overview of the principles of Fourier-transform infrared spectroscopy, the employed experimental setups, and the data treatment, including the procedure of data extrapolation and Kramers-Kronig transformation.

chapters 4-6 contain the experimental results of this work. Each chapter starts with a short review of the investigated material, continues with a general examination of the optical response, and ends up with a particular interpretation of the results with respect to the band structure of the materials.

- **chapter 4** discusses the optical response of the nodal line semimetal **ZrSiS** and its frequency-independent optical conductivity, which provides access to the length of the nodal line in the reciprocal space.
- **chapter 5** deals with the half-Heusler compound **YbPtBi**, its two-channel conduction, and the possible appearance of Dirac physics. The latter is supported by the results obtained on the sister compound GdPtBi.
- **chapter 6** describes the optical response of two Dirac semimetals **$CaMnBi_2$** and **$SrMnBi_2$**, and compares two possible scenarios to account for their mid-infrared conductivity: a (charge) density wave formation and the fingerprints of the anisotropic Dirac cones.

2. Theoretical and experimental background

This chapter will provide an overview of *Dirac fermions*[1] in solid state physics: i.e., the particles which obey the Dirac Hamiltonian instead of the conventional Schrödinger Hamiltonian. The underlying equations and the basic properties of these quasiparticles will be discussed first. In the second part, different types and classes of materials hosting Dirac fermions will be explained. Thirdly, the experimental fingerprints of Dirac fermions will be summarized and accompanied by main experimental results.

2.1. From Schrödinger to Dirac

The excitations of nearly free quasiparticles in conventional metals or doped semiconductors can usually be described by the Schrödinger equation [20, 21]:

$$i\hbar\frac{\partial}{\partial t}\left|\psi(t)\right\rangle = H_{\mathrm{S}}\left|\psi(t)\right\rangle \quad , \tag{2.1}$$

with $\hbar$ being the reduced Planck constant. The Schrödinger Hamiltonian is given as:

$$H_{\mathrm{S}} = \frac{\boldsymbol{p}^2}{2m^*} \quad , \tag{2.2}$$

with the effective mass[2] m^* and the momentum $\boldsymbol{p}$. Consequently, such excitations are often called *Schrödinger fermions* and their energy dispersion shows a quadratic

[1] Here, we follow the convention that materials hosting such kind of Dirac fermions are labeled as Dirac materials. Even when the linear crossing or band touching is gapped.

[2] In a solid, the bare electron mass m_e is commonly rewritten into the effective mass m^*, which takes interactions and the band structure into account.

momentum dependence, $E \propto p^2$.

What is now referred as *Dirac fermions* or a *Dirac material*, is when the low-energy excitations cannot be described with the Hamiltonian given in Equation 2.2, but with the Dirac Hamiltonian in two spatial dimensions [13, 15]:

$$H_{\mathrm{D}} = c\boldsymbol{\sigma} \cdot \boldsymbol{p} + mc^2\sigma_z \quad . \tag{2.3}$$

Here, $\boldsymbol{\sigma} = (\sigma_x, \sigma_y)$ and σ_z are the conventional Pauli matrices and c the effective speed of light, which is replaced by the Fermi velocity[3] v_F in condensed matter physics. This Dirac Hamiltonian is accompanied by a linear energy dispersion, $E \propto p$. The low-energy excitation spectrum of Equation 2.3 thus hosts linear energy bands. This property is what one usually thinks of when talking about Dirac fermions or Dirac states in solid state physics and is qualitatively different to what is observed in conventional metals or semiconductors, which show the parabolic dispersion mentioned before. Furthermore, the Hamiltonian provides no possibility for an energy gap in the limit of a vanishing Dirac mass $m \to 0$, because there is no perturbation term left [14, 15]. This will be further discussed when introducing Weyl semimetals in section 2.3.

Even for a non-zero Dirac mass, the Dirac Hamiltonian leads to an interconnection of particles and holes, so they obey the same effective mass m, being related to the spectral gap $\Delta = 2mc^2$ [15]. Again, this is different to conventional metals and semiconductors, where each type of charge carrier, electrons and holes, come with their own Schrödinger equation and thus with independent effective masses.

Historically, the Dirac Hamiltonian or, more generally, the Dirac equation [15]:

$$i\hbar\frac{\partial}{\partial t}\left|\psi(t)\right\rangle = \left(c\boldsymbol{\alpha} \cdot \boldsymbol{p} + \beta mc^2\right)\left|\psi(t)\right\rangle \quad , \tag{2.4}$$

was introduced not to describe quasiparticles in solids, but to give a quantum theory which is compatible with special relativity and able to explain the fine structure of an atomic spectrum. The original Dirac equation is Lorentz covariant and thus does not change its form under transformation between two inertial frames [13, 20]. This

[3] The Fermi velocity is given by the kinetic energy that causes particles to move even at zero temperature, while the kinetic energy is determined by the energy of the highest occupied bands (i.e., the Fermi energy E_F or Fermi level).

Lorentz covariance is lost for condensed matter systems as the Hamiltonian and the Fermi velocity are connected to the inertial frame of the underlying material.
Still, many phenomena being connected to relativistic quantum mechanics can be found in condensed matter. Whether a particle behaves relativistic or not is determined by the ratio cp/mc^2 of the momentum $p = |\boldsymbol{p}|$ to the mass m: for $cp \ll mc^2$ any particle is considered as quasi-non-relativistic, else it is dominated by relativistic effects. [15]

In the relativistic regime, a new conserved quantity occurs for $cp \gg mc^2$ (in the ultrarelativistic limit): the chirality $\Lambda = \boldsymbol{\sigma} \cdot \boldsymbol{p}/p$. The chirality describes whether spin and momentum of a (quasi)particle are aligned parallel or antiparallel. Thus, the chirality is $\Lambda = +1$ for the parallel or right-handed case, while $\Lambda = -1$ in the antiparallel or left-handed situation. A sketch describing the chirality can be found in panel (a) of Figure 2.1. There are two things to note: First, what we state here as chirality, is from the particle physics point of view usually referred to as the helicity [22]. The chirality in that context is much more complex but equals the helicity for massless particles, i.e., Dirac fermions. Since the community of condensed matter usually choses the term chirality, we will adapt this nomenclature. Second, the (pseudo-)spin in this context can come from any degree of freedom and does not need to be the electron spin, as will be the case in graphene discussed later on, see section 2.2.
The chirality brings along an effect that influences the particle dynamics. Back scattering processes $\boldsymbol{p} \to -\boldsymbol{p}$ need to be accompanied by a flip of the spin $\boldsymbol{\sigma} \to -\boldsymbol{\sigma}$. Without the spin-flip, the back scattering process is forbidden. Due to this phenomenon, ultrarelativistic particles are able to tunnel through arbitrarily high and thick potential barriers [15, 23]. In solid state physics, the suppressed back scattering causes the Dirac fermions to reach high mobilities μ [6, 7].
A second phenomenon, which can be adapted from relativistic quantum mechanics is the influence of an external magnetic field B on quantized energy levels. These so-called Landau levels are equally spaced in the non-relativistic regime (i.e., in conventional metals), but their spacing follows a $\sqrt{B}$-behavior in massless Dirac systems, see, e.g., Ref. [24].

These phenomena show that *Dirac materials* provide access to ultrarelativistic ef-

fects. Therefore, such effects can be observed in rather simple condensed matter experiments instead of complicated particle physics investigations. More and more materials hosting such Dirac fermions are discovered and synthesized and they can be separated into different classes: Dirac semimetals (DSM) in two (2D) and three (3D) dimensions, nodal line semimetals (NLSM), Weyl semimetals (WSM) and topological[4] insulators (TI), just to mention the most common ones. A more advanced table of classes and materials can be found in Ref. [15]. In the following, basic principles, properties and differences of these classes will be discussed.

2.2. Dirac physics in two dimensions

Without doubt, graphene is the most famous Dirac material. It consists of a monolayer of carbon atoms. These atoms are aranged in a honeycomb lattice and thus restricted to two dimensions. Two sublattices, A and B, exist due to the fact that one unit cell of the hexagonal lattice consists of two carbon atoms, as can be seen in panel (b) of Figure 2.1. A broad review on the electronic properties of graphene can be found in Ref. [23]. Here we will just touch the basics of Dirac physics in graphene and, if not other stated, the review serves as reference. The electronic states located close to the Fermi level E_F arise from the out-of-plane carbon p_z orbitals forming π-bonds with neighboring atoms. This leads to the famous band structure in momentum (k) space of graphene depicted in Figure 2.1 (c). The band structure hosts Dirac-like touching points, also called *Dirac nodes*, and the bands disperse linearly above and below these points. Such a band situation with a linear touching or crossing point, as depicted in the zoom-in, is commonly named a *Dirac cone*. Since the unit cell is made of two atoms, which contribute one p_z electron each, the lower band is completely filled and the upper band is empty. Therefore, the Fermi level in graphene should be located perfectly at the Dirac points [15].
The pseudo-spin in graphene is related to the sublattice degree of freedom (A or B). Therefore, one can say that the Dirac fermions in graphene directly arise due

[4]Topology can be seen as something like a modern version of geometry. It distinguishes different kinds of geometry from each other, which cannot be transformed into each other (under particular transformations) [25]. The first realization of topology in condensed matter was shown by K. von Klitzing with the discovery of the quantum Hall effect [26].

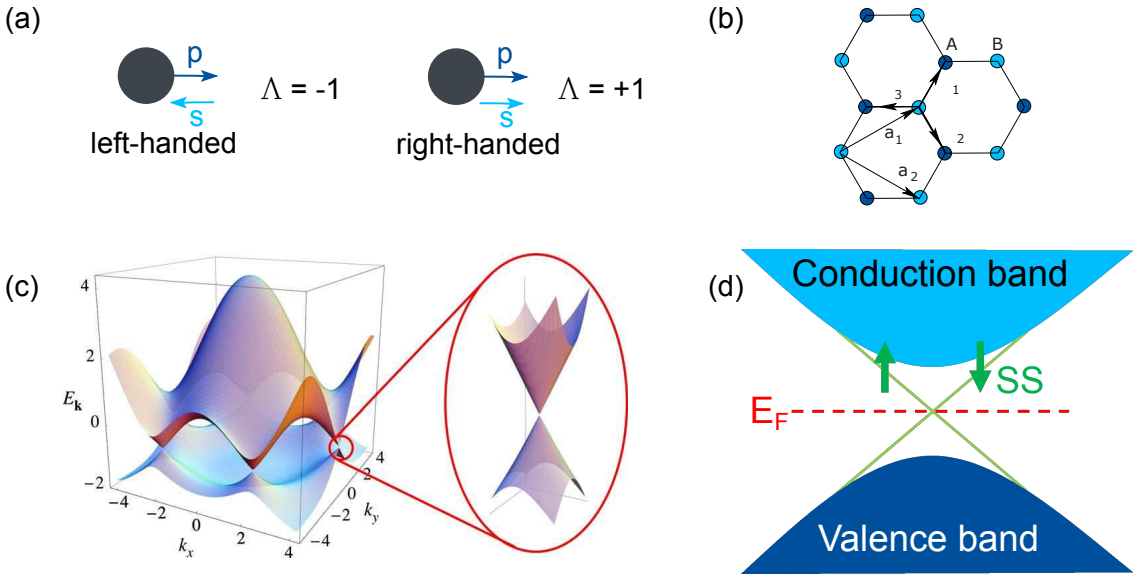

Figure 2.1.: Panel (a) depicts the chirality Λ: for the the spin s being parallel (antiparallel) to the momentum p the particle is referred as right-handed (left-handed) with Λ = 1 (Λ = −1). The honeycomb lattice of graphene, including the two sublattices A and B, is shown in panel (b). The energy bands of graphene drawn in the reciprocal space is given in panel (c). The zoom provides a closer look at the so-called Dirac cone. Panel (d) shows the band structure of a topological insulator including its surface states (SS). The Fermi level is situated in the energy gap between the bulk valence and conduction band, while the topologically protected SS (green) connect the two bands resulting in linear dispersing bands. Panels (b) and (c) are redrawn from Ref. [23].

to the two-sublattice-situation. The Dirac fermions in graphene, but also in other Dirac materials, come along with some interesting properties. As mentioned before, the electrons possess an ultra high mobility. Furthermore, the effective mass m^* for Dirac states is much smaller than the bare electron mass m_e, on the order of 0.01 m_e (e.g., Ref. [27]). In combination with a high Fermi velocity (usually 10^5 to 10^6 m/s [28]), these properties make Dirac materials good candidates for electronic devices.

A comparable situation, also including a honeycomb lattice, can be found in other materials, e.g., silicene [29, 30], but a detailed review goes beyond the scope of this work.

A particularly important case of a 2D Dirac system is a 3D topological insulator.[5] A topological insulator can be seen as an insulator which has conducting surface states, see Figure 2.1 (d). Commonly, these metallic states arise from a linear band crossing and thus are also related to Dirac physics. The origin of the surface states (SS) is of topological nature, giving rise to the name of this material class [33].
The insulating bulk of an TI hosts an inverted band structure: the conduction band drops below the valence band and they reverse roles. This topological band structure will always meet a topologically *trivial* insulator (e.g. vacuum) at the surfaces of the crystal [31]. As the bulk insulating bands are topologically different than the insulating bands of vacuum, the surface states are necessary for the transition from one topological type to the other. Therefore, the SS are protected by time reversal symmetry and will always be present at the surface/interface of the topological insulator. Cutting a crystal into two pieces will make the new surfaces metallic.
One of the first material families in which topological insulating states were found is $Bi_{1-x}Sb_x$, a so-called first generation topological insulator. More famous and also more broadly investigated were the Bi-compounds Bi_2Se_3 and Bi_2Te_3, which belong to the second generation of TIs [31].

Concluding this section, let us mention that it is not necessary to have a two dimensional material, to observe 2D Dirac states. Other examples are nodal line semimetals, where the Dirac cones do not disperse along one k-direction. A more detailed picture of these NLSM will be given in section 2.5. Another possibility is that the bands are gapped in one of the k-directions, as will be discussed in the context of the two materials $CaMnBi_2$ and $SrMnBi_2$ in chapter 6. Such Dirac states are commonly referred to as quasi-two dimensional.

2.3. Three dimensional Weyl semimetals

Before discussing to Dirac semimetals in 3D, let us first consider the so-called Weyl semimetals, since from a symmetry point of view, a Dirac semimetal is a special case of a Weyl semimetal. The Weyl physics takes the Dirac Hamiltonian in the

[5] In principle, TIs can exist basically in any dimensions [31, 32]. We only cosider the 3D TIs, as in practice they can be easily studied by the means of optics.

zero-mass limit leading to the Weyl Hamiltonian [14]:

$$H_{\mathrm{W}} = \pm c(\sigma_x p_x + \sigma_y p_y + \sigma_z p_z) \quad . \tag{2.5}$$

Since any perturbation in this case will be absorbed into the p_x, p_y and p_z coefficients, a single Weyl point is robust and does not necessarily require any symmetry protection [15, 34]. Note, that the Hamiltonian is a two-band model and already a single point is robust. The bands forming such a Weyl point are non-degenerate. Since in the Weyl point the two bands touch (or cross), the point itself is of two-fold degeneracy.

The Weyl cone resulting from Equation 2.5 can be seen as a topologically protected chiral charge [35] or as a pseudo-magnetic monopole in momentum space [36, 37]. Describing the monopole mathematically brings up the so-called *Berry curvature*, which is the flux induced by the monopole. If one now integrates over a small surface hosting such a Weyl point, it adds $\pm 2\pi$ to the flux [38]. The sign is determined by the chirality of the Weyl point. Over the whole Brillouin zone, the total flux needs to be zero. Therefore, Weyl points always need to come in pairs with opposite chirality, which is indicated by the $\pm$ in Equation 2.5.

Above, it was mentioned that a Weyl point is robust on its own. This is, however, not the complete story. The topological stability of a Weyl point inevitably requires the involved bands to be non-degenerate. In other words, the Weyl cones of opposite chirality need to be separated in momentum space, otherwise they will annihilate each other [39]. If this is not the case, a band hybridization could produce an energy gap and destroy the Weyl point. To assure non-degenerate bands, either time reversal (T.R.) or inversion (I.) symmetry needs to be broken. If we assume a particle with momentum k and spin up $\uparrow$, the T.R. symmetry enforces that a particle with opposite spin moves in the opposite direction, i.e., $E(k,\uparrow) = E(-k,\downarrow)$ [40]. In contrast, the I. symmetry requires a particle with the same spin moving in the opposite direction, i.e., $E(k,\uparrow) = E(-k,\uparrow)$. Considering two Weyl points at the same position in k-space, so a touching or crossing point of two doubly degenerate bands, breaking the inversion symmetry will lead consequently to a splitting of the degeneracy in one k-direction and hence, to a robust pair of Weyl points [41]. When breaking the time reversal symmetry, the degeneracy of the bands is lifted in energy.

The band crossings now, however, are not stable and a gap will open. This gap opening will again leave two Weyl crossings behind, which are separated along a certain k-direction [41].
Weyl semimetals, where the cones of opposite chirality are separated in k-space, exhibit interesting properties. The two most famous ones are Fermi arcs and the chiral anomaly, which will be explained in the following.

The Fermi arc has a topological origin and describes the surface states of a Weyl semimetal in real space [35, 36]. A Fermi arc is an open Fermi surface curve and connects projections of the bulk Weyl points with opposite chirality to the surface Brillouin zone. Usually one expects Fermi surfaces to be closed. In a Weyl semimetal, however, the second, complementing Fermi arc is located on the opposite crystal surface, resulting in an open Fermi surface as depicted in panel (a) of Figure 2.2.
Observing such a Fermi arc experimentally is an unambiguous evidence for a Weyl semimetal, as Dirac semimetals or other topological systems will not host an open Fermi surface. Possible techniques to do so will be discussed in section 2.6.

The chiral anomaly represents a violation of classical conservation laws [16, 37, 44]. In general, the chiral anomaly describes that the number of (quasi)particles of one specific chirality is not necessarily conserved. In more detail, the particles of one Weyl cone can be pumped into the cone with opposite chirality. In high-energy physics, this effect is known as the Adler-Bell-Jackiw anomaly, e.g., [36]. In condensed matter, the charge pumping can be realized by applying a magnetic and an electric field parallel to each other. A schematic drawing is shown in Figure 2.2 (b): The starting point are two cones with different chirality and the Fermi level directly at the crossing point. Thus, the chemical potential μ, i.e., the energy distance between Fermi level and crossing point, is zero. If the chirality of some particles is now changed, they will be pumped into the other cone, resulting in different chemical potentials for the different chiralities (here one positive and one negative value).

The most famous WSM family is the TaAs family, which TaAs, TaP, NbAs and NbP belong to. These were also the first Weyl semimetals, where theoretically predicted [45, 46] Weyl points were confirmed by various experimental techniques,

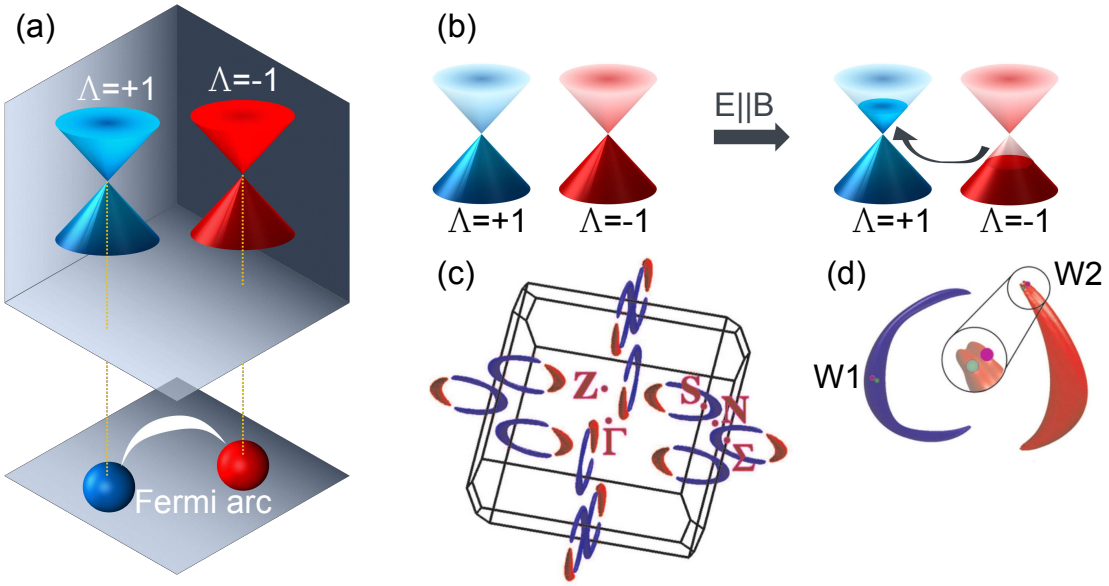

Figure 2.2.: Panel (a) sketches the surface states of a Weyl semimetal. The so-called Fermi arc (white banana-shaped link) connects Weyl points of different chirality and is located at the projection of the Weyl points onto the real crystal surface. The chiral anomaly is depicted in panel (b): the number of charges of one particular chirality is not conserved if parallel B- and E-field are applied. Charge carriers can be pumped into the cone of opposite chirality, leading to different Fermi levels for the different cones. The Fermi surfaces and two types of Weyl pairs in the Weyl semimetal NbP are shown in panels (c) and (d). Panel (c) is redrawn from Ref. [42] and (d) from Ref. [43].

see, e.g., Refs. [47–50]. Within this family, the spin-orbit coupling (SOC) varies, as it is reduced by replacing heavy elements (i.e., Ta or As) by lighter elements (i.e., Nb or P). The SOC plays an important role for the detailed band structure close to the Fermi level and, hence, also for the Weyl physics. The crystal structure is lacking an inversion center, so inversion symmetry is broken [51]. The combination of SOC and broken I. symmetry gaps the band structure almost over the complete Brillouin zone, resulting in two species of Weyl points, which are located off the high-symmetry axes. There are four pairs of the first species (W1) and eight pairs of the second one (W2), leading to a total number of 24 Weyl points. Their exact position with respect to the Fermi level differs for the various compounds. The Fermi surfaces and Weyl points of NbP as a representative of the TaAs family are redrawn from Refs. [42, 43] in panels (c) and (d) of Figure 2.2. These theoretically

predicted band pictures as well as the existence of the two types of Weyl pairs could be confirmed by techniques such as angle-resolved photoemission spectroscopy (ARPES), where the Fermi arcs could be mapped additionally [52, 53].

2.4. Three dimensional Dirac semimetals

On the one hand, 3D Dirac semimetals can be seen analogous to 2D graphene with the Dirac bands dispersing linearly in all three k-directions; on the other hand, they can be seen as a special case of a Weyl semimetal, although in literature, one often reads the opposite. This can be understood by having a closer look at the symmetry situation.
In a 3D SM, the two Weyl cones of opposite chirality are not separated in k-space. As mentioned before, one expects the two chiralities to annihilate leaving a gapped low-energy spectrum behind. This annihilation can, however, be blocked by protecting the Weyl points with special symmetries[15]. This usually involves conserved T.R. and I. symmetry plus an additional rotational symmetry. With this, the Weyl points of opposite chirality can exist at the same position in k-space, so a cone in a DSM (i.e., Dirac cone) is made of two Weyl cones with opposite chirality. The two involved bands causing the touching or crossing point are consequently both doubly degenerate and the Dirac point itself is thus of four-fold degeneracy [15, 34].

As the above mentioned symmetries are crucially required to avoid the annihilation of the Weyl points, one can transfer a Dirac semimetal into a Weyl semimetal by breaking one of them. If one destroys the T.R. symmetry, the two Weyl points usually get separated along the energy axis, while a lack of I. symmetry leads to a splitting along the k-axis [41].
The former one can be achieved by applying a magnetic field, as this breaks the time reversal symmetry. One can, thus, easily understand why the chiral anomaly can also be observed for a 3D DSM, e.g., Ref. [54]. To pump the charges from one chiral cone to the other, parallel magnetic and electric fields are applied. Consequently, the T.R. symmetry is broken and the DSM hosts separated Weyl cones.
Dirac semimetals do also host interesting surface states. These are, however, not as exotic as for the WSM. As stated before, the Fermi arc in a Weyl semimetal is an open Fermi surface that connects projections of Weyl points with opposite chirality.

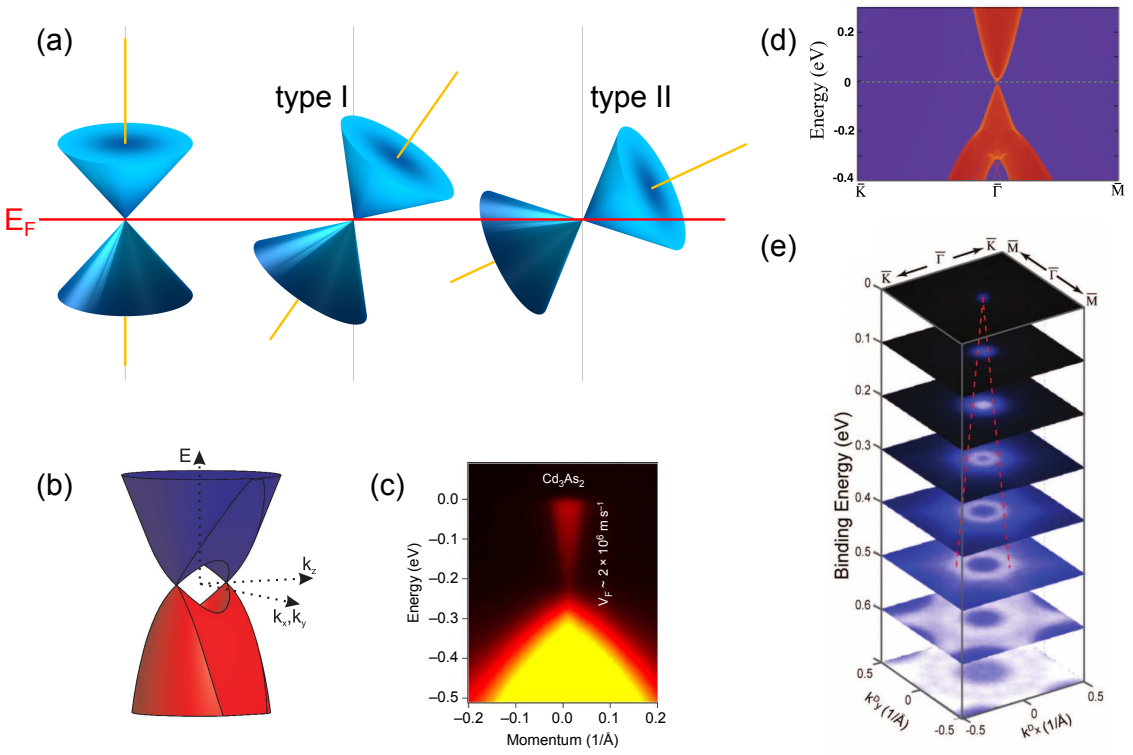

Figure 2.3.: The different possible tilting situations are sketched in panel (a). The untilted (left) and type I tilted (middle) Dirac cone host a closed Fermi surface, while the type II tilting (right) leads to an open Fermi surface, because the cone shells cross the Fermi level. The theoretical band structure of Cd_3As_2 is depicted in panel (b) and could be confirmed experimentally by means of ARPES (c). The same holds for the 3D DSM Na_3Bi given in panels (d) and (e). Panels (b)-(e) are redrawn from the following references: [51] for (b), [56] for (c), [57] for (d), and [58] for (e).

A Dirac point already hosts two Weyl points with opposite chirality. Therefore, the Fermi arcs in a DSM do not produce an open Fermi surface, but a closed one, as discussed and shown experimentally in Ref. [55].

So far, we have only considered more or less ideal Dirac/Weyl cones as depicted in Figure 2.1 (c). Such cones show a symmetric dispersion below and above the touching point. In real materials, the situation is usually not that ideal. First of all, finite temperature and scattering effects as well as mass-induced energy gaps can obscure or change the particular band structure. A more detailed discussion

will follow in section 2.7 in the context of the fingerprints of Dirac physics in the optical response.

One can, however, also imagine different dispersions along different k-directions leading to anisotropic cones. Well-known examples here are $CaMnBi_2$ and $SrMnBi_2$, for which detailed band structures will be discussed in chapter 6. Another possibility to deviate from an ideal cone situation is to tilt the Dirac/Weyl cone[6] into one direction, as sketched in Figure 2.3(a).

For tilted cones, no matter whether they are of Dirac or Weyl type, one distinguishes two different scenarios. While the first one is not so special, the second one is quite exotic and was proposed first by A. A. Soluyanov and co-workers in Ref. [59]. Let us consider, for simplicity, that the Fermi level is located at the Dirac/Weyl point, i.e., $\mu = 0$. For only small tilting angles, the valence bands stay below the Dirac/Weyl point and the conduction bands stay above. This is referred as tilting type I and is depicted in middle of panel (a) in Figure 2.3. Here, the cross section of the Fermi level, i.e., the Fermi surface, remains a point, as in the untilted case. With this, also the basic properties of the cone remain unchanged. One exception is the Fermi velocity (or dispersion), which now becomes anisotropic.

If the cone is tilted further, the conduction shell of the cone dips partly below the Fermi level and the valence shell is partly above it. The cone is now of type II. This situation, referred to as overtilting, is shown on the right of Figure 2.3(a) and is much more interesting. Such type II semimetals host an open Fermi surface, as each half of the cone is crossing the Fermi level. Consequently, the density of states (DOS) at the Fermi level is non-zero, even if the Fermi level is perfectly located at the Dirac point, which will lead to different electronic properties [59]. Furthermore, the Lorentz symmetry is broken in the type II case, which gives no possibility for an analogous particle in nature [60]. In a WSM, tilting of the Weyl cone can be realized if the inversion symmetry is broken [41].

Two well-known and widely investigated examples of three dimensional Dirac semimetals are Cd_3As_2 and Na_3Bi.

In Cd_3As_2, two parabolic bands overlap leading to two touching points protected

[6] From now on, if the context allows, we will not distinguish between Dirac and Weyl states and mention only one of them but refer to both, as scenarios like tilting or nodal lines are applicable to both of them.

by symmetry, as shown in panel (b) of Figure 2.3. Since both, time reversal and inversion symmetry are preserved, each of the bands is doubly degenerate. Hence, the touching points host both chiralities and Cd_3As_2 is a Dirac semimetal. The suggested band structure was confirmed by a comprehensive ARPES study [56], revealing the linear band dispersion in the different k-directions. One exemplary picture is given in panel (c).
The alkali pnictide Na_3Bi also hosts a doubly degenerate cone in the center of the Brillouin zone [57]. Again, T.R. and I. symmetry are preserved and the Dirac point is protected by crystal symmetry and both chiralities are located in the same degenerate cone. The result of first-principles calculations, taken from Ref. [57], is depicted in Figure 2.3 (d), which could in turn be confirmed by ARPES measurements [58], as shown in panel (e).

2.5. Other Dirac materials

In this section, two extraordinary situations of Dirac-like states in condensed matter will be discussed, as they will play important roles for some of the materials presented later. On the one hand, nodal line semimetals will be introduced, illustrating the situation of ZrSiS, which will be investigated in chapter 4. On the other hand, a brief picture of triple point fermions will be provided. These were recently proposed to exist in the half-Heusler compounds YbPtBi and GdPtBi [8] and chapter 5 will contribute a detailed examination of the two compounds.

Nodal line semimetals

In a nodal line semimetal (NLSM), the crossing of bands leading to the linear dispersion is not a point, but rather a line or a circle, as sketched in panels (a) and (b) of Figure 2.4. Thus, also the Fermi surface, which is a point for normal Dirac or Weyl semimetals, becomes a loop or at least a line. This will increase the concentration of Dirac electrons making NLSM preferable for, e.g., sensor application [41, 61].
Since there is no dispersion of the involved bands along a certain k-direction, the Dirac fermions in an NLSM have reduced symmetry compared to the k-space of the material. Hence, the Dirac states in a three dimensional NLSM, as for example in

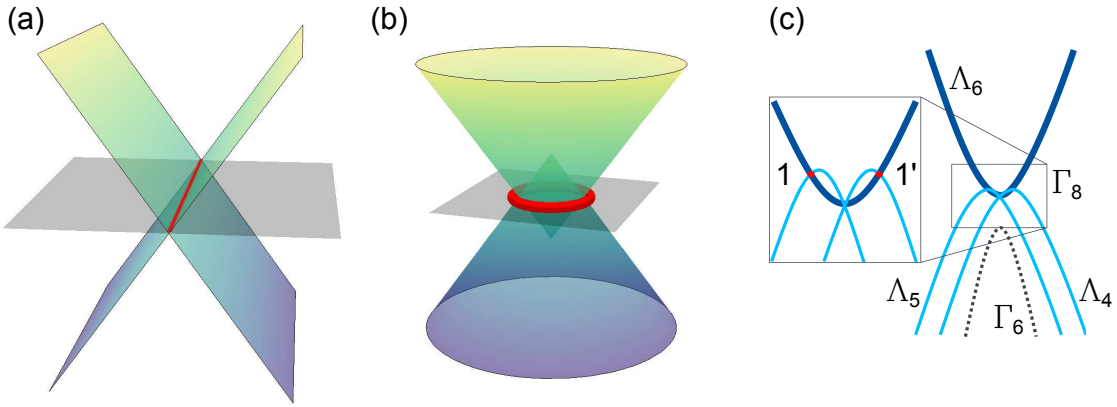

Figure 2.4.: Panels (a) and (b) show the Dirac states of a nodal line semimetal. While the bands disperse linearly in one (or two) k-direction(s), there is no dispersion along the remaining k-direction(s), leading to a line (a) or a circle (b) of Dirac nodes, marked by the red line. The possible triple point structure is displayed exemplary for half-Heusler compounds in panel (c). In the inverted band structure, with Γ_8 (blue) above Γ_6 (gray, dashed), Γ_8 splits and results in crossing points of the doubly degenerate Λ_6 (dark blue) with the non-degenerate Λ_4 and Λ_6 (light blue) bands. Panel (c) is redrawn from Ref. [8].

the most famous NLSM ZrSiS, are two dimensional and behave analogous to the Dirac fermions in graphene [3].
From the material point of view, NLSM have comparably low spin-orbit coupling. As mentioned before, SOC can gap a Dirac point. In an NLSM the crossing is required to exist along a line, which would easily be gapped by strong SOC. Examples for materials in which SOC destroys a nodal line can be found in Bismuth based compounds. When the Bi atoms form a square lattice, a nodal line can be found in k-space [41]. $CaMnBi_2$ and $SrMnBi_2$ represent this type of nodal ring, which is partly gapped by SOC and hybridization as discussed in more detail in chapter 6.

Triple point semimetals

Triple point (TP) fermions can be view as intermediate state between Dirac and Weyl fermions. As mentioned before, two doubly degenerate bands touch at a Dirac point, while two non-degenerate bands create a Weyl point. In a triple point, a doubly degenerate band crosses or touches a non-degenerate band. Consequently, the triple point is of three-fold degeneracy [62]. One of the early publications consid-

ering such a TP can be found in Ref. [63]. In this work, Zaheer *et al.* discuss the situation of tensile-strained HgTe, where the valence band degeneracy is lifted while the conduction band remains degenerate. This is protected by the mirror symmetry of the zinc-blende lattice. The starting point in HgTe is a spin-orbit induced band inversion at the Γ-point of the Brillouin zone. As examined later, the band structure in the half-Heusler compounds YbPtBi and GdPtBi is comparable and they are even considered to belong to the HgTe family. A more detailed picture of possible triple points based on *ab initio* calculations in the half-Heusler compounds can be found in Ref. [8] and is redrawn in Figure 2.4 (c). Here the initial bands Γ_6 (gray) and Γ_8 (blue) are inverted so that Γ_8 is located above Γ_6. Furthermore, Γ_8 is split into the doubly degenerate Λ_6 and the non-degenerate Λ_4 and Λ_5 bands. Thus, the crossing points are of three-fold degeneracy.
Since one of the band's degeneracy is lifted, triple points always come in pairs for the same reason Weyl points do, see section 2.3. Furthermore, TP materials come along with the same exotic features like Fermi arcs or modified Landau level spectrum.

2.6. Experimental techniques to study Dirac materials

In this thesis, optical spectroscopy is used to detect Dirac states of different types in condensed matter. There are, of course, other techniques to observe the fingerprints of Dirac fermions and their low-energy properties. Thus, a brief overview of the most commonly applied techniques will follow in this section.

ARPES

The most direct way to experimentally search for Dirac or Weyl states in solid state research is angle-resolved photoemission spectroscopy (ARPES). In this technique, high energy photons are used to release an electron from the investigated crystal. Measuring the angle of emission and the kinetic energy of the emitted electron provides access to the electronic band structure of the material. Therefore, ARPES can be seen as a mapping tool of the band structure. If this band structure hosts Dirac fermions, their linearly dispersing bands will be directly visible.

Additionally, exotic band features like Fermi arcs, which are located on the surface of the crystal, can be observed directly, as shown, e.g., in Ref. [55].
To first order, the emitted electrons come from the surface of the crystals and, hence, the mapped band structure represents the surface states of the material. By varying the photon energy one can, however, influence the penetration depth of the photon into the crystal. This will lead to a vanishing intensity of bands arising from surface states and provides an opportunity to distinguish them from bulk bands.

ARPES has three main disadvantages. The first one is connected to the physical effect which ARPES is based on: the extraction of electrons. Consequently, ARPES can only provide information about the band structure of occupied states, i.e., below the Fermi level. States above the Fermi level are not filled with electrons and cannot be investigated by ARPES. Therefore, parts of a Dirac/Weyl cone might be inaccessible with this technique.
The second disadvantage is the comparably poor energy resolution of ARPES. State of the art setups can resolve down to a few meV in energy space[7]. This can inhibit making an ultimate statement about the exact band dispersion, as it might deviate slightly from perfectly linear bands. Such a situation is discussed, e.g., in Cd_3As_2, where the bands are suggested to disperse with a power-law of 0.6 [65].
The third negative aspect of ARPES is that a magnetic field cannot be applied simultaneously to the sample. Thus, features like the chiral anomaly or the splitting of a Dirac cone into two Weyl cones cannot be observed with ARPES.

Magneto-transport & quantum oscillations

The second useful and widely applied technique to investigate Dirac or Weyl candidates is magneto-transport with the purpose of observing quantum oscillations in high magnetic fields. In general, magneto-transport experiments can be used to identify high mobilities and low carrier densities, which point towards Dirac states but, of course, do not provide a proof. From quantum oscillations, one is able to draw conclusions about the cross-section of the Fermi surface [43, 66]. On the one hand, this allows to confirm suggested band structure calculations. Additionally, a

[7] E.g., the Shen laboratory at Stanford University can go down to 3 meV corresponding to $24\,\mathrm{cm}^{-1}$ [64].

node-like Fermi surface of a Dirac cone or Fermi arcs of a Weyl semimetal can also be traced. For the latter, the Fermi arc on the upper sample surface and the one on the lower sample surface will be connected forming a closed cyclotron loop. This will contribute periodic-in-$1/B$ quantum oscillations in the density of states [67, 68].

Another unambiguous evidence is suggested to arise from the chiral anomaly by pumping carriers from one chiral cone into the opposite one. This is supposed to give rise to a negative response of the longitudinal magneto-resistance [16, 17]. There is, however, an experimental issue which raises doubts at the realization of this feature: The high mobility of the carriers can lead to so-called current jetting, an inhomogeneous current distribution, if the electrical contacts to the crystal are not perfectly placed [69]. This current jetting will provide the same negative longitudinal magneto-resistance as the chiral anomaly should. Hence, ideally shaped crystals with accurately placed contacts are required to produce trustworthy results.

Disadvantages of this technique can directly be extracted from above. The quantum oscillations are restricted to the Fermi surface, i.e., the band structure directly at the Fermi level, thus, unable to map a cone or even one half of it. Secondly, current jetting might obscure the fingerprints of the chiral anomaly in magneto-transport measurements.

STM

In contrast to above discussed techniques, quasiparticle interference (QPI) based on scanning tunneling microscopy (STM) can be used to access occupied and unoccupied states [60, 70]. Standard STM maps the real space by scanning over the sample letting electrons tunnel through the atomically sharp tip. With this, it is not able to resolve the energy-momentum space $E(k)$ nor provide information about the dispersion of bands. Crystal defects or impurities, however, cause elastic scattering processes which mix the eigenstates of different k-vectors with the same $E(k)$. These mixed states due to scattering at an impurity result in standing waves which can be seen in real space. A Fourier transformation of the QPI directly reveals the momentum transfer across the Fermi surface [71, 72].

Drawing the Fermi surface via the observed scattering vectors allows a direct investigation of the exotic surface physics of Dirac and Weyl semimetals or topological

insulators. For example the Fermi arcs of the WSM TaAs could be mapped successfully by the means of QPI-STM, as described in Refs. [73, 74] in more detail. The main disadvantages are the requirement of a perfectly controlled environment, e.g., vibrations, and of clean and atomically flat sample surfaces. A pro of STM is the possibility to apply an external magnetic field.

Optics

Last but not least, conventional optical spectroscopy can trace fingerprints of Dirac physics. At first glance, this measurement technique does not resolve k-space. For a certain excitation energy, transitions at all positions of the reciprocal space with this energy will be excited. It was shown, however, that if the band dispersion follows a power law behavior $E(k) = k^z$, the real part of the frequency-dependent optical conductivity obeys the particular formula [9, 10]:

$$\sigma_1(\omega) \propto \omega^{(d-2)/z} \quad , \tag{2.6}$$

with the frequency[8] ω and d being the dimensionality of the system. This proportionality can be confirmed with the already well-known behavior: three dimensional semiconducting materials ($d = 3$) with parabolic dispersing energy bands ($z = 2$) result in a square root dependence of $\sigma_1 \propto \omega^{1/2}$ [21].

With Equation 2.6, one is able to verify the linear dispersion relation ($z = 1$) of Dirac-like bands by a characteristic frequency dependence, which will depend on the dimensionality.

Compared to, e.g., ARPES, optical spectroscopy has some benefits: First of all, the energy resolution is much higher, usually better than $1\,\mathrm{cm}^{-1}$ corresponding to $0.1\,\mathrm{meV}$. Thus, features like energy gaps can be resolved with more accuracy. Secondly, optical spectroscopy excites electrons from occupied to unoccupied states, so across the Fermi level, and can therefore probe a complete Dirac cone if the Dirac point is located at (or very close to) the Fermi level. Thirdly, the rather easy possibility of applying additional magnetic field, electric field and/or pressure provides

[8] As the Planck constant $\hbar$ can be used to transform frequencies into energies, the two terms are directly connected and will be used as kind of synonyms in this thesis.

access to tune physical properties like the splitting of a Dirac cone into two Weyl cones. Additionally, applying a magnetic field is needed to investigate Landau level quantization, which also behaves differently for Dirac and Weyl semimetals than for conventional semimetals with parabolic bands, as stated before.

The main disadvantage of this technique is that it averages over the entire k-space. If other (trivial) bands are located close to the Fermi level or maybe even cross it, the spectrum will not only show the Dirac response, but additionally an itinerant carrier response and other interband transitions. This might obscure the characteristic frequency dependence of the Dirac fermions and can make it impossible to identify them.

A more detailed picture of how the different Dirac-like states can be traced by the means of optical spectroscopy will be given in the next section.

2.7. Optical response of Dirac materials: theory

With Equation 2.6, one can directly see that optical spectroscopy can be used to determine the dimensionality of the Dirac states, as for $z = 1$ one obtains for a two dimensional ($d = 2$) case a frequency-independent optical conductivity[9] $\sigma_1(\omega) \propto \omega^0$. This was confirmed by optical measurements on graphene, where the 2D Dirac cones lead to a frequency-independent, universal conductivity of $\sigma_{\text{universal}} = \pi/4\ G_0$ with the quantum conductance $G_0 = 2e^2/h$ [75].
In contrast, a three dimensional ($d = 3$) Dirac cone will lead to a linear frequency dependence of the real part of the optical conductivity $\sigma_1(\omega) \propto \omega^1$. The 3D case was successfully applied to, e.g., the Dirac semimetals Cd_3As_2 [65] and $ZrTe_5$ [76, 77] or the Weyl semimetal family TaAs [51, 78, 79].

Beyond the sensitivity of the optical response to the dimensionality, an in-depth investigation can reveal further details of the Dirac states. From theoretical side, most of the models are provided by J. P. Carbotte and his coworkers, see Refs. [2,

[9] In this section, the term *optical conductivity* as well as σ_1 are mainly used to talk about the interband contributions, while intraband transitions are only taken into account if mentioned.

18, 19, 24, 80–94]. In the following, mainly the three dimensional case will be discussed as 3D Dirac semimetal candidates are the basis of this thesis. However, most of the subsequently introduced special cases are also applicable in two dimensions.

The most general final version of Equation 2.6 was first published by P. Hosur *et al.* in Ref. [9]:

$$\sigma_1(\omega) = \frac{e^2 N_W}{12h} \frac{|\omega|}{v_F} \quad . \tag{2.7}$$

Here, N_W is the number of non-degenerate cones in the first Brillouin zone and v_F the Fermi velocity of the linear bands. Consequently, the linear optical response can be used to determine the Fermi velocity if N_W is known. Since a Dirac cone hosts both chiralities $\Lambda \pm 1$, each Dirac cone is associated with $N_W = 2$. A Weyl cone itself is non-degenerate, so $N_W = 1$, but the Weyl cones always come in pairs, as stated above, leading also to $N_W = 2$ for each pair of Weyl points.
As $\sigma_1(\omega)$ is proportional to the inverse of v_F, a more narrow cone, i.e., with a higher v_F, will lead to a shallow slope in $\sigma_1(\omega)$. This is depicted in Figure 2.5(a).

One further disadvantage of optical spectroscopy can be understood on the basis of Equation 2.7: a difference between Dirac, Weyl or triple points can only be found in different values of N_W. So, by only measuring a linear frequency dependence of the optical conductivity on a material where N_W and the v_F are unknown, one cannot distinguish the types of linearly dispersing states. A complementing experimental technique or theoretical calculations of the band structure are required to draw an ultimate conclusion in such a situation. This can, however, be difficult in some cases, as will be shown in chapter 5.

As mentioned before, Equation 2.7 is only describing the linearity of the optical conductivity on the basis of certain assumptions. It requires that the Dirac point is ungapped and perfectly located at the Fermi level. Furthermore, temperature and scattering are considered to be zero. In a real material, the situation is usually not that ideal and at least a finite temperature and scattering processes will influence the optical response, e.g., Refs. [18, 19].

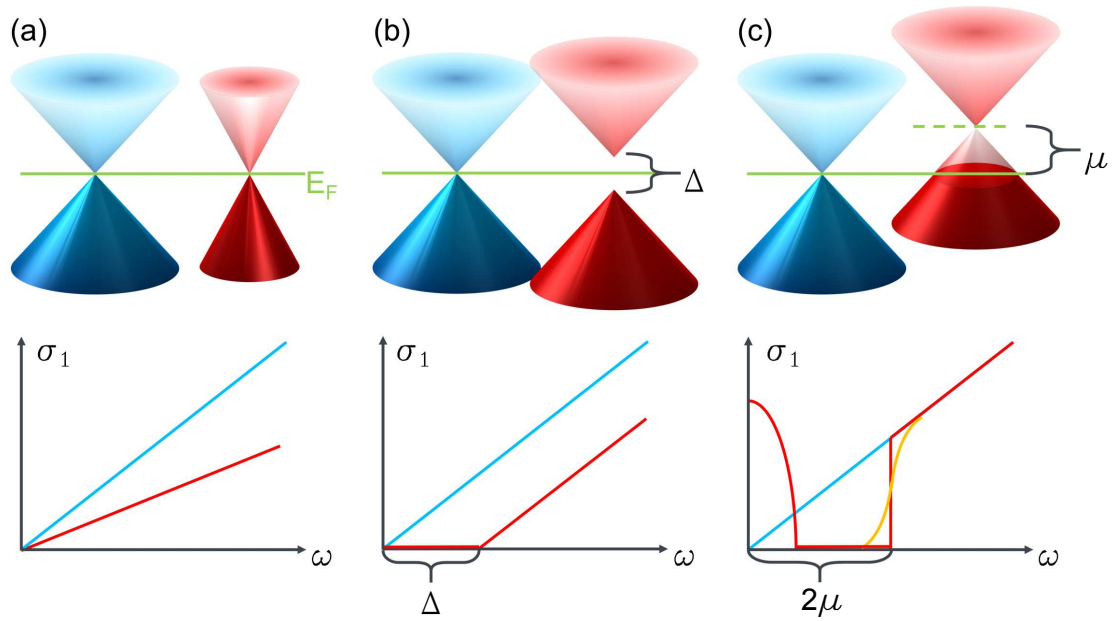

Figure 2.5.: The influence of different effects on the optical response of a three dimensional Dirac cone. (a) The slope of the linear frequency dependent optical conductivity is inversely proportional to the Fermi velocity v_F, thus, a more narrow cone leads to a flatter conductivity. (b) A massless gap Δ opening at the Dirac points shifts the linear optical conductivity away from the origin, leading to $\sigma_1(\omega) = 0$ for $\omega < \Delta$. (c) If the Fermi level E_F is not at the Dirac point, $\sigma_1(\omega)$ is suppressed for $\omega < 2\mu$, with μ being the distance between the node and E_F. At 2μ, a step appears recreating the initial linear conductivity above. At low frequencies, itinerant carriers cause a Drude-like response.

Let us, however, first investigate how an energy gap at the Dirac point will change Equation 2.7. As sketched in panel (b) of Figure 2.5, the bands remain linear down to the closest points if a massless gap Δ is introduced at the crossing point [19]. To excite occupied states from below to above the energy gap, an energy $\omega \geq \Delta$ is required. If the bands remain completely linear, this will shift the linearly dispersing σ_1 horizontally away from the origin, see lower graph in panel (b), as Equation 2.7 will change to:

$$\sigma_1(\omega) = \frac{e^2 N_W}{12h} \frac{|\omega| - \Delta}{v_F} \quad . \tag{2.8}$$

Introducing a mass to the Dirac cone, e.g., via spin-orbit coupling, which usually gaps the Dirac cone, will lead to a small deviation of the bands from linearity in

the vicinity of the gap. Consequently, this will also cause the optical conductivity to deviate from the linear frequency dependence.

Next, we will consider that the Dirac point is not located directly at the Fermi level, but at a finite distance to it. The energy distance is commonly referred as chemical potential[10] μ [18]. Such a shift of the Fermi level produces empty (filled) states in the lower (upper) half of the Dirac cone, suppressing transitions for $\omega < 2\mu$. In contrast to an energy gap, the linearly rising optical conductivity does not start at $\sigma_1 = 0$, but at the initial value corresponding to $\omega = 2\mu$, as shown in Figure 2.5(c). This energy shift can be taken into account by adding a step function to Equation 2.7:

$$\sigma_1(\omega) = \frac{e^2 N_W}{12h} \frac{|\omega|}{v_F} \Theta\{\hbar\omega - 2\mu\} \quad . \tag{2.9}$$

The suppression of $\sigma_1(\omega)$ due to a shifted Fermi level is known also for non-Dirac-like states as a Pauli edge. The shift of the Fermi level away from the Dirac point does not only influence the interband transitions from one half of the Dirac cone to the other half, but also gives rise to transitions within the energy band where the Fermi level is located. Such intraband excitations are commonly referred as metallic or itinerant carriers and can be described with the so-called Drude model, as explained in section 3.6.

Temperature T and scattering Γ have a similar impact on the response of a Dirac cone in the optical spectrum. As they produce a broadening of the Fermi level, they also lead to itinerant carriers at small energies.

In the energy gap scenario, both will have a similar impact as an effective mass will have: a small deviation from linearity of the bands in the vicinity of the energy gap. Thus, the optical conductivity will also deviate from the linear-in-frequency response in this energy range.

For the chemical potential scenario, finite temperature and scattering will smear out the Pauli edge as the Fermi level is broadened. Therefore, it will change from a sharp step function into a smooth rise. This can be taken into account by replacing

[10] Sometimes this distance is wrongly labeled as E_F, which should remain at the Fermi energy itself and not be related to the Dirac point.

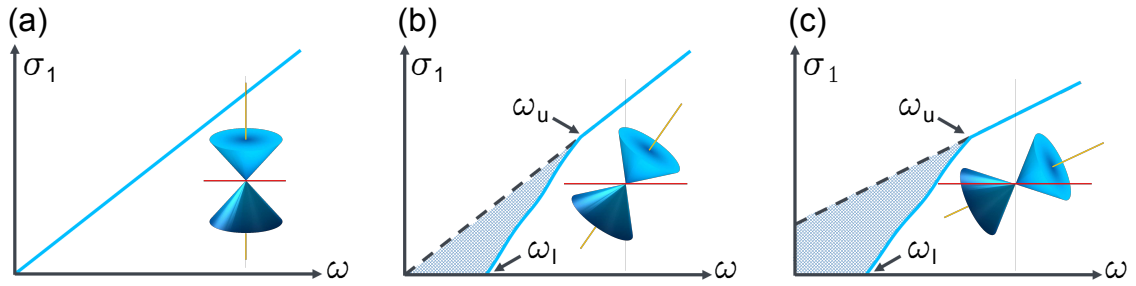

Figure 2.6.: The optical response of a Dirac cone for different tilting angles. (a) The untilted cone gives the previously discussed response. (b) For both tilting types (I and II), $\sigma_1(\omega)$ is quasi-linear for $\omega_l < \omega < \omega_u$ and zero for $\omega < \omega_l$. Above ω_u, both cases reveal a linear frequency dependency, which extrapolates to zero for type I tilting and to a finite value of σ_1 for the type II scenario.

the Θ-function in Equation 2.9 with an arctan-function [1, 19, 51]:

$$\sigma_1(\omega) = \frac{e^2 N_W}{12h} \frac{|\omega|}{v_F} \left[\frac{1}{2} + \frac{1}{\pi} \arctan \frac{\hbar\omega - 2\mu}{\hbar\gamma}\right] \quad . \tag{2.10}$$

Here, γ is the scattering rate, but can also be used to include finite temperature. This smearing is indicated by the orange line in panel (c) of Figure 2.5. It should be noted, that one can of course combine different scenarios, e.g., include the effect of an energy gap into Equation 2.10.

Another aspect that influences the optical response of a Dirac cone is the tilting of the cone, as mentioned in section 2.4. A theoretical model to describe the optical conductivity of a tilted cone is given in Refs. [89, 94] and will shortly be discussed in the following. One has to distinguish here between type I and type II tilting, as the response will differ. Figure 2.6 shows both cases and indicates that the optical conductivity can be used to draw conclusions about the amount of tilting w as well as the position of the Fermi level.
For small tilting angles (type I), the high-frequency response is linear and extrapolates to zero, as indicated by the dashed line in Figure 2.6(b). In the low-frequency range, for $\omega \leq \omega_u = \frac{2\mu/\hbar}{1-\mathrm{w}}$, the optical conductivity differs from this linear slope (shaded area). In this range, $\sigma_1(\omega)$ is lower and cuts the frequency axis at $\omega_l = \frac{2\mu/\hbar}{1+\mathrm{w}}$. These two characteristic frequencies, ω_u and ω_l, can be used to determine the chemical potential μ and the tilt w. Note that for $\frac{2\mu/\hbar}{1+\mathrm{w}} \leq \omega \leq \frac{2\mu/\hbar}{1-\mathrm{w}}$, the optical conduc-

tivity is not perfectly linear in frequency but rather hosts little humps. Below ω_l, the interband response of the tilted cone is zero. The type I tilt is considered for a tilt of $w < 1$.

In the type II case ($w > 1$), the so-called overtilted cone depicted in panel (c) of Figure 2.6, the two characteristic frequencies ω_u and ω_l are defined in the same way. Again, $\sigma_1(\omega)$ is linear in frequency for $\omega > \omega_u = \frac{2\mu/\hbar}{1-w}$. In contrast to the type I, this linear conductivity does not extrapolate to zero but to a finite value on the σ_1 axis. This involves a slope change of the linear conductivity by adding the factor $[\frac{1}{4w^3}(1+3w^2)]$ to Equation 2.7. From this, one can directly distinguish between type I and type II from the optical experiment. For $\omega_l < \omega < \omega_u$, $\sigma_1(\omega)$ is comparable to the type I tilt, is only quasi-linear and cuts the frequency axis at ω_l. For $\omega < \omega_l$, the response is again zero.

Thus, one can distinguish type I and II either from the extrapolation of the high frequency linear response or, with more accuracy, by calculating w from the characteristic frequencies ω_u and ω_l.

Last but not least, the fingerprints of a nodal line semimetal will be discussed, as this will be relevant for ZrSiS presented later. As stated before, in a NLSM, the dimensionality of the Dirac cone is reduced and a line of Dirac nodes can be found in k-space. Up to date, only two theoretical works, Ref. [2] by J. P. Carbotte and Ref. [95] by S. Ahn *et al.*, provide information about the optical response of a nodal line. While both works share many common points, here we will focus on the first one, as is restricted to a more comparable situation for the later discussed ZrSiS. In this theoretical study, the starting point are two 3D cones sitting one in the other and the nodal line forms a circle in k-space, as sketched in Figure 2.4 (b). Consequently, the effective dimensionality on this nodal circle is two, but for energies further away from this nodal line, the response will merge the three dimensional case.

Here, a more general picture of a nodal line semimetal will be considered. The starting point is a Dirac point in three dimensional k-space, as depicted in Figure 2.7 (a). Along one direction, a line is drawn, on which the Dirac point remains unchanged, so there is no dispersion. Along the other two k-directions, a linear band dispersion creates the cone structure. It is obvious, that the Dirac dispersion only exists in two dimensions although we are in a 3D k-space. Thus, in the optical spectrum one

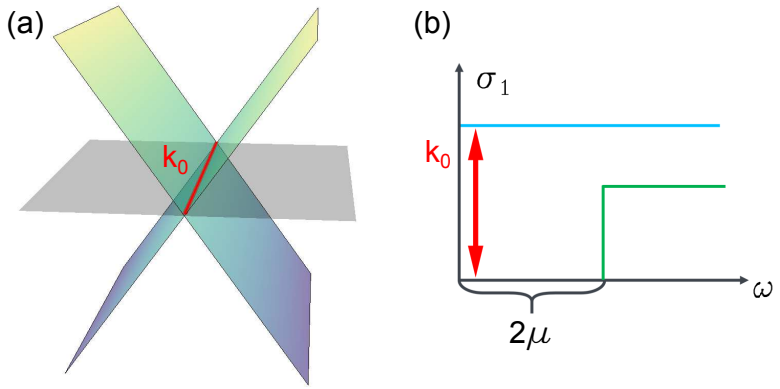

Figure 2.7.: The optical response of a three dimensional nodal line. The reduced dimensionality of the linearly dispersing bands leads to a frequency-independent optical conductivity $\sigma_1(\omega)$. The length k_0 of the line in reciprocal space determines the absolute value of $\sigma_1(\omega)$ as sketched by the different levels for the different colors. Additionally, a shifted Fermi level or an energy gap can suppress the conductivity in the low-frequency range, as indicated for the green case.

does not expect the linear frequency dependence for a 3D semimetal, but rather a frequency-independent optical conductivity as for a 2D cone like in graphene, see Figure 2.7 (b). In contrast to graphene, however, the response does not reflect the universal value $\sigma_{\text{universal}} = \pi/4G_0$, but is determined by the length k_0 of the nodal line in k-space, as sketched by the different levels for the two cases in panel (b). To calculate k_0, a formula given in Ref. [2] was amended and published in Ref. [1]:

$$\sigma_1(\omega) = \sigma_{\text{flat}} = \frac{e^2 k_0}{16\hbar} \quad . \tag{2.11}$$

This formula is valid for a circularly shaped nodal line. If this is not the case, as in ZrSiS, small deviations for k_0 can occur. Note, that also here one can add previously discussed extensions to take, e.g., the position of the Fermi level or an energy gap into account.

3. Experimental details

As described in the previous chapter, optical spectroscopy is a powerful technique to confirm the existence of Dirac fermions in condensed matter and reveal some of the exotic properties. There are, however, different techniques to obtain the optical conductivity of a material. Mostly these can be separated into the different energy ranges, e.g., THz spectroscopy (frequency- and time-domain), Fourier transform spectroscopy, grating spectroscopy and ellipsometry. Each energy range hosts very interesting physical phenomena and an extended list can be found in Ref. [96]. Addressing electronic transitions across the Fermi level to investigate Dirac physics, measuring in the range from several meV to some eV is the method of choice, which is referred to as the infrared (IR) range, partly also the THz range. The light (electromagnetic wave) with a certain wavelength λ and frequency ν used to investigate the optical properties can, of course, also be described as photon with a certain energy E:

$$E = \hbar\omega = h\nu = hc/\lambda = eU = k_B T \quad , \tag{3.1}$$

with U being a voltage, k_B the Boltzmann constant and T the temperature. These relations lead to a connection between the following units:

$$[\mathrm{J}] \mathrel{\widehat{=}} [\mathrm{Hz}] \mathrel{\widehat{=}} [\mathrm{cm}^{-1}] \mathrel{\widehat{=}} [\mathrm{eV}] \mathrel{\widehat{=}} [\mathrm{K}] \quad . \tag{3.2}$$

In this work, mainly wave number, cm^{-1}, is used as unit of frequency/energy and in some particular cases appended by electron volts, eV. Furthermore, ω will be used as symbol no matter whether we deal with frequencies or angular frequencies. As there is no spectrometer available to measure the complete investigated frequency range with high accuracy, several modified infrared spectrometers are used in the context of this thesis. Before having a closer look at the different setups

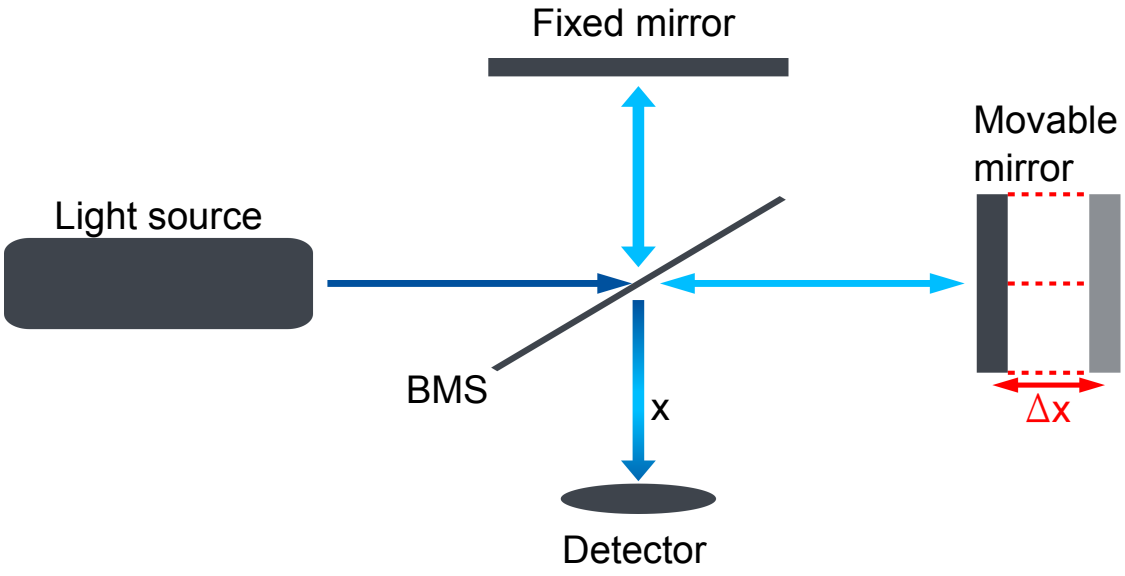

Figure 3.1.: A schematic drawing of a basic Michelson interferometer, the central compound of FTIR spectrometers. After leaving the source, the beam is divided into two parts at the beam splitter (BMS). One of the beams is reflected by a fixed mirror, the other one by a movable mirror. After recombining at the BMS, the light goes to the detector. Depending on the path difference Δx, which is controlled by the movable mirror, the interference after the recombination varies. The possible sample position is marked with x.

and their pros and cons, the basic principle of Fourier-transform infrared (FTIR) spectrometry will be explained, as this is how all operated spectrometers work. In the second half of this chapter, a detailed description of the data processing and a rough picture of other applied experimental techniques will be provided.

3.1. Fourier-transform infrared spectrometry

The heart of any FTIR spectrometer is a so-called Michelson interferometer, invented by A. A. Michelson. A minimalistic sketch to explain the concept is given in Figure 3.1: A light source shines towards a beam splitter (BMS), which divides the light beam into two. Each light path is reflected by a mirror and the two beams interfere at the BMS passing into the same direction to the detector. One of the two mirrors is fixed and so is the path length of this interferometer arm. The second mirror is movable and by changing its position, and thus the path length,

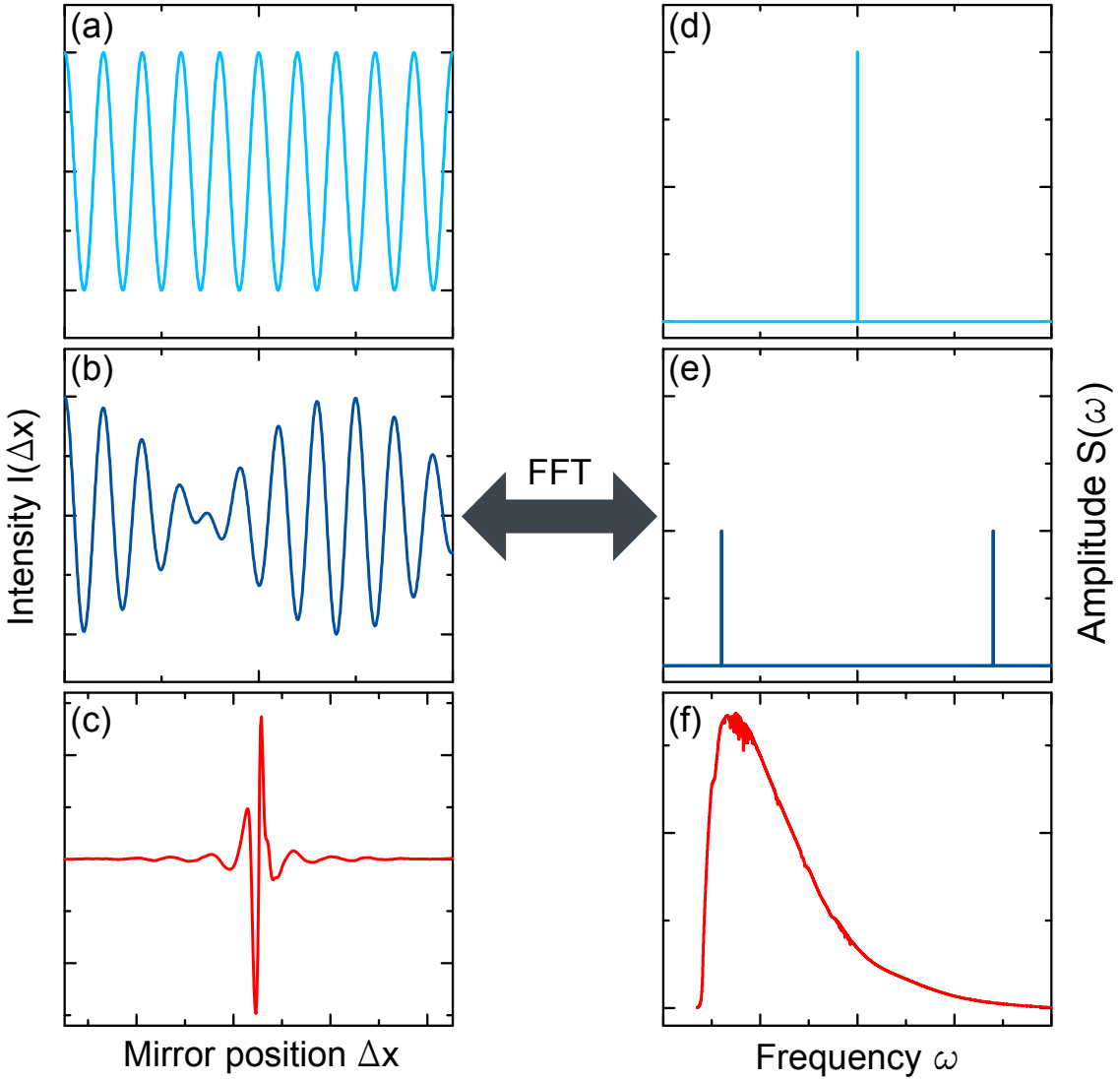

Figure 3.2.: Typical interferograms (left column) and spectra (right column) for different light sources are compared. A monochromatic laser, emitting only a single frequency, is given in (a) and (d). Panels (b) and (e) depict the situation for the beat of two lasers. A thermal light source, as used for FTIR spectroscopy, results in a more complex interferogram (c), but provides a spectrum over a large frequency range (f).

constructive or destructive interference can be achieved at the detector.

Therefore, the resulting intensity profile I commonly called interferogram collected by the detector is a function of the length difference Δx between the two arms. Additionally, the shape of the interferogram $I(\Delta x)$ depends on the type of light

source that is used, which is discussed in Figure 3.2. For a monochromatic light source (i.e., a laser), $I(\Delta x)$ obeys a cosine shape while scanning the movable mirror, see panel (a). By adding a second frequency to the light source, the interferogram reveals a beat of the two cosines. This is depicted in panel (b). Last but not least, a typical interferogram of a thermal light source (in this case the Globar source for the mid-infrared range) is shown in panel (c).
To obtain the frequency-dependent spectrum $S(\omega)$ of a certain interferogram, a Fourier transformation[1] is performed. The results for the three discussed interferograms are given in the right column of Figure 3.2. The monochromatic source, as it contains only one single frequency, produces a δ-function in the spectrum, while the beat signal gives two δ-peaks. The Globar source emits a broad spectrum, giving a high amplitude over a wide frequency range.

Usually, either the frequency-dependent transmittance $T(\omega)$ or reflectance $R(\omega)$ is measured as a starting point to calculate the optical conductivity. Reference measurements are required to get absolute values for the investigated materials. For transmission measurements, the reference is an empty hole, while for reflectivity measurements a mirror is used. This reference mirror should have a well-known and rather high reflectivity. Hence, gold and protected silver mirrors are used to cover the infrared range.
As the frequency range that can be covered by a single measurement is limited by the light source, the detector, the beam splitter and window material, the infrared range (50 to 25 000 cm^{-1}) is commonly divided into different subranges: far-infrared (FIR) $\sim$ 50 to 700 cm^{-1}, mid-infrared (MIR) $\sim$ 500 to 8000 cm^{-1}, near-infrared (NIR) $\sim$ 2000 to 12 000 cm^{-1} and visible (VIS) $\sim$ 10 000 to 25 000 cm^{-1}. An extension by THz spectroscopy and ellipsometry is possible in both directions, to lower and higher frequencies respectively. To cover the different frequency ranges with the best achievable accuracy, different experimental setups with small modifications can be used. A general introduction will follow below. A more detailed description can be found in previous theses, e.g., Refs. [51, 97]. At all setups, cryostats are used to measure at temperatures between 10 and 300 K. The low temperatures provide

[1] The general relation between a function $f(t)$ and its Fourier transform $F(\omega)$ can be found in many textbooks and reads $F(\omega) = \int_{-\infty}^{\infty} f(t)\, e^{-i\omega t} \mathrm{d}t$. More details are given in, e.g., Ref. [21].

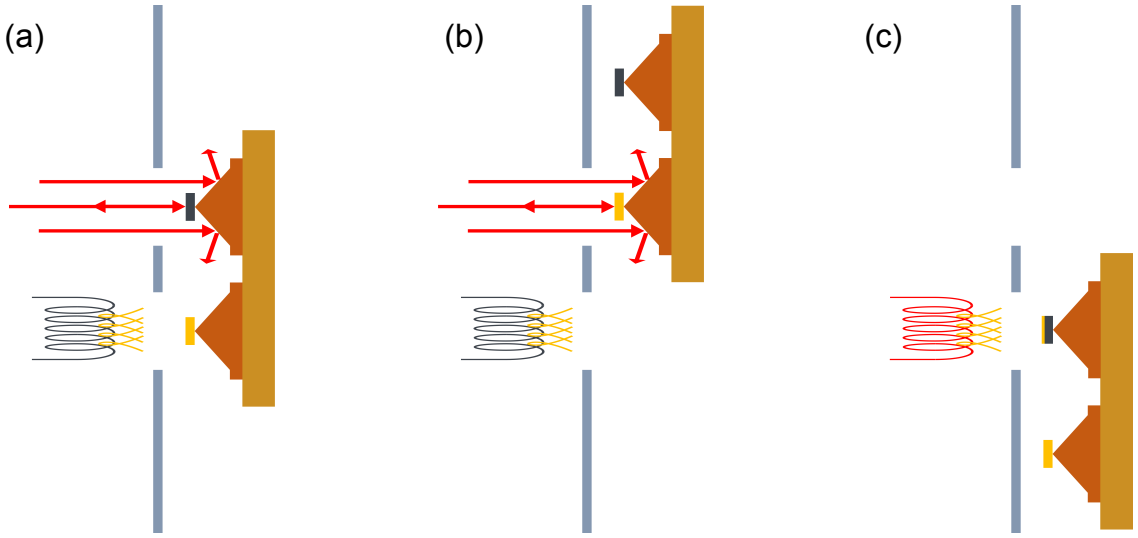

Figure 3.3.: Sketch of the gold evaporation technique applied to measure the FIR range. First, the sample, panel (a), and the gold mirror, panel (b), are measured for all desired temperatures. Before the second run, the sample surface is covered in-situ with a gold layer, panel (c). Due to this gold evaporation - details given in the text - the coated sample serves as perfect reference mirror for the first sample measurement. This eliminates the particular shape and size of the sample surface. Sample and gold mirror are mounted on cones to ensure that only light from the sample/mirror will be reflected to the detector.

a better separation of intraband and interband contributions, as explained later.

3.2. Bruker 113 spectrometer: far-infrared region

The Bruker IFS 113v is best suited for the FIR range. The fact that the complete beam path is evacuated ($p = 10\,\mathrm{mbar}$), is essential to measure this frequency range, as water and other components of air cause absorption lines in this range. Furthermore, a lower measuring frequency (larger wavelength) requires a larger measurement spot. This is limited by diffraction when the wavelength is of comparable size. To comply with this, the beam size in this setup is chosen to be larger than the investigated sample. Hence, the complete area of the sample surface will be measured. To ensure that only light from the sample is reflected to the detector, sample and reference mirror are mounted on copper cones, as depicted in Figure 3.3. Light missing the sample, will be reflected into other directions and will not inter-

fere with the measurement signal.

As the complete sample surface will be measured, it is necessary, that the gold reference has the same shape and size as the sample. To take the particular shape into account an in-situ gold evaporation technique is applied [98]. The procedure is sketched in Figure 3.3.
In a first run, sample s and gold mirror m are measured for all desired temperatures, see panel (a) and (b) respectively. In this particular cryostat, the two are mounted next to each other on the same movable holder. In this first run, the gold mirror serves as reference to compensate drifts, e.g., in the source intensity or the detector sensitivity. After this, the sample surface is coated with a gold layer. To do so, a tungsten wire is heated, evaporating small gold curls onto the sample.[2] This is shown in panel (c) of Figure 3.3. In the second run, the gold coated sample s_{au} and the reference mirror m_{au} are measured again. The final reflectivity of the sample is calculated with:

$$R = \frac{s/m}{s_{\mathrm{au}}/m_{\mathrm{au}}} \quad . \tag{3.3}$$

In the far-infrared range, the intensity of the thermal radiation sources is rather weak. To compensate for this, a bolometer is used as detector. Such a bolometer works at liquid Helium temperature (4.2 K) or even lower (1.2 K), providing a good signal-to-noise ratio even with low light intensity. Either a Globar thermal bulb or a mercury discharge lamp is used as light source in this frequency range. The beam splitter is made of Mylar foil. The measurable frequency range can be varied by changing the thickness of the foil. A good window material with high transparency in the FIR range is polypropylene foil. A more detailed discussion of the different components can be found in Refs. [51, 97].

Magneto-optics

An extension of this setup allows to apply a magnetic field with a strength of up to 7 T. This extension was designed and specified by D. Neubauer in Ref. [51], where

[2] For the gold evaporation, a current of 1.8 A is sent through the tungsten wire for about 70 s. Written instructions for preparing and carrying out the gold evaporation can be found in Ref. [99].

details about the operating procedure can be found. The direction of the applied magnetic field $\vec{B}$ with respect to the propagation vector $\vec{k}$ of the measurement light can be either Voigt or Faraday geometry. In the former, it is $\vec{B} \perp \vec{k}$, while it is $\vec{B} \parallel \vec{k}$ for the latter. Apart from the magnetic field, the measurement procedure is comparable to the gold evaporation measurement without field.

3.3. Optical microscope: from mid-infrared to visible

For the higher frequency ranges, a Bruker Hyperion 1000 microscope is attached to a Bruker VERTEX 80v spectrometer. The advantage of the microscope is a comparably small circular measurement spot on the sample surface, as depicted in panel (a) of Figure 3.4. This is achieved by an aperture, whose size can be varied to create a measurement spot between 20 and 250 µm. Exactly the same spot size and shape are measured on the gold mirror, which makes the gold evaporation technique unnecessary when measuring at high enough frequencies. The resulting reflectivity of the sample can be calculated directly via:

$$R = \frac{s}{m} \quad . \tag{3.4}$$

The disadvantage of the direct reference to the gold mirror is the prerequisite of excellent alignment. The surface of the sample needs to be clean and flat, but most importantly, it has to be perfectly parallel to the surface of the reference. Therefore, sample and gold mirror are mounted on tiltable stages next to each other. The cryostat can be moved with respect to the measurement spot without changing this tilt, see Figure 3.4. A detailed description of this setup can be found in Refs. [97, 100].

For the different ranges, different light sources, detectors, beam splitters and window materials are required. For the MIR range, a Globar light source and a MCT (mercury cadmium telluride) detector are used. KBr serves as window and BMS material. In the NIR range, a tungsten light bulb and an InSb detector are operated. Both, the InSb and the MCT detector work at liquid nitrogen temperature (77 K). The BMS is made of CaF_2, while KBr can still be taken as window material in the NIR range. The VIS range can be measured with a room temperature silicon diode. Quartz glass provides the best windows for this range. BMS and light source can

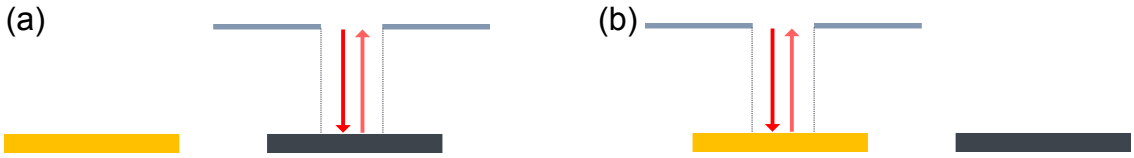

Figure 3.4.: A schematic drawing of the measurement procedure with the Hyperion microscope. An aperture provides a small measurement spot on the sample (a) and gives the possibility to measure the same spot size on the gold reference (b). Sample and mirror need to be aligned perfectly parallel to each other.

be taken similar to the NIR range. Overall, one can cover frequencies from 500 to 25 000 cm^{-1} with the VERTEX 80v + microscope. Of course, one can also measure the FIR range at this setup, but the large wavelength leads to poor results when the measurement spot is too small. Additionally, the Microscope is not evacuated, so air absorptions are disturbing.

3.4. Optical measurements of air sensitivity materials

One main project of this work was to enable optical measurements on air (water or oxygen) sensitive materials, since many of the existing Dirac or Weyl semimetals as well as new candidates are unstable under ambient conditions. In the procedure of preparing optical experiments, the mounting of the crystals as well as the alignment of the sample with respect to the reference mirror is done with an open cryostat. These procedures usually take several hours, during which the crystal is exposed to water and oxygen in air. This exposure time is far too long for many sensitive materials. Two different air exposure junctures were improved to be able to measure air sensitive samples.

On the one hand, in-situ cleaving of the sample after mounting followed by a rough alignment helps to reduce the exposure time down to several minutes, which are needed for the fine alignment. With this, materials which are only slightly sensitive to water or oxygen, e.g., $CaMnBi_2$, $SrMnBi_2$ and YbPtBi, can be measured.

On the other hand, a direct transfer system from a so-called glovebox to the various spectrometers was designed and assembled. This system sets the exposure time to zero, since the crystals are either in argon atmosphere or in high vacuum ($p < 10^{-5}$ mbar). The challenges of the usage of this transfer system for the different

setups are described below. The successful transfer of Sr_3SnO, a highly sensitive materials, is outlined in Appendix A. Sr_3SnO degrades within seconds or even faster when being exposed to air. This proves the applicability of the transfer system.

Glovebox

A glovebox is a closed system with glove-feed-throughs to provide the possibility to work in a controlled gas atmosphere. Commonly, argon 5.0 is used as inert gas to work on water and oxygen sensitive projects. Argon 5.0 has a purity of 99.999% [101]. For this thesis, a MBRAUN glovebox (type: MB200B) was set up. The glovebox achieves an argon atmosphere with less than 0.5 ppm O_2 and less than 0.5 ppm H_2O, measured with MBRAUN sensors MB-OX-SE1 and MB-MO-SE1. Such a high purity atmosphere allows to work on highly sensitive materials at least for several hours, for, e.g., Sr_3SnO, or even days, e.g., ZrSiTe. In both cases, the degradation can be seen by the deterioration of the shiny metallic surface of the crystals or films when exposed to air. The employed glovebox offers three connections to transfer samples and cryostats into the glovebox. Two load locks, a small one for a short loading time and a big one for large equipment. The third connection is an ISO-F 100 flange, which will be used for the newly designed transfer system between the glovebox and the Bruker 113 magnet setup.

Transfer to Bruker 113

For FIR measurements on air sensitive samples, the cryostat of the magneto-optical setup is employed. To be able to mount and align the sample already in the glovebox, the sample holder was redesigned. The cones, on which both reference mirror and sample are mounted, are not fixed directly on the cold finger cryostat but on a removable brass plate. This brass plate and the new sample holder are depicted in Figure 3.5.
After the mounting and alignment under argon atmosphere inside the glovebox, the brass plate can be transferred with a transport box from the glovebox into the cryostat. The transfer system includes a linear translation arm to operate in high vacuum. Inside the cryostat the plate is fixed with screws as indicated in Figure 3.5. The measurement procedure follows the one for normal measurements on non air sensitive samples.

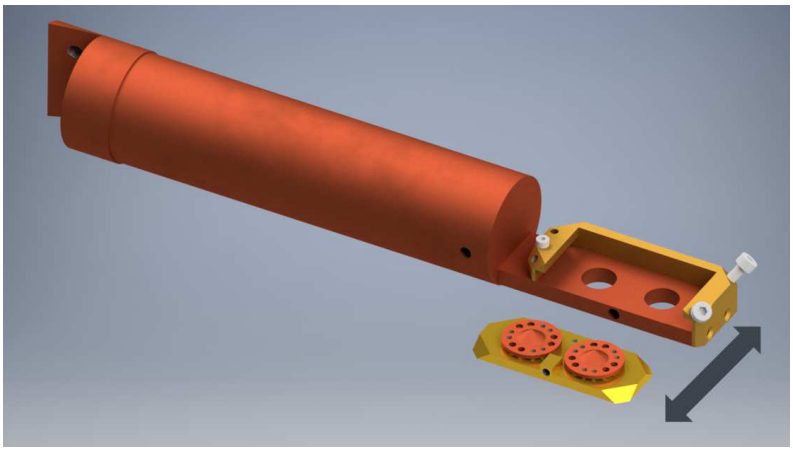

Figure 3.5.: Drawing of the newly designed sample holder and brass plate. With this, the mounting and alignment procedure can be performed under argon atmosphere inside the glovebox. The movable brass plate is transferred with the use of a linear translation arm to the cryostat without any contact to air.

As the gold coated sample serves as second reference in this measurement procedure, the alignment between gold mirror and sample does not have to be as accurate as for the microscope measurements. Thus, a well-performed alignment with a laser pointer is already sufficient.

Transfer to Microscope

The cryostat which is used for measurements with the Hyperion microscope is rather small and fits into the larger loading chamber of the glovebox. Therefore, it can be removed from the microscope and transferred completely into the glovebox. After mounting the sample inside the glovebox, one can easily close the cryostat and fasten the cover with a belt. Thus, the cryostat is filled with argon which will be directly transferred into high vacuum after taking the cryostat out of the glovebox and attaching it to the microscope setup.
The main challenge of this procedure is, that the alignment of the sample surface to the reference mirror needs to be done under the microscope and, hence, with an open cryostat. To avoid this issue, a gold reference is needed which is automatically parallel to the sample surface. By covering half of the investigated sample with a gold layer, a perfectly parallel aligned reference is achieved. For the measurement

of deposited films, this gold layer can be produced directly on the substrate during the film manufacturing. For single crystals, the gold evaporation unit of the FIR setup can be used to cover the sample with gold. After transferring the gold covered crystal back to the glovebox, only half of the gold is removed, resulting in a reference mirror on the sample surface. The subsequent measurement procedure again follows the standard one.

3.5. Kramers-Kronig transformation and data treatment

The physical quantities discussed in the context of optical response functions are usually complex quantities. So is the reflection coefficient $\hat{r} = r(\omega)e^{i\phi_r(\omega)}$. What is experimentally measured for this thesis, is the square of the reflection amplitude $(r(\omega))^2 = R(\omega)$ and will be referred as *reflectivity*.

There are some issues causing a small mismatch in the reflectivity of the absolute values of the different frequency ranges, see Figure 3.6: Measuring at different setups, using various sources, detectors or BMS material or having a slightly different alignment. Physical effects of the investigated material can be excluded for this mismatch, as the different frequency ranges are overlapping. Thus, the individual measurements can be multiplied by a constant factor to eliminate the mismatch. As basis for this shifting, the FIR measurement remains unchanged, since the gold evaporation technique provides the most accurate absolute values.

To fully understand the electrodynamic properties of a material, having only the real part of a response function is not enough. There is, however, no possibility to measure the phase $\phi_r(\omega)$ of the reflection coefficient with the FTIR technique. To overcome this problem, the Kramers-Kronig transformation can be used. It connects the imaginary part G_2 of a response function to the real part G_1 and vice versa.[3] This relation can be found in fundamental text books and reads [21]:

[3] At this point the reader is referred to text books for further information about response functions and their properties, e.g., Ref. [21].

$$G_1(\omega) = \frac{2}{\pi}\mathcal{P}\int_0^\infty \frac{\omega' G_2(\omega')}{\omega'^2 - \omega^2} d\omega' \tag{3.5}$$

$$G_2(\omega) = -\frac{2\omega}{\pi}\mathcal{P}\int_0^\infty \frac{G_1(\omega')}{\omega'^2 - \omega^2} d\omega' \quad . \tag{3.6}$$

The equations above allow to calculate the phase of the reflection coefficient $\phi_r(\omega)$. $\mathcal{P}$ donates the Cauchy principal value. It should be highlighted, that the integration goes from 0 to ∞ in both equations.
Hence, the measured data need to be extrapolated to extend the range. The larger the data range is, the more accurate the Kramers-Kronig transformation will be.

At the low-frequency end, the investigated samples all reveal a metallic behavior due to intrinsic charge carriers. This is commonly described by the Hagen-Rubens (HR) relation [103]:

$$R(\omega) = 1 - 2\sqrt{\frac{2\varepsilon_0\omega}{\sigma_{\mathrm{dc}}}} \quad , \tag{3.7}$$

where σ_{dc} is the conductivity at zero frequency. This formula can be used to extrapolate the measured data below the FIR range. It is indicated by the yellow line in the light gray area of Figure 3.6. Note, the Hagen-Rubens relation is only valid for frequencies much smaller than the scattering rate (or damping) γ, i.e., $\omega \ll \gamma$.
Dirac and Weyl semimetals usually obey a smaller scattering rate compared to conventional semimetals: in the order of a few wave numbers instead of tens or hundreds of wave numbers. Thus, the HR relation might not be valid up to the lowest measured frequency. This problem and a solution will be discussed in more detail in section 5.2.

On the high-frequency end of the measurement window the extrapolation includes two different parts. From 80 000 to $2.4 \times 10^8\,\mathrm{cm}^{-1}$ the experimental data is expanded by X-ray atomic scattering calculations (XRO) according to the procedure of D. B. Tanner in Ref. [102]. These calculations depend on the chemical composition and the lattice parameters of the investigated material. An illustration is given by the pink curve in the dark gray area of Figure 3.6.

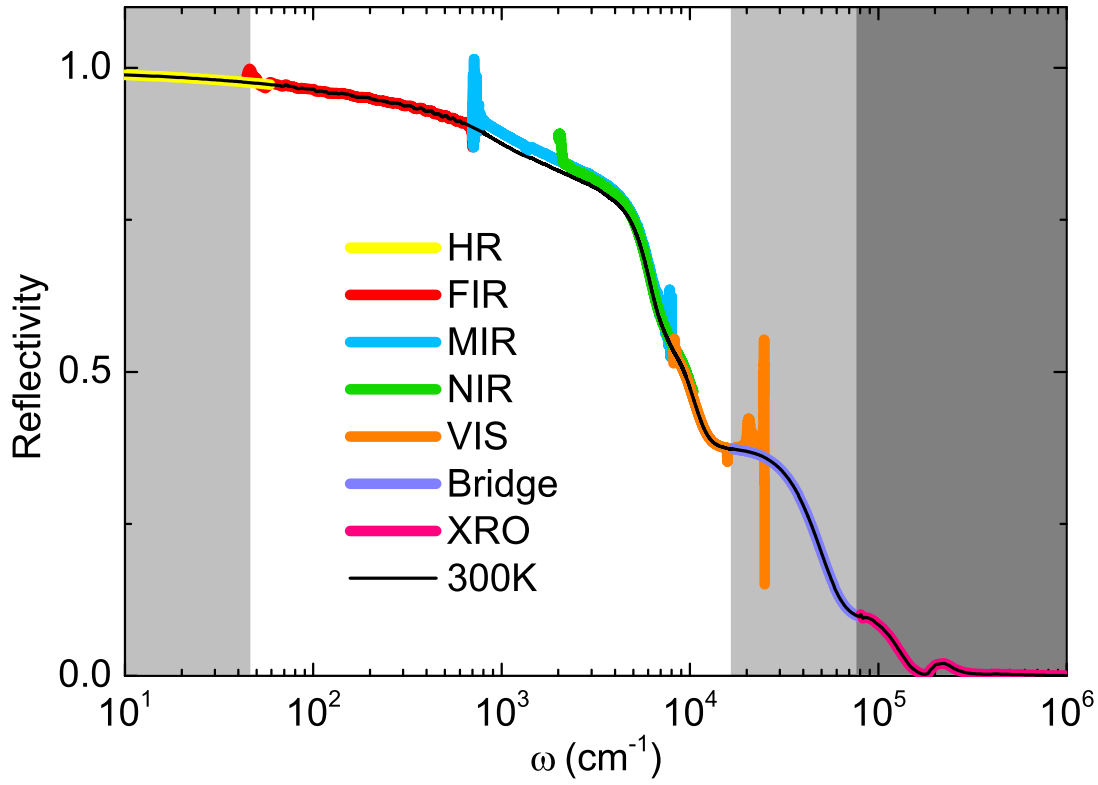

Figure 3.6.: The complete optical reflectivity, here shown for $SrMnBi_2$ at 300 K, is assembled from measurements with different components or setups. The raw data may be slightly shifted to match the absolute value of the FIR range. For this particular set of data, the MIR data was multiplied by 0.98 and the NIR data by 0.985. For a reliable Kramers-Kronig transformation, the measurement window is extended by models (light gray) and calculations (dark gray). At the lower end, the Hagen-Rubens (HR) relation provides metallic reflectivity extrapolation. At the upper end, X-ray atomic scattering calculations (XRO) [102] and a Drude-Lorentz model (Bridge) complete the spectrum.

The gap between the measured data ($25\,000\,\mathrm{cm}^{-1}$) and these XRO calculations ($80\,000\,\mathrm{cm}^{-1}$) is filled by a rough fit of the reflectivity $R(\omega)$ with the Drude-Lorentz model described later. This bridge ensures a more reliable result of the Kramers-Kronig analysis at the upper end of the measured frequency window and is also demonstrated in Figure 3.6.

Note, while the extrapolations are essential for the Kramers-Kronig transformation, they should not be completely included into the interpretation of the optical

response. Therefore, the results presented later will mainly be restricted to the measured frequency window, i.e., 50 to 25 000 cm^{-1}.

Optical response functions

After calculating the imaginary part of the complex reflection index via the Kramers-Kronig transformation, other complex optical functions can be calculated to discuss the results. Equations and interpretations are based on Ref. [21]. For simplification, the equations below consider a non-magnetic material, i.e., the material's permeability $\mu_1 = 1$.
The complex refractive index $\hat{N}(\omega) = n(\omega) + ik(\omega)$ can be determined directly from $\hat{r}(\omega)$ as follows:

$$R(\omega) = |\hat{r}(\omega)|^2 = \left|\frac{1-\hat{N}(\omega)}{1+\hat{N}(\omega)}\right|^2 = \frac{(1-n(\omega))^2 + (k(\omega))^2}{(1+n(\omega))^2 + (k(\omega))^2} \tag{3.8}$$

$$\phi_r(\omega) = \arctan\frac{-2k(\omega)}{1-(n(\omega))^2-(k(\omega))^2} \quad . \tag{3.9}$$

The real refractive index $n(\omega)$ and the extinction coefficient $k(\omega)$ are commonly used to discuss the propagation and dissipation of electromagnetic waves in the medium.

Next, the complex dielectric function $\hat{\varepsilon}(\omega) = \varepsilon_1(\omega) + i\varepsilon_2(\omega)$ is related to the complex refractive index $\hat{N}(\omega)$:

$$\hat{\varepsilon}(\omega) = (\hat{N}(\omega))^2 \tag{3.10}$$

$$\varepsilon_1(\omega) = (n(\omega))^2 - (k(\omega))^2 \tag{3.11}$$

$$\varepsilon_2(\omega) = 2n(\omega)k(\omega) \quad . \tag{3.12}$$

The complex dielectric function $\hat{\varepsilon}(\omega)$ is defined by the change of an electromagnetic field entering a medium. The real part $\varepsilon_1(\omega)$ and the imaginary part $\varepsilon_2(\omega)$ take the change of the amplitude and phase into account.

Last but not least, the complex optical conductivity $\hat{\sigma}(\omega) = \sigma_1(\omega) + i\sigma_2(\omega)$ can be calculated from the complex dielectric function $\hat{\varepsilon}(\omega)$:

$$\hat{\sigma}(\omega) = i\varepsilon_0\omega\ (1 - \hat{\varepsilon}(\omega)) \tag{3.13}$$

$$\sigma_1(\omega) = \varepsilon_0\omega\ \varepsilon_2(\omega) \tag{3.14}$$

$$\sigma_2(\omega) = \varepsilon_0\omega\ (1 - \varepsilon_1(\omega)) \quad . \tag{3.15}$$

Note, while the relations between $\hat{r}$, $\hat{N}$ and $\hat{\varepsilon}$ always involve the real and imaginary parts to calculate another quantity, Equations 3.13-3.15 provide an equivalence between the dielectric function and the optical conductivity. The real (imaginary) part of the optical conductivity is connected to the imaginary (real) part of the dielectric function.

From now on, the real part of the optical conductivity $\sigma_1(\omega)$ and the real part of the dielectric function $\varepsilon_1(\omega)$ will be used to discuss the optical properties of the materials. This is the common way of the infrared spectroscopy community and is based on the fact, that only these two quantities are defined at $\omega = 0$ [21]. The fact that dc ($\omega = 0$) values are taken as low frequency extrapolation verifies this choice.

3.6. Drude-Lorentz model

There are two basic models, the Drude and the Lorentz model, which can be combined to describe any optical response [104]. At the beginning, this model usually does not allow a direct physical interpretation of the obtained results, but helps to achieve quantitatively reasonable extrapolations and Kramers-Kronig results. This does not mean, that no physical interpretation can be derived by applying the Drude-Lorentz model. For conventional materials, e.g., metals or semiconductors, interband transitions and quantities such as the amount of itinerant carriers and their scattering rate can be identified. In the following, both models will be explained, while a more detailed derivation can be found in many fundamental books, e.g., Ref. [21].

The Drude model

The Drude model, more precisely the Drude-Sommerfeld model, is based on the idea of a relaxing system. Within an average relaxation time $\tau = 1/\gamma$, the system returns to equilibrium. The Sommerfeld extension takes an effective mass m^*, i.e., the curvature of the Fermi surface into account. This extension provides much better absolute values for the optical response. In this model, the electrons of the material behave like a classical gas which only interacts via collisions. The resonance of the motion caused by measurement light is located at zero frequency ($\omega = 0$). In terms of the optical conductivity, the Drude-Sommerfeld model leads to the following optical response:

$$\hat{\sigma}(\omega) = \frac{\sigma_{\mathrm{dc}}}{1 + i\omega/\gamma} \tag{3.16}$$

$$\sigma_1(\omega) = \frac{\sigma_{\mathrm{dc}}}{1 + \omega^2/\gamma^2} \tag{3.17}$$

$$\sigma_2(\omega) = \frac{\omega\sigma_{\mathrm{dc}}/\gamma}{1 + \omega^2/\gamma^2} \quad , \tag{3.18}$$

with $\sigma_{\mathrm{dc}} = \frac{Ne^2}{\gamma m}$ being the conductivity at zero frequency, i.e., $\sigma_1(\omega = 0)$. Furthermore, the plasma frequency ω_{pl} is defined as the oscillation frequency of the charge density:

$$\omega_{pl} = \sqrt{\frac{Ne^2}{\varepsilon_0 m}} \quad . \tag{3.19}$$

The Drude-Sommerfeld model can be used to describe the electrodynamic response of free (itinerant) electrons. Such electrons can be found, e.g., in metals and semimetals.

The optical response of the Drude model in terms of the reflectivity $R(\omega)$, the real part of the optical conductivity $\sigma_1(\omega)$, and the real part of the dielectric function $\varepsilon_1(\omega)$ is depicted in the top row of Figure 3.7 for typical values. The scattering rate (or damping) γ and the dc conductivity σ_{dc} are varied. In such a clean case, the plasma frequency ω_{pl} can be determined from the sharp edge in the reflectivity spectrum. The damping defines the width of the peak in $\sigma_1(\omega)$.

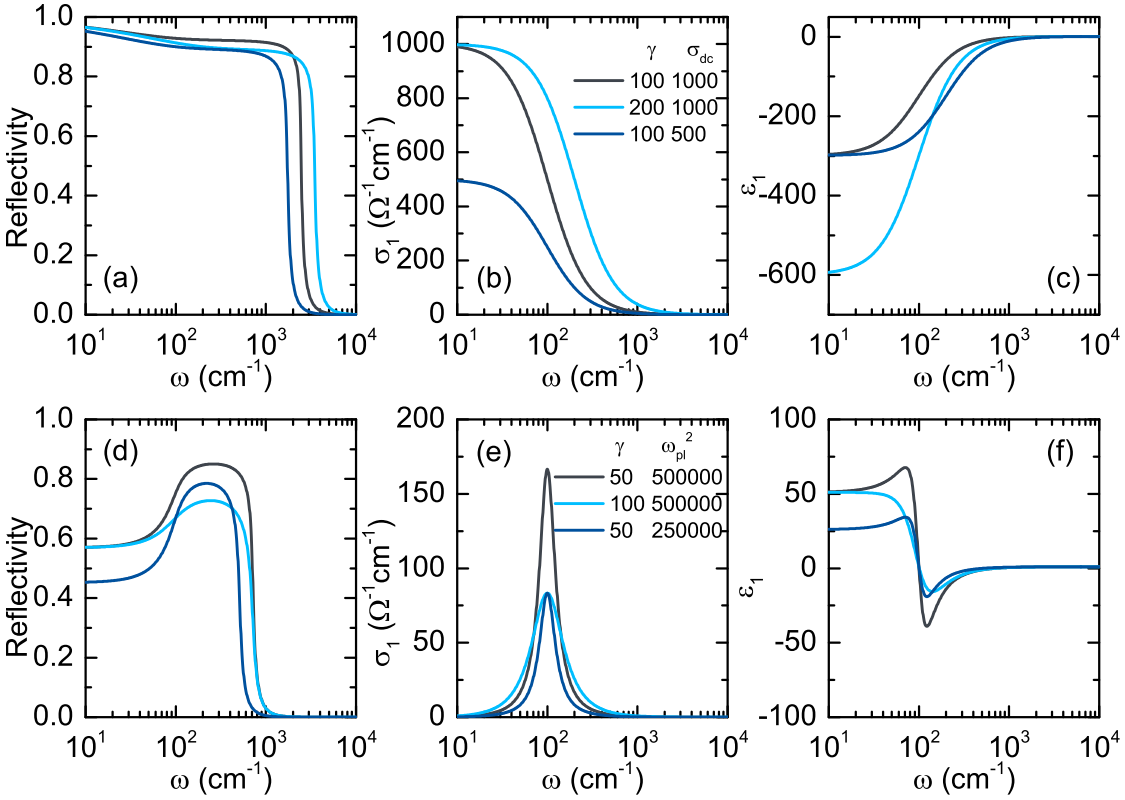

Figure 3.7.: Top row: Optical response functions of the Drude model in terms of the reflectivity $R(\omega)$ in panel (a), the real part of the optical conductivity $\sigma_1(\omega)$ in panel (b), and the real part of the dielectric function $\varepsilon_1(\omega)$ in panel (c). Different values for the damping γ [cm^{-1}] and the dc conductivity σ_{dc} [$\Omega^{-1}\mathrm{cm}^{-1}$] are compared. The sharp edge in $R(\omega)$ is located at ω_{pl}. Bottom row: The same functions for the Lorentz model in panel (d), (e) and (f) respectively. Besides the damping γ [cm^{-1}], here the so-called oscillator strength ω_{pl}^2 [cm^{-2}] is varied, while the resonance frequency ω_{res} is chosen to be $100\,\mathrm{cm}^{-1}$.

The Lorentz model

The Lorentz model can be seen as a generalized version of the Drude model. By adding a restoring force, electrons are bound to the nuclei in the lattice. This force leads to a non-zero resonance frequency ω_{res}, leading to a damped harmonic oscillator model. The optical response, again in terms of the complex optical conductivity,

reads:

$$\hat{\sigma}(\omega) = \frac{Ne^2}{m} \frac{\omega}{i(\omega_{\text{res}}^2 - \omega^2) + \omega\gamma} \tag{3.20}$$

$$\sigma_1(\omega) = \frac{Ne^2}{m} \frac{\omega^2\gamma}{(\omega_{\text{res}}^2 - \omega^2)^2 + \omega^2\gamma^2} \tag{3.21}$$

$$\sigma_2(\omega) = \frac{Ne^2}{m} \frac{\omega(\omega_{\text{res}}^2 - \omega^2)}{(\omega_{\text{res}}^2 - \omega^2)^2 + \omega^2\gamma^2} \quad . \tag{3.22}$$

These can be transformed into the Drude model (Equations 3.16-3.18) by setting the restoring force and, hence, the resonance frequency ω_{res} to zero.
While investigating the optical response of a material, the Lorentz model can be applied to describe phonons, molecular vibrations, interband charge excitations and more.
The optical response of a Lorentz resonance in terms of the reflectivity $R(\omega)$, the real part of the optical conductivity $\sigma_1(\omega)$ and the real part of the dielectric function $\varepsilon_1(\omega)$ is depicted in the bottom row of Figure 3.7. The resonance frequency ω_{res} is fixed at $100\,\text{cm}^{-1}$. Again, the influence of the damping γ is investigated. Furthermore, the oscillator strength ω_{pl}^2 is changed. Comparable to the Drude model, the full width at half maximum of the peak in $\sigma_1(\omega)$ is given by γ, while the plasma frequency ω_{pl} provides a zero crossing from negative to positive values in $\varepsilon_1(\omega)$.

3.7. Other experimental techniques utilized in this thesis

In the last section of this chapter, the basic principles of other applied experimental techniques will be mentioned. As measurements with these techniques were not directly done by the author, detailed instructions should be found elsewhere.

(Magneto-)Transport

Knowing the resistivity $\rho(T)$ of a material allows not only fast and deep insights into the material's properties. As described above, the dc resistivity is commonly used to extrapolate the optical data in the low frequency range. To obtain $\rho(T)$, a standard four-contact technique is applied to measure the resistance $R(T)$. A detailed description can be found in the PhD-thesis of A. Löhle [105], who was

mainly executing the (magneto-)transport measurements, or in Ref. [106]. With the four-contact method, the voltage dropping at the sample can be measured without including inaccuracies caused by resistance at the contacts. The resistivity of the material can be calculated by knowing the sample's dimensions:

$$\rho(T) = R(T) \cdot \frac{A}{l} = \frac{V(T)}{I} \cdot \frac{A}{l} \quad , \tag{3.23}$$

with the voltage drop V, the applied current I, the sample's cross section A, and length l.

Applying a magnetic field to the resistivity measurement provides access to three different quantities: the transversal magneto-resistance, where the B-field is aligned perpendicular to the measurement current I; the longitudinal magneto-resistance, with $B \parallel I$; last but not least, the Hall resistance, which is caused by a voltage drop perpendicular to the applied current and the B-field.
These magneto-transport quantities will be used to identify a two-channel conduction in YbPtBi.

EDX

The quality of a crystal cannot only be determined by the residual resistivity ratio (e.g., section 5.2), but also by measuring the elemental composition and homogeneity. To do so, energy-dispersive X-ray (EDX) spectroscopy is used. The measurements were performed with the assistance of C. Kamella at the Max-Planck-Institut für Festkörperforschung in Stuttgart.
In EDX spectroscopy, electrons are removed from an inner shell. This empty state is then occupied by the relaxation of an electron from a higher shell. This relaxation goes hand in hand with the emitting of X-rays. The energy of the emitted radiation is characteristic for different chemical elements, see, e.g., Ref. [107].
This technique was applied to verify the quality and homogeneity of the $SrMnBi_2$ and $CaMnBi_2$ crystals.

Magnetic susceptibility

In some cases, the magnetic susceptibility $\chi(T)$ provides essential information about general properties of a material. It helps to identify spin alignments as ferromag-

netic (FM) or antiferromagnetic (AFM), or trace spin and charge density waves. The magnetization is measured with a commercial MPMS (magnetic property measurement system) from Quantum Design based on a superconducting quantum interference device (SQUID). For a detailed description the reader is referred to Ref. [108].

4. ZrSiS - a nodal line semimetal with non-symmorphic symmetry

In the following chapter, the results obtained for the NLSM ZrSiS are presented. Therefore, section 4.1 will summarize the properties of the material found in literature, followed by a detailed discussion of the optical response of ZrSiS in terms of Dirac physics in section 4.2. A summary will be given in section 4.3.
Parts of the data and analysis presented in this chapter are published in Ref.[1].

4.1. The material

Already in 1995, the structural dimensionality of different compounds of the ZrSiS family were investigated [109]. Twenty years later, Q. Xu *et al.* searched for topologically non-trivial states within this family [110]. In their first-principles calculations, they found ZrSiO to be a three dimensional weak topological insulator. Furthermore, their calculations on other WHM compounds (W = Zr/Hf/La, H=Si/Ge/Sn/Sb and M=O/S/Se/Te) suggested a comparable electronic structure and possible topological insulating states.

Only one year later, several studies found ZrSiS to be a Dirac semimetal instead of a 3D topological insulator [3, 111–115]. To obtain a deeper insight into the electronic band structure, generalized gradient approximation (GGA) calculations performed by L. M. Schoop *et al.* in Ref. [3] are redrawn in Figure 4.1.
Panel (a) depicts the bulk electronic bands without the influence of spin-orbit coupling (SOC). Bands crossing the Fermi level involved in forming Dirac cones with linear dispersion are given in different colors, while other bands are black. Dirac

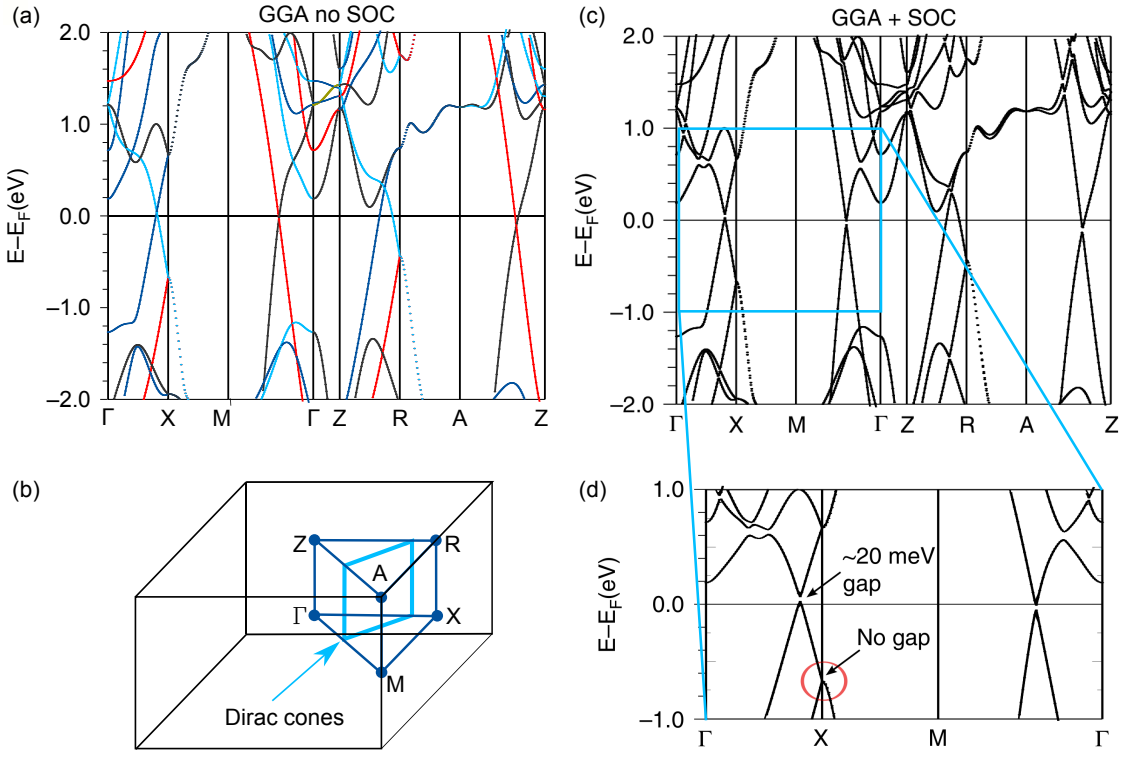

Figure 4.1.: The electronic band structure of ZrSiS obtained by first-principles calculations without (panel (a)) and with (panels (c) and (d)) spin-orbit coupling. The bands involved in forming the Dirac cones with linear dispersion are colored. Close to the Fermi level, a line of Dirac nodes can be found as depicted in panel (b). These Dirac nodes are gapped when SOC is included. The Dirac nodes at the X-point, which are located further off the from the Fermi level, are protected by non-symmorphic symmetry and, hence, remain ungapped. Adapted from Ref. [3].

points can be found very close to the Fermi level on the lines between several high symmetry points, i.e., Γ-X, M-Γ and A-Z. Note, that there are more Dirac points connecting these cones off the high symmetry lines. This leads to a so-called nodal line, as introduced in section 2.5. The line of Dirac cones in the first Brillouin zone is sketched in panel (b) of Figure 4.1.

From the band structure of the high symmetry lines in panel (a), one can see that the position of nodes varies with respect to the Fermi level. While it is above E_F between the Γ- and the X-point, it is slightly below E_F between the A- and Z-point, for example. This energy difference between the nodes and E_F is referred to as the chemical potential μ, as described in section 2.7.

The Dirac-like bands of the nodal line do not disperse along the direction of the nodal line at all. Hence, the dimensionality of the Dirac bands is reduced from 3D to 2D. This can be confirmed by investigating the Fermi pockets created by these bands by means of quantum oscillations, as described later.
The nodal line leads to a comparably high density of Dirac fermions in the vicinity of the Fermi level. In ZrSiS, all bands involved around E_F disperse linearly. This holds over a range of $\pm 0.5\,\mathrm{eV}$, as shown in Figure 4.1. Thus, ZrSiS is, so far, the Dirac semimetal with the largest range of linear dispersion. Some of the bands even disperse linearly over more than 2 eV.
Furthermore, additional Dirac nodes can be found directly at the X-point. These nodes are approximately 0.7 eV below and above the Fermi level. As they do not belong to the line node, they are supposed to be three dimensional.

By including the spin-orbit coupling into the calculations, the linear band crossings become partly gapped, as shown in panels (c) and (d) of Figure 4.1. In more detail, an energy gap opens at all linear crossings in the vicinity of the Fermi level. This gap is estimated to be roughly the size of 20 meV. The rather small value of the energy gap is related to the light elements of ZrSiS, which are associated with only weak spin-orbit coupling.
Remarkably, the Dirac points at the X-point are not influenced by the spin-orbit coupling. This can be pinned down to the non-symmorphic[1] symmetry, which is present in the ZrSiS family. The non-symmorphic symmetry requires a touching of the upper and the lower band even in the presence of strong SOC [116]. Thus, the Dirac nodes at the X-point are robust and remain ungapped.

These extraordinary Dirac nodes protected by non-symmorphic symmetry are influenced by the lattice parameters. Thus, different members of the ZrSiS family host these Dirac nodes at distinct energy values with respect to the Fermi level. A detailed investigation can be found in Ref. [117] and is summarized in panel (a) of Figure 4.2.
Since both, the upper and the lower node are located below E_F in HfSiTe, it offers

[1] The non-symmorphic space groups host symmetry operations which combine point group operations with translations that are a fraction of a Bravais lattice vector. An extended description can be found, e.g., in Ref. [116].

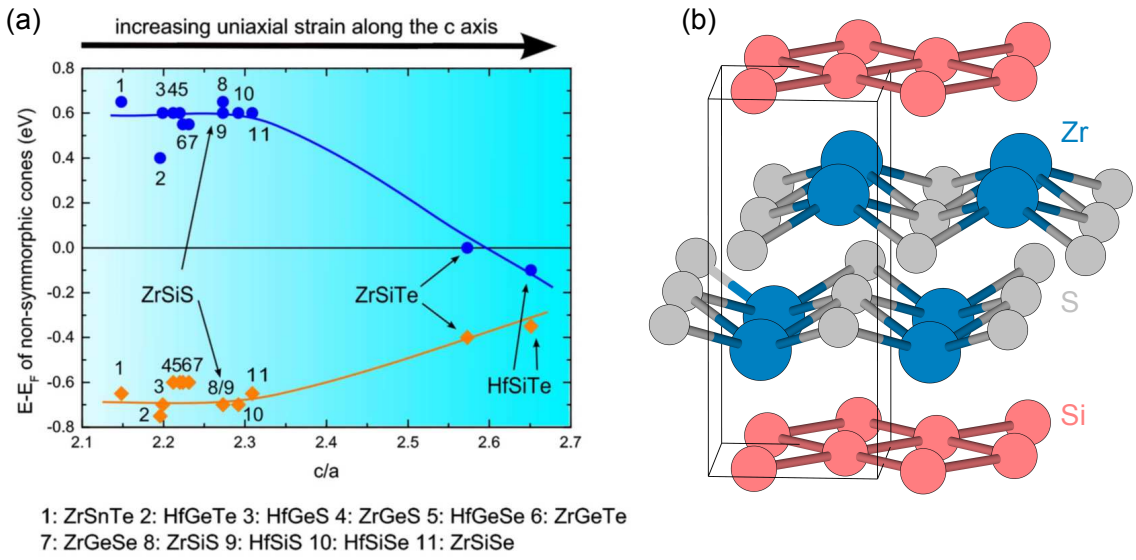

Figure 4.2.: Panel (a) compares the position of the Dirac nodes protected by non-symmorphic symmetry for different members of the ZrSiS family. Redrawn from Ref. [117]. The unit cell of ZrSiS drawn with VESTA [118] is given in panel (b). It is of PbFCl type: tetragonal geometry and space group P4/nmm (no. 129). The crystals can be cleaved easily between the sulfur layers.

the possibility to investigate the physics with ARPES. ZrSiTe is an ideal candidate for optical spectroscopy to investigate the Dirac physics protected by non-symmorphic symmetry. Here, the upper node is located at the Fermi level, while the lower one is approximately 400 meV below. This is, however, only ideal when considering the Dirac nodes protected by non-symmorphic symmetry. The situation might be blurred by the nodal line which is also located also in the vicinity of the Fermi level. For ZrSiS, the states are separated from the nodal line, providing an ideal situation to investigate only the nodal line physics.

Besides the robust Dirac nodes, ZrSiS hosts surface states (SS) of exotic nature, which are not included in Figure 4.1. The non-symmorphic symmetry is broken at the surface of the crystal due to the reduced dimensionality [119]. The electronic bands at the X-point of the Brillouin zone, which are locked in the bulk, become unpinned at the surface. These unpinned bands can float, making the SS distinguishable from the bulk states. Furthermore, the bands of the surface states hybridize with the bulk bands, but are forbidden to cross them by symmetry [3].

A consistent picture of band calculations and ARPES measurements can be found in Refs. [3, 115, 119]. Since the SS are independent of the Dirac states in ZrSiS, but created by the non-symmorphic symmetry, they should also be present in other materials with non-symmorphic symmetry.

The transport properties of ZrSiS were investigated thoroughly by several studies [111–115, 120–123]. These provide information about the charge carrier type and mobility by the means of Hall measurements and give details (e.g., effective mass) about the Fermi surface and its pockets by quantum oscillations. The latter can be extended by more advanced techniques like thermoelectric power measurement [124] and scanning tunneling spectroscopy (STS) [125]. Magneto-transport measurements reveal a hole dominated transport with a mobility of $\mu_h \approx 30\,500\,\mathrm{cm}^2/\mathrm{Vs}$. Furthermore, the transversal magneto-resistance does not saturate up to a magnetic field strength of 53 T increasing it by 10000% compared to zero field [112]. These values are typical for Dirac or Weyl fermions, which can be taken as first indication for their presence in this compound. A negative longitudinal magneto-resistance was measured by R. Singha *et al.*,and was interpreted as the chiral anomaly [122]. Doubts due to current jetting, as described in section 2.6, cannot be excluded for their work, so the results should be used with care.
Quantum oscillations reveal two main pockets of different size, a smaller one of electron type and a larger one of hole type. A more detailed study in combination with ARPES measurements concludes a diamond-shaped hole pocket at the Γ-point, an elliptical hole pocket around the M-point, and the small electron pocket close to the X-point [115]. All pockets have a reduced effective mass, with $m_{\mathrm{eff}} = 0.11$, 0.16 and 0.27 m_e, respectively [113]. Furthermore, all pockets lead to a Berry phase of π, which indicates the non-trivial topology of the charge carriers. The extension by thermoelectric power and STS measurements reveal sub-pockets within the hole pockets leading to a total number of five pockets [124, 125].

More recent work of L. Aggarwal *et al.* discusses the possibility to induce superconductivity in ZrSiS with a metallic tip [126]. First-principles calculations suggest, that the induced superconducting states and the topological Dirac states coexist. Thus, ZrSiS provides a suitable platform to investigate topological superconductivity in a robust material.

R. Singha *et al.* investigate the effect of isotropic pressure on ZrSiS by means of Raman spectroscopy and X-ray diffraction measurements [127]. They observe a structural change at 3.7 GPa leading to a coexistence of an orthorhombic structure and the ambient tetragonal geometry. At even higher pressure, around 16.2 GPa, a monoclinic phase starts to coexist with the previous two, which was confirmed by additional peaks in the X-ray spectra and anomalous behavior of the optical phonon peaks in the Raman measurement.

After the publication of our optical results in Ref. [1], T. Habe and M. Koshino calculated the dynamical conductivity of ZrSiS by using a multi-orbital theoretical model based on first-principles calculations [4]. In this work, the flat, frequency-independent optical conductivity response of the nodal line is investigated in more detail. The results of this publication will be compared to the experimental results of the optical measurements later in this chapter.

Our ZrSiS single crystals were provided by L. M. Schoop from the Max-Planck-Institut für Festkörperforschung (Stuttgart, Germany). The crystals were grown by loading equimolar amounts of zirconium, silicon and sulfur with a small amount of iodine into a sealed quartz tube. This tube was baked at 1100 °C for one week. With a temperature gradient of 100 °C, the crystals form at the cold end of the tube. With this method, large, pure single crystals of several mm size can be produced.

The structure, given in panel (b) of Figure 4.2, belongs to the PbFCl type, which is the tetragonal $P4/nmm$ space group (no. 129) [128]. This was confirmed with x-ray and electron diffraction measurements performed by the sample grower [3]. The lattice parameters are found to be $a = 3.5450$ Å and $c = 8.0575$ Å. In Figure 4.2, a is within the horizontal plane, while c denotes the vertical direction.

Most remarkably, the single crystals of ZrSiS are non-toxic and and highly stable when exposed to water and air [3]. These material properties are rare within the existing Dirac and Weyl semimetals, which makes ZrSiS a very promising candidate for future applications.

4.2. Optical response of the nodal line

In the following, we concentrate on the results of the broadband optical measurements for different temperatures and draw conclusions on the carrier dynamics and Dirac properties of ZrSiS. We trace the optical response of the nodal line and adapt a general model to calculate the length of the nodal line in reciprocal space. This length is found to be approximately $4.3\,\text{Å}^{-1}$. Furthermore, we discuss the origin of two low-frequency modes. These are revealed at lower temperatures when the scattering rate of the metallic carriers is reduced.

The temperature-dependent dc resistivity measurements were provided by the sample grower and published in Ref. [113]. These serve as basis for the low-frequency extrapolation of the optical data, as described in section 3.5.
The frequency-dependent optical reflectivity $R(\omega)$ was measured on freshly cleaved (001) surfaces, to ensure flat and clean measurement surfaces. The employed optical setups and the data treatment are described in chapter 3. There is, however, an issue with the low-frequency extrapolation: The commonly applied Hagen-Rubens relation is only valid for $\omega \ll \gamma$. Due to the extremely high and flat response of $R(\omega)$, the Hagen-Rubens relation does not match the measured data. From this, one can already claim that the scattering rate γ of the Drude term in ZrSiS is extremely small. To overcome the problem, we roughly fit the reflectivity with a Drude-Lorentz model based on the dc resistivity measurements and extrapolate the experimental data with this model.

The temperature-dependent dc resistivity $\rho_{\text{dc}}(T)$ is depicted in Figure 4.3. The comparably small absolute values indicate highly metallic states and pave the way for carriers with a high mobility. The resistivity decreases monotonously with temperature until it saturates below 30 K. The inset reveals a residual resistivity at low temperatures of only $\sim 50\,\text{n}\Omega\text{cm}$, leading to a dc conductivity of $\sigma_{\text{dc}} = 1/\rho_{\text{dc}} = 20 \times 10^6\,\Omega^{-1}\text{cm}^{-1}$. The high quality of the investigated single crystals is confirmed by the large residual resistivity ratio of ~ 310.

The optical reflectivity $R(\omega)$ was measured over the complete accessible frequency range (50 to $25\,000\,\text{cm}^{-1}$) and is given in Figure 4.4. To ensure reliable results

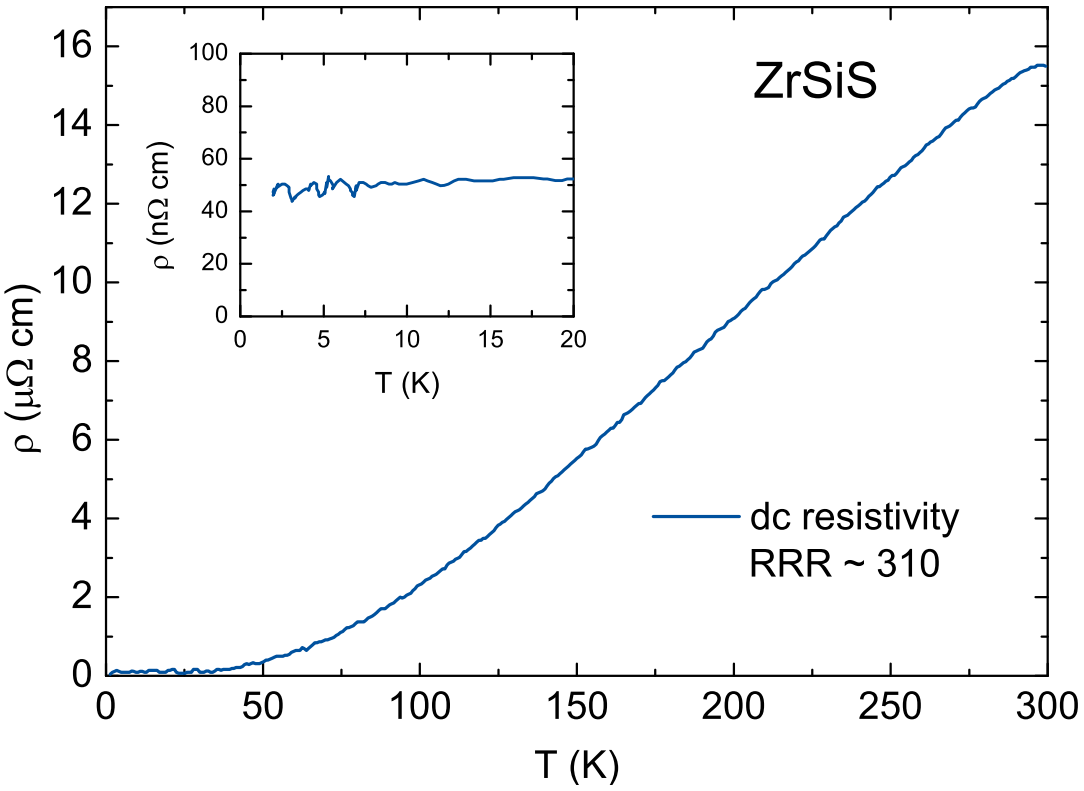

Figure 4.3.: The temperature-dependent resistivity $\rho_{dc}(T)$ of ZrSiS provided and published by the sample grower in Ref. [113]. A residual resistivity ratio RRR of 310 proves the high quality of the investigated crystals. While the absolute value is already comparable to good metals at high temperatures, the inset reveals a residual resistivity of only $\sim 50\,\mathrm{n\Omega cm}$. This leads to a very high dc conductivity.

from the Kramers-Kronig transformation, the infrared data were extended up to $40\,000\,\mathrm{cm}^{-1}$ by ellipsometry measurements. The itinerant metallic states cause an impressively high reflectivity of $R(\omega) > 0.98$ below $600\,\mathrm{cm}^{-1}$ for all temperatures. Below 100 K, even 0.99 is exceeded for frequencies smaller than $400\,\mathrm{cm}^{-1}$. These findings are in good agreement with the extremely low dc resistivity.

The impact of temperature is limited to the metallic FIR range and specifically the bump around $4000\,\mathrm{cm}^{-1}$. This bump and the structure of the reflectivity at higher frequencies indicates interband transitions. For trivial bands, the optical response typically narrows while lowering the temperature. As this seems not to be the case, the observation of transitions between Dirac-like energy bands are likely to cause these features.

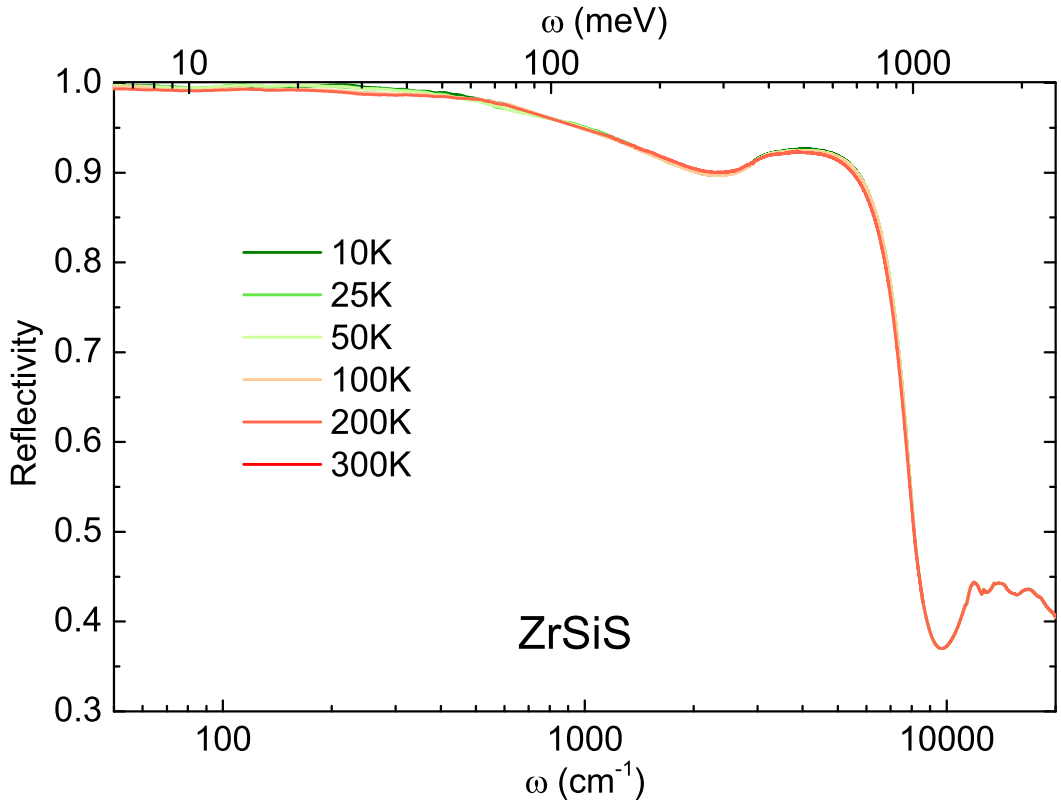

Figure 4.4.: The frequency-dependent reflectivity $R(\omega)$ of ZrSiS for the complete measured frequency range and selected temperatures. The influence of temperature is limited to the FIR range below $600\,\mathrm{cm}^{-1}$. *In this range, the absolute value is above* 0.98, *which is consistent with the high dc conductivity and caused by itinerant carriers. The bump around* $4000\,\mathrm{cm}^{-1}$ *indicates interband transitions located in the MIR range.*

As described before, the Kramers-Kronig analysis is used to obtain the complex optical functions, $\hat{\sigma}(\omega)$ and $\hat{\varepsilon}(\omega)$. The real part of the optical conductivity $\sigma_1(\omega)$ is shown in Figure 4.5. At very low frequencies (below $500\,\mathrm{cm}^{-1}$), the upturn in $\sigma_1(\omega)$ can be assigned to itinerant carriers with a Drude-like response. As the dc resistivity values serve as low-frequency extrapolation, this strong upturn is consistent with the low absolute values of ρ_{dc}.

At higher frequencies, starting from $\sim 250\,\mathrm{cm}^{-1}$, a frequency-independent conductivity is observed up to $2500\,\mathrm{cm}^{-1}$. The absolute value in this range is $6600\,\Omega^{-1}\mathrm{cm}^{-1}$. This frequency range is where the response of the nodal line of Dirac cones is ex-

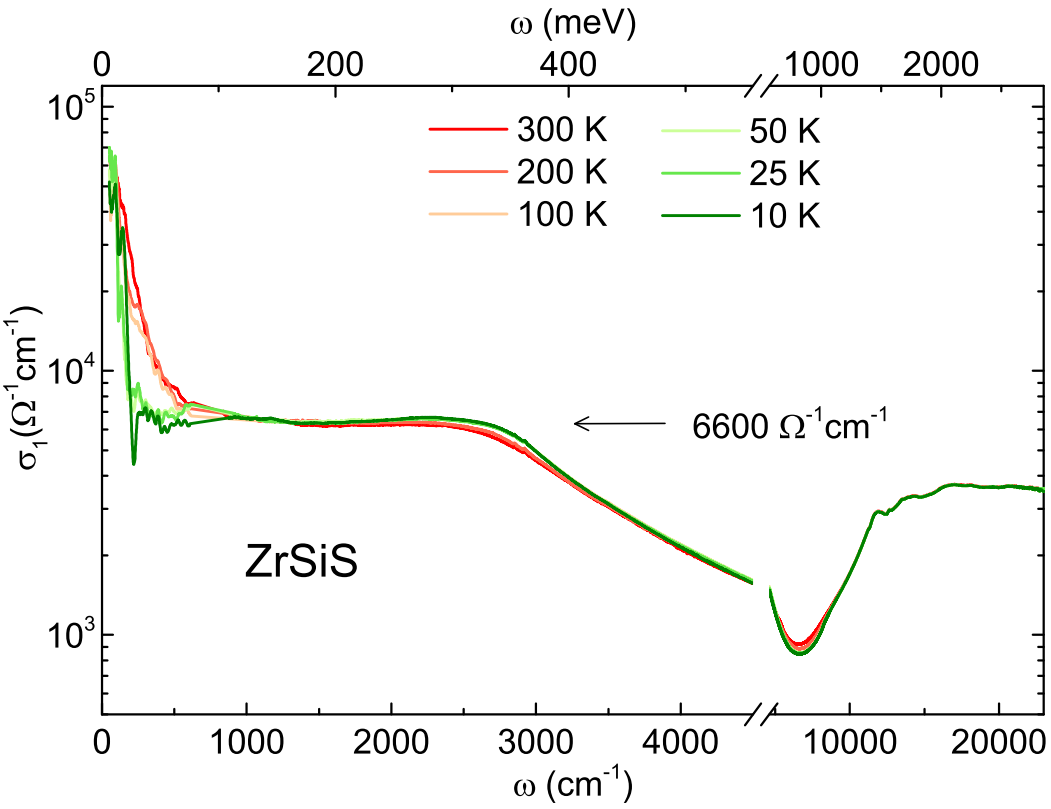

Figure 4.5.: The frequency-dependent real part of the optical conductivity $\sigma_1(\omega)$ of ZrSiS for selected temperatures. To emphasize the important features, the frequency axis is chosen to be linear and contains an axis break, while the conductivity axis is set to log-scale. At the low-frequency end, the conductivity shoots up, being consistent with the low dc resistivity data and caused by the metallic response. From 250 to 2500 cm^{-1}, $\sigma_1(\omega)$ is frequency independent. At higher frequencies, more interband transitions lead to several peaks.

pected. Note, that even though the Dirac states of a nodal line are two dimensional, one does not expect the universal absolute value ($\pi/4G_0$) found in graphene, as mentioned in section 2.7. A more detailed investigation in this context will follow below. Above this flat response, the conductivity drops before additional interband transitions reveal themselves as an increase of $\sigma_1(\omega)$ above 7000 cm^{-1}.

The imaginary part of the optical conductivity $\sigma_2(\omega)$ and the real part of the dielectric function $\varepsilon_1(\omega)$ are given in Figure 4.6. The metallic charge carriers can be traced in the upturn of $\sigma_2(\omega)$ at the lower end of the measurement window. When

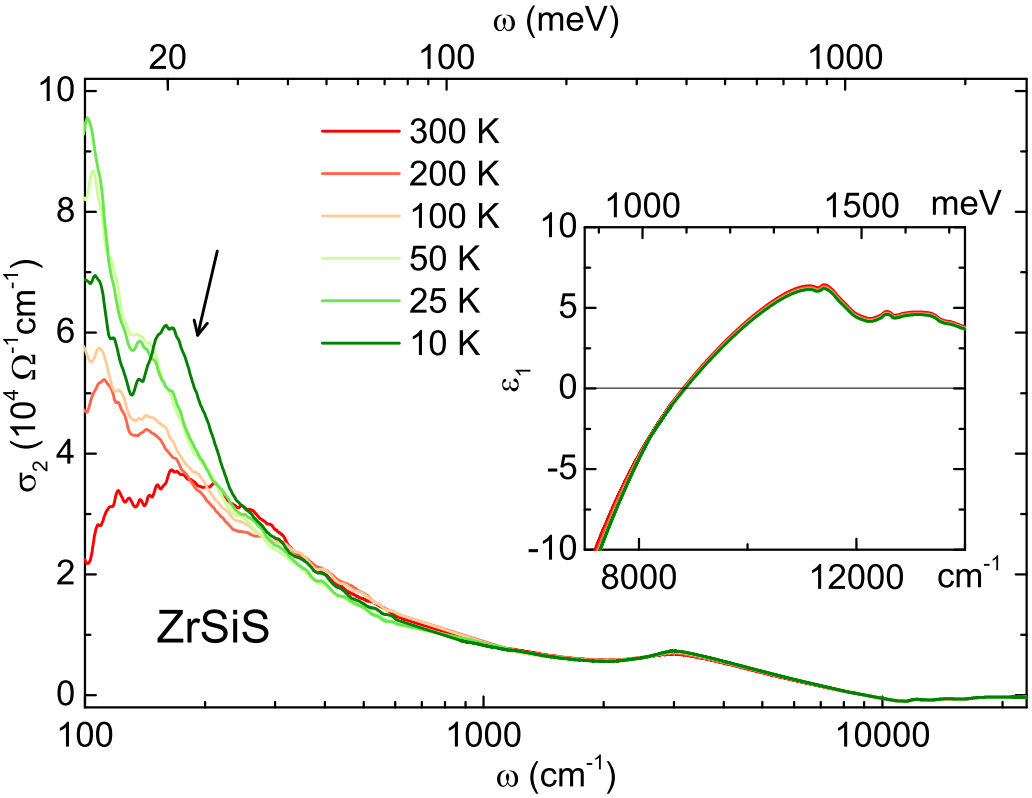

Figure 4.6.: The frequency-dependent imaginary part of the optical conductivity $\sigma_2(\omega)$ for selected temperatures. The itinerant carriers cause an upturn at lower frequencies. The black arrow indicates the Pauli edge for the 10 K measurement. The inset shows the real part of the dielectric function $\varepsilon_1(\omega) = 1 - \sigma_2(\omega)/(\varepsilon_0\omega)$ in the vicinity of the screened plasma frequency, i.e., the zero-crossing of $\varepsilon_1(\omega)$.

lowering the temperature, this upturn becomes steeper, since the scattering rate of the metallic carriers is reduced. At the high-frequency end of the spectrum, several peaks indicate the different contributions of interband transitions. The black arrow indicates the Pauli edge for the lowest measured temperature, which manifests itself as a peak in $\sigma_2(\omega)$ [129].

The inset of Figure 4.6 shows $\varepsilon_1(\omega)$ in the vicinity of the zero-crossing, which is at $\sim 8817\,\mathrm{cm}^{-1}$. This zero-crossing can be assigned to the screened plasma frequency $\omega_{\mathrm{pl}}^{\mathrm{scr}} = \sqrt{\frac{ne^2}{m^*\varepsilon_0\varepsilon_\infty}}$, which is the plasma frequency ω_{pl} renormalized by the high-frequency contribution ε_∞ [21]. Here, n is the free carrier density and m^* reflects the effective carrier mass. The crossing point shows no significant temperature dependence, which indicates that the ratio between the charge carrier density n

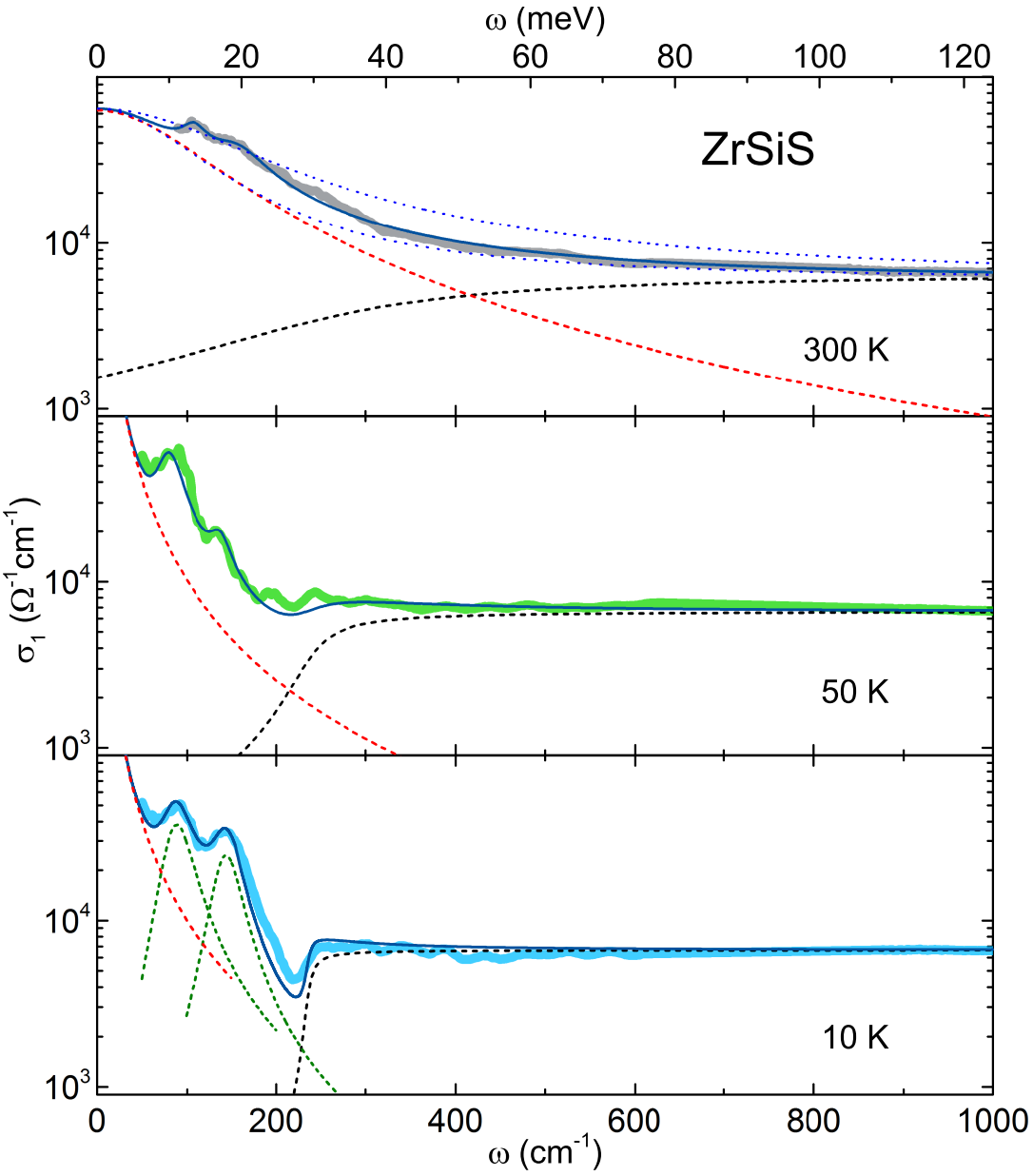

Figure 4.7.: Fits of the real part of the optical conductivity of ZrSiS in the low-frequency range for lowest and highest temperature. The thick solid lines represent the experimental data, while the thin ones are cumulative fits. The dashed lines illustrate contributions of the Drude term (red), Lorentz terms (green, only shown for the 10 K *measurement) and the Pauli-edge (black).*

and the effective mass m^* of ZrSiS does not change with temperature.

For a rough estimation of the carrier density n, the effective mass obtained by quantum oscillations ($\sim 0.1\ m_e$, see, e.g., Ref. [113]) can be used to calculate n. This

leads to $n \approx 2.2 \times 10^{18}\,\mathrm{cm}^{-3}$, which is comparable to the carrier density of other Dirac materials [114].

As mentioned before, the optical conductivity reveals a frequency-independent response between 250 and $2500\,\mathrm{cm}^{-1}$. This coincides with the energy range of the nodal line, obtained in band structure calculations and ARPES measurements [3, 115, 130]. The nodal line hosts two dimensional Dirac fermions in a three dimensional material. The optical response expected for such a nodal line is indeed a frequency independent conductivity, as described in section 2.7. To attain deeper insight, $\sigma_1(\omega)$ is fitted and the result is presented in Figure 4.7 for selected temperatures.
Note, that models to describe the optical response of Dirac fermions are usually given only for the real part of the optical conductivity $\sigma_1(\omega)$. This is due to the fact that these models are usually not Kramers-Kronig consistent and, thus, neither the imaginary part $\sigma_2(\omega)$ nor the reflectivity $R(\omega)$ can be described with these models.

The fitting functions applied to the optical data of ZrSiS in the low-frequency range contain three different contributions.
Firstly, a Drude term is employed to take the itinerant carriers into account and is depicted as red dashed lines in Figure 4.7. This is verified by the Fermi level lying within the conduction band of the nodal line, leading to metallic states, e.g., Refs. [3, 4]. A schematic drawing of the nodal line structure on the basis of literature information is given in Figure 4.9. The σ_{dc} value of the Drude term is required to match the dc resistivity measurement of Ref. [113]. Upon cooling, the scattering rate of this Drude term is reduced from $144\,\mathrm{cm}^{-1}$ at 300 K to $\sim 2\,\mathrm{cm}^{-1}$ at 10 K. The latter value is well below our measured frequency window. Due to the large dc conductivity value of $\rho_{\mathrm{dc}}(T = 10\,\mathrm{K}) = 20 \times 10^6\,\Omega^{-1}\mathrm{cm}^{-1}$, however, a large tail of the Drude term still enters the measured frequency range of the reflectivity spectrum. Note, such a small scattering rate results in a rather long momentum-relaxing time $\tau = 1/\gamma$ in the range of $\sim 2.7\,\mathrm{ps}$. From this, the momentum-relaxation length $l_{\mathrm{mr}} = v_F\tau$ can be determined. Using an average Fermi velocity of the low-energy Dirac bands of $v_F = 5 \times 10^5\,\mathrm{m/s}$ [3], we obtain $l_{\mathrm{mr}} \geq 1\,\mu\mathrm{m}$ at low temperatures. This indicates that the hydrodynamic behavior of electrons, which

was recently reported in clean graphene samples [131, 132] and the Weyl semimetal WP_2 [133], might also be realized in ZrSiS.
Secondly, the fits contain two Lorentz terms. The resonance frequencies of the two terms are $90\,\mathrm{cm}^{-1}$ and $140\,\mathrm{cm}^{-1}$ at 10 K. While the peaks are clearly visible in the low-temperature range, thermal broadening blurs the situation at higher temperatures. Still, the best fit can be achieved by including them also at 300 K. This is indicated by two possible fitting curves (blue dashed lines) without the Lorentz terms in Figure 4.7. Possible origins of these modes will be discussed in more detail later.
Last but not least, a model based on Equation 2.11 given in section 2.7 is included to describe the response of the nodal line. The equation is extended by the Heaviside step function to take the spin-orbit coupling induced gap as well as the position of the Fermi level into account, leading to:

$$\sigma_1(\omega) = \sigma_{\mathrm{flat}} = \frac{e^2 k_0}{16\hbar}\Theta\{\hbar\omega - \max\{\Delta, 2\mu\}\} \quad . \tag{4.1}$$

Thermal broadening of the onset can be incorporated by replacing the Heaviside step function by the arctan-function, more details are given in section 2.7. This kind of onset is well known for semiconductors [134] and Dirac and Weyl semimetals [129, 135, 136] and is related to the Pauli blocking of transitions which do not cross the Fermi level.

The fit of the frequency-independent response can consequently be used to provide further information about the length of the nodal line in reciprocal space k_0 and to estimate a maximum energy gap value from the Pauli edge. Solving Equation 4.1 for k_0 and using the value of the flat response in the MIR range of $\sigma_{\mathrm{flat}} = 6600\,\Omega^{-1}\mathrm{cm}^{-1}$, yields to a length of the nodal line of $k_0 = 4.3\,\text{Å}^{-1}$.
Note that the absolute value of σ_{flat} is temperature independent and hence, k_0 is too. This is in good agreement with no structural change appearing in ZrSiS upon cooling, see, e.g., Ref. [124]. The value of $4.3\,\text{Å}^{-1}$ seems to be reasonable, since band structure calculations predict a length of the nodal line projections on the [100] and [001] surfaces of 3.5 and $6\,\text{Å}^{-1}$ per Brillouin zone [137]. The small deviation can be explained by the fact, that the model assumes a circularly shaped nodal line, while the sketch in Figure 4.1(b) indicates, that this is not the case for ZrSiS. The nodal line is rather comparable to a cage-like structure in the Brillouin zone.

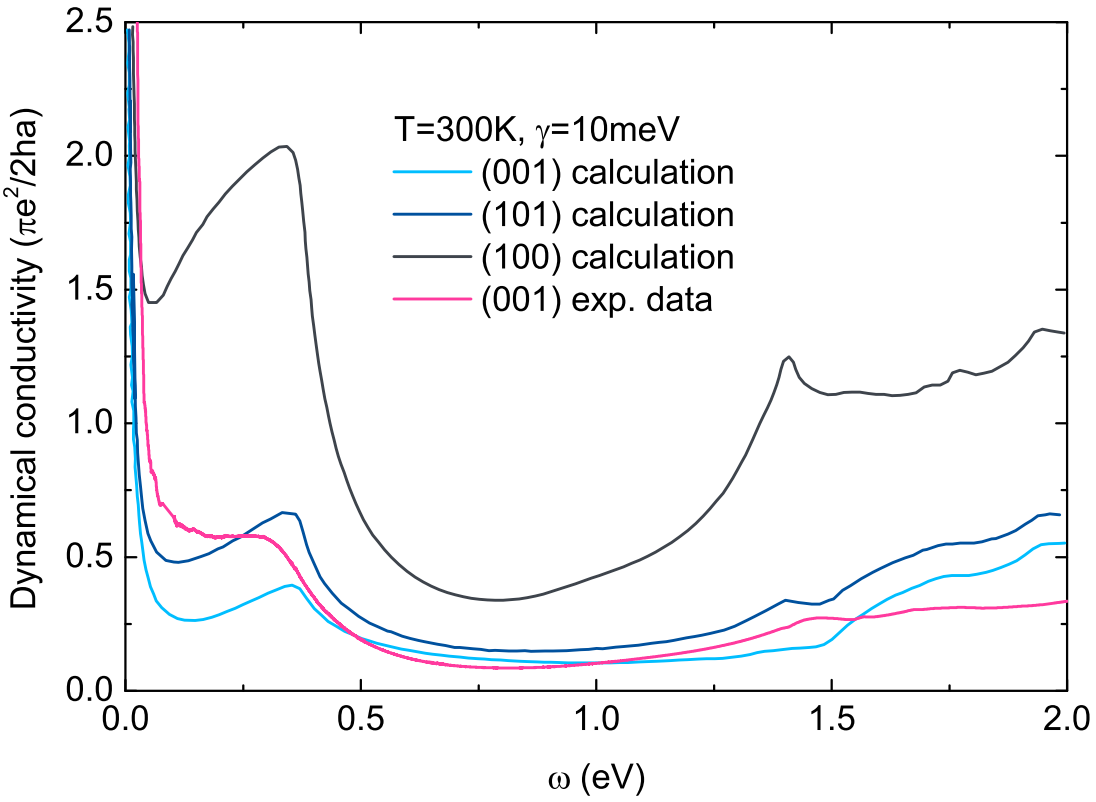

Figure 4.8.: The calculated dynamical conductivity of ZrSiS for different polarizations are compared. The data are redrawn from Ref. [4]. For comparison, the experimental data of the same temperature is added. The overall shape as well as the absolute values provide an astonishingly high agreement of the theoretical and experimental data.

From the fit of the low-temperature data, one can state that $\max\{\Delta, 2\mu\}$ must be smaller than $250\,\mathrm{cm}^{-1}$, 30 meV respectively. This can be seen as an upper limit of the energy gap Δ induced by spin-orbit coupling in the nodal line. The value is in good agreement with 15 meV as suggested by band structure calculations, e.g., Ref. [3]. A broadening of the Pauli edge observed in the optical measurements can be attributed to the change of the relative position of the Dirac nodes with respect to the Fermi level along the nodal line, see Figure 4.9. It is important to note, that even if the Fermi level appears within the energy gap for some k-space positions, the conclusion for the upper limit of Δ is still valid.

Next, the experimental results will be compared to the dynamical conductivity ob-

tained by theoretical calculations published by T. Habe and M. Koshino in Ref. [4]. The latter are based on first-principles calculations using a multi-orbital model. While a detailed discussion of the calculations can be found in the publication, here only the influence of the crystallographic surfaces, the scattering rate γ and temperature T will be examined. While the first one is given in Figure 4.8, the scattering rate and the temperature are depicted in Figure 4.10. The graphs are redrawn from Ref. [4].

The dynamical conductivity, in the units of $\pi e^2/2$ha (a is the unit cell axis and h the Planck constant), is given for the polarization of the measurement light being parallel to (001), (101) and (100) in Figure 4.8. While the polarization[2] influences the absolute values and relative strength of the different contributions, the overall shape remains mostly unchanged. At very low frequencies, itinerant carriers cause a Drude-like peak. At slightly higher frequencies, a rather flat conductivity can be found up to 350 meV. Following a valley, additional peaks related to interband transitions are located at 1.4 eV and higher.

The shape described above matches the experimentally observed conductivity well. Astonishingly, also the absolute values are in very good agreement. To prove, the experimental data at 300 K is converted into the same units and added to Figure 4.8. A small shift of the peaks in frequency can be explained by a shift of the Fermi level, which seems to be slightly different for the calculations. The strongest divergence is found in the frequency range of the frequency-independent range related to the line of Dirac nodes. In the calculations, the conductivity increases with frequency for all polarizations. This is assigned to the change of the chemical potential μ of the nodal line when moving along the k_z-direction, as depicted in Figure 4.9. The calculations seem to overestimate this tilt, since the experimental curve is much flatter than the theoretical one.

The shape and frequency dependence of the calculated conductivity in this flat range can additionally be modulated by changing the scattering rate γ. This is shown in Figure 4.10 for values from $\hbar\gamma = 5$ to 40 meV. Note, the publication of T. Habe *et al.* only provides these data for $T = 50$ K and E||(100). This prevents a

[2] We want to mention that there is some inconsistency in the work of T. Habe and M. Koshino between the labeling of the curves and the information given in their text. Thus, it is possible, that the curves of (001) and (100) are mixed up in Figure 4.8.

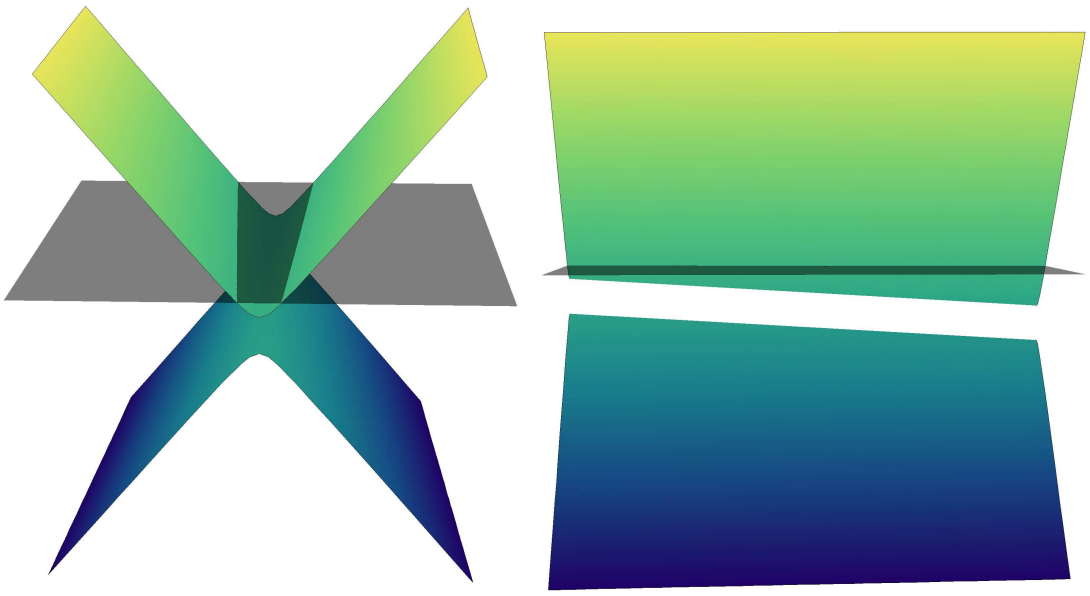

Figure 4.9.: A sketch of the nodal line in ZrSiS. The energy position of the nodal line is shifting with respect to the Fermi level when moving along the k_z-direction. Additionally, a gap $\Delta \leq 30\,\mathrm{meV}$ is opened by spin-orbit coupling. Calculations and experimental results suggest that the Fermi level lies within the conduction band of the nodal line.

direct comparison with the experimental data, which were measured with E||(001). The theoretical investigation of the influence of γ, however, shows that the flat conductivity changes the most with varying the scattering rate. A value of 20 meV seems to best match the experimental data.

The inset of Figure 4.10 depicts the influence of temperature on the spectrum. Again, only E||(100) is provided with $\gamma = 10\,\mathrm{meV}$. The change due to varying temperature is limited to the flat conductivity range, which matches the experimental results well. Note that the influence on the Drude contribution is neglected, so that the dc conductivity and the scattering of the metallic carriers is fixed. This is, of course, not true for the experimental results and leads to some deviation.

All in all, the calculated conductivity and the experimental data are in good agreement with each other and confirm the interpretation of the obtained results.

Next, the low-frequency modes at 100 and $150\,\mathrm{cm}^{-1}$ will be discussed and four

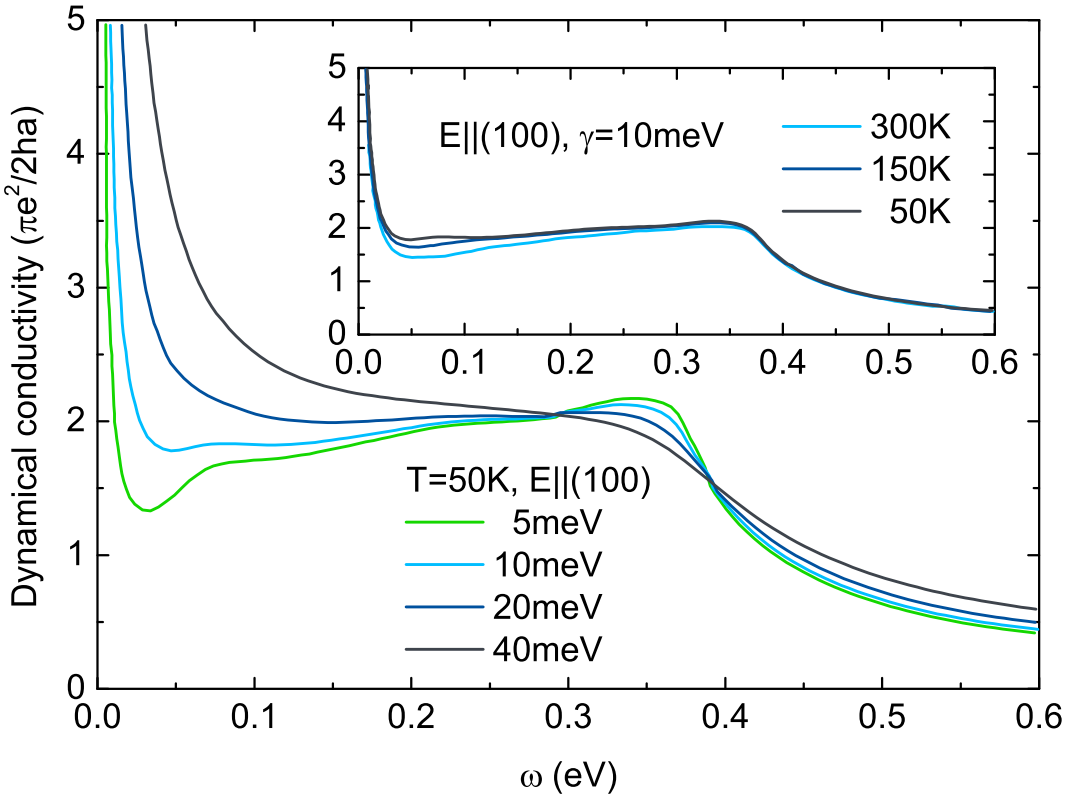

Figure 4.10.: The calculated dynamical conductivity of ZrSiS for scattering rates γ between 5 and 40 meV. The increase of γ broadens the Drude component of the itinerant carriers and changes the response in the energy range of the nodal line. The data are redrawn from Ref. [4]. The inset depicts the small influence of temperature on the conductivity.

different scenarios for their origin are provided.

A first idea are phonon related peaks. However, this seems to be unlikely since calculations do not suggest any infrared-active phonon modes in this particular frequency range [138]. Furthermore, the experimentally observed modes are broad and strong, which is rather untypical for phonon modes. An exception to this would be a soft phonon mode in ferroelectrics, but no ferroelectricity was reported or suggested to exist in ZrSiS.

The second possible scenario would be electron localization in the bulk crystal. Such localization, usually induced by disorder, is also extremely unlikely. The material and available crystals are very pure [121]. Additionally, the dc resistivity monotonically decreases with temperature and obeys remarkably low absolute values of only

a few nΩcm, which can be taken as a proof of high quality and low disorder [113, 122].

Thirdly, surface contributions could play a noticeable role. While the skin depth in our measurement is larger than 40 nm for the entire investigated frequency range, some surface contributions cannot be completely excluded. As discussed in section 4.1, rather strong surface states have been predicted and observed in ZrSiS, see, e.g., Ref. [119]. These surface states even hybridize with the bulk states and could become visible in the infrared measurements. An investigation of a thickness dependence of the dc conductivity in ZrSiS on microstructured samples, however, did not reveal any surface contributions to the conductivity properties [139]. The appearance of inhomogeneities in the electron surface density, e.g., related to electron localization, might reconcile the results of Refs. [119] and [139] and, in addition, provide an explanation of the low-frequency modes obtained by the infrared measurement.

Fourthly, excitons are considered as possible origin of the low-frequency modes. This seems to be, at first glance, not very plausible, as the strong screening of the itinerant carriers might prevent an excitonic mode. Nonetheless, the exciton binding energy E_b can be calculated to verify this scenario. To do so, the simplest hydrogenic exciton model is applied [140], using the effective mass of the carriers in the low-energy 2D Dirac band, $m^* = 0.025 m_e$ [121]. With the static lattice dielectric constant obtained from the optical measurement ($\varepsilon_0 \sim 7.5$), the binding energy is calculated to be $E_b \sim 100\,\mathrm{cm}^{-1}$. In the optical spectra, excitons should be found at $\Delta - E_b$. The previously determined energy gap limit $\Delta \leq 250\,\mathrm{cm}^{-1}$ leads to $\Delta - E_b \leq 150\,\mathrm{cm}^{-1}$, i.e., directly in the range of the low-frequency modes. The appearance of excitonic modes may manifest itself on or near the surface, where the free-electron screening is weaker than in the bulk. This scenario may be further supported by an excitonic instability discussed in the first-principles calculations of Ref. [141]. The instability is caused by electron-electron interactions and might vary for different positions of the Fermi level.

To make a final statement about the low-energy absorption peaks and completely clarify their nature in ZrSiS, further studies with complementing experimental techniques are required.

Last but not least, the high-frequency end of the optical spectra is investigated.

The frequency-dependent optical conductivity $\sigma_1(\omega)$, shown in Figure 4.5, reveals an increasing absolute value with several small peaks for frequencies above the axis break, i.e., $7000\,\mathrm{cm}^{-1} \approx 860\,\mathrm{meV}$. This energy range coincides with the energy distance between the lower and the upper Dirac branch of the states protected by non-symmorphic symmetry [117]. Furthermore, the peak positions and structure matches well with the theoretical calculations of Ref. [4], as shown in Figure 4.8. T. Habe *et al.* confirm that the conductivity in this range mainly arises from the non-symmorphic bands. As these bands do not form a concrete, typical three dimensional Dirac cone, the optical response is not expected to be perfectly linear (Equation 2.6). Thus, no further details about the non-symmorphic Dirac bands can be extracted from the optical measurement.

4.3. Conclusions

Motivated by the ideal situation of the Dirac physics in ZrSiS and the linear dispersion of electronic bands over a fairly large energy range, we investigated the electrodynamic properties of this compound by means of optical spectroscopy. With this, we do not only provide information about the nodal line and the energy gap, but also amend the only existing model for the optical response of a nodal line and validate its correctness experimentally. The model we apply can be used to determine the length of the nodal line in reciprocal space, which is found to be $k_0 = 4.3\,\text{Å}^{-1}$. This is in good agreement with theoretical values [137]. Our fit additionally gives an upper limit for the energy gap of $\Delta \leq 250\,\text{cm}^{-1} \approx 30\,\text{meV}$, which matches the theoretical expectations well and corrects the poor value obtained by ARPES [3]. Furthermore, the optical spectra reveal two modes in the low-frequency range. We discuss several scenarios for the origin of these modes and call for complementing experimental investigation to draw final conclusions.
Overall, our experimental results nicely agree with recent theoretical calculations of T. Habe *et al.* from Ref. [4]. This is also valid for the high-frequency response which is related to the Dirac bands protected by non-symmorphic symmetry.

5. YbPtBi - a topologically non-trivial half-Heusler compound

In this chapter the results obtained on YbPtBi will be discussed. Section 5.1 will give a brief introduction to the material and its literature, while the magneto-transport and optical results will be presented in section 5.2. Last but not least the experimental results will be investigated in terms of topological non-triviality (e.g., Dirac/Weyl physics) in section 5.3 in comparison with the optical results obtained on GdPtBi.
Parts of the data and analysis presented in this chapter are published in Refs. [5, 142].

5.1. The material

The half-Heusler material YbPtBi has been known as a heavy-fermion compound for decades and exhibits one of the highest effective electron masses among strongly correlated electron systems [143, 144]: specific heat (C_P) measurements show a linear temperature dependence below 0.35 K with a Sommerfeld coefficient of $\gamma = C_P/T = 8\,\mathrm{J/K^2}$ (mole Yb). The Kondo temperature of YbPtBi is around 1 K and an antiferromagnetic (AFM) transition is observed at 0.4 K. Thus, most experimental studies focus on temperatures below 2 K to investigate the heavy-fermion state and a possible quantum critical point [143–149].
There is, however, another way to interpret the large Sommerfeld coefficient except of the high renormalized quasiparticle mass, as it was pointed out by Graf *et al.* in Ref. [150]: the stability of different electronic configurations, i.e., the magnetic Yb^{3+} state, the non-magnetic Yb^{2+} state and a mixture of both might influence

the Sommerfeld coefficient. Thus, the $4f$ electronic states, which are the valence states of Yb, are substantial for the detailed band structure in the vicinity of the Fermi level in YbPtBi.

In 1992, Eriksson *et al.* already indicated that relativistic effects play a crucial role for the band structure of YbPtBi [151]. The authors point out that solving the fully relativistic Dirac equation of the crystal with the linear muffin-tin orbital (LMTO) method[1] is the only way to describe the metallic ground state of YbPtBi. Otherwise, the closing of the semiconducting gap between valence and conduction bands while going from the related compound YPtBi to YbPtBi is not reproducible.

More recently, YbPtBi and other representatives of the half-Heusler family were suggested to possess topologically non-trivial states [150, 153–156] and hence quasiparticles with a linear band dispersion might appear in these half-Heusler compounds. This is of particular interest since the half-Heusler family is rich in different electronic properties (e.g., superconductivity, heavy-fermion, AFM ordering) which may interact with Dirac or Weyl states and thus being promising candidates for functional materials.

A sketch comparing a topologically trivial and a non-trivial band situation close to the Γ-point in half-Heusler compounds is reproduced from Ref. [153] in panel (a) of Figure 5.1. In this reference, the authors claim the existence of Weyl points induced by an external magnetic field in some of the ternary half-Heusler compounds (e.g., GdPtBi). They provide an experimental evidence of the chiral anomaly, the ultimate proof for Weyl fermions, in their magneto-transport measurements. The Weyl points and the topologically non-trivial band inversion are proposed to rise from an enhanced exchange field of the $4f$ states due to an alignment of the magnetization of the antiferromagnetic structure upon applying the external magnetic field.
A band picture of YbPtBi pointing towards the non-trivial band inversion even without an external magnetic field was calculated in Ref. [154] and is reproduced in panel (b) of Figure 5.1. In their calculations, W. Al-Sawai *et al.* try to overcome the problem of an underestimated band gap for semiconductors in the density-functional theory (DFT) by applying a semilocal exchange-correlation potential. As a result,

[1]Details about this method can be found in, e.g., Ref. [152].

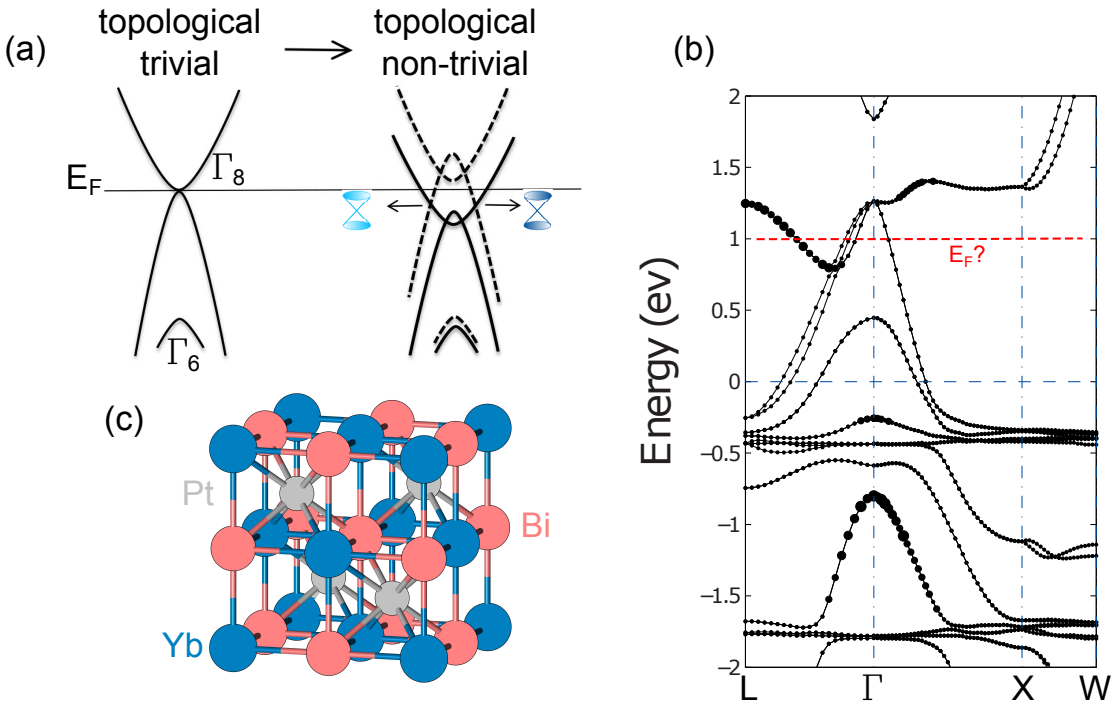

Figure 5.1.: Panel (a) depicts a schematic band structure of a topologically trivial (left) and non-trivial (right) half-Heusler material. A transition to the non-trivial state is achieved by increasing the exchange field of the 4f states (adapted from Ref. [153]). A possible band structure of YbPtBi, reproduced from Ref. [154], is shown in panel (b). The red dashed line indicates the position of the Fermi level as suggested by our calculations (section 5.3), our experimental results, and Refs. [8, 153], leading to electron and hole pockets. A topologically non-trivial band inversion is discussed at the Γ-point. The unit cell of YbPtBi drawn with VESTA [118] showing the cubic, face-centered structure is given in panel (c). This kind of arrangement belongs to the half-Heusler family which has a Pt atom in every second Yb-Bi sub-cube only, compared to Heusler compounds where each sub-cube is filled.

10 out of 30 investigated ternary half-Heusler compounds reveal a topologically non-trivial band inversion at the Γ-point. At that stage, a much lower Fermi level E_F caused by hole doping was considered for YbPtBi and also for GdPtBi. However, more recent publications show E_F being comparable to other compounds of this half-Heusler series [8, 153], around 1 eV higher, indicated by the red dashed line in Figure 5.1 (b). This Fermi level position is also confirmed by the band calculations provided by Jun. Prof. Dr. H. Zhang from the Technische Universität Darmstadt

to understand the optical results in section 5.3.

In these half-Heusler compounds, the strength of the correlated $4f$ electrons of the Lanthanide atoms (i.e., Yb) can drive a band inversion of the Γ_6 and Γ_8 band at the Γ-point and hence create topologically non-trivial states [153, 154]. In this context, the different half-Heusler compounds are supposed to have different topologically non-trivial states and therefore Weyl semimetals or topological insulators are possible. As the Kondo effect is present at low temperatures in YbPtBi, it is a candidate for being a 3D topological Kondo insulator [155], where also the insulating states are of topologically non-trivial nature [157]. This occurs in particular if electronic f-states are near the top or the bottom of the conduction band, typically found in heavy-fermion materials. It should, however, only be found in the temperature range of the heavy-fermion physics, which is below 1 K in YbPtBi.

The theoretical study of Ruan *et al.* suggests strain induced Weyl points in the HgTe-class, which the half-Heusler compounds investigated here also belong to [158]. Strain generates a perturbation which affects the lattice parameters slightly. They show that in-plane strain gives rise to four pairs of Weyl nodes along the Γ-L- and the Γ-X-direction located exactly at the Fermi level. These ideal Weyl nodes and their Fermi arcs should be detectable with, e.g., ARPES (directly) or magneto-transport (via the chiral anomaly).
Another theoretical investigation advocates so-called triple points (TP) in some half-Heusler compounds, where a doubly degenerate conduction band interacts with two non-degenerate valence bands (and crosses one of them). A general discussion of TPs in semimetals was already given in section 2.5. Here we follow Ref. [8] to clarify the situation in the half-Heusler compounds. Yang *et al.* predict the triple point fermions by *ab initio* calculations and the Kane model. The triple points are found along the four C_3 symmetry axes. Depending on the compound, the number of triple point pairs on each C_3 axis varies between one and three and, hence, also the total number of TPs changes. For GdPtBi one pair of TPs is proposed leading to eight TPs within the first Brillouin zone. In that paper, YbPtBi is not mentioned. Our calculations and measurements in section 5.3 show, however, that the situation is very much like for GdPtBi.

These mainly theoretically based ideas do not provide a consistent picture and call for further investigations. It was pointed out by Peters *et al.* that the treatment of the $4f$ states in rare earth compounds is challenging and can lead to strongly diverging results depending on the calculation method applied [159]. The importance of the $4f$ electrons for the Fermi surface and detailed band structure around the Γ-point in the half-Heusler compounds (especially in YbPtBi) was highlighted in Refs. [149, 150, 153, 160]. These facts call for a more comprehensive examination of the electronic properties of the half-Heusler compounds and YbPtBi, beyond the heavy-fermion state. Experimental results obtained by different techniques should be used to provide new information to calculations and gain more advanced and refined band structure results. Therefore, we apply optical spectroscopy to YbPtBi and GdPtBi which was not done previously. Our investigations, including the complementing magneto-transport measurements, focus on the temperature range above the heavy-fermion state as well as the AFM ordering and Kondo temperature.

Our YbPtBi and GdPtBi single crystals, provided by C. Shekhar from the Max-Planck-Institut für Chemische Physik fester Stoffe (Dresden, Germany), were grown by the solution growth method, where Bi acts as a flux. A detailed description of the growth procedure is given in Ref. [5]. The samples are 3 to 5 mm regular triangular-shaped crystals and preferably grow in the (111) direction.
The space group of our YbPtBi crystals is found to be $F\bar{4}3m$ (face-centered, cubic) with a lattice parameter of 6.591 Å, consistent with previous reports [161–163]. Panel (c) in Figure 5.1 shows the cubic crystal structure of YbPtBi, representing the ternary half-Heusler family. Compared to the Heusler structure, only every second Yb-Bi sub-cube is filled with a Pt-atom. The same crystal structure is also valid for GdPtBi discussed in section 5.3, where merely the lattice parameter is changed to 6.680 Å.

5.2. Two-channel conduction in YbPtBi

In the following, we concentrate on the results of our transport, magneto-transport and broadband optical measurements for temperatures well above the Kondo temperature, i.e., $2.5 - 300$ K. From this, we draw conclusions about the carrier dy-

namics in YbPtBi.
We provide evidence for two different types of charge carriers coexisting in compound presented here: on the one hand, highly mobile electrons with a strongly temperature-dependent carrier concentration in the order of $10^{18}\,\mathrm{cm}^{-3}$; on the other hand, holes with a temperature-independent carrier concentration of $10^{20}\,\mathrm{cm}^{-3}$ that possess a very low mobility. The electron mobility is found to be record high for the half-Heusler family. The presence of such highly mobile carriers is typical for materials with linearly dispersing bands [153, 164]. The presence of such Dirac or Weyl states in YbPtBi is under debate [153–155, 165], a concluding picture, however, is missing. Our finding of highly mobile electrons in YbPtBi suggests that Dirac physics indeed can be relevant, however, further experimental and theoretical investigations are required to draw a final statement here.

Direct-current resistivity measurements were performed in a self-built setup. The transversal magneto-resistance (MR) and the Hall resistivity measurements were performed at the same temperatures down to 2.5 K in magnetic fields up to 6.5 T. The voltage and current were measured and applied within the (111) plane, while the magnetic field was orientated along the [111] axis.
The frequency-dependent optical reflectivity $R(\omega)$ was also measured in the (111) plane. Due to the optical windows, the temperature range for the optical measurements was limited to $12 - 300\,\mathrm{K}$. Furthermore, all optical experiments were conducted on freshly cleaved surfaces to avoid any influence of oxidation or water. While further information on the different experimental setups and data treatment were described in chapter 3, the extrapolation of the measured reflectivity data will be discussed in more detail here. The commonly applied Hagen-Rubens extrapolation is not adequate and does not provide a consistent connection between the optical data and the dc conductivity values obtained from the resistivity measurement. This can be understood and verified by the narrow Drude component added later on, which has a scattering rate $1/\tau$ comparable to the lowest measured frequency ω_{min}, while the Hagen-Rubens regime is only valid for $\omega \ll 1/\tau$. To avoid this issue, we use a set of Drude and Lorentzian terms to fit the measured reflectivity. Between $\omega = 0$ and ω_{min}, this fit was applied as low-frequency extrapolation. On the high-frequency end, the standard extrapolation technique as outlined in section 3.5 was used.

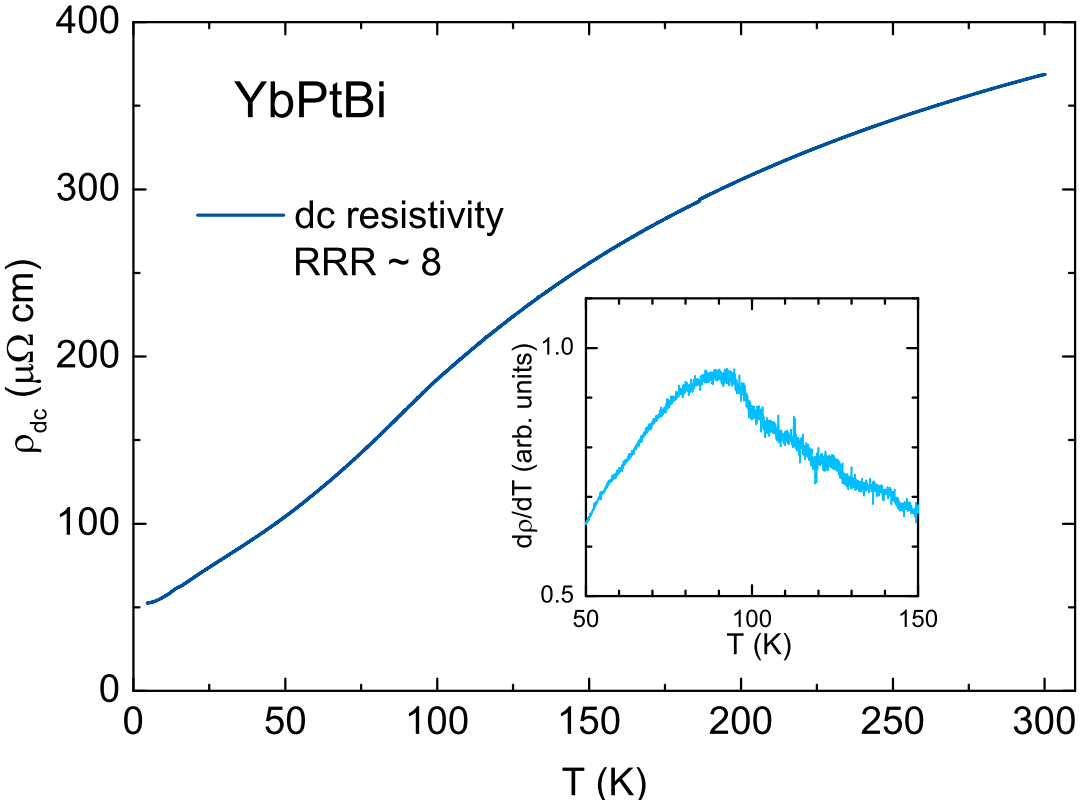

Figure 5.2.: The temperature-dependent resistivity $\rho_{dc}(T)$ of YbPtBi obtained by a conventional four-point measurement. The monotonous decrease upon cooling is typical for metals and semimetals. A residual resistivity ratio RRR= $\rho_{dc}(300\,\mathrm{K})/\rho_{dc}(4.5\,\mathrm{K})$ of 8 is comparable to values reported in literature [143, 147]. The inset shows the first derivative $d\rho/dT$ which directly depicts the point of inflection in $\rho_{dc}(T)$ at $T = (90 \pm 5)\,\mathrm{K}$.

The temperature-dependent dc resistivity $\rho_{\mathrm{dc}}(T)$ is displayed in Figure 5.2. Upon decreasing the temperature, $\rho_{\mathrm{dc}}(T)$ monotonically decreases: With a residual resistivity ratio RRR= $\rho_{\mathrm{dc}}(300\,\mathrm{K})/\rho_{\mathrm{dc}}(4.5\,\mathrm{K})$ of ~ 8, our single crystal is of comparable quality to crystals discussed in literature [143, 147]. A point of inflection was reported by Ref. [147] and is confirmed by our measurement, as shown by $\mathrm{d}\rho/\mathrm{d}T$ in the inset of Figure 5.2. The local (and global) maximum of $\mathrm{d}\rho/\mathrm{d}T$ is around $T = (90 \pm 5)\,\mathrm{K}$ and matches a shoulder in the thermoelectric power results given in Ref. [147]. The point of inflection is associated with the influence of crystalline-electric field effects.

Within our temperature range, the measurement does not reveal a residual resistivity as ρ_{dc} still decreases at lowest temperatures. This is consistent with literature and points towards the antiferromagnetic transition at $T = 0.4\,\mathrm{K}$ [143, 147].
Later on, the dc measurement will be used to determine the low-frequency extrapolation of the optical data and connect them to the transport data.

Magneto-transport

Let us now turn to the transport response of YbPtBi under magnetic fields. These data were mainly contributed by StEx. A. Löhle from the 1. Physikalisches Institut - Universität Stuttgart, while the optical measurements were performed by the author.

The magneto-transport measurements were carried out by sweeping the magnetic field B from -6.5 to $6.5\,\mathrm{T}$ at each temperature. The field-dependent resistivity $\rho_{xx}(B)$ is commonly transformed into the so-called magneto-resistance $\mathrm{MR} = \frac{\rho_{xx}(B)-\rho_{xx}(B=0)}{\rho_{xx}(B=0)}$. The resulting curves are shown in Figure 5.3 for all temperatures. The graph is supplemented with data of Mun *et al.* [147] taken at $T = 1\,\mathrm{K}$ and $0.02\,\mathrm{K}$ to prove the consistency of our data with already existing results obtained in the heavy-fermion state temperature range of YbPtBi.

The MR sharply increases with B in the range of small magnetic fields for all temperatures. Upon cooling, this increase is enhanced until it saturates (within the error bars) between 100 and 80 K which coincides with the point of inflection in the zero-field resistivity measurement shown before (Figure 5.2). For elevated temperatures, the MR flattens out and reaches approximately 60% as B increases to 6.5 T. Such behavior indicates two types of carriers with significantly different scattering rates and Hall mobilities. In more detail, the low magnetic field data provides evidence for highly mobile (i.e., with a low scattering rate) carriers which are localized by a small field strength of $\sim 0.5\,\mathrm{T}$, while another type of carriers with a high scattering rate and low mobility still provides the dc transport.

For temperatures below 20 K, the magneto-resistance is not monotonic anymore: a well-defined maximum develops and shifts to lower fields as the temperature is

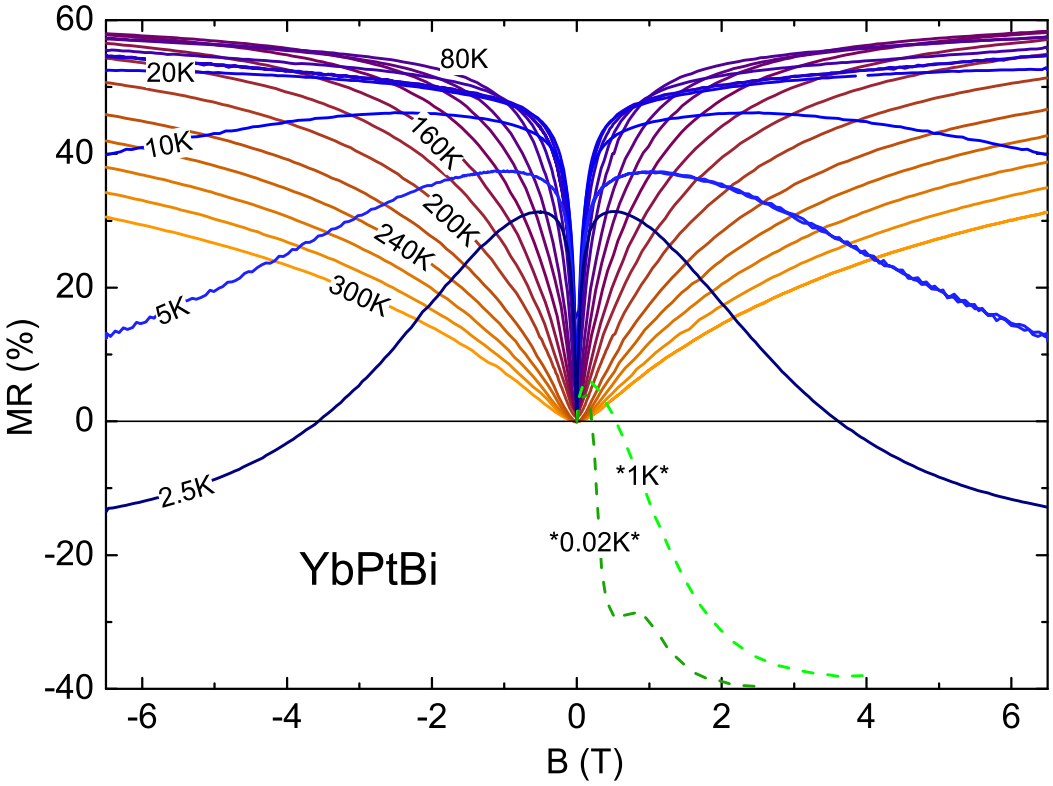

Figure 5.3.: The magneto-resistance MR of YbPtBi collected at different temperatures between 2.5 and 300 K. The magnetic field was swept from −6.5 to 6.5 T. The MR shoots up at low magnetic fields for all temperatures while it decreases upon cooling in the high-field range. The data at 1 and 0.02 K are extracted from Ref. [147] and confirm the consistency of our measurement with published data around the AFM ordering temperature.

further decreased. At very low temperatures, i.e., $T \leq 2.5\,\mathrm{K}$, the MR changes sign within our measurement range: at $B = 3.6\,\mathrm{T}$ for $T = 2.5\,\mathrm{K}$ and consistently around 0.5 T for the 1 K data of Mun *et al.* [147]. The negative MR in YbPtBi is usually related to Kondo physics [143, 147], although no comprehensive discussion was provided so far. It is worth mentioning, that comparable, but somewhat different behavior was observed recently in magneto-resistance measurements for the two related compounds ScPtBi [166] and HoPdBi [167]. For ScPtBi, the MR was positive in the whole range of applied fields (up to 10 T) and temperatures (down to 2 K), but the shape is very much alike our high temperature curves. For HoPdBi, a negative MR is observed already at 50 K and 7 T and the overall shape

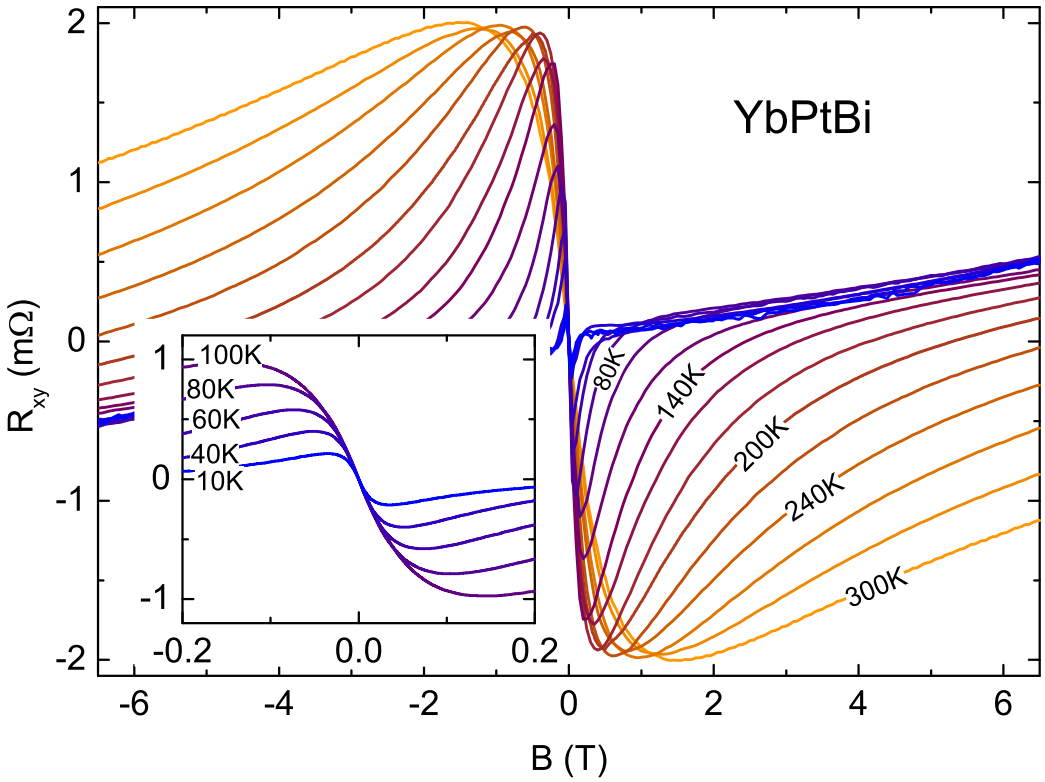

Figure 5.4.: The field-dependent Hall resistance R_{xy} for temperatures from 300 to 10 K indicates an interplay of electrons and holes in the transport properties of YbPtBi: the negative slope in the low-field range is caused by electrons while holes induce the positive slope at higher magnetic fields. The inset provides a closer look at the electron contribution at low magnetic fields and low temperatures.

is even more similar to our curves, also in the low temperature range. However, the position of the maximum in the low-field range does not shift at lower temperatures for HoPdBi, but does so in YbPtBi.

The first part of the Hall measurements on YbPtBi, the Hall resistance $R_{\mathrm{xy}}(B,T)$ is shown in Figure 5.4 as a function of the applied magnetic field for various temperatures. The low-field results (up to 0.2 T) are expanded in the inset to demonstrate the negative slope of R_{xy} for all temperatures. At fields above 1.7 T, the slope is positive for all temperatures which seems to be temperature-independent in the high-field limit.

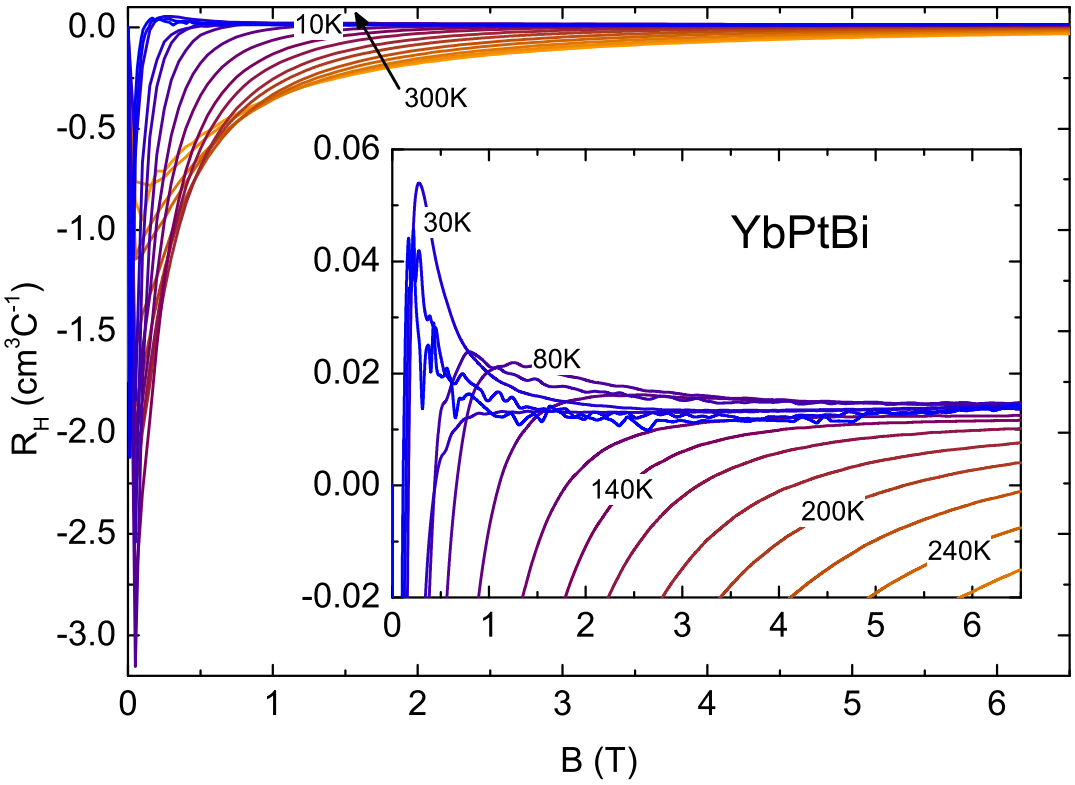

Figure 5.5.: The field-dependent Hall coefficient R_H of YbPtBi calculated from the Hall resistance provides direct access to the different charge carrier types. The negative R_H at low fields is caused by electron-dominant transport while the positive R_H at high fields implies holes as the dominating charge carriers. The inset reveals a positive absolute value for almost all temperatures and a saturation of R_H at the upper limit of our magnetic field range.

A more conventional way to discuss the Hall results is to examine the Hall coefficient $R_{\mathrm{H}}(B,T) = \rho_{\mathrm{xy}}/B$ which is given in Figure 5.5. For low magnetic fields, the Hall coefficient is always negative while it becomes positive for higher fields. The sign of R_{H} represents the type of charge carriers dominating the transport: a negative R_{H} stands for electrons while a positive R_{H} is caused by a hole dominated transport. Thus, the Hall measurement is consistent with what was discussed for the MR results: one type of charge carriers, namely electrons, is localized in the low-field range, where a temperature-independent type, namely holes, takes over the transport properties.

The Hall coefficient turns positive for all temperatures below 240 K within our mag-

netic field range and saturates at $0.015\,\mathrm{cm^3C^{-1}}$. Apparently, the same value would be reached for the highest temperatures if the measurements would be extended to higher magnetic fields, as demonstrated by the inset of Figure 5.5. For intermediate magnetic fields, the positive saturation value is exceeded at temperatures below 100 K which agrees again with the point of inflection in the zero-field resistivity measurements (see Figure 5.2).

The Hall measurement allows to calculate the charge carrier concentration n with $R_\mathrm{H} = 1/(ne)$. At this state, we use a one-carrier type model and apply it separately to the low-field (electron) and high-field (hole) range to determine the electron n_e and hole n_h concentration.
Furthermore, the Hall coefficient provides the opportunity to calculate the mobility μ of the two different charge carrier types with $\mu = R_\mathrm{H}\sigma_\mathrm{dc}$. Nevertheless, the two-carrier type scenario does not allow us to compute the different carrier mobilities in a straightforward way as we are not able to separate the contributions of electrons and holes to the total dc conductivity σ_dc. Therefore, we take a one-carrier-type (OCT) approach and use the measured dc conductivity to calculate both, electron and hole mobilities.

Both results, the charge carrier concentrations and the mobilities for electrons and holes are given in Figure 5.6. As mentioned before, the dominant carriers at high magnetic fields are holes as R_H is positive for almost all temperatures. We assign the deviation from the saturation value to remaining contributions from the electrons and evaluate the hole carrier concentration to be independent of temperature leading to $n_h = (5.2 \pm 0.6) \times 10^{20}\,\mathrm{cm^{-3}}$, as shown in panel (b) of Figure 5.6. In contrast, the carrier concentration of the electrons n_e (panel (a)) demonstrates a strong temperature dependence and its absolute value is at least one order of magnitude lower than n_h. Above 50 K, $n_e(T)$ follows a T^2 behavior while it saturates for the low-temperature range.
The OCT Hall mobilities of the electrons μ_e^{OCT} as well as of the holes μ_h^{OCT} decay exponentially with increasing temperature, see panels (c) and (d) of Figure 5.6. The absolute value, however, is two orders of magnitude larger for the electrons than for the holes. At lowest temperatures, we get $\mu_e^{OCT} \approx 53\,000\,\mathrm{cm^2/Vs}$ which is the highest mobility observed for any half-Heusler compound so far; the hole mobility

is in the range of conventional metals.

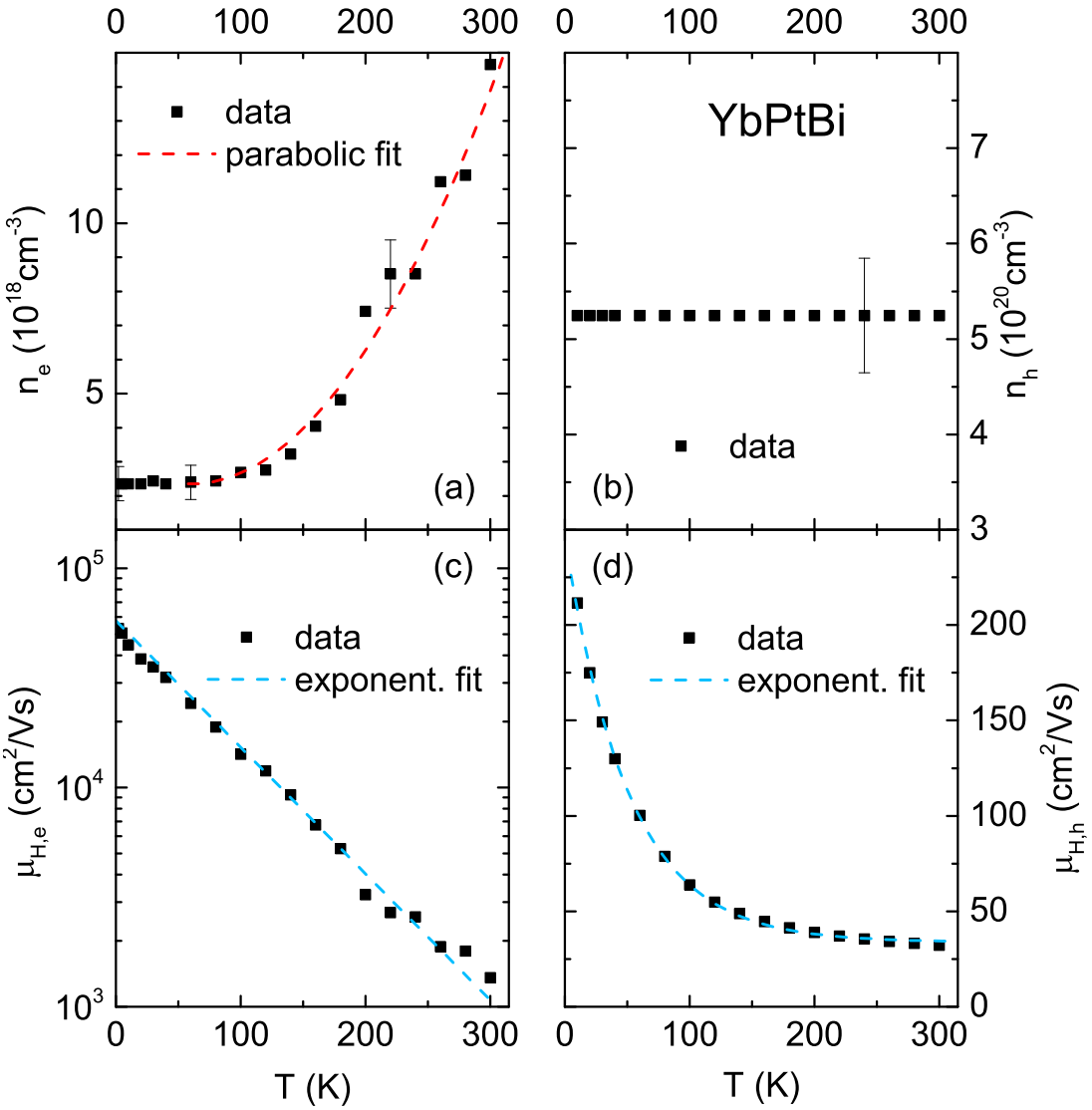

Figure 5.6.: The charge carrier concentration n and the Hall mobility μ_H of the electrons (left) and holes (right) in YbPtBi extracted from Hall measurements by applying a one-carrier-type model separately for low and for high magnetic fields. While the holes, dominant at higher fields, have a temperature-independent carrier concentration (b), the electrons, only present in the low-field range, follow a T^2 behavior (a). The mobility of the latter (c) is record high for the half-Heusler family: $\mu_e^{OCT} \approx 53\,000\,\mathrm{cm}^2/\mathrm{Vs}$ at lowest temperature. In contrast, the holes possess a rather normal metal-like mobility at least two orders of magnitude lower than μ_e^{OCT}.

Optics

Here, we will show how our optical measurements on YbPtBi confirm the two-carrier-type idea from the magneto-transport experiments and additionally help to separate the contributions of electrons and holes from the overall transport in YbPtBi.

The optical reflectivity $R(\omega)$ was measured for frequencies from 50 to 25 000 cm^{-1} and is displayed in Figure 5.7 (a) for selected temperatures. The intraband contributions with a Drude-like shape are settled below 2000 cm^{-1} and separated from the the interband transitions at higher frequencies. The plasma edge in $R(\omega)$ (characteristic downturn at $\sim 1000\,\mathrm{cm}^{-1}$) does, however, only reach an absolute value of 0.45 indicating some overlap of intra- and interband transitions in the mid-infrared range.

From the measured reflectivity $R(\omega)$, the complex optical functions $\hat{\sigma}(\omega)$ and $\hat{\varepsilon}(\omega)$ are obtained via Kramers-Kronig analysis as described in section 3.5. As mentioned before, we will mainly discuss the real part of the optical conductivity $\sigma_1(\omega)$ and, instead of the imaginary part $\sigma_2(\omega)$, the real part of the dielectric function $\varepsilon_1(\omega)$ as is usually done in the community. Thus, $\sigma_1(\omega)$ and $\varepsilon_1(\omega)$ can be found in Figure 5.7 in panels (b) and (c) respectively.

The optical conductivity does not only support the separation of intra- and interband contributions, but also suggests that the low-frequency response consists of two different Drude-like terms: the rather flat conductivity between 200 and 1000 cm^{-1} with a drop-down at the upper end corresponds to a broader (i.e., relatively large scattering rate) Drude while a sharp upturn at the lower end of the measurement range indicates a much more narrow (i.e., smaller scattering rate) Drude response. The latter Drude term is located primarily in a frequency range which is influenced by the extrapolation of the reflectivity data before the Kramers-Kronig analysis (dashed line in Figure 5.7). It is, however, validated by the fact that the optical conductivity in the zero-frequency-limit needs to match the dc conductivity which can be extracted from the transport measurement, as shown later. Furthermore, the narrow Drude leaves its fingerprint in the reflectivity spectrum to much higher frequencies than the scattering rate, as the edge of the Drude term in $R(\omega)$ is given

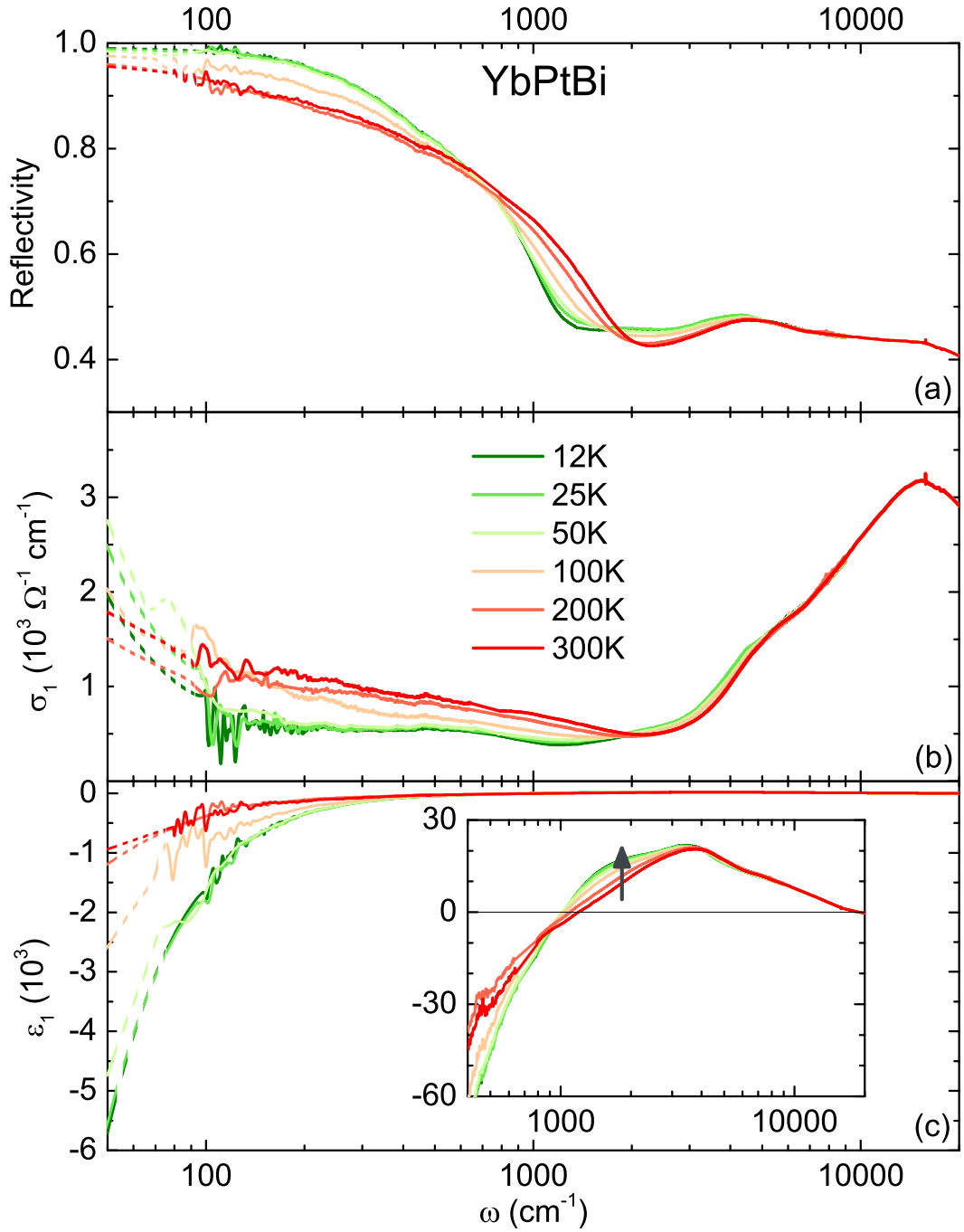

Figure 5.7.: (a) The frequency-dependent reflectivity of YbPtBi over the entire frequency range for selected temperatures. While temperature does have an influence on the plasma edge around $1000\,\mathrm{cm}^{-1}$*, the high-frequency range remains more or less unchanged. The real parts of the optical conductivity* $\sigma_1(\omega)$ *and the dielectric function* $\varepsilon_1(\omega)$ *are shown in panels (b) and (c), respectively. The shape of the curves, in particular* $\sigma_1(\omega)$ *suggest two Drude terms with different scattering rates. The inset of panel (c) clarifies the zero crossing of* $\varepsilon_1(\omega)$ *and the development of an additional interband contribution around* $1600\,\mathrm{cm}^{-1}$*.*

by the plasma frequency which is between 2000 and 4000 cm^{-1}.
The dielectric function $\varepsilon_1(\omega)$ is negative for frequencies below 1000 cm^{-1} for all temperatures due to a free-carrier response (Drude) and possesses a broad maximum around 3500 cm^{-1} indicating a pronounced interband transition in this range [21]. Upon cooling, $\varepsilon_1(\omega)$ increases at 1600 cm^{-1}, revealing the development of an additional interband transition. This shoulder is first noticeable at $\sim$ 100 K and becomes more pronounced at lower temperatures. Consequently, a connection to the point of inflection in the resistivity curve (Figure 5.2) is possible and might indicate a feasible band structure modification at this temperature.
The zero-crossing of $\varepsilon_1(\omega)$ occurs at the screened plasma frequency $\omega_{\mathrm{pl}}^{\mathrm{scr}} = \sqrt{\frac{ne^2}{m^*\varepsilon_0\varepsilon_\infty}}$, as explained in chapter 4. n is again the free carrier density and m^* reflects the effective carrier mass[2]. Thus, the zero-crossing of $\varepsilon_1(\omega)$ confirms the temperature dependence of the carrier concentration. As the zero crossing shifts to lower frequencies (from 1200 to 1000 cm^{-1}) the carrier concentration described by the optical response is consistent with the reduction of the concentration determined from the Hall measurements.

To achieve a deeper insight into the charge carrier dynamics of YbPtBi, we simultaneously fit the spectra of $R(\omega)$, $\sigma_1(\omega)$ and $\varepsilon_1(\omega)$ for each temperature by a Drude-Lorentz model. Above, we already mentioned that $\sigma_1(\omega)$ indicates two Drude-like terms in the low-frequency range. Here we want to state, that we are not able to describe the complete data set ($R(\omega)$, $\sigma_1(\omega)$ and $\varepsilon_1(\omega)$) with only a single Drude term as commonly done in normal metals or semimetals. We do, however, obtain a satisfactory fit to describe our measurement data if we include two Drude terms in the model.
Results of this fitting procedure are given in Figure 5.8: the complete set ($R(\omega)$, $\sigma_1(\omega)$ and $\varepsilon_1(\omega)$) for $T = 12$ K in panels (a), (b) and (c) respectively, also including the separate contributions of the two Drude terms; panel (d) provides the fits of $\sigma_1(\omega)$ for 300 K to cover the complete temperature range.

The fits are in very good agreement with all three fitted quantities and thus provide a suitable description of the complex optical functions of YbPtBi. The two Drude

[2] As there is no evidence for a temperature-dependent effective mass given in literature, we consider it to be constant.

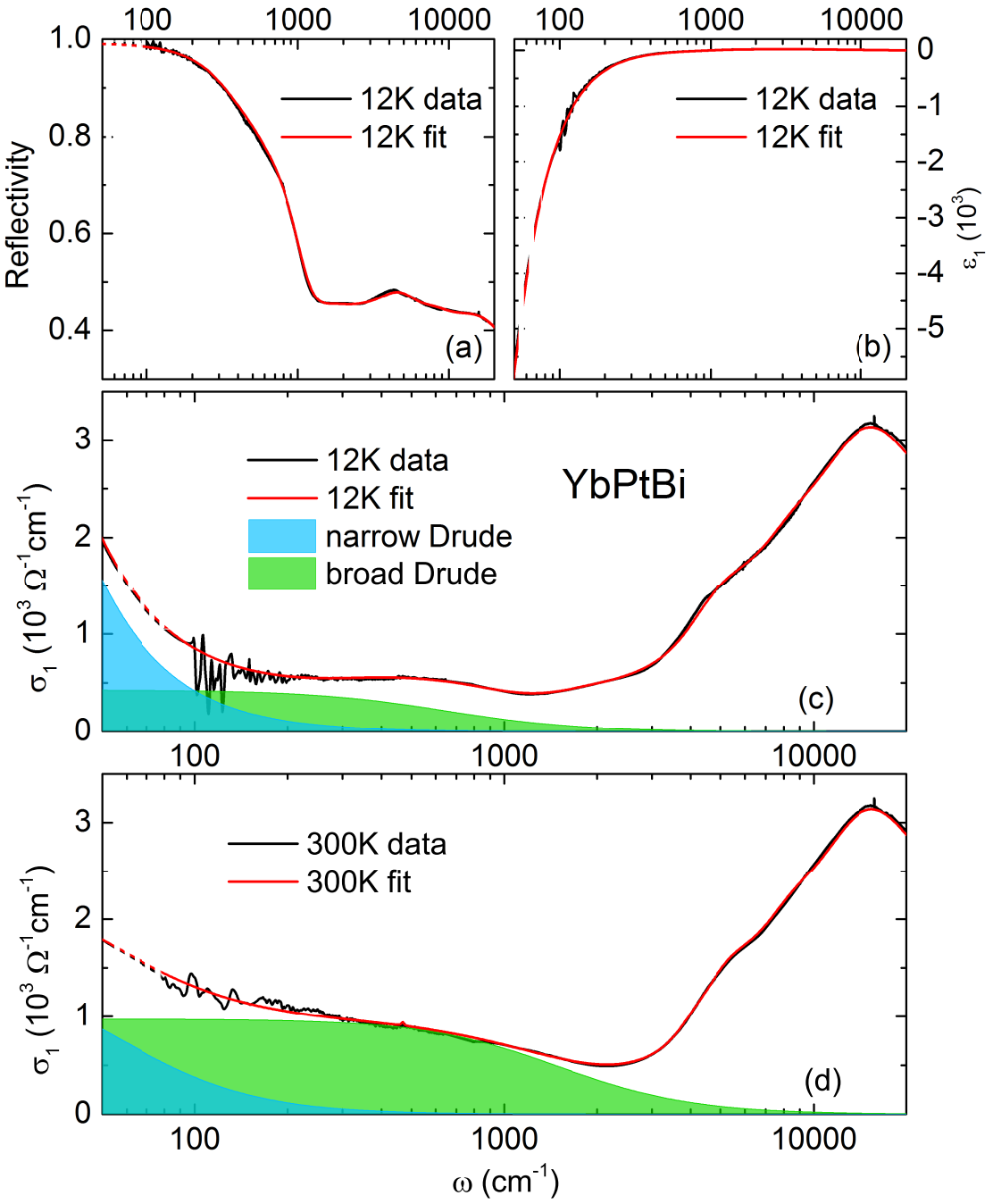

Figure 5.8.: The Drude-Lorentz model describing the experimental data of YbPtBi contains two Drude terms with different scattering rates $1/\tau$ to take care of the large difference in the mobilities of electrons and holes. A model with only one Drude term could not produce a satisfying fit. Panels (a), (b) and (c) provide the complete fit of all three quantities at 12 K. For $\sigma_1(\omega)$, the contributions of the two Drude terms are depicted as shaded areas. Panel (d) shows the fit of $\sigma_1(\omega)$ at 300 K, proving that the same model holds for the complete measured temperature range.

terms have scattering rates $1/\tau$ that differ by more than an order of magnitude and from now will on be labeled as broad (bD) and narrow (nD) Drude. The effective carrier masses m^* extracted from Shubnikov–de Haas oscillations is close to the free-electron mass m_e for any band ($\sim$ 0.5 to 1.5 $\mathrm{m_e}$) [149]. Keeping this in mind, the huge difference between the electron and hole mobilities observed in the magneto-transport results is most likely be related to different scattering rates as it reads $\mu = e\tau/m^*$. Thus, the highly mobile electrons can be assigned to a small scattering rate $1/\tau$, represented by the narrow Drude term, while the low mobility of the holes entails a larger scattering rate described by the broad Drude term. From our fits, we determine τ between 54 $\mathrm{cm^{-1}}$ at 300 K and 16 $\mathrm{cm^{-1}}$ at 12 K for the former one and values between 1500 $\mathrm{cm^{-1}}$ at 300 K and 785 $\mathrm{cm^{-1}}$ at 12 K for the latter one.

The optical fits allow us now to split the total conductivity with the help of the two Drude terms into the different contributions of electrons and holes, so we redraw Figure 5.2 by adding the dc transport conductivity $\sigma_{\mathrm{dc}} = 1/\rho_{\mathrm{dc}}$ in Figure 5.9. Additionally, the dc conductivities of the narrow Drude (σ_0^{nD}) and the broad Drude (σ_0^{bD}) as well as the total optical dc conductivity ($\sigma_0^{\mathrm{nD}} + \sigma_0^{\mathrm{bD}}$) obtained by the optical fits are displayed as open symbols.
One can see that the conductivity at high temperatures is more or less equally distributed between the Drude terms and consequently stems from electrons and holes. In contrast, the narrow Drude (i.e., the electrons) covers more than 90% of the total conductivity in the low-temperature range. The sum $\sigma_0^{\mathrm{nD}} + \sigma_0^{\mathrm{bD}}$ confirms that the optical data and fits are consistent with the transport measurements as it falls nicely onto the σ_{dc} curve.

The newly gained insights into the conductivity contributions can be used to recalculate the mobilities from the Hall measurements with the adjusted conductivity values, since we used $\mu^{OCT} = R_{\mathrm{H}}\sigma_{\mathrm{dc}}$ before. Since the conductivity of the holes differs a lot from the total conductivity, the change in the hole mobility compared to the one-carrier-type approximation assumed before will be more pronounced than the one for the electrons. We get $\mu_h = (10 \pm 5)\,\mathrm{cm^2/Vs}$ and barely any temperature dependence within the given error bar. However, a weak temperature dependence of μ_h cannot be excluded and the scattering rate of the broad Drude does change somewhat as a function of T.

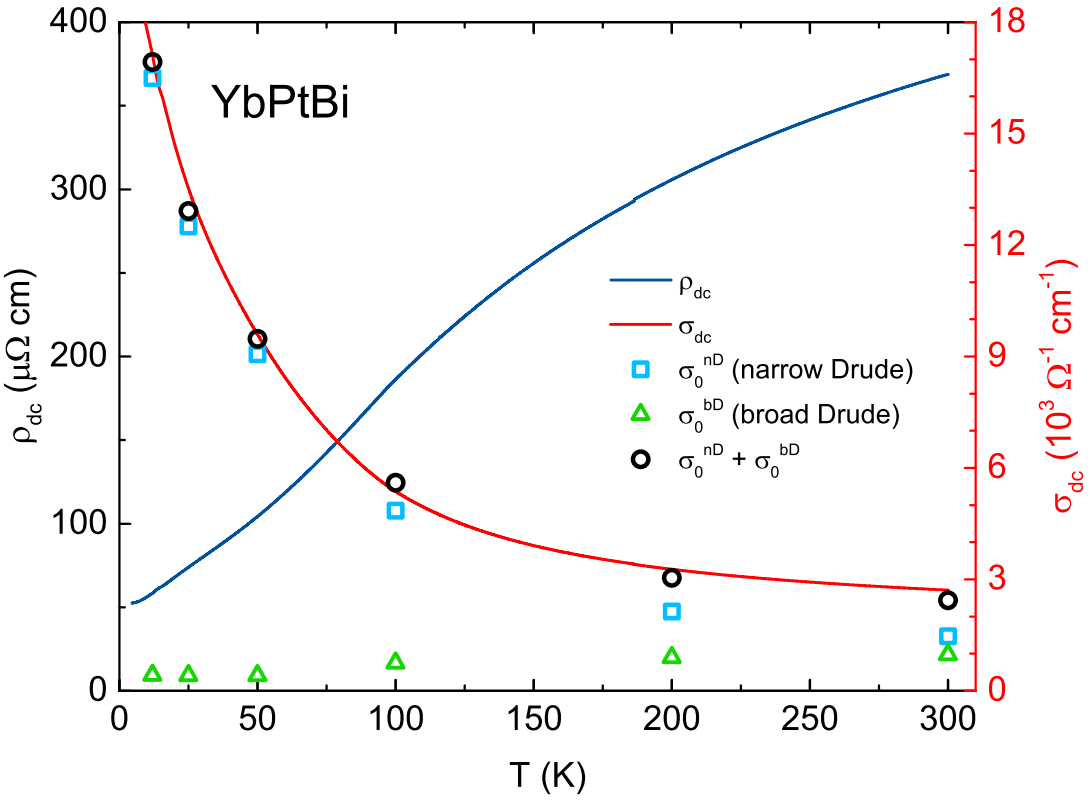

Figure 5.9.: The temperature-dependent resistivity $\rho_{dc}(T)$ of YbPtBi is complemented by the dc conductivity $\sigma_{dc} = 1/\rho_{dc}(T)$. The open symbols represent the zero-frequency conductivity of the Drude terms: σ_0^{nD} for the narrow Drude and σ_0^{bD} for the broad Drude, obtained by the optical fitting procedure. As the sum $(\sigma_0^{nD} + \sigma_0^{bD})$ coincides with the dc conductivity of the transport measurements, our fit model is consistent with all experimental data.

The mobility of the electrons changes minimally upon replacing the OCT by σ_0^{nD} and also the temperature dependence rather stays the same. As mentioned before, μ_e increases exponentially upon cooling. We use $\mu_e(T) = \mu_e(0)\exp(-T/T_0)$ and get $\mu_e(0) = 51\,000\,\mathrm{cm}^2/\mathrm{Vs}$ and $T_0 = 75\,\mathrm{K}$. This exponential increase of μ_e is remarkable: other materials with such high mobilities, e.g., the Weyl semimetal NbP, reveal a saturation of $\mu(T)$ at temperatures below $20 - 30\,\mathrm{K}$ [164]. The exponential behavior in YbPtBi holds even for our lowest measured temperature of $2.5\,\mathrm{K}$ indicating a collapse of electron scattering at low temperatures.

The magneto-transport and optical measurement results on YbPtBi presented above

demonstrate two different conduction channels, one caused by highly mobile electrons and the second channel by holes with a low mobility.

5.3. Dirac physics in YbPtBi & GdPtBi

While, so far, we mainly discussed the itinerant free-carrier contribution of the optical data, let us now turn to the interband physics of YbPtBi. Here, we will draw conclusions about possible Dirac or Weyl states in the half-Heusler material YbPtBi. Furthermore, optical data obtained on GdPtBi will serve as comparison, which were mainly measured by M.Sc. cand. Felix Hütt from the 1. Physikalisches Institut - Universität Stuttgart, supervised by the author. A full analysis of the measurements on GdPtBi will be given in Ref. [168].

Compared to YbPtBi, the $4f$ electrons in GdPtBi obey a stronger exchange field, thus being closer to Weyl physics [153]. Therefore, it is likely, that any features observed in this context are stronger and easier to resolve in GdPtBi. As already mentioned before, experimental evidence for Weyl states in an external magnetic field are already published for GdPtBi [169–171]. In this context, the band structure in zero magnetic field was proposed to consist of two degenerate parabolic bands touching each other at the Γ-point of the Brillouin zone. Only the lifting of the degeneracy by the external magnetic fields would introduce the crossing of linear bands. Early ARPES measurements revealed linear bands in GdPtBi without any external field, however, the Fermi level was much lower than in more recently investigated samples and therefore far away from any touching or crossing point of the valence and conduction band [172]. Additionally, the linear bands were assigned to surface states and not to a band crossing in the bulk, and hence do not provide a final proof of the band structure.

As mentioned in section 5.1, recent theoretical calculations propose triple points without external magnetic field in some of the half-Heusler compounds, including GdPtBi. To conclude the state of the art, there are contradicting theoretical and experimental results for the compounds here presented. This calls for further investigations and supplementary experimental methods to gain additional information.

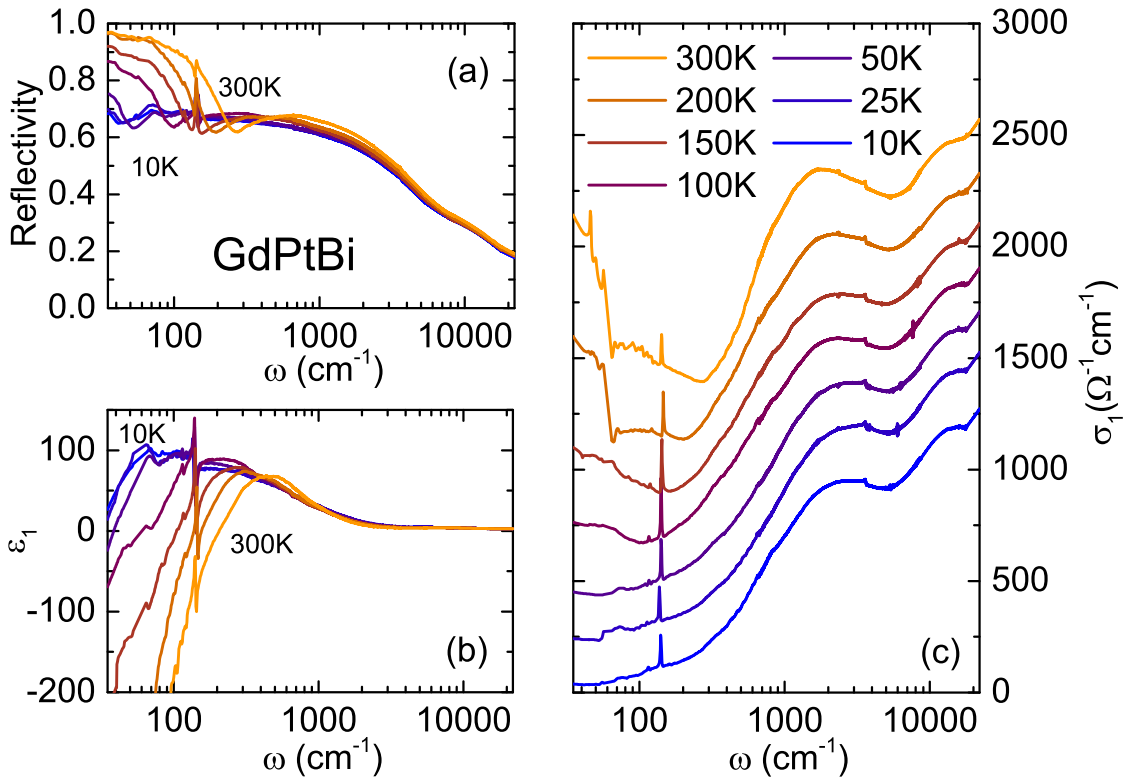

Figure 5.10.: The reflectivity (a), the real part of the dielectric function (b) and the optical conductivity (c) of GdPtBi given for different temperatures over the measured frequency range. The low-frequency response is clearly dominated by itinerant carriers as its shape is Drude-like. This narrow Drude component shifts to the lowest measured frequency upon cooling. A phonon is observed around $140\,\mathrm{cm}^{-1}$. *Above* $50\,\mathrm{cm}^{-1}$, *the spectrum is already influenced by interband transitions because* $\varepsilon_1(\omega)$ *is positive. Redrawn from Ref.[142].*

The data treatment and the Kramers-Kronig analysis for the GdPtBi measurements is the same as for YbPtBi described in section 5.2. The results in terms of reflectivity $R(\omega)$, the real part of the dielectric function $\varepsilon_1(\omega)$ and the real part of the optical conductivity $\sigma_1(\omega)$ are given in Figure 5.10.

The influence of reducing the temperature is negligible for frequencies above approximately $4000\,\mathrm{cm}^{-1}$. A sharp phonon peak can be found in the reflectivity data, see panel (a), at $\omega_{\mathrm{phonon}} = (140 \pm 5)\,\mathrm{cm}^{-1}$. Furthermore, the plasma edge of the free-carrier response is located above $100\,\mathrm{cm}^{-1}$ at room-temperature, and shifts to the very low end of the measurement window upon cooling. This indicates either a

very small carrier density n or a large effective mass m^*, as was indicated already in section 5.2. The results of the Kramers-Kronig analysis are depicted in panels (b) and (c). The intrinsic free-carriers are confirmed by the negative absolute values of $\varepsilon_1(\omega)$ in the low-frequency range, especially for the higher temperatures. After the zero-crossing, $\varepsilon_1(\omega)$ shoots up to an absolute value of 99, unambiguously revealing interband transitions at rather low frequencies. The optical conductivity in panel (c) is stacked for clarity. For higher temperatures, a Drude peak can be seen at the lower end of the measured frequency range. Upon cooling, this Drude component shifts to lower frequencies and is not clearly visible anymore already at 100 K. In accordance, the spectrum flattens for decreasing temperatures between 50 and 300 cm^{-1}, which looks like a vanishing shoulder of the Drude component. The smooth increase of $\sigma_1(\omega)$ peaks at around 1500 cm^{-1} followed by a second increase at higher frequencies, indicating additional interband transitions.

In Figure 5.11, the real part of the optical conductivity is given on a linear scale for the lowest measured temperature (10 K). With this, the smooth increase is revealed to depend linear on the frequency: $\sigma_1 \propto \omega$. A linear fit to this data perfectly extrapolates to zero and matches the data for more than an order of magnitude. In a 3D system, this is associated with a linear band crossing without a gap, as explained in section 2.7 (Equation 2.8). At this stage, we are unable to distinguish whether this linear conductivity arises from Dirac, Weyl or triple point states. However, with Equation 2.7 we are able to calculate the Fermi velocity of the linear bands with respect to the number of non-degenerate cones N_W. With a slope of 0.78 $\frac{\Omega^{-1}\mathrm{cm}^{-1}}{\mathrm{cm}^{-1}}$, we obtain $\frac{v_F}{N_W}[\mathrm{Gd}] = (7.8 \pm 0.5) \times 10^3\,\mathrm{m/s}$. We do not observe a significant step at the lower end of the linear region, which could be related to the position of the chemical potential (distance between Fermi level and linear band crossing), as discussed in section 2.7. Thus, we can only provide an upper limit with $2\mu \leq 50\,\mathrm{cm}^{-1}$, resulting in $\mu \leq 3\,\mathrm{meV}$.

Our experimental observation indicates a linear band crossing in GdPtBi without applied magnetic field. At first glance, this contradicts earlier theoretical [153] and experimental [169] work, where the Dirac or Weyl states only exist when an external magnetic field is applied. Only the work by H. Yang *et al.* discuss Dirac states without magnetic field resulting in the proposed triple points [8].

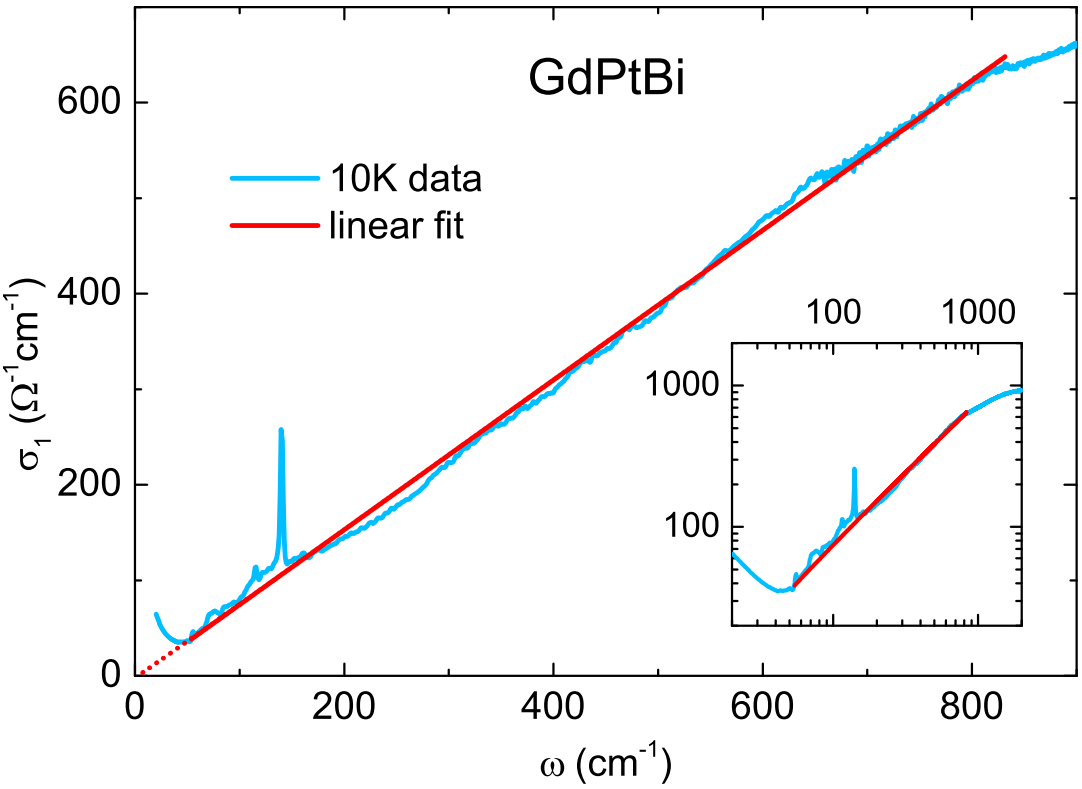

Figure 5.11.: The real part of the optical conductivity $\sigma_1(\omega)$ on a linear scale at 10 K. The linear fit is used to describe the interband contribution of GdPtBi from 50 to 800 cm^{-1}, reproducing Dirac-like states with a linear dispersion relation. The fit extrapolates to zero and its slope will be used to calculate the Fermi velocity. The inset proves a perfect linear frequency dependence as a linear fit with a slope of 1 is revealed on a log-log-plot.

In Figure 5.12 we compare the optical conductivity of GdPtBi to the bare interband conductivity of YbPtBi $\sigma_{\mathrm{int,Yb}}(\omega)$. The latter is obtained by subtracting the two different Drude components, the narrow and the broad one, from the total optical conductivity discussed before. For the GdPtBi measurement, we do not need to subtract the Drude component, because it is at the lowest end of our frequency range. The inset also reveals a range where σ_1 is linearly depending on the frequency for the YbPtBi compound. This goes up to approximately 450 cm^{-1} with a only slightly smaller slope than for GdPtBi. Again, the linear fit extrapolates to zero indicating a linear energy band crossing without gap. Following the procedure above, we

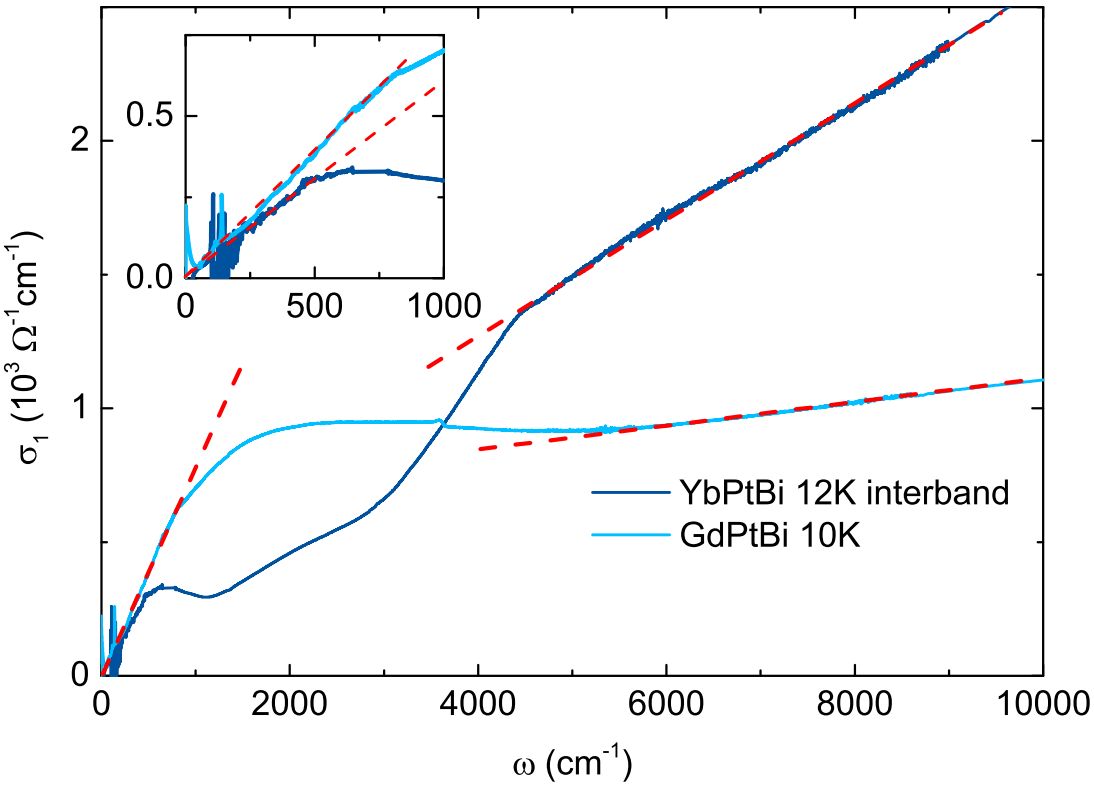

Figure 5.12.: The interband optical conductivity of YbPtBi at 12 K is achieved by subtracting the Drude components from the initial spectrum and compared to the conductivity of GdPtBi. A linear rise is revealed in the low-frequency range for both compounds. Above 5000 cm^{-1}, a second linear dependence on the frequency is found, also indicating a comparable band structure in this energy range. The inset provides a closer look at the low-frequency conductivity.

determine a Fermi velocity for the YbPtBi measurement, where the slope of the linear part is 0.72 $\frac{\Omega^{-1}\mathrm{cm}^{-1}}{\mathrm{cm}^{-1}}$, of $\frac{v_F}{N_W}[\mathrm{Yb}] = (8.4 \pm 0.5) \times 10^3$ m/s. In the range between 1000 and 4000 cm^{-1} the two spectra are somewhat different. While the GdPtBi spectrum is rather flat after the linear increase, the YbPtBi measurement shows two more or less linearly increasing sections which are separated by pronounced kinks. Above 5000 cm^{-1}, the optical response is again comparable between the two compounds once again. Both show a linear dependence on the frequency, again. The slope of the Yb compound is larger in this case with 0.20 $\frac{\Omega^{-1}\mathrm{cm}^{-1}}{\mathrm{cm}^{-1}}$, whereas the Gd compound yields 0.04 $\frac{\Omega^{-1}\mathrm{cm}^{-1}}{\mathrm{cm}^{-1}}$. These values lead to much higher Fermi velocities compared to the larger slopes in the low-frequency range, as discussed below.

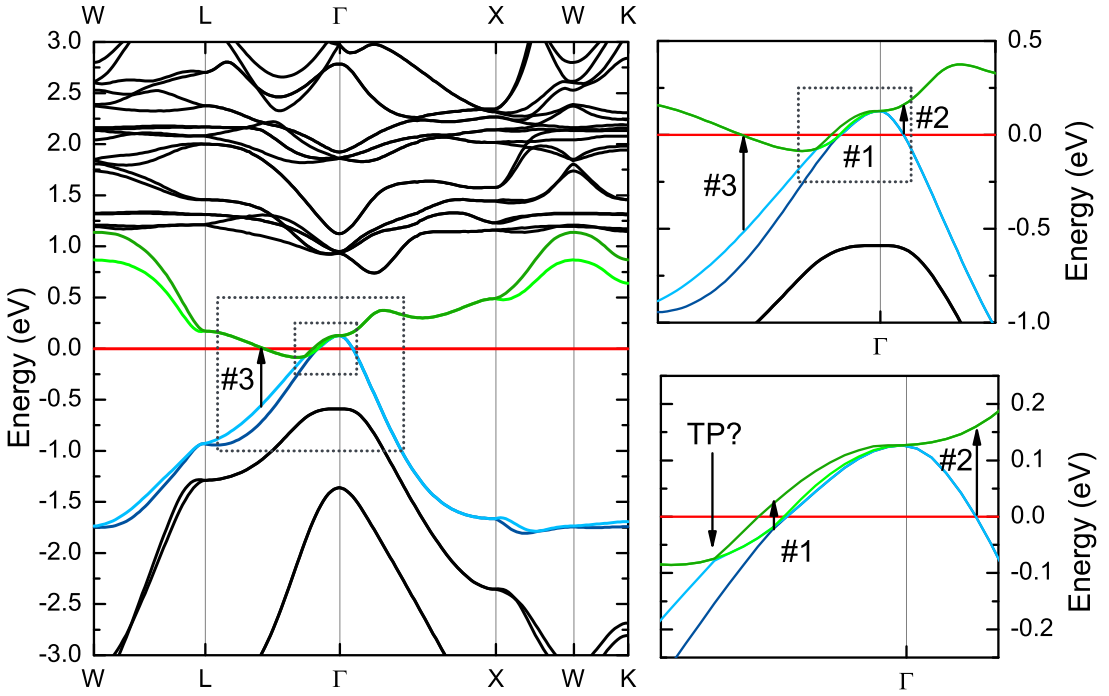

Figure 5.13.: Band structure calculations on YbPtBi provided by Jun. Prof. Dr. H. Zhang. The bands close to the Fermi level are depicted in blue (valence bands) and green (conduction bands), while the bands which are not relevant for our optical results are shown in black. Three different areas can be identified hosting transitions from occupied to empty states, labeled #1, #2 and #3. The possible location of the triple point is also indicated.

To further analyze our results and draw conclusions about the underlying band structure in the half-Heusler compounds, especially in YbPtBi, we compare it to the calculated band structure given in Figure 5.13.
These calculations were provided by Jun. Prof. Dr. H. Zhang from the Technische Universität Darmstadt. In this band structure picture, all bands which are irrelevant at our energy scale are given in black, while the two valence bands and the two conduction bands close to the Fermi level are given in blue and green, see panel (a). These four bands cross the Fermi level in the vicinity of the Γ-point, leading to electron and hole pockets. This is in good agreement with the two channel conduction discussed in the previous section. The four bands cross and touch each

other creating three interesting areas along the Γ-L- and the Γ-X-direction, labeled with #1, #2 and #3. To address these in our optical measurements, we need to excite charge carriers from occupied states (below the Fermi level) to empty states (above the Fermi level). This limits the frequency range in which to examine for the particular transitions in our optical spectra.

In area #1, the distance between occupied and empty states is the smallest and, hence, should cause a contribution to the optical conductivity in the lower frequency range. Transitions in this area are possible up to approximately 50 meV = 400 cm^{-1}. Area #2 is limited to an energy range from 160 to 620 meV, 1290 to 5000 cm^{-1}, on the Γ-X-direction. Above, the conduction bands bend in area #2, leading to a more complex situation. Last but not least, area #3 is restricted to a range from 580 to 1100 meV, 4700 to 8900 cm^{-1}, on the Γ-L-direction. Notice, that the areas do not overlap which helps assigning the different areas in the optical spectrum. It is worth mentioning, that in all three areas the contributing bands are close to linearity. The bent and curved parts are automatically excluded, as either all four bands are above or below the Fermi level and, thus, do not provide interband transitions from occupied to empty states. There is, however, a noteworthy difference: areas #2 and #3 can be seen as a part of a Dirac cone, since the valence and conduction bands disperse in different directions, i.e., one has a positive the other a negative slope; in contrast, the bands in area #1 disperse roughly in the same direction.

From the band structure calculations, we can extract the Fermi velocity of the dispersing bands. To do so, one needs to know the distance between the symmetry points Γ, L and X, so we use Ref. [173] to gain information about the Brillouin zone of cubic face-centered structures. The Γ-point is located in the center of the Brillouin zone, the L-point is located at $(\frac{\pi}{a}/\frac{\pi}{a}/\frac{\pi}{a})$ and the X-point at $(0/\frac{2\pi}{a}/0)$. With a lattice parameter of $a = 6.591\,\text{Å}$ we get $d[\Gamma\text{-L}] = 0.826\,\text{Å}^{-1}$ and $d[\Gamma\text{-X}] = 0.953\,\text{Å}^{-1}$. In area #1, the bands thus disperse with a velocity of approximately $(1.45 \pm 0.10)\,\text{eVÅ} = (2.20 \pm 0.15) \times 10^5\,\text{m/s}$; the small difference between the different bands lays within the error bars. The dispersion is higher in area #2, where the valence bands (blue) possess a velocity of $(3.18 \pm 0.05)\,\text{eVÅ} = (4.83 \pm 0.08) \times 10^5\,\text{m/s}$ and the conduction bands (green) of $(1.95 \pm 0.05)\,\text{eVÅ} = (2.96 \pm 0.08) \times 10^5\,\text{m/s}$. Note, that the conduction bands are curved in the begin-

ning. Thus a small deviation from Dirac-like transitions in the optical spectrum can be expected. In area #3, the conduction bands disperse with $(0.61 \pm 0.05)\,\mathrm{eV\AA} = (0.92 \pm 0.08) \times 10^5\,\mathrm{m/s}$ while the upper valence band gives $(0.76 \pm 0.05)\,\mathrm{eV\AA} = (1.15 \pm 0.08) \times 10^5\,\mathrm{m/s}$. The lower valence band (dark blue) shows a slightly steeper dispersion, but transitions only set in at higher energies as the distance to the conduction bands is larger.

Let us now trace the three areas in the optical spectrum of YbPtBi as depicted in Figure 5.14. Area #1 perfectly overlaps with the range of linear conductivity, which is comparable to what was found in GdPtBi. We propose, that the linear dependence of σ_1 as a function of frequency in this area rises from Dirac (or Weyl/TP) states. As mentioned before, the situation in GdPtBi is clearer since the Drude contribution does not have to be subtracted to trace the linearity. However, the detailed band structure is only available for YbPtBi, so far. Our experimental results suggest Dirac-like states without any external magnetic field in both compounds, YbPtBi and GdPtBi. The only theoretical model taking Dirac-like states in zero magnetic field into account is the triple point picture for half-Heusler compounds [8]. It is worth mentioning, while YbPtBi is not explicitly addressed in this reference, our own band structure calculations indicate a comparable situation as shown for GdPtBi. This includes a triple point on the Γ-L-direction. Our linear optical conductivity is in agreement with this picture, but cannot rule out other scenarios like conventional Dirac states or pairs of Weyl points.

In order to finally determine the Fermi velocity v_F of the linearly dispersing states, we have to identify out the correct value for N_W. According to Yang *et al.*, the triple points lie on the C_3 axes, where four of them are located inside the first Brillouin zone. On each axis, a pair of TPs is located, in GdPtBi at least, leading to eight TPs in total. In contrast to Weyl points, where the point is non-degenerate, one of the bands creating the TP is doubly degenerate. This yields in a final value of $N_W = 16$. From the conductivity slopes extracted above, the Fermi velocities of GdPtBi and YbPtBi then finally read $v_F[\mathrm{Gd}] = 1.25 \times 10^5\,\mathrm{m/s}$ and $v_F[\mathrm{Yb}] = 1.35 \times 10^5\,\mathrm{m/s}$, respectively. The possible location of the triple point in YbPtBi is marked in Figure 5.13 between the Γ- and the L-point. If we compare the Fermi velocity to the one extracted from the band calculations ($v_{F,\#1} = (2.20 \pm 0.15) \times 10^5\,\mathrm{m/s}$),

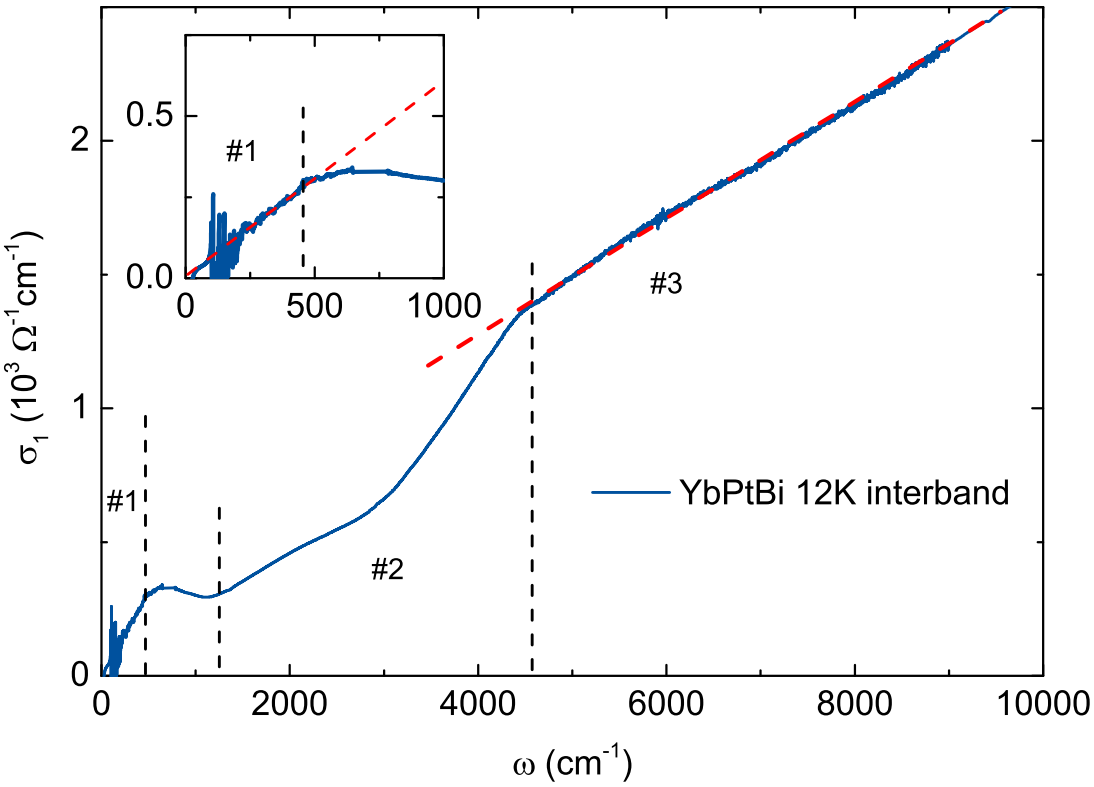

Figure 5.14.: The interband spectrum of YbPtBi at 12 K is connected to the band structure calculations by identifying the three different areas which allow transitions across the Fermi level. The characteristic frequencies, e.g., starting and end frequencies, of all three areas can be traced easily, e.g., by pronounced kinks.

roughly a factor of two is missing. As pointed out before, in area #1, both the valence and the conduction band disperse into the same direction (upwards) and, thus, the formula used to calculate the Fermi velocity from the slope of the optical conductivity for a conventional Dirac cone might not fit perfectly. Furthermore, the cones of the TPs are tilted, as the bands do not disperse symmetrically on both sides of the triple point, see Figure 5.13. The tilting of such a cone, however, cannot be easily resolved by means of optical spectroscopy as it cannot directly resolve momentum space. A model given by J. P. Carbotte in Ref. [89] requires a larger range of the linear conductivity to provide more information about the tilting. The fact that our linear fit extrapolates to zero, does indicate that the tilting is weak enough to stay in the type I tilting which is consistent with the band structure calculations.

Returning to the comparison between the two compounds, we will now focus on the two other areas. In area #2, the optical conductivity first increases with a slope of $0.19\,\frac{\Omega^{-1}\mathrm{cm}^{-1}}{\mathrm{cm}^{-1}}$ which is enhanced around $3000\,\mathrm{cm}^{-1}$ to $0.51\,\frac{\Omega^{-1}\mathrm{cm}^{-1}}{\mathrm{cm}^{-1}}$. If one follows the procedure used before, these slopes lead to Fermi velocities of $5.12 \times 10^5\,\mathrm{m/s}$ and $1.91 \times 10^5\,\mathrm{m/s}$, respectively. From the band structure, the values for this area are $4.83 \times 10^5\,\mathrm{m/s}$ for the valence bands and 1.95 to $2.96 \times 10^5\,\mathrm{m/s}$ for the conduction bands. The anisotropy between valence and conduction bands cannot be resolved by our optical measurements. The kink in $\sigma_1(\omega)$ around $3000\,\mathrm{cm}^{-1}$ might arise from a change of the slope (and linearity) of the conduction bands. In general, however, the results confirm that the optical conductivity in this frequency range arises from the transitions in area #2.

For area #3, the band dispersion diverges the most from linear bands and the splitting of the two valence bands additionally makes #3 diverge most from a linear band crossing situation. Nonetheless, we apply the same procedure to verify that the optical conductivity arises from transitions in area #3. $\sigma_1(\omega)$ rises more or less linearly above $4700\,\mathrm{cm}^{-1}$ with a slope of $0.20\,\frac{\Omega^{-1}\mathrm{cm}^{-1}}{\mathrm{cm}^{-1}}$. As mentioned before, this energy range matches the range of the transitions in area #3. The slope of $\sigma_1(\omega)$ leads to a Fermi velocity of $2.43 \times 10^5\,\mathrm{m/s}$. Note, that we set $N_W = 8$ here, since the distance between the two valence bands is large enough to expect a separated response. Compared to the dispersion extracted from the band structure calculations, we end up with a small mismatch again. As stated before, the band structure is not precisely like a Dirac cone, but only roughly. Therefore, a small deviation is not surprising. The overall agreement between the optical experiment and the band structure calculations is satisfying and the calculations can be used to separate the interband contributions to different transition areas in momentum space.

The optical results on YbPtBi and GdPtBi presented above reveal Dirac-like states (a linear band crossing) in the Gd compound in zero magnetic field, while a comparable feature can be traced in zero-field measurement of the Yb compound after subtracting the intraband contributions. Furthermore, the band structure calculations serve as a good basis to assign the interband conductivity to different parts of the Brillouin zone.

5.4. Conclusions

Motivated by the diverging theoretical and experimental results obtained for the half-Heusler compounds discussed here, we provide a comprehensive investigation on YbPtBi and GdPtBi including transport, magneto-transport, optics and band structure calculations. Our work provides deep insight into the electrodynamics and band structure of these compounds and can be summarized in mainly two aspects: On the one hand, we reveal a two-channel conduction in YbPtBi. This contains highly mobile electrons with μ_e up to $51\,000\,\mathrm{cm}^2/\mathrm{Vs}$, which is a record for any half-Heusler compound. The second channel is caused by holes with low mobility. The results are confirmed by the consistency of the optical and magneto-transport measurements.

On the other hand, our low-energy interband investigations are dominated by a Dirac-like band crossing with a linear dispersion relation. This is verified by a linear frequency dependence of the optical conductivity. We find the same behavior for YbPtBi and GdPtBi and extract Fermi velocities of $\frac{v_F}{N_W}[\mathrm{Yb}] = (8.4 \pm 0.5) \times 10^3\,\mathrm{m/s}$ and $\frac{v_F}{N_W}[\mathrm{Gd}] = (7.8 \pm 0.5) \times 10^3\,\mathrm{m/s}$. We cannot give a final proof for triple points, because Dirac or Weyl points lead to the same results in optical spectroscopy. Our experimental results are, however, consistent in all aspects with the existence of triple point fermions in some of the half-Heuslers, as proposed by Yang *et al.* [8]. Last but not least, we are able to connect our optical results on YbPtBi to our band structure calculations and successfully assign all features of the spectrum.

6. $CaMnBi_2$ & $SrMnBi_2$ - anisotropic Dirac semimetals

This chapter will provide the comprehensive results gained for the two materials $CaMnBi_2$ and $SrMnBi_2$ and is structured as follows: Section 6.1 will introduce the materials and their properties based on existing literature. In section 6.2, the optical results on $CaMnBi_2$ will be investigated. This will contain a general overview of the optical properties, as well as an interpretation of the data in terms of a density wave and possible Dirac fermion response. The results of $SrMnBi_2$ will be provided in section 6.3. The data will be compared to $CaMnBi_2$. Additionally, the fingerprints of Dirac states will also be discussed in $SrMnBi_2$. At the end, section 6.4 will conclude the chapter.

6.1. The materials

Already in 2011, $SrMnBi_2$ was found to host Dirac states in the Bi square net by means of first-principles calculations and angle-resolved photoemission spectroscopy (ARPES) [174, 175]. Only one year later, $CaMnBi_2$ was added to the discussion and investigation, since the two materials share many common properties [176–178].
The crystal structures of $SrMnBi_2$ and $CaMnBi_2$ are depicted in panels (a) and (b) of Figure 6.1. Both contain a Mn-Bi layer and a Bi square net, which are separated by X atoms (X = Sr, Ca). The Bi atoms forming the square net are referred to as Bi(1), while the ones forming the Mn-Bi layer are labeled as Bi(2). The main difference between the two materials is the stacking of the X atoms around the Bi square net: For $SrMnBi_2$, the atoms below and above one square net layer are located at the same position, while there is a shift to the Sr atoms surrounding

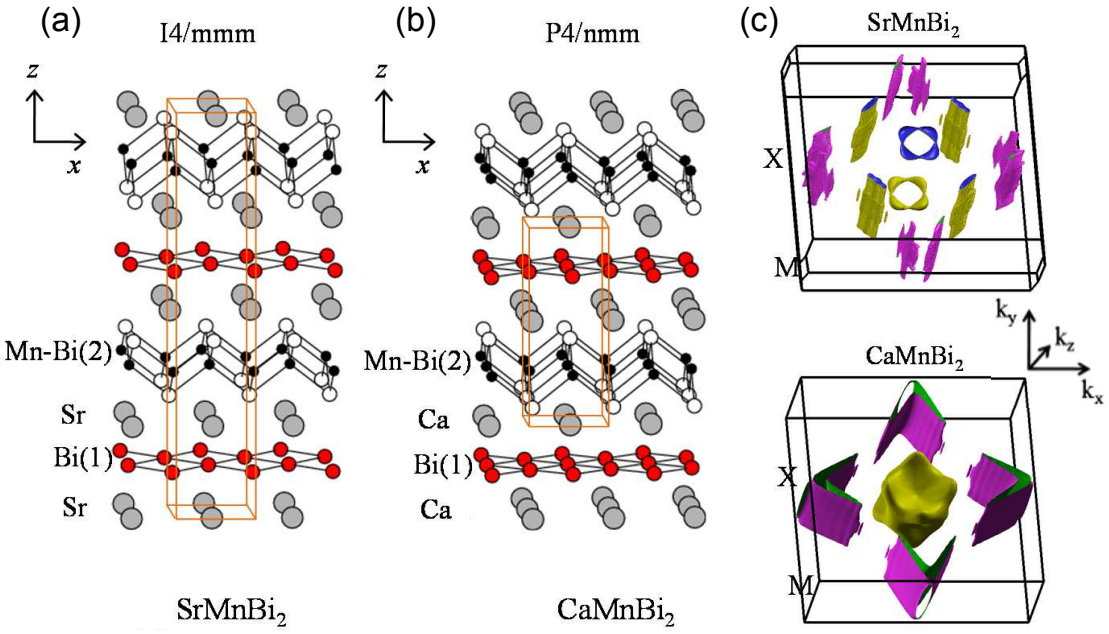

Figure 6.1.: The crystal structures of $SrMnBi_2$ and $CaMnBi_2$ are shown in panels (a) and (b). The two different types of Bi atoms are labeled Bi(1) in the square net and Bi(2) in the Mn-Bi arrangement. The general structure and the arrangement of the layers are similar. Only the arrangement of the X atoms (X = Sr, Ca) around the Bi(1) square net leads to a doubling of the unit cell in $SrMnBi_2$. The Fermi surfaces based on first-principles calculation of both compounds are given in panel (c). Both host a hole pocket around the Γ-point and highly anisotropic pockets along the X-points. Reproduced from Ref. [179].

the neighboring Bi(1) square net. For $CaMnBi_2$, the Ca atoms alternate already in the environment of one single Bi square net. This difference leads to a doubling of the unit cell for $SrMnBi_2$ compared to $CaMnBi_2$. Consequently, the space group of $SrMnBi_2$ is found to be $I4/mmm$, compared to $P4/nmm$ for $CaMnBi_2$, see, e.g., Ref. [179].

Both compounds have a comparably high magnetic ordering temperature. $SrMnBi_2$ orders antiferromagnetically at $T_N = 290\,\mathrm{K}$ [174]. For $CaMnBi_2$, the ordering temperature is found to be between 250 and 270 K [177, 178].

The calculated Fermi surfaces of the two compounds are redrawn from Ref. [179] and shown in panel (c) of Figure 6.1. The results based on the calculations are in good agreement with insights gained by, e.g., ARPES measurements [11] and quantum

oscillations [174]. Both compounds host a hole pocket at or in close vicinity of the Γ-point. Furthermore, highly anisotropic pockets are located on the symmetry lines connecting the X-points, i.e., perpendicular to the Γ-M-direction. Their relation to Dirac physics will be discussed later on. The differences of these pockets between the two compounds is linked to the different stacking of the X atoms above and below the Bi(1) square net as well as a small difference in the spin-orbit coupling strength [11, 179].

Besides the antiferromagnetic ordering, $CaMnBi_2$ hosts a second anomaly around $T_A \approx 50\,\mathrm{K}$. This anomaly was observed by various experimental techniques, i.e., transport [176–178, 180], magneto-resistance [178], susceptibility [177] and thermopower [176]. The anomaly is absent in the transport measurement of Ref. [181] and in the two-magnon Raman spectra [182]. The contradiction with respect to the former measurements may have been due to different crystal quality and purity. Thus, we will provide electron diffraction x-ray (EDX) measurements along with transport measurements on the same single crystals to verify the high quality of our samples. The absence of the anomaly in the two-magnon Raman spectra may have been caused by the same issue. A. Zhang *et al.*, however, do not provide any dc transport measurement to clarify whether their crystals show the anomaly or not. Thus, the Raman measurement cannot be used to exclude possible scenarios for the origin of this anomaly.
The magneto-resistance of $CaMnBi_2$ increases below T_A [177, 178] and a plateau was observed in the susceptibility χ and the thermopower S around T_A [176, 177]. These signatures suggest a spin-related process, e.g., spin canting, causing the anomaly at 50 K. The two-magnon Raman measurement of A. Zhang *et al.* would rule out any spin-related processes, but a transport measurement would be required to confirm that the anomaly exists in their crystal.

As stated before, $SrMnBi_2$ and $CaMnBi_2$ were found to host anisotropic Dirac cones [11, 174, 179]. Here, we introduce how the Dirac states arise in the two compounds, which will help to understand the optical response later.
The Dirac states in $XMnBi_2$ stem from the Bi(1) square net, which is surrounded by the X atoms, see Figure 6.1. It was shown, that these Dirac states are mainly produced by the p_x- and p_y-orbitals of the Bi(1) atoms forming the square net, e.g.,

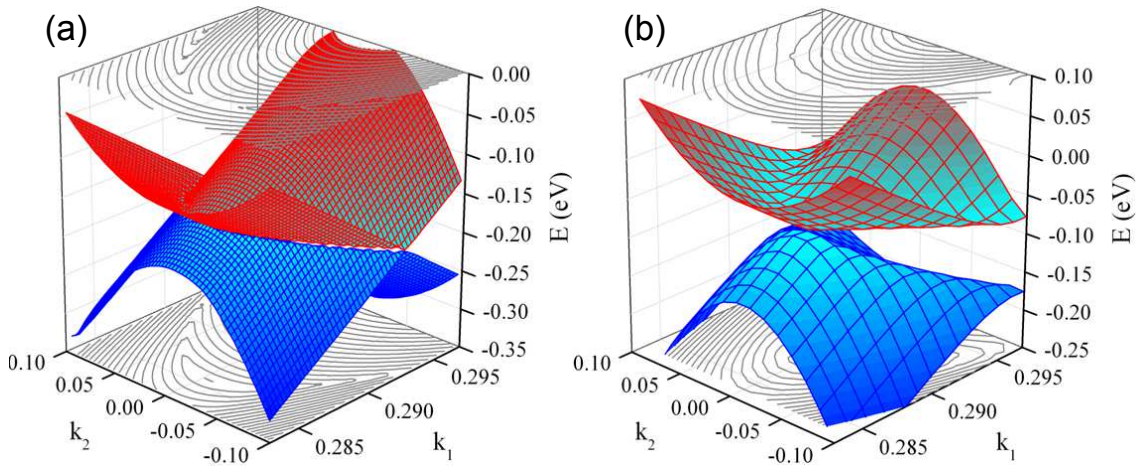

Figure 6.2.: Panel (a) sketches the band situation of the Bi square net when neglecting the surrounding atoms: a nodal line connecting the X-points in the reciprocal space is found. By including the hybridization with the surrounding X atoms (X = Sr, Ca), the nodal line is lifted and four discrete Dirac nodes remain, as depicted in panel (b). It is $k_1 = (k_x + k_y)/\sqrt{2}$ *and* $k_2 = (-k_x + k_y)/\sqrt{2}$*. SOC is neglected for the calculations. Reproduced from Ref. [179].*

Ref. [179]. In a pure Bi square net, without considering neighboring atoms or spin-orbit coupling, these orbitals create a line of Dirac nodes within the k_x-k_y-plane as depicted in panel (a) of Figure 6.2. This so-called nodal line is perpendicular to the Γ-M-direction, connecting the X-points of the reciprocal space. From now on, this direction will be referred as the X-X-direction. In this picture, the assumption is made that the minor role of the p_z-orbitals can be neglected completely. Our optical results will later raise doubt to this assumption.

In the two investigated compounds, the Bi(1) square net is not isolated, but surrounded by the X atoms. G. Lee *et al.* show in their calculations, that these X atoms hybridize with the Bi(1) square atoms [179]. In more detail, the d-orbitals of the X atoms interact with the p-orbitals of the Bi(1) atoms. Due to this hybridization, the nodal line of the Dirac states is lifted, as shown in Figure 6.2 (b). Along the complete nodal line, only four discrete Dirac nodes remain after including the hybridization. These are located where the Γ-M-line crosses the nodal line, see, e.g., Figure 6.3. The interaction between the X atoms and the Bi(1) atoms is rather weak. Thus, the lifting of the nodal line is only small in energy and the dispersion along the former nodal line is much smaller compared to the Γ-M-line. This leads

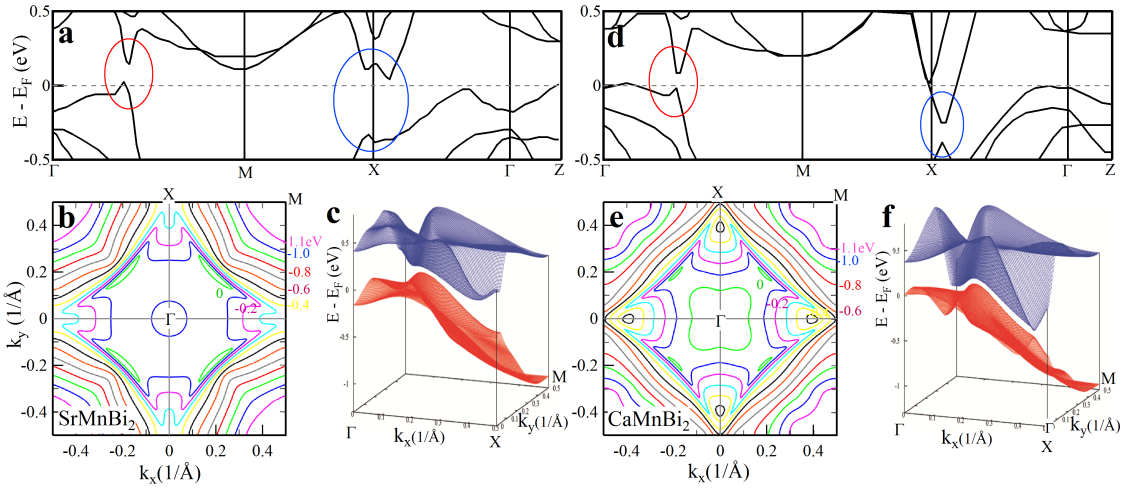

Figure 6.3.: (a) and (d) show the calculated band structures along the high symmetry lines for $SrMnBi_2$ and $CaMnBi_2$, respectively. The hybridization between the Bi(1) atoms and the X atoms as well as spin-orbit coupling are involved. The bands forming the Dirac cones are highlighted by the red and blue circles. (b) and (e) provide the Fermi surface within the k_x-k_y-plane, i.e., at $k_z = 0$. The cone structure within this plane is sketched in (c) for $SrMnBi_2$ and in (f) for $CaMnBi_2$. Reproduced from Ref. [11].

to highly anisotropic band dispersions of the Dirac cone with an anisotropy factor of ~ 100 [11]. Note, that due to the different stacking types, the hybridization is slightly stronger for $SrMnBi_2$ and so is the lifting of the nodal line. Thus, the anisotropy is, at this stage, believed to be larger for the Ca compound [179].

Next, the influence of spin-orbit coupling (SOC) is considered. In Bi-based compounds, the effect of SOC is commonly large [3]. The resulting band structure along the high symmetry lines from Ref. [11] is shown in Figure 6.3 panels (a) and (d). First of all, SOC shifts the linear band crossing (Dirac node) from below the Fermi level to above it, leading to the Fermi level lying in the lower Dirac band. Secondly, SOC splits the bands even further than the hybridization of the d- and p-orbitals did before. This opens an energy gap at the four discrete Dirac points on the order of 50 meV [11, 179]. The resulting lower Dirac branch forms the Fermi pockets along the line connecting the X-point. This was already sketched in Figure 6.1 and a cross section at $k_z = 0$ can be seen in panel (b) of Figure 6.3 for $SrMnBi_2$ and in panel (e) for $CaMnBi_2$. Thirdly, the SOC induces an additional anisotropy

along the Γ-M-direction [11]. This is, of course, much smaller than the anisotropy between Γ-M-direction and perpendicular to it. While the latter is on the order of 100, the SOC induced anisotropy factor is ~ 5.
A three dimensional sketch of the Dirac bands based on these considerations is shown in panels (c) and (f) of Figure 6.3. The Fermi velocities for $CaMnBi_2$ are found to be $v_{F,Ca}(\Gamma\text{-M}) = 1.61 \times 10^6\,\mathrm{m/s}$ along the Γ-M-direction and $v_{F,Ca}(\text{X-X}) = 0.02 \times 10^6\,\mathrm{m/s}$ perpendicular to it, i.e., along the former nodal line. For $SrMnBi_2$, the values are $v_{F,Sr}(\Gamma\text{-M}) = 1.66 \times 10^6\,\mathrm{m/s}$ and $v_{F,Sr}(\text{X-X}) = 0.08 \times 10^6\,\mathrm{m/s}$. All values are extracted from Ref. [11] and are in good agreement with other publications, e.g., Refs. [174, 180, 183, 184].

Additionally, the magneto-resistance and Hall study of X. Yan *et al.*, published in Ref. [185], reveal two charge carrier types being responsible for the transport properties of their $SrMnBi_2$ thin films. Their results reveal a hole-dominated transport yielding a carrier density of $n_h = 3.75 \times 10^{14}\,\mathrm{cm^{-2}}$ and a mobility of $\mu_h = 850\,\mathrm{cm^2/Vs}$ for the holes. For the electrons, the carrier density is one order of magnitude smaller with $n_e = 1.47 \times 10^{13}\,\mathrm{cm^{-2}}$, while their mobility is $\mu_e = 4120\,\mathrm{cm^2/Vs}$. The general situation of the charge carriers in $SrMnBi_2$ and $CaMnBi_2$ is comparable to what was discussed for YbPtBi in chapter 5: Dirac as well as conventional bands cross the Fermi level. The two channel conduction leads to two Drude components in the optical spectra. Thus, the results of X. Yan *et al.* provide a possible verification, for the case of two Drude terms being essential for the optical response of $SrMnBi_2$ and $CaMnBi_2$.
A recent publication of H. J. Park *et al.* investigates the electrodynamic properties of $SrMnBi_2$ by means of optical spectroscopy. In their fitting procedure, they follow the idea of the modeling of YbPtBi provided in this thesis in chapter 5 and Ref. [5]. When discussing the optical results of $SrMnBi_2$ in section 6.3, we will directly compare our data to those of H. J. Park *et al.*. There is another a publication on optical measurements on the two sister compounds $YbMnBi_2$ and $EuMnBi_2$ [186]. Due to the band structure being completely different, the absence of Dirac physics in the latter compound, and strongly deviating optical spectra, we will not provide a detailed comparison here.
Our single crystals were provided by Y. G. Shi from the Beijing National Laboratory for Condensed Matter Physics of the Chinese Academy of Science (Beijing, China).

All measurements presented below were performed in the *ab*-plane of the crystal, i.e., along the x-direction in Figure 6.1. Due to the air sensitivity of the crystals, they were cleaved in-situ before each measurement. Further information, also about the crystal growth method, will be given elsewhere.

6.2. $CaMnBi_2$

In this section, we discuss the results obtained for $CaMnBi_2$. We investigate the optical data with a general Drude-Lorentz model and provide two different scenarios for the underlying physical processes. On the one hand, we apply the picture of a density wave to shine light on the origin of the 50 K anomaly. On the other hand, we trace the fingerprints of the anisotropic Dirac states in optical spectra. Both scenarios are consistent with information extracted from literature as discussed above, making further experimental and theoretical work necessary to draw a final conclusion.

Temperature-dependent dc resistivity $\rho_{\mathrm{dc}}(T)$ measurements were performed in house to clarify the existence of the 50 K anomaly in our particular crystals.
The frequency-dependent optical reflectivity $R(\omega)$ was measured for temperatures between 300 and 10 K. All optical measurements were performed on freshly cleaved surfaces, since a weak air sensitivity was noticed during the alignment procedure. This is consistent with the air sensitivity mentioned in Refs. [181, 187]. Additional information on the experimental setups and data treatment are provided in chapter 3. Due to a temperature-dependent mismatch of the obtained dc conductivity and the low-frequency optical response, we apply the same extrapolation technique developed in chapter 5, which is based on a Drude-Lorentz model. This model contains two Drude terms, a narrow and a broad one, for the itinerant carriers, while interband transitions and other features are described with Lorentz terms. The reflectivity is fitted with this model and extrapolation data based on the fitting parameters are obtained for the Kramers-Kronig transformation.

The temperature-dependent dc resistivity $\rho_{\mathrm{dc}}(T)$ is shown in Figure 6.4. It decreases with decreasing temperature resulting in a residual resistivity ratio of RRR ≈ 9.5. Our dc curve is in good agreement with previously reported dc measurements [176–

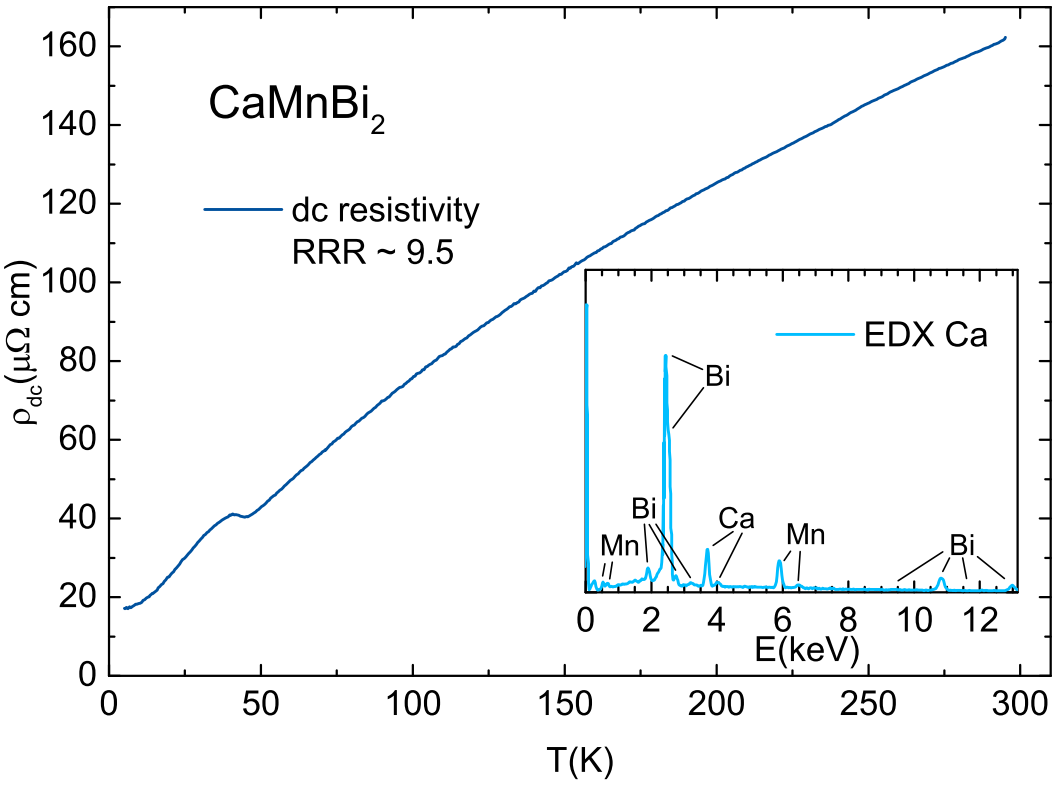

Figure 6.4.: The temperature-dependent resistivity $\rho_{dc}(T)$ of $CaMnBi_2$ measured in a conventional four-point measurement. The (semi-)metallic character is confirmed by the monotonous decrease with decreasing temperature. The residual resistivity ratio of $RRR \approx 9.5$ is comparable to literature values [176, 177]. The 50 K anomaly is observed as a bump in $\rho_{dc}(T)$. The inset displays the EDX measurement which proves the high quality of our crystals.

178, 180]. Around 50 K, the anomaly is observed as a pronounced peak in the dc curve. This makes it possible to trace the anomaly in the optical spectrum and discuss its physical origin in more detail.

To exclude poor sample quality or defects as origin, we provide EDX measurements on our $CaMnBi_2$ crystals, see inset of Figure 6.4. As mentioned in section 3.7, the measurements were performed by C. Kamella at the Max-Planck-Institut für Festkörperforschung in Sutttgart. The EDX measurements show that our crystals only contain Ca, Mn and Bi. Furthermore, the elements occur in an atomic percentage of 24.01 for Ca, 25.21 for Mn and 50.79 for Bi. This confirms homogeneous, high quality crystals.

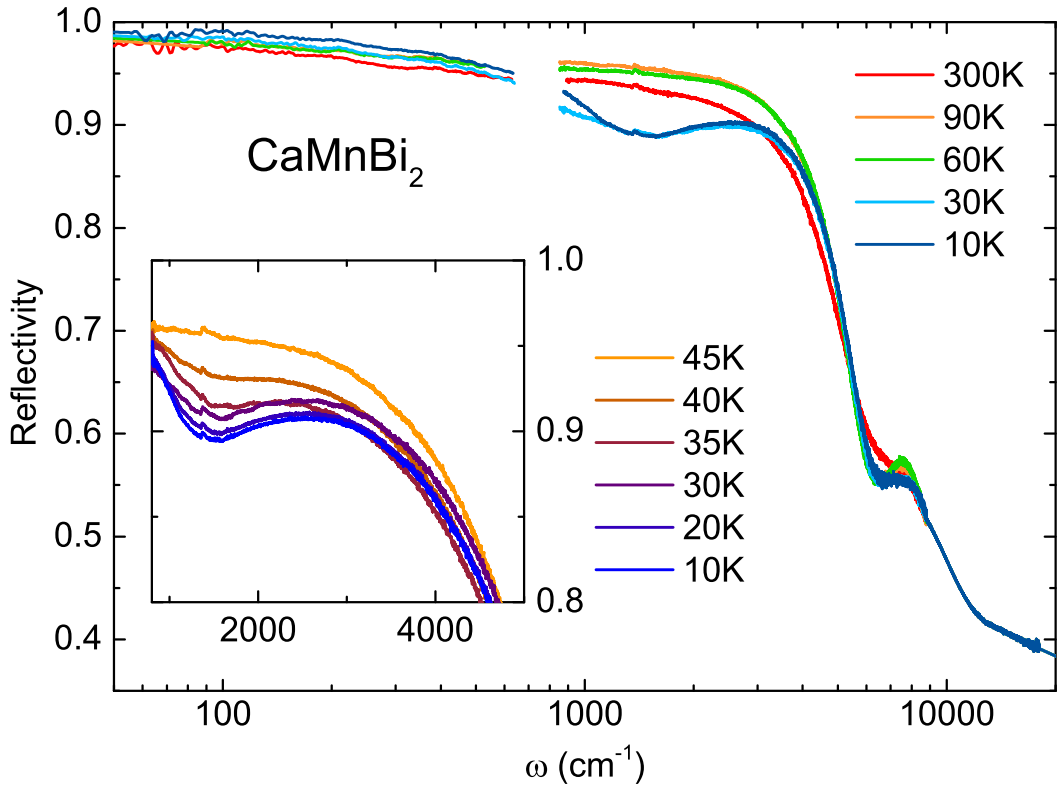

Figure 6.5.: The frequency-dependent reflectivity of $CaMnBi_2$ for selected temperatures. Upon cooling, mainly two effects occur: on the one hand, an additional feature develops in the low-temperature range; on the other hand, the metallic response changes by increasing absolute values at lowest frequencies. The inset provides a higher temperature resolution for the 50 K anomaly. The small gap in the data between 650 and 800 cm^{-1} is caused by low signals of the utilized detectors.

The dc measurement serve as basis for the low-frequency extrapolation of the optical data by relating the σ_0 values of the Drude terms to σ_{dc}. A comprehensive discussion will be given in Figure 6.8.

Optics on $CaMnBi_2$

We measured the optical reflectivity $R(\omega)$ of $CaMnBi_2$ from 50 to 20 000 cm^{-1}, shown in Figure 6.5 for selected temperatures. Smaller temperature steps were recorded in the vicinity of the 50 K anomaly in the mid-infrared range and are presented in the inset.

In the low-frequency range, the reflectivity increases upon cooling and tends to-

wards unity for all temperatures. Such behavior indicates (semi-)metallic charge carriers, as proven later. The 50 K anomaly reveals itself as a dip in the reflectivity spectrum for temperatures below 45 K. This dip sharpens and increases with decreasing the temperature. Its minimum is located around 1500 cm^{-1}. At higher frequencies, the plasma edge can be assigned to the sharp drop of the reflectivity at 5000 cm^{-1}. An additional feature causes a shoulder at approximately 7500 cm^{-1}.

Following the procedure outlined in section 3.5, we obtain the complex optical functions and present the real part of the optical conductivity $\sigma_1(\omega)$ and the real part of the dielectric function $\varepsilon_1(\omega)$ in Figure 6.6. Note, the x-axes of both graphs are changed to highlight the important features. $\sigma_1(\omega)$, depicted in panel (a), shoots up in the low-frequency range, confirming the intraband transitions of itinerant carriers. Usually, the scattering rate of this Drude component is expected to decrease continuously upon cooling. In the $CaMnBi_2$ spectra, however, a drastic collapse of the Drude edge between 60 and 30 K occurs, which will be investigated in more detail later.
The dip in reflectivity related to the 50 K anomaly results in a peak in $\sigma_1(\omega)$, as shown in the inset of Figure 6.6, again for a higher temperature resolution. The maximum of this peak is at $\sim$ 1550 cm^{-1} for the 10 K measurement. The high-frequency range of $\sigma_1(\omega)$ is rather flat with two local maxima, one around 7500 cm^{-1} and the other at the upper end of the measurement window.

The real part of the dielectric function is shown in panel (b) of Figure 6.6 over the entire measured range, while the inset zooms into the zero-crossing at 12 000 cm^{-1}. Below 5000 cm^{-1}, $\varepsilon_1(\omega)$ drops sharply due to the free-carrier response. The only exception, a small shoulder, is caused by the 50 K anomaly. The zero-crossing being related to the screened plasma frequency, as described in section 5.2, is temperature independent. This also holds for the response at higher frequencies, where the absolute value is comparably low: for the YbPtBi results presented before, ε_∞ is above 20, while we obtain a value of only $\sim$ 0.4 here. This is consistent with the weak interband response observed in $\sigma_1(\omega)$.

To draw conclusions from the optical response of $CaMnBi_2$ and gain deeper insight into the charge carrier dynamics, we fit the quantities presented above simultane-

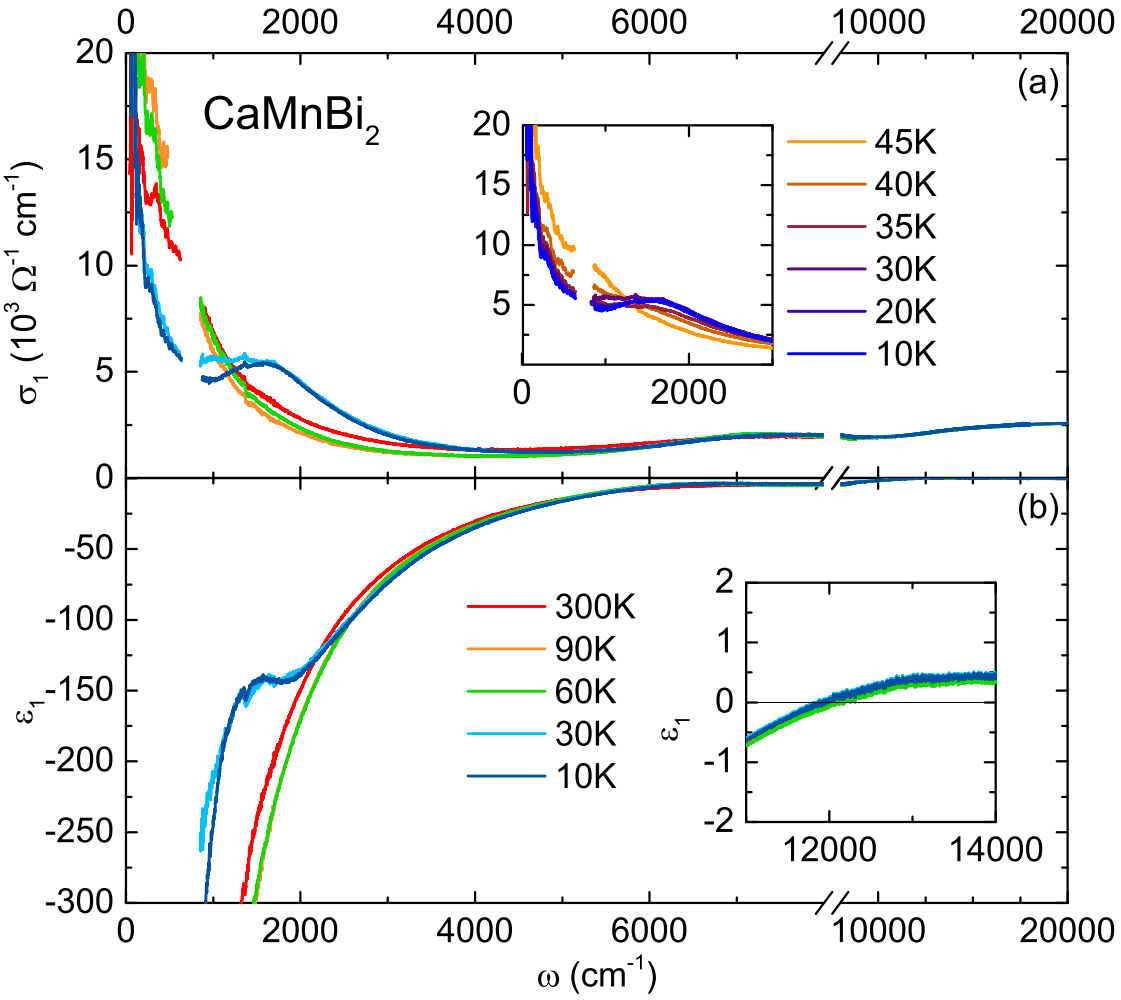

Figure 6.6.: The frequency-dependent real parts of the optical conductivity $\sigma_1(\omega)$ and the dielectric function $\varepsilon_1(\omega)$ are shown in panels (a) and (b), respectively. Both are consistent with a metallic response of free charge carriers in the low-frequency range and only comparably weak interband transitions at higher frequencies. The 50 K anomaly results in a peak in $\sigma_1(\omega)$ (inset) and a shoulder in $\varepsilon_1(\omega)$. Except for the anomaly and the change of the metallic carriers, temperature has a minor influence only. The inset of panel (b) provides a closer look at the zero-crossing of $\varepsilon_1(\omega)$, related to the screened plasma frequency.

ously with the same Drude-Lorentz model. As stated in section 6.1, several pockets of both holes and electrons exist in $CaMnBi_2$. A variation of the effective carrier mass and the mobility suggests that the different pockets require more than one Drude term. This is confirmed by failing to apply a Drude-Lorentz model con-

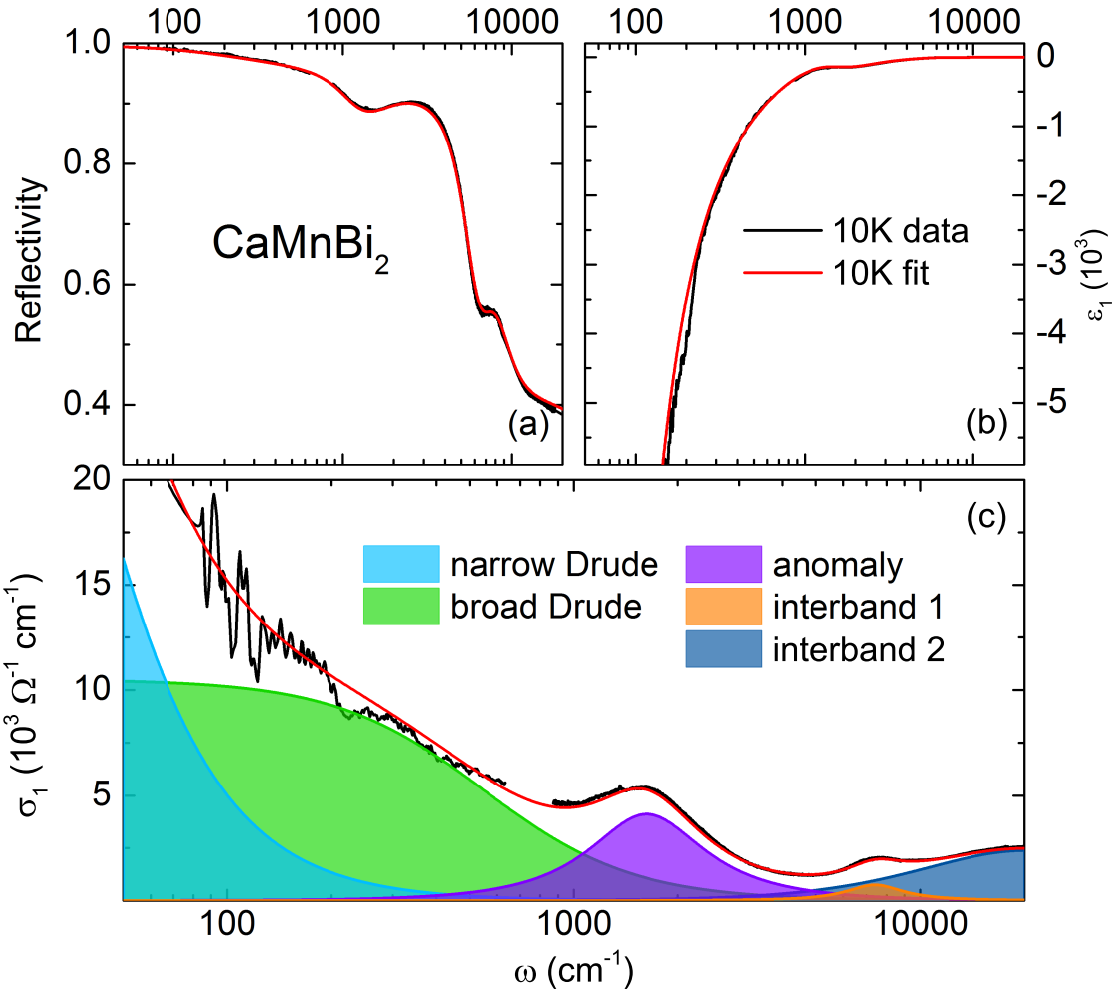

Figure 6.7.: The results of the Drude-Lorentz fit applied to the optical data of CaMnBi$_2$, showing the reflectivity (a), the real part of the dielectric function (b), and the real part of the optical conductivity (c) for the lowest measured temperature (10 K). The experimental data are given in black and the total fit in red. The colored areas represent the different fitting terms.

taining only one Drude term to fit the complete set of data (i.e., $R(\omega)$, $\sigma_1(\omega)$ and $\varepsilon_1(\omega)$) in the low-temperature range. Thus, we follow the Drude-Lorentz model employed for the measurements of YbPtBi in section 5.2 and Ref. [5]. It contains two Drude terms, a narrow one and a broader one to describe the itinerant carrier response. This idea is also suggested by H. J. Park *et al.* when investigating the optical properties of SrMnBi$_2$ [187]. In more detail, we assign the narrow Drude with a scattering rate between 20 and 30 cm^{-1} to itinerant carriers with a high

mobility such as relativistic Dirac fermions and the broader Drude to conventional metallic electrons. Since $CaMnBi_2$ is a Dirac semimetal in which both Dirac and trivial bands cross the Fermi level, it is not surprising that one Drude term is not sufficient to describe the optical data. Note, at higher temperatures, i.e., above 60 K, the broader Drude term with a scattering rate of $\sim 600\,\mathrm{cm}^{-1}$ is sufficient to fit the experimental data.

The results of the fitting for the lowest temperature are depicted in Figure 6.7, with the reflectivity in panel (a), the real part of the dielectric function in panel (b), and the real part of the optical conductivity in panel (c). Besides the two Drude terms for the itinerant carriers, we include one Lorentz term for the peak of the 50 K anomaly (purple area) and two Lorentz terms for the higher interband transitions (orange and dark blue). For $T > T_A = 50\,\mathrm{K}$, the anomaly-Lorentz term is omitted. Furthermore, the narrow Drude term can be neglected for $T > 60\,\mathrm{K}$, since the broad Drude suffices connect the optical data to the dc resistivity measurement in a consistent way.
A possible interpretation of the temperature evolution of the fitting model will be given below, hand in hand with a detailed investigation of the 50 K anomaly. This will include the idea of a density wave (DW) in $CaMnBi_2$.

Density Wave in $CaMnBi_2$

We investigate two quantities of the fitting procedure. On the one hand, the temperature dependence of the dc conductivity of the Drude terms σ_0 in relation with the dc transport measurement. On the other hand, the evolution of the squared plasma frequency ω_{pl}^2 of the Drude terms and the Lorentz term describing the anomaly at low temperatures. The latter is related to the spectral weight of each fitting term via [21]

$$\frac{\omega_{\mathrm{pl}}^2}{8} = \int_0^\infty \sigma_1(\omega)\mathrm{d}\omega \quad , \tag{6.1}$$

i.e., the area below the conductivity curve. The spectral weight can be seen as analogue to the amount of charge carriers included to a certain transition. σ_{dc} is given in panel (a) and ω_{pl}^2 in panel (b) of Figure 6.8.

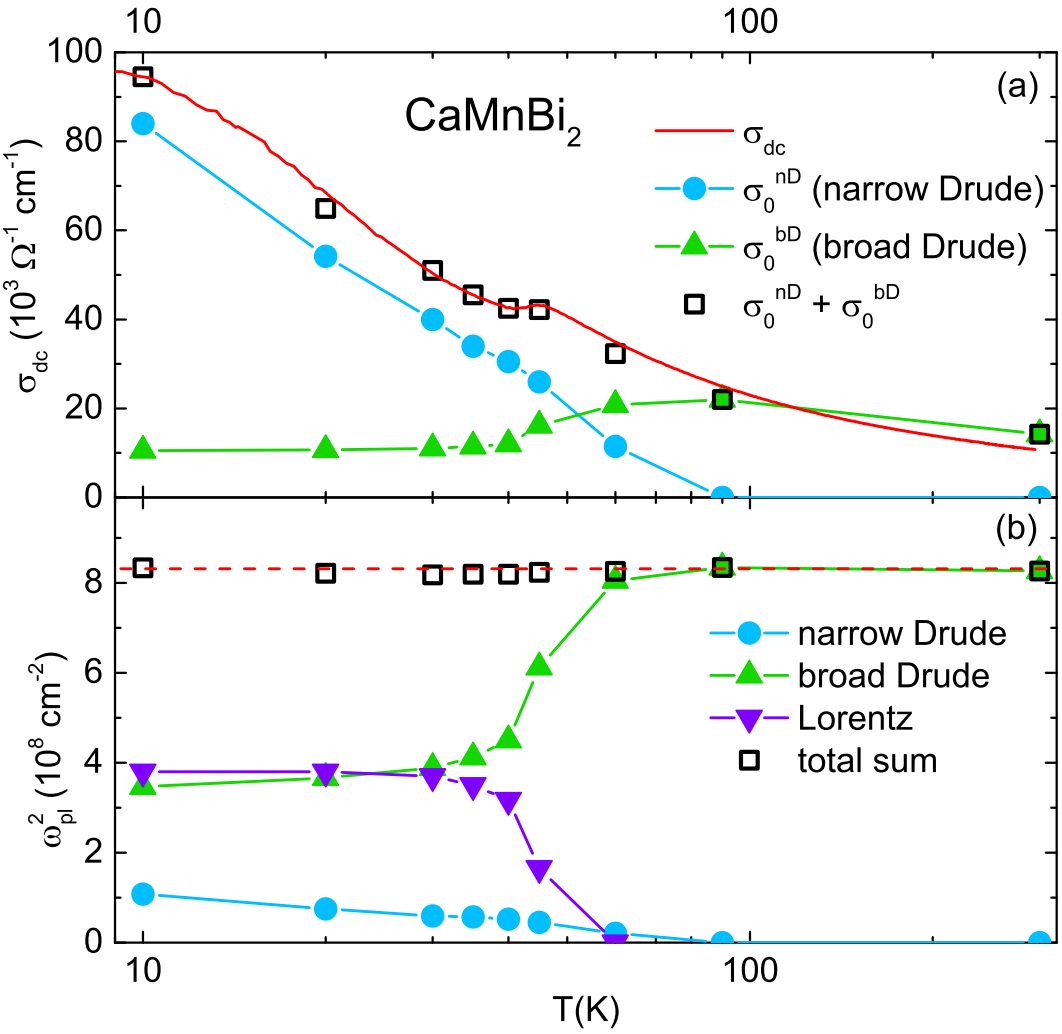

Figure 6.8.: (a) Temperature-dependent dc conductivity $\sigma_{dc}(T) = 1/\rho_{dc}(T)$ extracted from the resistivity measurement in relation to the σ_0 values of the Drude fitting terms. At high temperatures, the broad Drude is sufficient to describe both, the optical and resistivity measurement. Below 60 K, the narrow Drude is needed for the fitting procedure. The square of the temperature-dependent plasma frequency $\omega_{pl}^2(T)$ is given in panel (b). It represents the spectral weight of the fitting terms and reveals a transfer from the broad Drude into the MIR peak. The red dashed line is a guide to the eye visualizing the constant total sum.

At high temperatures, i.e., $T > 60\,\mathrm{K}$, the narrow Drude is not required to describe the optical data. Thus, its dc conductivity σ_0^{nD} and its spectral weight $\omega_{\mathrm{pl}}^2[\mathrm{nD}]$ are

set to zero. Additionally, the spectral weight of the Lorentz term remains zero until $T \leq T_A$. The term σ_0^{bD} is chosen to fit the dc conductivity σ_{dc} calculated from the resistivity measurement.
At 60 K, the narrow Drude term is indispensable to fit the optical spectra. Furthermore, the sum of the dc values $\sigma_0^{\mathrm{nD}} + \sigma_0^{\mathrm{bD}}$ can only match σ_{dc} when the narrow Drude is included. As the narrow Drude has quite a small scattering rate γ, the spectral weight is comparably small although it covers the larger part of the dc conductivity at lower temperatures. Note, the appearance of the narrow Drude is only slightly above T_A, so that a connection to the 50 K anomaly cannot be excluded.

Below T_A, the spectral weight (SW) of the broad Drude is halved. The total sum of the SW, however, is conserved, since the Lorentz term of the anomaly peak is of exactly the same size. Upon further cooling, the broad Drude looses some spectral weight, which is balanced by the narrow Drude.

The sum of the dc conductivities of the two Drude terms perfectly matches the resistivity and the spectral weight is conserved for all temperatures. These facts confirm a successful fitting procedure. The overall behavior strongly remind of the signatures of density waves [21], as found in, e.g., iron pnictides [188].
Such a density wave goes hand in hand with the opening of an energy gap in the density of states, since one of the metallic bands is (at least partly) gapped. The size of this density wave gap can be estimated by removing the Drude contributions from the optical conductivity as shown below. With this, we obtain a gap value of $\Delta_{\mathrm{DW}} = 440\,\mathrm{cm}^{-1} = 54\,\mathrm{meV}$ at 10 K.

To further verify the origin of the 50 K anomaly, we measured the magnetic susceptibility $\chi(T)$ given in the inset of Figure 6.9 (b) and compared it to the temperature evolution of the resistivity measurement in panel (a). $\chi(T)$ displays a small shoulder in exactly the same temperature range. The same shoulder was observed by J. B. He *et al.* in Ref. [177]. To obtain a clearer picture, we model $\chi(T)$ above the shoulder with a polynomial fit 2nd order (gray dotted line) and subtract the fit from the experimental data leading to $\Delta\chi(T)$ given in panel (c) of Figure 6.9. Here, the feature can be determined more exactly to occur at $T_{\mathrm{DW}} = 48$ K. For temperatures below the bump in $\rho_{\mathrm{dc}}(T)$, $\Delta\chi(T)$ also stays constant. This behavior

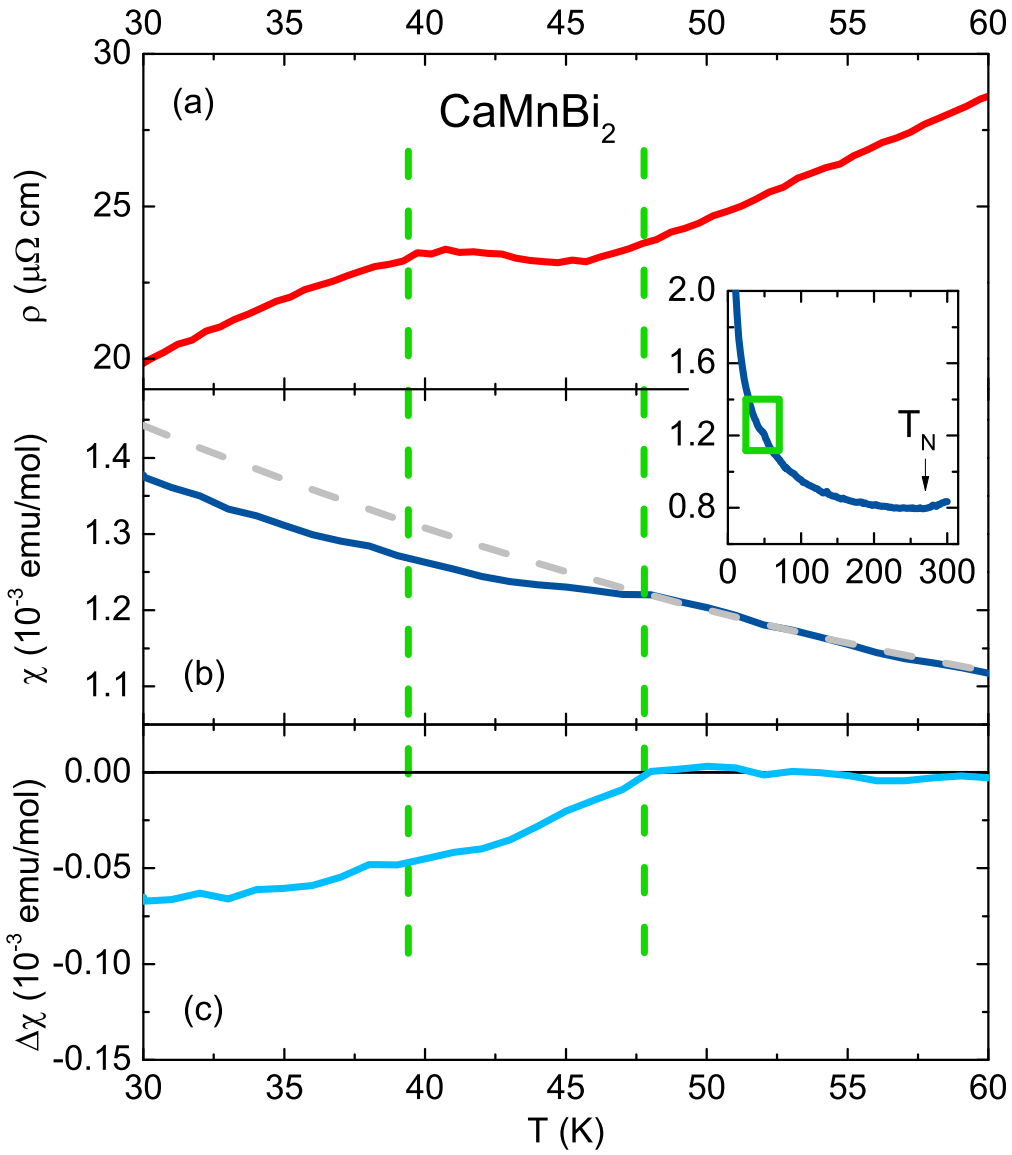

Figure 6.9.: (a) A zoom-in of the resistivity $\rho_{dc}(T)$ around the 50 K anomaly reveals a link to a small shoulder in the magnetic susceptibility $\chi(T)$ shown in panel (b). The full measured temperature range of $\chi(T)$ is depicted in the inset with the zoom-in area marked by the green rectangle. The deviation of $\chi(T)$ from a high temperature fit (gray dotted line) is given as $\Delta\chi(T)$ in (c).

is expected for a density wave on an antiferromagnetic background [189], but could also be explained by a spin reorientation or spin canting [177].

It was pointed out by S. Ray and L. Alff that a possible Fermi surface nesting in

$XYBi_2$ materials may lead to a charge density wave in the Bi(1) square net [190]. A nesting of the Fermi surface requires different parts of the surface to be parallel to another. With this, a nesting vector can transfer charge carriers from one pocket to the other [21]. Furthermore, a nesting of the so-called α-pocket in $CaMnBi_2$ was highlighted by Y. J. Jo *et al.* in Ref. [12] and may also be relevant for $SrMnBi_2$ described in section 6.3. Since $CaMnBi_2$ fulfills these requirements, a density wave is possible.

All in all, the scenario of a (charge) density wave is consistent for all experimental results presented here and literature. The existence of Dirac fermions, however, is not included in this picture. As we will show next, the Dirac bands should give a response in exactly the same energy range. Thus, we open the discussion for a possible link between the density wave and the Dirac fermions in $CaMnBi_2$.

Dirac Physics in $CaMnBi_2$

As mentioned before, $CaMnBi_2$ was found to host anisotropic Dirac cones, e.g., Refs. [11, 179]. The Dirac states are mainly created by the p_x- and p_y-orbitals of the Bi(1) atoms. In the detailed explanation of Ref. [179], the assumption is made, that the minor role of the p_z-orbitals can be neglected completely and no Dirac dispersion is found along the z-direction.
Thus, the Dirac states are considered to be quasi-two dimensional. We want to emphasize, that no spin-orbit coupling is included in the beginning of the development of the Dirac picture in $CaMnBi_2$. In contrast, the ARPES measurements and calculations of Y. Feng *et al.* show that SOC plays a crucial role for the Dirac physics in $CaMnBi_2$ and $SrMnBi_2$ [11].

We propose, that a detailed theoretical investigation should be made, where all orbitals of the Bi(1) square net and SOC are included. For the interpretation of our optical data, we are able to draw conclusions on the dimensionality of the Dirac states, following Equation 2.6. The response of three dimensional Dirac states should result in a linearly dispersing optical conductivity, i.e., $\sigma_1(\omega) \propto \omega$, while quasi-two dimensional Dirac fermions are associated hand in hand with a frequency-independent conductivity ($\sigma_1(\omega)$ =const.).

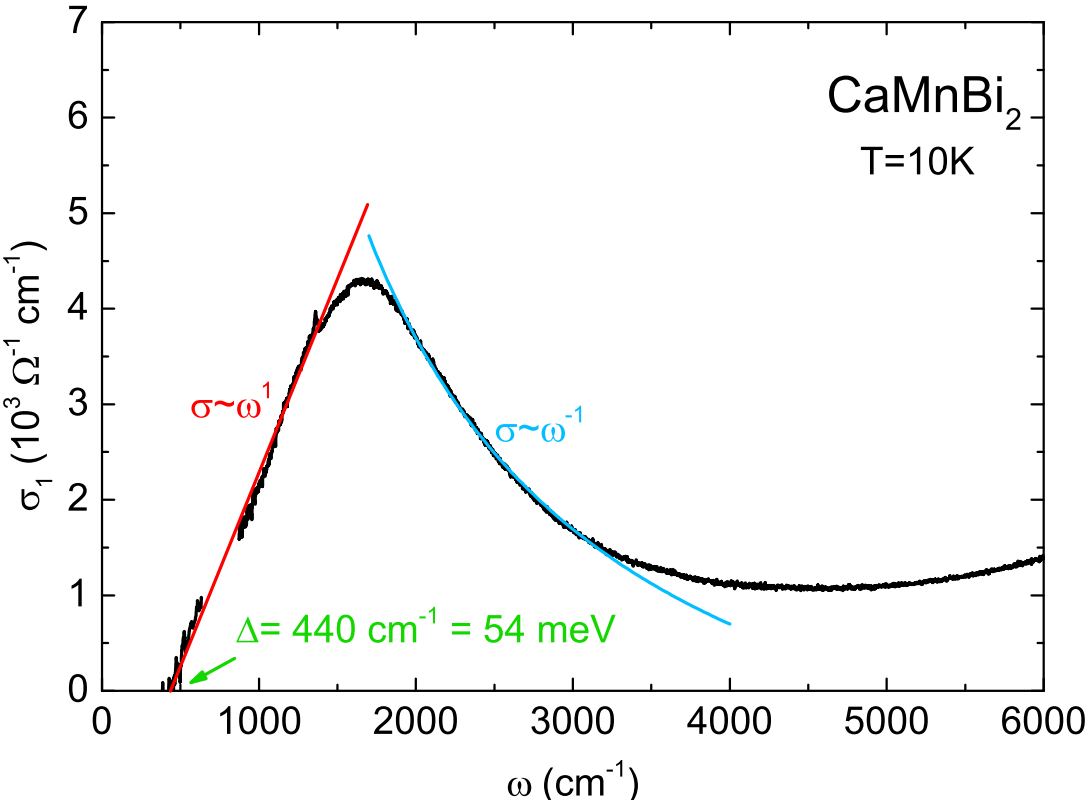

Figure 6.10.: The frequency-dependent interband conductivity of $CaMnBi_2$ given at the lowest measured temperature of 10 K. *From 440 to* 1400 cm^{-1}, *a linear dependence on the frequency suggests the response of 3D Dirac states. Above* 1850 cm^{-1}, *a* ω^{-1}*-decay is found, which may indicate a one dimensional Dirac dispersion. The onset of the interband conductivity at* $\Delta = 440\,\mathrm{cm}^{-1}$ *is assigned to an energy gap in the density of states.*

We subtract the itinerant, metallic carrier response, i.e., the Drude terms, from the optical spectrum to gain the pure interband optical conductivity. The results are given for the 10 K measurement in Figure 6.10. First of all, the interband contribution starts at $440\,\mathrm{cm}^{-1} = 54\,\mathrm{meV}$, indicated by the green arrow. This value was considered as the density wave gap in the previously described scenario. For this discussion, we assign it to the energy gap introduced by spin-orbit coupling to the Dirac bands and find a perfect agreement with the calculated energy gap value of Ref. [11].

Above this gap, the interband conductivity of $CaMnBi_2$ rises linearly (red line)

until approximately $1500\,\mathrm{cm}^{-1}$. The energy range matches the one where a Dirac response is expected in $CaMnBi_2$ [11]. This linear dispersion of $\sigma_1(\omega)$ suggests $d = 3$ for Equation 2.6, i.e., 3D Dirac states instead of quasi-two dimensional ones. The linear conductivity has a slope of $4.1\,\frac{\Omega^{-1}\mathrm{cm}^{-1}}{\mathrm{cm}^{-1}}$. This value can be used to calculate the Fermi velocity of the Dirac states with Equation 2.8. The four discrete Dirac points in $CaMnBi_2$ lead to $N_W = 8$. The resulting Fermi velocity is calculated to be $v_F(\mathrm{Ca}) = 1.2 \times 10^4\,\mathrm{m/s}$. The Dirac cones in $CaMnBi_2$ are highly anisotropic as depicted in Figure 6.3. The slope of $\sigma_1(\omega)$ should be related to the smallest Fermi velocity, since a higher Fermi velocity leads to a smaller slope of $\sigma_1(\omega)$, as explained in section 2.7. Furthermore, the energy range in which Dirac states can be found is expected to be smaller for smaller Fermi velocities, because the dispersion of the bands is weaker.
Our extracted Fermi velocity is slightly smaller than the value found perpendicular to the Γ-M-direction, i.e., $1.5 \times 10^4\,\mathrm{m/s}$ [11]. This can have two different reasons: On the one hand, the poor resolution of ARPES might blur the exact band slope leading to the deviation; on the other hand, our optical value can represent the dispersion along the z-direction with a comparable value to the X-X-direction. With the results on $SrMnBi_2$ we will draw a final conclusion later on.

For frequencies above the linear conductivity we find a decay with $\sigma_1(\omega) \propto \omega^{-1}$, as shown by the blue line in Figure 6.10. This holds from 1850 to $3200\,\mathrm{cm}^{-1}$. Applying the same formula as above, this is related to one dimensional Dirac states. Since the dispersion along the z-direction and perpendicular to the Γ-M-direction is flat, only the dispersion along the Γ-M-direction should exist above a certain energy. We extract this energy to be $1850\,\mathrm{cm}^{-1} \approx 230\,\mathrm{meV}$.

The results of our interband conductivity spectrum are in good agreement with all experimental studies on $CaMnBi_2$ so far. The contradiction to the quasi-two dimensional picture drawn from theoretical calculations suggests real three dimensional Dirac states in $CaMnBi_2$, with a small dispersion of $v_F = 1.2 \times 10^4\,\mathrm{m/s}$ along the z-direction. Thus, a more detailed theoretical study on $CaMnBi_2$ is required to finalize the picture of anisotropic Dirac states in this compound.

6.3. $SrMnBi_2$

In the following, we focus on the optical results of $SrMnBi_2$. We apply the same idea discussed for $CaMnBi_2$ in the previous section: Fitting with a Drude-Lorentz model with two Drude terms, shortly discussing a peak similar to the 50 K anomaly in $CaMnBi_2$ and investigating the interband conductivity in terms of Dirac physics. Additionally, we will compare our results to those published by H. J. Park in Ref. [187].

Again, the temperature-dependent resistivity $\rho_{\mathrm{dc}}(T)$ was measured to draw a consistent picture with the Drude terms in the fitting procedure. For comparison, the frequency-dependent optical reflectivity was recorded at the same temperatures as for $CaMnBi_2$ measurements. Furthermore, the same low-frequency extrapolation concept, the Drude-Lorentz model, was applied to achieve satisfying results from the Kramers-Kronig transformation. The $SrMnBi_2$ crystals follow similar degradation as the $CaMnBi_2$ crystals and, hence, all measurements were performed on freshly cleaved surfaces.
The results of the dc measurement are shown in Figure 6.11. Slope, absolute values, and the residual resistivity ratio of $SrMnBi_2$ are similar to what was observed for $CaMnBi_2$ before. The main difference is the absence of the 50 K anomaly in $\rho_{\mathrm{dc}}(T)$. Our measurement is also in good agreement with Refs. [12, 174, 176, 183, 187], while the antiferromagnetic ordering is more clearly seen in Refs. [175, 181]. The EDX measurement on our $SrMnBi_2$ crystals is given in the inset of Figure 6.11 and, again, confirms high quality and homogeneity of the samples with the expected atomic percentages of 25.21 for Sr, 24.11 for Mn and 50.69 for Bi.

Optics on $SrMnBi_2$

The reflectivity $R(\omega)$ of $SrMnBi_2$ was measured from 50 to 20 000 cm^{-1} and is depicted in Figure 6.12. For the main figures on this compound we chose a linear frequency axis and focus on the range up to 1 eV, i.e., 8065 cm^{-1}. This allows a direct comparison with the results of H. J. Park *et al.* in Ref. [187], which are plotted in the same way. The inset of Figure 6.12 provides the full range of $R(\omega)$ with a logarithmic frequency axis.
Our reflectivity data perfectly match the experimental results of H. J. Park *et al.*.

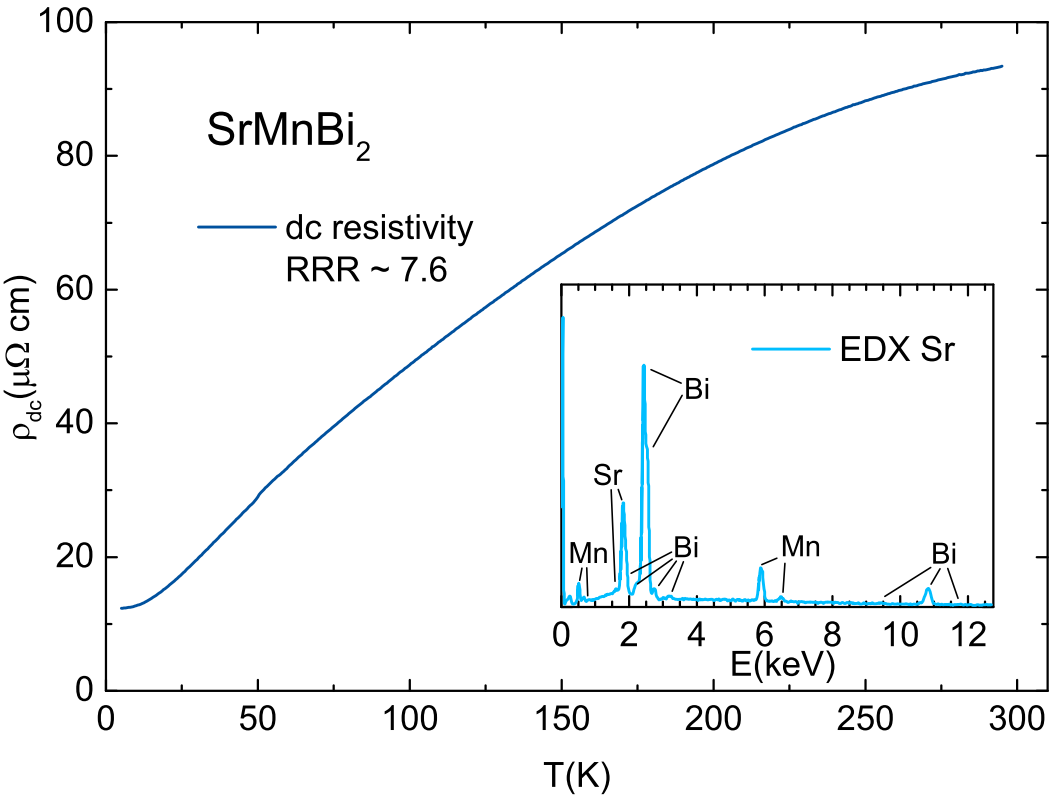

Figure 6.11.: The temperature-dependent resistivity $\rho_{dc}(T)$ of $SrMnBi_2$ measured with conventional four-point measurement geometry. The (semi-)metallic character is confirmed by the monotonous decrease with decreasing temperature. The residual resistivity ratio of RRR $\approx$ 7.6 is comparable to literature values [12, 174, 176, 183, 187]. The inset displays the EDX measurement which proves the high quality of our crystals.

The plasma edge is located around $900\,\mathrm{cm}^{-1}$. Below that high absolute values of $R(\omega) > 0.95$ indicate metallic charge carriers in $SrMnBi_2$. Above the plasma edge, several features, most likely interband transitions, are located in the optical spectrum.

Reducing the temperature not only sharpens the plasma edge and increases the low-frequency reflectivity, but also emphasizes the bumps of the interband features. In comparison to the reflectivity of $CaMnBi_2$, more peaks are present in the high-frequency range.

As described before, we obtain the complex optical functions in terms of $\sigma_1(\omega)$ and

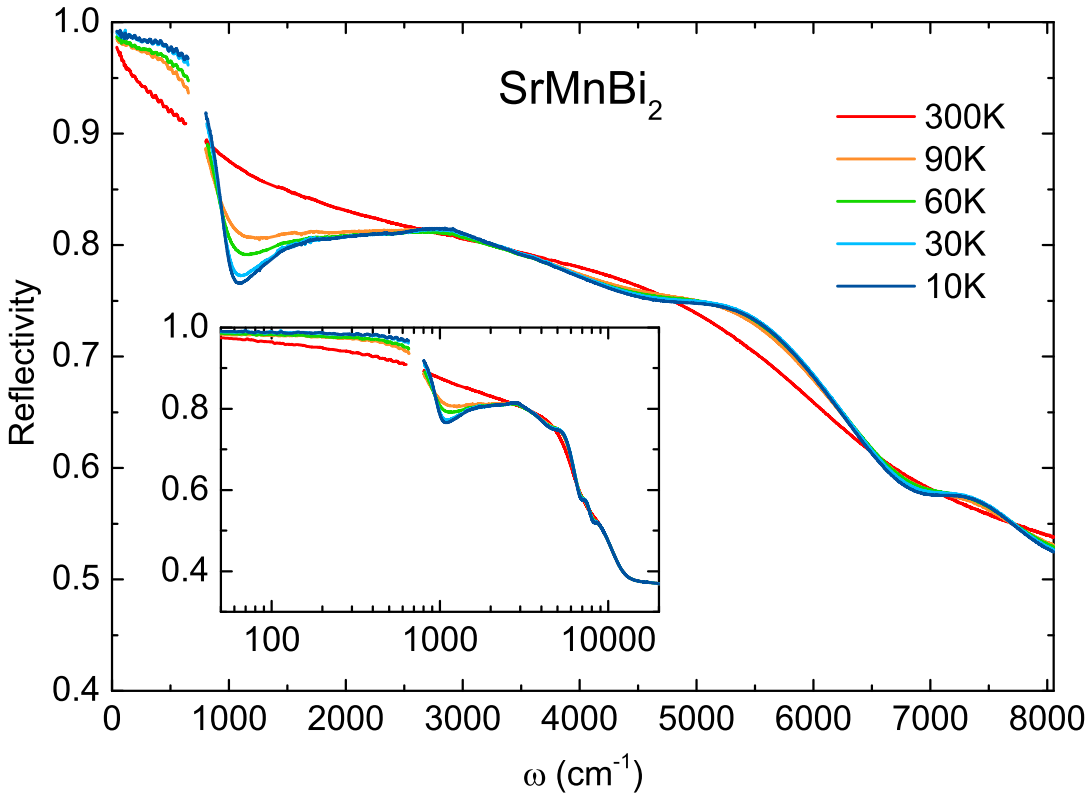

Figure 6.12.: The frequency-dependent reflectivity $R(\omega)$ of SrMnBi$_2$ for selected temperatures. By reducing the temperature, the metallic response is narrowed down to the low-frequency range, resulting in a sharp plasma edge at 900 cm^{-1} and high absolute values of $R(\omega) > 0.95$. Additionally, the structure of the interband dominated reflectivity above 1000 cm^{-1} becomes more pronounced. The inset depicts the entire measured range, while the main panel provides a direct comparison to the results of Ref. [187].

$\varepsilon_1(\omega)$ via the Kramers-Kronig transformation. The resulting spectra of SrMnBi$_2$ are depicted in Figure 6.13. Again, we chose the same axes as in Ref. [187] for direct comparison.

The optical conductivity $\sigma_1(\omega)$, panel (a) of Figure 6.13, rises in the low-frequency range, while the dielectric function $\varepsilon_1(\omega)$, panel (b), drops to large negative values. Both confirm the free-carrier response of bands crossing the Fermi level as shown in Figure 6.3. Above 700 cm^{-1}, $\sigma_1(\omega)$ shows a clear separation between the Drude response and interband transitions. At 300 K, the large scattering of the Drude-like feature blurs this situation. The peak around 2000 cm^{-1} reminds of the MIR

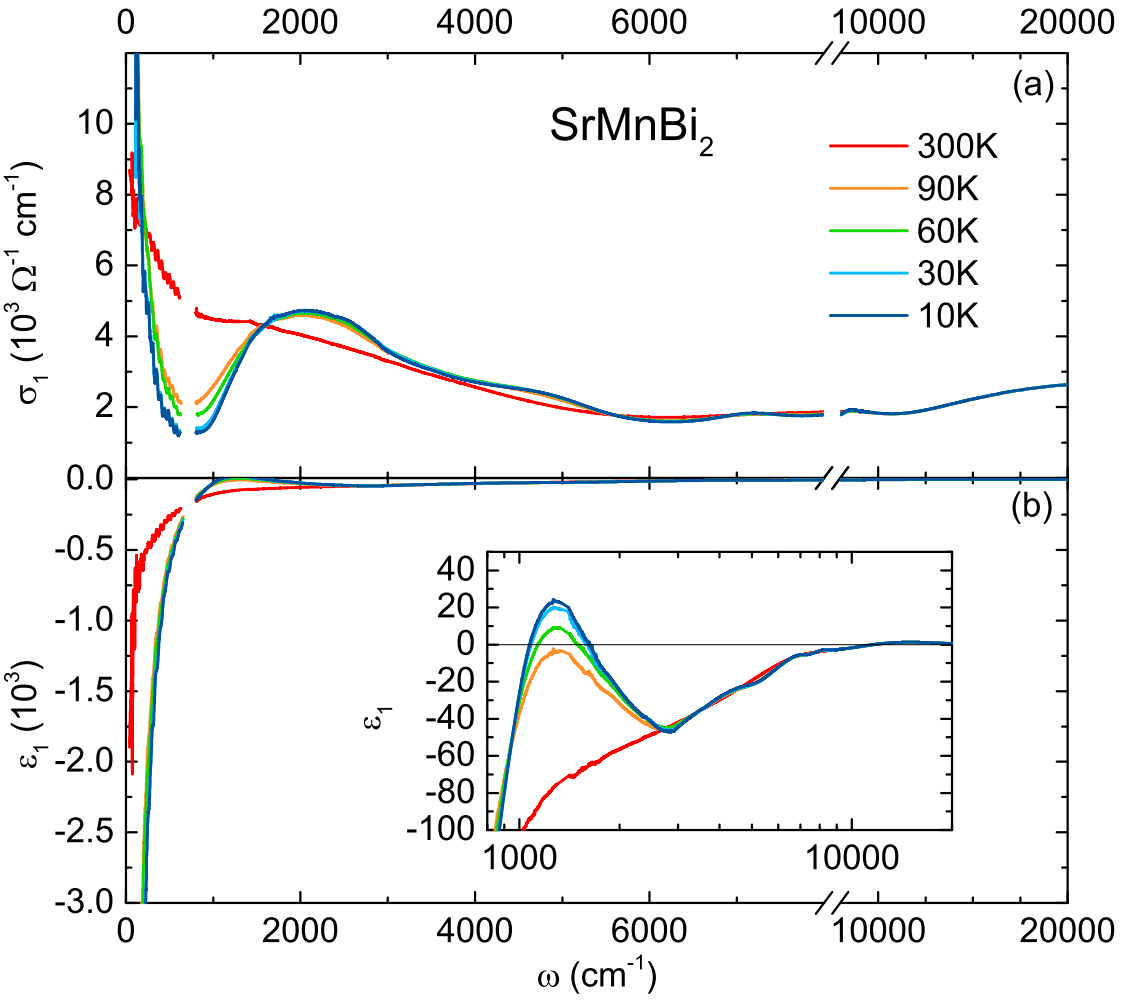

Figure 6.13.: The frequency-dependent real parts of the optical conductivity $\sigma_1(\omega)$ and the dielectric function $\varepsilon_1(\omega)$ of $SrMnBi_2$ are given in panels (a) and (b), respectively. The metallic charge carriers can be traced by the upturn (downturn) of $\sigma_1(\omega)$ ($\varepsilon_1(\omega)$) at low frequencies. Upon cooling, a clear separation between the intraband and the interband response develops in $\sigma_1(\omega)$. The interband peaks become more pronounced when decreasing the temperature, leading to a clearer structure. In $\varepsilon_1(\omega)$, a second zero-crossing appears at low temperatures at around $1000\,\mathrm{cm}^{-1}$.

peak developing below 50 K in $CaMnBi_2$. The main difference is, that the peak in $SrMnBi_2$ is also present at room temperature. At higher frequencies, several bumps indicate a more complex interband structure in $SrMnBi_2$ compared to $CaMnBi_2$.

The separation of the intraband response from the interband transitions at temperatures below 100 K is confirmed by an additional zero-crossing of $\varepsilon_1(\omega)$ appear-

ing around $1000\,\mathrm{cm}^{-1}$. The temperature-independent zero-crossing is located at $11\,840\,\mathrm{cm}^{-1}$. It is strikingly close to the value of $CaMnBi_2$, revealing a large common ground for the two compounds.
The Kramers-Kronig results presented here are again in good agreement with the results of Ref. [187]. This holds also for the general interpretation of the optical data. Below, we apply the same fitting model as for $CaMnBi_2$, containing two Drude terms for the metallic carriers and several Lorentz terms for the different interband transitions. The idea of two Drude terms, taking the different Fermi pockets of $SrMnBi_2$ into account, was also adapted by H. J. Park *et al.*. A possible explanation is again the existence of Dirac and conventional bands crossing the Fermi level.

The fitting results are given in Figure 6.14 for the lowest measured temperature (10 K). The two Drude terms describe the low-frequency data satisfactorily for all temperatures. In contrast to $CaMnBi_2$, the narrow Drude is required at room temperature already. Its scattering rate decreases from $120\,\mathrm{cm}^{-1}$ at 300 K to $11\,\mathrm{cm}^{-1}$ at 10 K, while the broad Drude changes from $860\,\mathrm{cm}^{-1}$ at 300 K to $120\,\mathrm{cm}^{-1}$ at 10 K. Note, that also the MIR peak is visible at room temperature already in $SrMnBi_2$. Thus, a possible connection between the narrow Drude term and the MIR peak should be considered. As for $CaMnBi_2$, the multiple Fermi pockets and the appearance of Dirac bands crossing the Fermi level verify this two Drude model in $SrMnBi_2$.
The fitting of the MIR area from 700 to $6000\,\mathrm{cm}^{-1}$ is done with three Lorentz terms. However, an adequate fit of all three optical functions, $R(\omega)$, $\sigma_1(\omega)$ and $\varepsilon_1(\omega)$, in this range is not achieved, even if the number of Lorentz terms is increased. This indicates a special band situation causing this response. A detailed discussion will follow later. Above $6000\,\mathrm{cm}^{-1}$, the optical spectra can be described adequately by Lorentz terms, pointing towards conventional interband transitions in this range.

In Figure 6.15, we compare our two Drude fits, the narrow one (σ_0^{nD}) and the broad one (σ_0^{bD}), with the dc resistivity measurement shown in Figure 6.11. The same model was applied by H. J. Park *et al.*. Therefore, we include their fitting parameters as triangular symbols. Altogether, a perfect agreement between their data and ours can be seen over the complete temperature range. This holds for each Drude

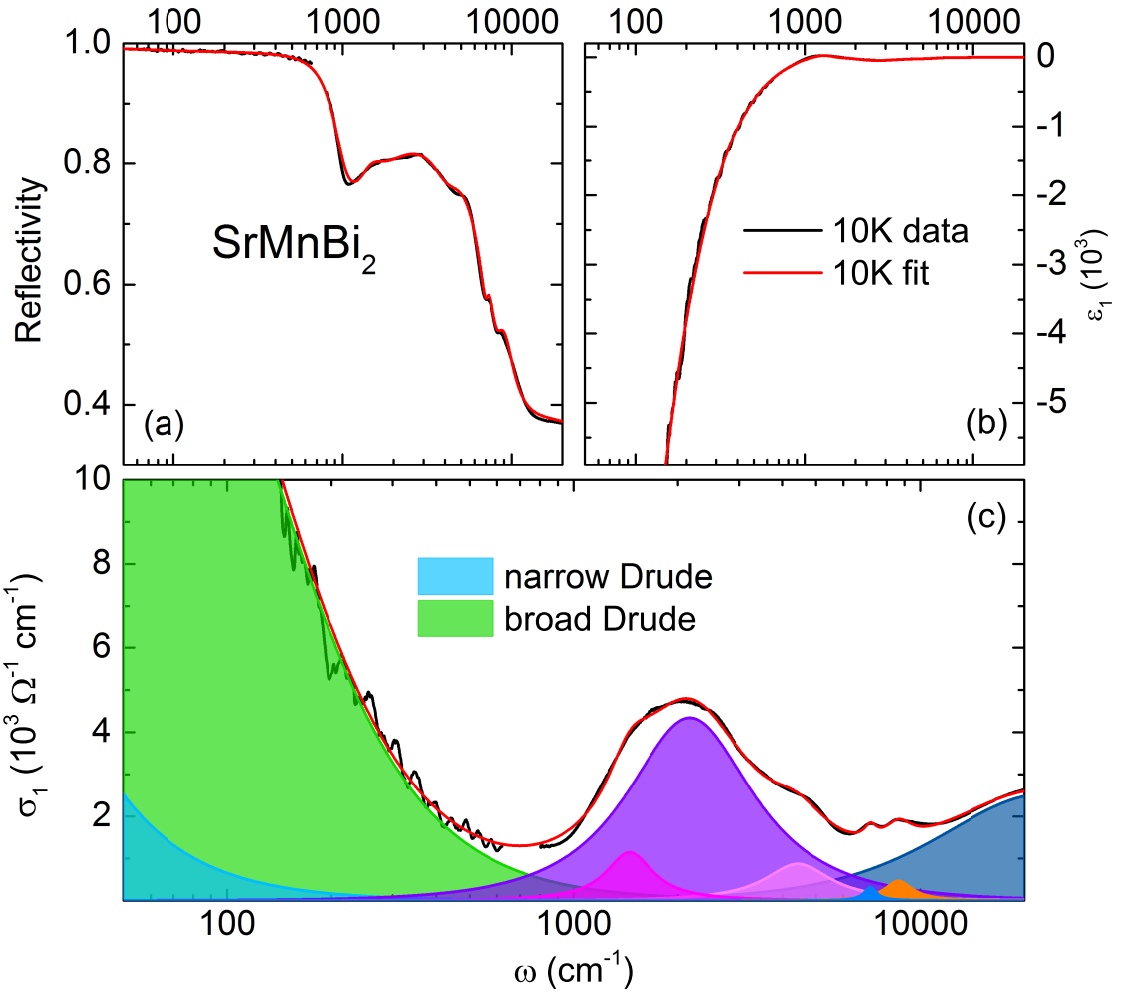

Figure 6.14.: The fitting of the optical data of $SrMnBi_2$ with a Drude-Lorentz model at the lowest measured temperature, i.e., 10 K, for the reflectivity (a), the real part of the dielectric function (b) and the optical conductivity (c). The colored areas represent contributions of different Drude or Lorentz terms. A detailed analysis of the components is given in the text.

term individually, but also for the sum of the two and is furthermore confirmed by the sum $\sigma_0^{\mathrm{nD}} + \sigma_0^{\mathrm{bD}}$ matching the dc conductivity σ_{dc}.

The interpretation of the interband response given by H. J. Park *et al.* is somewhat different to what we discussed for $CaMnBi_2$ before. As the Dirac states in $SrMnBi_2$ (and $CaMnBi_2$) are considered to be quasi-two dimensional, they compare their results to the universal conductivity found for the 2D Dirac states in graphene.

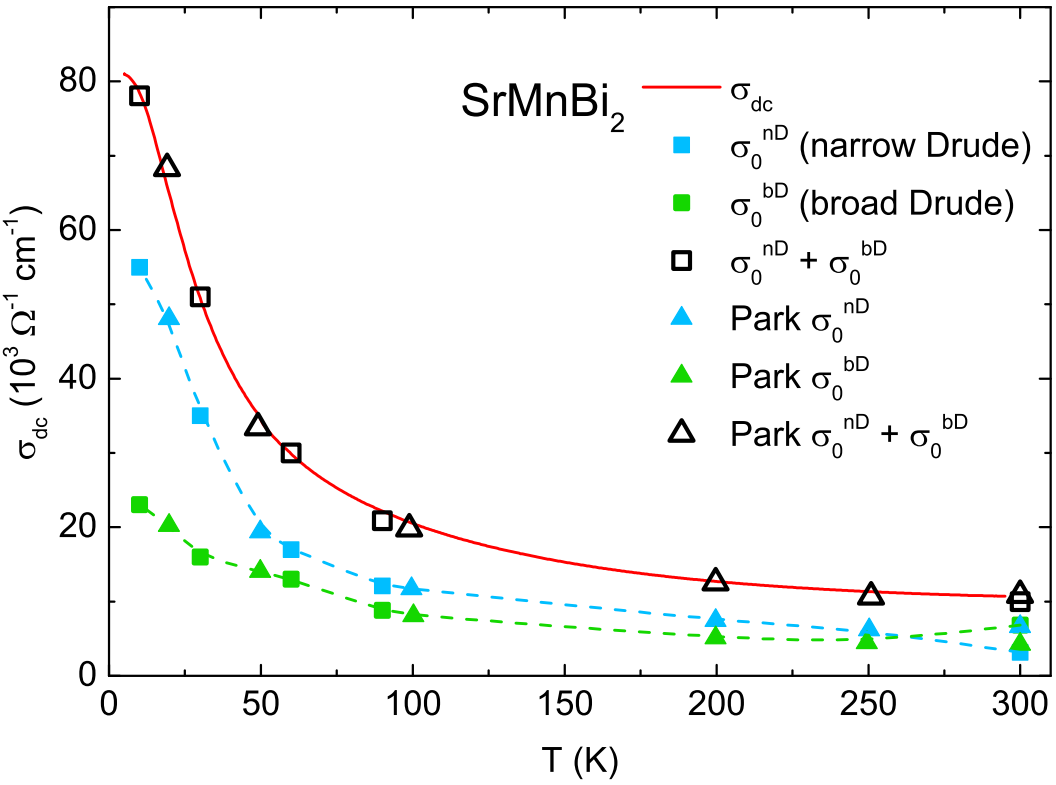

Figure 6.15.: The temperature-dependent dc conductivity $\sigma_{dc}(T) = 1/\rho_{dc}(T)$ (red line) of SrMnBi$_2$ is compared to the individual σ_0-values of the Drude components (blue and green squares) and their sum (black squares). Our results are directly compared to what was found by H. J. Park et al. in Ref. [187] (triangular symbols).

The MIR response of SrMnBi$_2$ is, however, two to three times larger than what they expect. Furthermore, the structure in the MIR range reveals several bumps, clearly deviating from a frequency-independent conductivity, which is expected for 2D Dirac states.

For lack of of an explanation for a connection between the MIR response and the Dirac physics in SrMnBi$_2$, H. J. Park *et al.* assign the MIR peaks to indirect interband transitions along the Γ-X-line in the reciprocal space. In their picture, transitions between the valence and the conduction band of the anisotropic Dirac cones are, however, neglected completely. It should be mentioned, that indirect transitions involve phonons and usually have a lower probability of being excited than direct transitions. Furthermore, transitions between the linear Dirac bands are in all likelihood due to the extremely low scattering rate of these bands.

The Dimensionality of the Dirac States in $SrMnBi_2$

Being dissatisfied with the interpretation of Ref. [187], we take our concept of Dirac physics in $CaMnBi_2$ and transfer it to the optical spectra of $SrMnBi_2$. This seems plausible due to the many shared features and properties between the optical response of $CaMnBi_2$ and $SrMnBi_2$ and the large agreement between their band structures.

Again, we remove the intraband contribution from the optical conductivity by subtracting the Drude terms from the initial spectrum. The resulting $\sigma_1(\omega)$ for the lowest measured temperature, i.e., 10 K, is shown in Figure 6.16. A quick comparison to the interband spectrum of $CaMnBi_2$ in Figure 6.10 reveals the same characteristic features for both compounds: the energy gap and the ω as well as the ω^{-1} dependency.

The onset of the interband conductivity can be used to determine the value of the energy gap, which is introduced by spin-orbit coupling to the density of states. From our experimental data, we extract a value of $\Delta = 430\,\mathrm{cm}^{-1} = 53\,\mathrm{meV}$. This value is again in good agreement with ARPES results [11, 174] and also what is found in the optical measurement of Ref. [187].
Above the gap, the conductivity rises linearly, i.e., $\sigma_1(\omega) \propto \omega$, with a slope of $5.5\,\frac{\Omega^{-1}\mathrm{cm}^{-1}}{\mathrm{cm}^{-1}}$. This can be connected via Equation 2.6 to three dimensional bands with a linear dispersion relation, as shown for $CaMnBi_2$ before. Applying Equation 2.8 to the linear rise with $N_W = 8$, the Fermi velocity can be calculated to be $v_F(\mathrm{Sr}) = 0.9 \times 10^4\,\mathrm{m/s}$. This value is smaller than the Fermi velocities for both, the Γ-M- and the X-X-direction, extracted from the ARPES measurements: $7.5 \times 10^4\,\mathrm{m/s}$ and $1.6 \times 10^6\,\mathrm{m/s}$ [11, 174]. Thus, we connect our v_F to the dispersion in z-direction.
At frequencies above the linear conductivity, a more or less flat maximum is located. Compared to the $CaMnBi_2$ spectrum, the width of this is slightly larger. We claim that while in $CaMnBi_2$ the dimensionality changes from 3D directly to 1D, a small range of 2D Dirac states can be found in $SrMnBi_2$. This idea is supported by

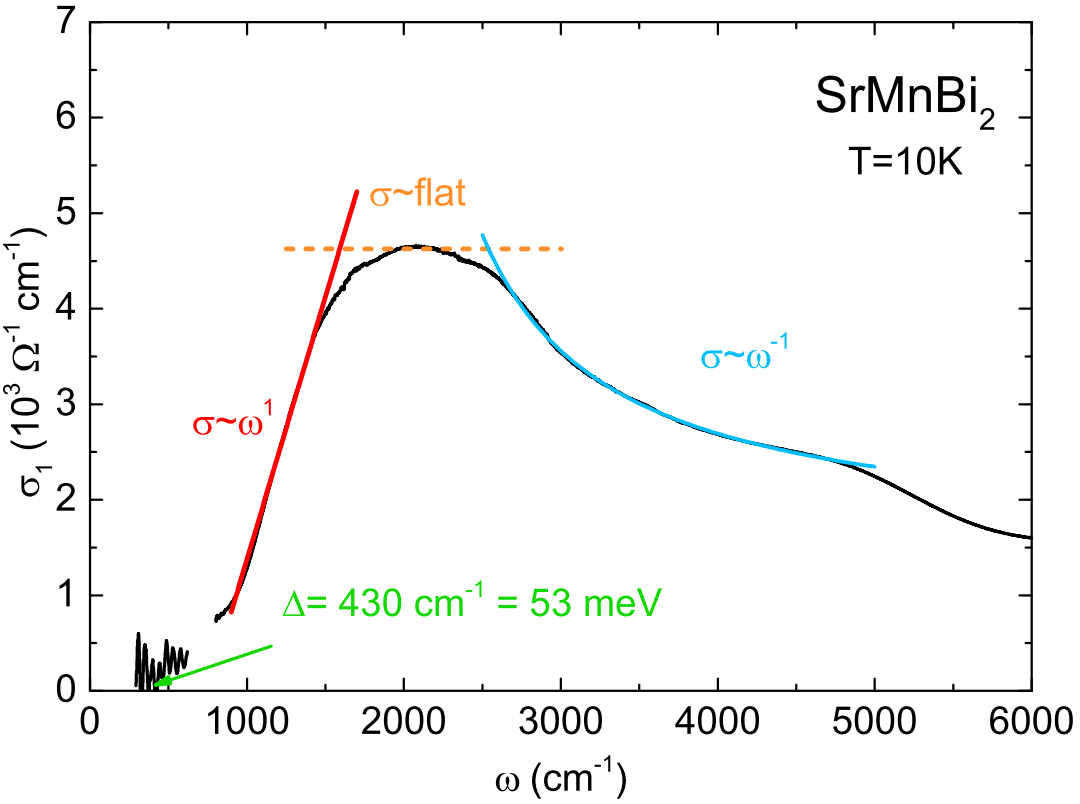

Figure 6.16.: The frequency-dependent interband conductivity of SrMnBi$_2$ for the lowest measured temperature of 10 K*. The onset of the interband conductivity can be assigned to an energy gap in the density of states of* $\Delta = 430\,\mathrm{cm}^{-1}$*. Above* $1000\,\mathrm{cm}^{-1}$*,* $\sigma_1(\omega)$ *rises linearly ending in a rather flat maximum around* $2000\,\mathrm{cm}^{-1}$*. The remaining MIR conductivity decays with* ω^{-1}*.*

the fact that the dispersion relations perpendicular to the Γ-M-direction and along the z-direction are similar for CaMnBi$_2$, while a factor of eight difference is found between the two directions for SrMnBi$_2$. Thus, while the linear bands stop at an energy of approximately $1500\,\mathrm{cm}^{-1}$ along the z-direction, they continue more perpendicular to the Γ-M-direction. From a material point of view, we connect this to the slightly stronger hybridization between the Sr atoms and the Bi(1) square net compared to the Ca atoms.

A ω^{-1}-decay is found for $\sigma_1(\omega)$ between $2500\,\mathrm{cm}^{-1}$ and $5000\,\mathrm{cm}^{-1}$. This indicates a one dimensional Dirac dispersion, as we also found in CaMnBi$_2$. We associate this to the steeper dispersion of the Dirac cones along the Γ-M-direction.

With the interpretation above, we claim that also for $SrMnBi_2$, the simplified model of quasi-two dimensional Dirac states is not correct. Instead, our optical results suggest a three dimensional dispersion with highly anisotropic Fermi velocities for the different directions.

6.4. Conclusions

Inspired by exotic anisotropic Dirac cones in $CaMnBi_2$ and $SrMnBi_2$, we investigated the optical properties of the two compounds and interpret our results within existing literature. We reveal two different channels of itinerant charge carriers, which are described by two Drude terms with strongly diverging scattering rates. We assign the narrow Drude contribution to the Fermi pockets of the Dirac cones located along the X-X-lines, while the broader one probably rises from the hole pockets close to the Γ-point. In both compounds, the narrow Drude term goes hand in hand with a characteristic peak located in the MIR range. We decompose this peak into the contributions of the linearly dispersing Dirac bands. Our optical results suggest a three dimensional Dirac response for lower energies. Due to the large anisotropy, the dispersion along the Γ-M-direction survives to much higher energies than along the other directions. Thus, above the linear conductivity a ω^{-1}-decay reveals one dimensional Dirac states. Based on these findings, we propose that the theoretical model given in literature are too simple and underestimate the contributions of the Bi(1) p_z-orbitals and the interaction via SOC.
Furthermore, we reveal a connection between the 50 K anomaly in $CaMnBi_2$ and the peak in $\sigma_1(\omega)$ in the MIR range. Our optical measurements are consistent with the picture of a (charge) density wave due to a transfer of spectral weight from the Drude contributions to the MIR peak. Since this peak is also connected to the appearance of the narrow Drude term, a link to the Dirac physics in the compound should be considered. In $SrMnBi_2$, the situation is very similar, but both, the narrow Drude and the MIR peak exist at room temperature already. Hence, the corresponding anomaly might be located above 300 K in $SrMnBi_2$. We do, however, lack a satisfying explanation why the Dirac physics in $CaMnBi_2$ is revealed below 50 K only.

7. Conclusions

The optical investigations carried out in the framework of this thesis reveal the low-energy electrodynamics of the measured compounds and provide a deep insight into the properties of Dirac quasiparticles, present in these materials. Broadband (50 to $25\,000\,\mathrm{cm}^{-1}$) reflectivity measurements on high-quality single crystals are used to calculate the complex optical functions and discuss their physical origin.

We investigate the optical response of the nodal line semimetal ZrSiS in chapter 4. In this material, the crossing points of the Dirac bands are located on a cage-like structure in reciprocal space, see Figure 4.1. Along these lines, the dispersion of the bands is zero, so the Dirac states are two dimensional in a three dimensional material.

We unveil this nodal line by observing a frequency-independent optical conductivity σ_{flat}, comparable to the response of the 2D Dirac states in graphene. In contrast to the universal conductance in a real 2D material, the absolute value of σ_{flat} in a nodal line semimetal is connected to the length of the line in reciprocal space [2]. For ZrSiS, we calculate k_0 from the real part of the optical conductivity to be $4.3\,\mathrm{\AA}^{-1}$. With this, we provide the first optical fingerprint of a nodal line ever observed. Additionally, we derive an upper limit for the energy gap of the nodal line with $\Delta \leq 250\,\mathrm{cm}^{-1} \approx 30\,\mathrm{meV}$. Comparing our optical conductivity to theoretical calculations of T. Habe *et al.* [4] we find a good agreement regarding the main aspects.

Furthermore, we observe two modes in the low-frequency range of the ZrSiS data. We discuss different scenarios for their origin, but complementing experimental techniques are required to draw a final conclusion.

In chapter 5, the magneto-transport and optical results on YbPtBi reveal a two-channel conduction for the itinerant carriers in the compound. This manifests itself by two Drude terms with strongly diverging scattering rates γ: values between 54 and 16 cm^{-1} are obtained for the narrow Drude, while γ of the broad Drude lies between 1500 and 785 cm^{-1}. The holes, caused by conduction bands crossing the Fermi level, are temperature-independent with a carrier concentration of $n_h = (5.2 \pm 0.6) \times 10^{20}\,\mathrm{cm}^{-3}$ and a mobility of $\mu_h = (10 \pm 5)\,\mathrm{cm}^2/\mathrm{Vs}$. In contrast, the properties of the electrons are changing strongly with temperature. At low temperatures, i.e., $T < 100\,\mathrm{K}$, we determine a charge carrier concentration of $n_e = (2.5 \pm 0.5) \times 10^{18}\,\mathrm{cm}^{-3}$, while it follows a T^2 behavior at higher temperatures. For the mobility of the electrons we get $\mu_e(0) = 51\,000\,\mathrm{cm}^2/\mathrm{Vs}$, which is the highest mobility of charge carriers in any half-Heusler compound reported up to date. Such a high mobility is usually connected to relativistic Dirac fermions and caused by suppressed back scattering processes [6, 164].
In the second part of the chapter, we compare the interband conductivity to the one obtained on the sister compound GdPtBi and connect it to the band structure calculations provided by Jun. Prof. Dr. H. Zhang from the Technische Universität Darmstadt. We successfully ascribe the optical features to three different areas in the band structure. Due to a linear frequency dependence, our experimental data suggest that these bands disperse linearly and give a second hint for Dirac physics in YbPtBi [9, 10]. We calculate reasonable Fermi velocities from the slope of the conductivity between 2 and $5 \times 10^5\,\mathrm{m/s}$. Our investigation is in agreement with recently proposed triple points in half-Heusler compounds, hosting a crossing point of a doubly degenerate band with a non-degenerate band.
To further clarify the existence of Dirac-like fermions in YbPtBi (and also GdPtBi) we call for ARPES measurements, since the possible Dirac fermions are of electron type and, thus, located below the Fermi level E_F. This should be nicely measurable with ARPES, which can map the detailed band structure below E_F.

Last but not least, we discuss the optical response of the two anisotropic Dirac semimetals $CaMnBi_2$ and $SrMnBi_2$in chapter 6. The low-frequency data of both materials require two Drude terms, as already introduced for YbPtBi. Again, the narrow Drude with a scattering rate in the order of a few cm^{-1} indicates a Dirac band crossing the Fermi level, while the broad Drude is related to conventional

metallic states.

We provide further information about the 50 K anomaly in $CaMnBi_2$ by fitting its optical response: an additional peak appearing in the mid-infrared range (around 1550 cm^{-1}) and a possible relation to the narrow Drude, which enters the fitting model at just slightly higher temperatures, i.e., 60 K. Supported by magnetic susceptibility measurements, we discuss the scenario of a (charge) density wave as origin for the anomaly. Since the spectral weight gain of the MIR peak perfectly matches the loss of spectral weight of the broad Drude, the overall spectral weight is conserved. The optical response of $CaMnBi_2$ is similar to some iron-pnictides, where density waves cause exactly such a MIR peak [188]. Furthermore, Fermi surface nesting is discussed in literature for $CaMnBi_2$, which is a key ingredient for density waves [190]. From the optical spectrum we extract the density wave gap to be $\Delta_{DW} = 440\,cm^{-1} = 55\,meV$.

After subtracting the Drude contributions from the initial optical spectra, we investigate the interband response of both, $CaMnBi_2$ and $SrMnBi_2$. They host a similar MIR peak, which is located in the energy range of the anisotropic Dirac cones arising from the Bi(1) square net, so we provide a second scenario and decompose the interband spectra in terms of the Dirac response. The linear rise in the beginning of the interband conductivity, i.e., $\sigma_1(\omega) \propto \omega$, suggests a three dimensional Dirac cone, which is in strong contradiction to the assumptions made for band structure calculations in literature, e.g., Ref. [179]. As the Dirac cones in the two compounds are strongly anisotropic, the energy range of linear bands is different for the different k-directions. Thus, we reveal a transition from 3D to 1D by observing a ω^{-1}-decay in $\sigma_1(\omega)$. In this scenario, the onset of the interband conductivity is assigned to the energy gap induced by spin-orbit coupling and reads $\Delta = 430\,cm^{-1} = 53\,meV$ for $SrMnBi_2$. The gap values and also the extracted Fermi velocities, i.e., $v_F(Ca) = 1.2 \times 10^4\,m/s$ and $v_F(Sr) = 0.9 \times 10^4\,m/s$, are in good agreement with band calculations and ARPES measurements [11].

Our optical results suggest a more three dimensional Dirac cone situation for $CaMnBi_2$ and $SrMnBi_2$. Hence, we suggest revised band structure calculations which do not neglect the p_z-orbitals of the Bi(1) atoms, since they may play a more important role when spin-orbit coupling is included.

All in all, we show in the framework of this thesis, that optical spectroscopy is a

powerful technique to investigate special properties of Dirac materials and can go beyond the linear frequency dependence of the optical conductivity widely discussed in literature. Due to the probing of transitions across the Fermi level E_F, the applied technique grants access to energy ranges, where other experimental techniques fail.

Appendices

A. Sr_3SnO - an antiperovskite Dirac material

In this chapter, the status quo of an additional project is discussed and recommendations for further measurements are made. It involves the strongly air sensitive material Sr_3SnO, so the measurements were only possible after improving the alignment concept and assembling the transfer system from the glovebox to the infrared setups. The measurements did, however, not lead to satisfying results to draw final conclusions about the material's optical properties. Below, the preliminary results of the measurements are shown and we discuss possible improvements, which are necessary to achieve an insight into the electrodynamic response of the investigated material.

A.1. The material

The compound Sr_3SnO belongs to the so-called antiperovskite structures [191]. In this type of structure, the anion (O) is surrounded by six cations (Sr), see Figure A.1 (a). Due to the strong degeneration of the samples under ambient conditions, the number of investigations on this material is limited to two publications which we are aware of: One provides a comparison of the band structure of the antiperovskite

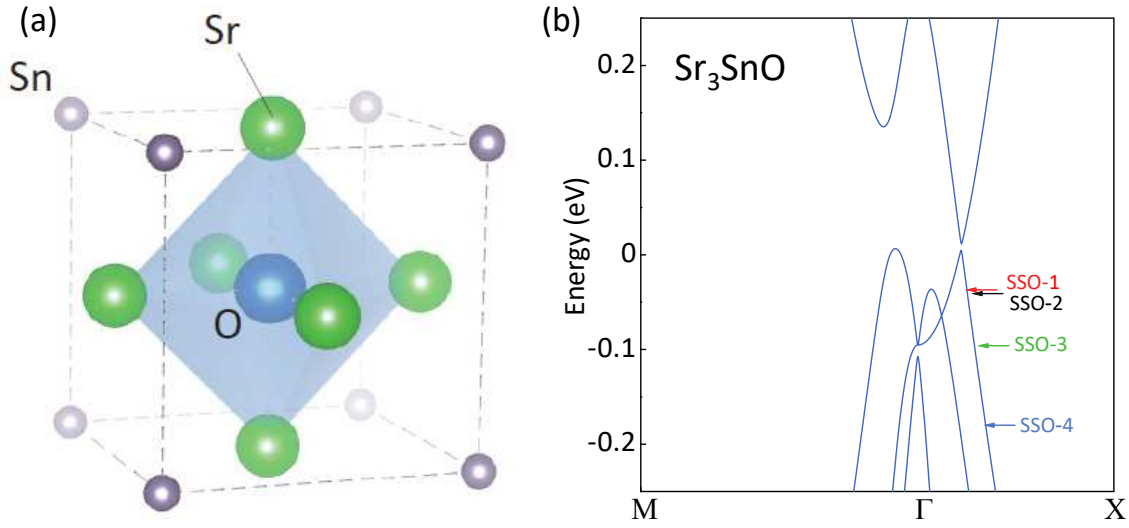

Figure A.1.: The crystal structure of Sr_3SnO is redrawn from Ref. [191] in panel (a). It belongs to the antiperovskite type. The calculated band structure in the vicinity of the Dirac point is provided by Dr. H. Nakamura and given in panel (b).

family [192], the other one combines band structure calculations with quantum interference measurements on Sr_3SnO [191].

The band structure calculations of Sr_3SnO reveal a crossing of linearly dispersing bands in the vicinity of the Fermi level, as depicted in panel (b) of Figure A.1. This Dirac point is located between the Γ-, the X-, and the M-point of the Brillouin zone. In the ideal case, this point is located only a few eV above the Fermi level. Thus, it should be nicely addressable by means of optical spectroscopy.

Our Sr_3SnO thin films (110 to 130 nm), provided by Dr. H. Nakamura from the Max-Planck-Institut für Festkörperforschung (Stuttgart, Germany), were grown by molecular beam epitaxy [191]. The film growth was performed on Yttria stabilized ZrO_2 (YSZ) substrates at a temperature of 450 °C. The charge mobility and the carrier density obtained for the film here presented are $\mu_h = 92\,\mathrm{cm}^2/\mathrm{Vs}$ and $n_h = 6.75 \times 10^{19}\,\mathrm{cm}^{-3}$ [193]. Thus, the film was hole doped with an estimated distance between Fermi level and Dirac point of −107 meV. The Fermi level varies between −30 and −180 meV from one film to another, as indicated in Figure A.1 (b), where our film belongs to the SSO-3 group.

If the samples come in contact with water, they degenerate within seconds, which can be seen by the loss of its shiny metallic color. This strong sensitivity of the samples requires a direct transfer between the film growth vacuum chamber and the measurement setup. Thus, we make use of the newly designed transfer system with a stopover in the argon atmosphere of the glovebox. As the films keep their shiny color throughout the complete transfer and measurement, the success of the transfer system is proven.

A.2. Optics

Restricted to measurements performed with the Hyperion microscope, we provide reflectivity data from 500 to 25 000 cm^{-1}. Because of the strong degeneration of the sample when coming into contact with water, we limit our measurements to temperatures below 200 K.
The temperature dependence of the reflectivity is given in Figure A.2. Upon cooling, only minor changes are observed. This is consistent with only the Dirac bands crossing the Fermi level. The strong decrease of the reflectivity between 560 and 760 cm^{-1} may be assigned to the plasma edge of the itinerant carriers. To ultimately clarify this, however, measurements to lower frequencies are necessary. Thus, we provide three different types of low-frequency extrapolation: A Drude extrapolation for the itinerant carriers, a constant line for a charge neutral low-frequency response, and a Lorentz model located below 560 cm^{-1} which could also be responsible for the drop of the reflectivity.
The different extrapolations and the results of the Kramers-Kronig analysis are given in Figure A.3. The influence of the extrapolation is restricted to frequencies below 650 cm^{-1}. Above 1500 cm^{-1} and up to 3500 cm^{-1}, the real part of the optical conductivity $\sigma_1(\omega)$ is negative, as indicated by the horizontal zero-line (red). This is, of course, not physical. Since the samples we measured are thin films, we assign this negative conductivity to the fact that the material is too transparent. In this case, reflectivity measurements are not sufficient to describe the optical response of Sr_3SnO.

The optical response of a material is defined as $1 = R + T + A$, with the reflectivity R, the transmission T and the absorption A. If T is small enough, i.e., no light

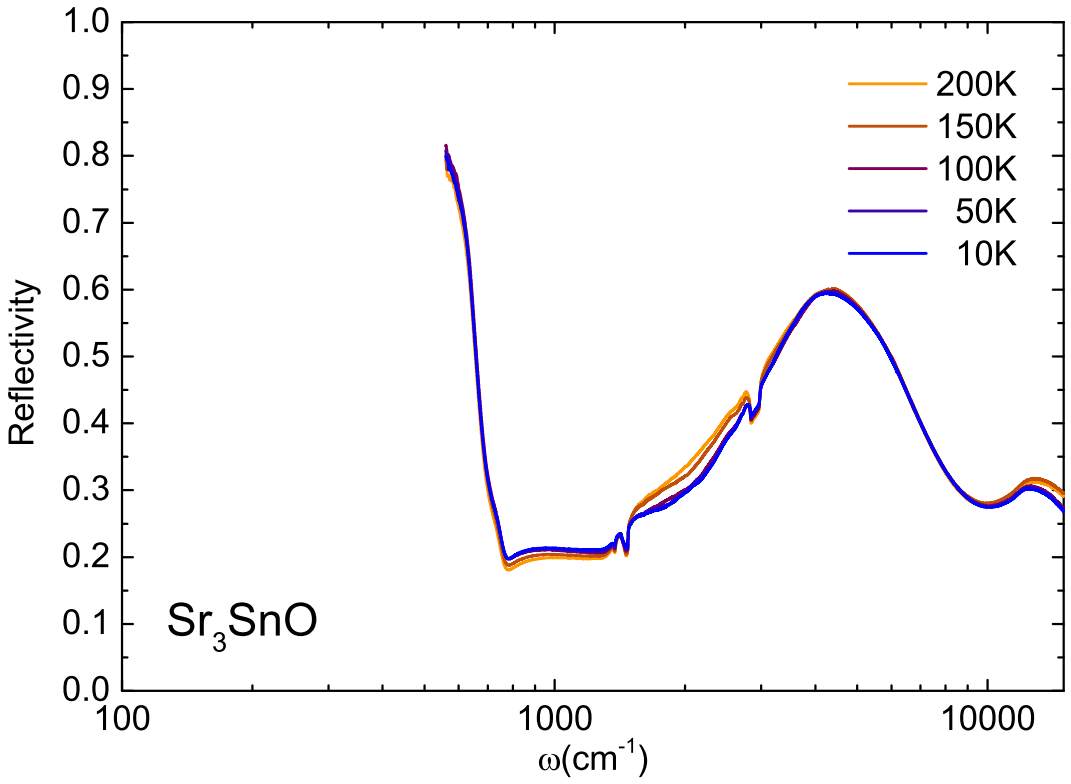

Figure A.2.: The frequency-dependent reflectivity of Sr_3SnO for selected temperatures. The influence of the temperature is only minor, which is in good agreement with the band structure. Details about the spectra are discussed in the text.

passes through the sample, reflectivity measurements combined with a Kramers-Kronig analysis are sufficient to describe the optical properties. As this does not hold for the thin films measured here, we suggest two solutions: Either, besides the reflectivity, also the transmission needs to be measured; otherwise, thicker films are required, so that the measurement light does not penetrate the sample. The former is currently not possible, since the cryostat of the Hyperion setup is only made for reflectivity measurements. The latter one implies difficulties with the sample quality. Thicker films lead to a poorer film quality changing the physical properties of the material. Thus, designing a new cryostat for the setup which

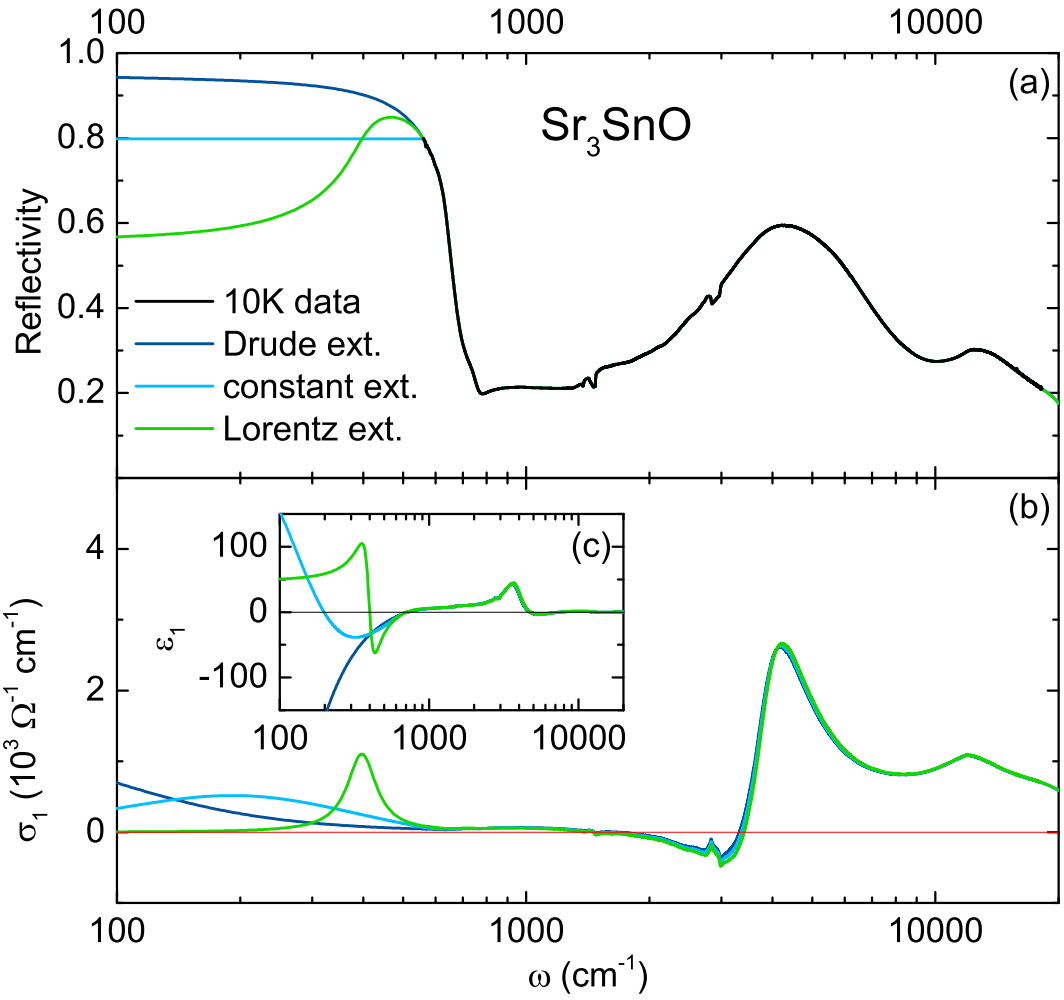

Figure A.3.: Different low-frequency extrapolations for the reflectivity of Sr_3SnO are depicted in panel (a). The results of the Kramers-Kronig analysis, i.e., the optical conductivity $\sigma_1(\omega)$ and the real part of the dielectric function $\varepsilon_1(\omega)$, are given in panels (b) and (c), respectively.

allows reflectivity and transmission measurements is the way to go.

B. Magneto-optical measurements

Here, we present magneto-optical studies on different Dirac and Weyl semimetals. As described in section 3.2, the Bruker 113 is extended by a superconducting magnet

with a field strength up to 7 T [51]. Thus, the magneto-optical measurements are usually limited to the FIR range, i.e., 50 to 700 cm^{-1}. The geometry of the magnet, so the orientation of the magnetic field $\vec{B}$ with respect to the propagation vector $\vec{k}$ of the measurement light, is chosen to be Voigt geometry. With this geometry, cyclotron resonances, i.e., Landau level transitions, should be observable with unpolarized light. The results given below do, however, not lead to final information and, thus, should be expanded by further investigations.

B.1. ZrSiS

Firstly, magneto-optical measurements on the nodal line semimetal ZrSiS of chapter 4 are discussed. The measurements are supposed to reveal Landau levels induced by the magnetic field. The relative reflectivity $R(B)/R(0\,\mathrm{T})$ is given in Figure B.1. All measurements in the magneto-optical setup are performed at 10 K. Within the investigated frequency range, no influence of the magnetic field on the optical response of ZrSiS is observed. This holds for all fields between 0 and 7 T.

The absence B-field induced features can have different origins. One possible explanation is the extremely high mobility and low effective mass of electrons in Dirac and Weyl semimetals. This can require comparably high magnetic fields to observe transitions between two Landau levels. Furthermore, the different B-field dependence of the cyclotron energy E_c:

$$E_c = E_{n+1} - E_n = v_F\sqrt{2e\hbar B}\left(\sqrt{|n+1|} - \sqrt{|n|}\right) \quad , \tag{B.1}$$

which is the energy difference between two Landau levels, can lead to higher frequency values for the transitions. Thus, the FIR range might be too low to observe Landau level transitions in ZrSiS and measurements in the MIR range in a magnet with a higher field range should be performed.

B.2. WTe_2

Secondly, we investigate the magneto-optical response of the type II Weyl semimetal WTe_2. The zero field electrodynamics of this material were already discussed in Refs. [194, 195]. C. C. Homes *et al.* apply a two Drude model for the itinerant

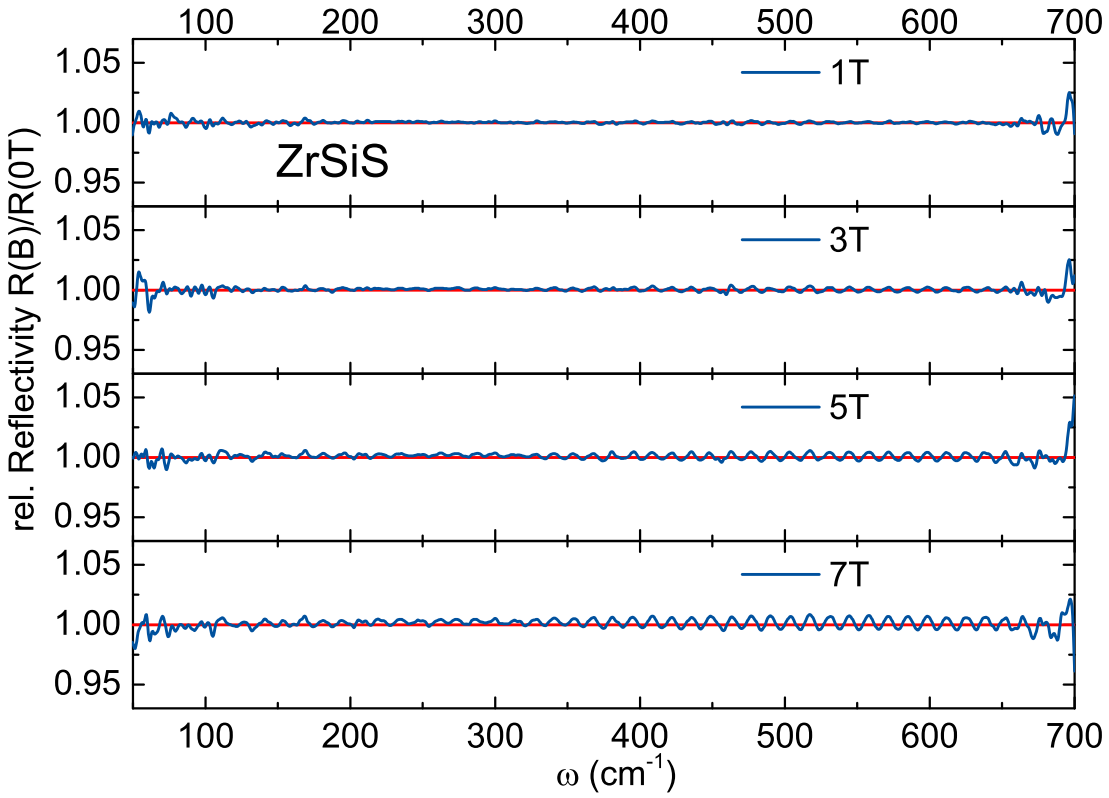

Figure B.1.: The relative reflectivity $R(B)/R(0\,\mathrm{T})$ of ZrSiS measured in the far-infrared at 10 K for magnetic fields between 0 and 7 T. Within our resolution, no field dependence can be observed. The small oscillations increasing with the field are artificially caused by the measurement procedure.

carriers and prove WTe_2 to be a perfectly compensated semimetal [194]. The scattering rate of one of the Drude terms collapses upon cooling and is in the other of a few wave numbers below 100 K. In this work, the meausurement light is, however, unpolarized. The more accurate investigation of A. J. Frenzel *et al.* includes polarization-dependent measurements [195]. It reveals a strongly anisotropic optical response of WTe_2. Thus, the two Drude terms should be assigned to the different direction[1], i.e., $E \parallel a$ and $E \parallel b$. The crystal directions a and b are defined in the crystal structure given in Ref. [195].

Both investigations could, however, not reveal the Weyl semimetal character of WTe_2. Therefore, we perform magneto-optical measurements to observe Landau

[1]The polarization direction is usually determined by the direction of the electric field component E of the measurement light

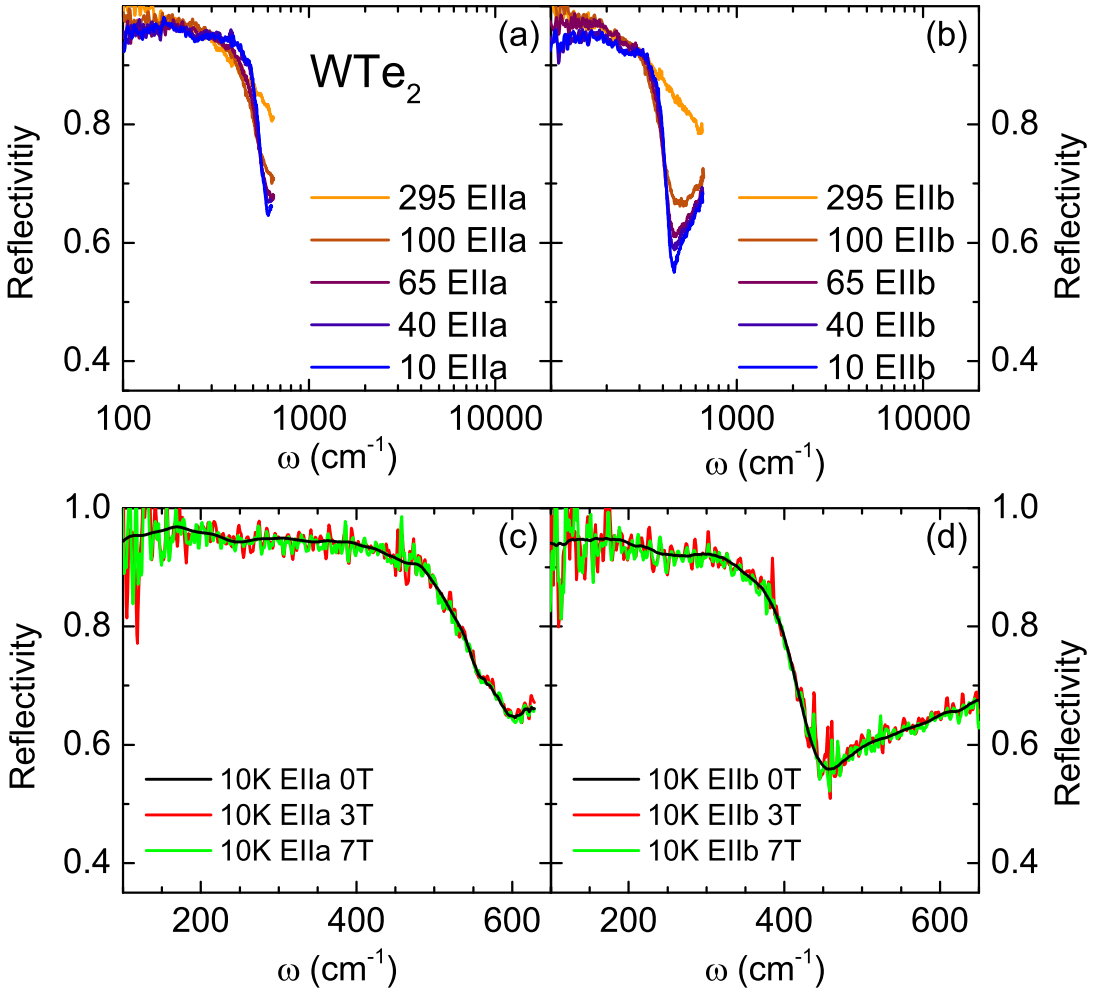

Figure B.2.: The reflectivity of WTe_2 for selected temperatures measured in the FIR range is given for the two polarizations $E \parallel a$ and $E \parallel b$ in panels (a) and (b), respectively. The magneto-optical measurements given in panels (c) and (d) do not reveal any influence of the magnetic field.

levels, which B-field dependence should help to verify the Weyl states. To prove a comparable crystal quality, we performed additional zero field measurements with polarized light in the FIR range, which are given in Figure B.2 (a) and (b). Both directions, $E \parallel a$ and $E \parallel b$, are in good agreement with the optical data of Ref. [195]. This holds for the absolute values of the reflectivity as well as for characteristic features, e.g., the plasma edge.

The magnetic-optical measurements are shown in panels (c) and (d) of Figure B.2.

Within our resolution, we again do not observe any influence of the magnetic field on the optical response. Possible explanations for the absence of B-field features are again too small magnetic fields and the wrong frequency range.

B.3. NbAs

Thirdly, the (magneto-)optical measurements of the Weyl semimetal NbAs presented. NbAs belongs to the TaAs family which was briefly mentioned in section 2.3. A detailed discussion on the optical results on the related compounds NbP and TaAs are given in Refs. [51, 79]. Since the results shown below reveal some problems, only a quick comparison the optical response of NbP and TaAs is made.

NbAs obeys the same kind of crystal structure as TaAs, with only slightly larger lattice vectors [196]. Also the band structure is comparable, hosting two different types of Weyl pairs off the high symmetry lines, leading to a total number of 24 Weyl points. A comprehensive comparison of the lattice and electronic structure for the TaAs family can be found in Ref. [196].

The optical results of the $B = 0\,\mathrm{T}$ measurement are shown in Figure B.3: The reflectivity $R(\omega)$ in panel (a), the real part of the optical conductivity $\sigma_1(\omega)$ in panel (b), and the real part of the dielectric function $\varepsilon_1(\omega)$ in panel (c). The inset of the latter provides a closer look on several zero-crossings of $\varepsilon_1(\omega)$.

The low-frequency response of NbAs reveals an expected metallic behavior, i.e., high absolute values in $R(\omega)$, an increasing $\sigma_1(\omega)$ towards lower frequencies, and negative absolute values in $\varepsilon_1(\omega)$. Above $700\,\mathrm{cm}^{-1}$, $\sigma_1(\omega)$ increases due to the onset of interband transitions. Between 200 and $700\,\mathrm{cm}^{-1}$, the conductivity, however, is rather flat, matching neither a metallic Drude response nor the expected Weyl response. Such a behavior was also observed for the related compounds NbP and TaAs in Refs. [51, 79]. For fitting the optical data, this can be taken into account either by a second Drude term or by a low-frequency Lorentz term. A possible verification is given by trivial and Weyl bands crossing the Fermi level.

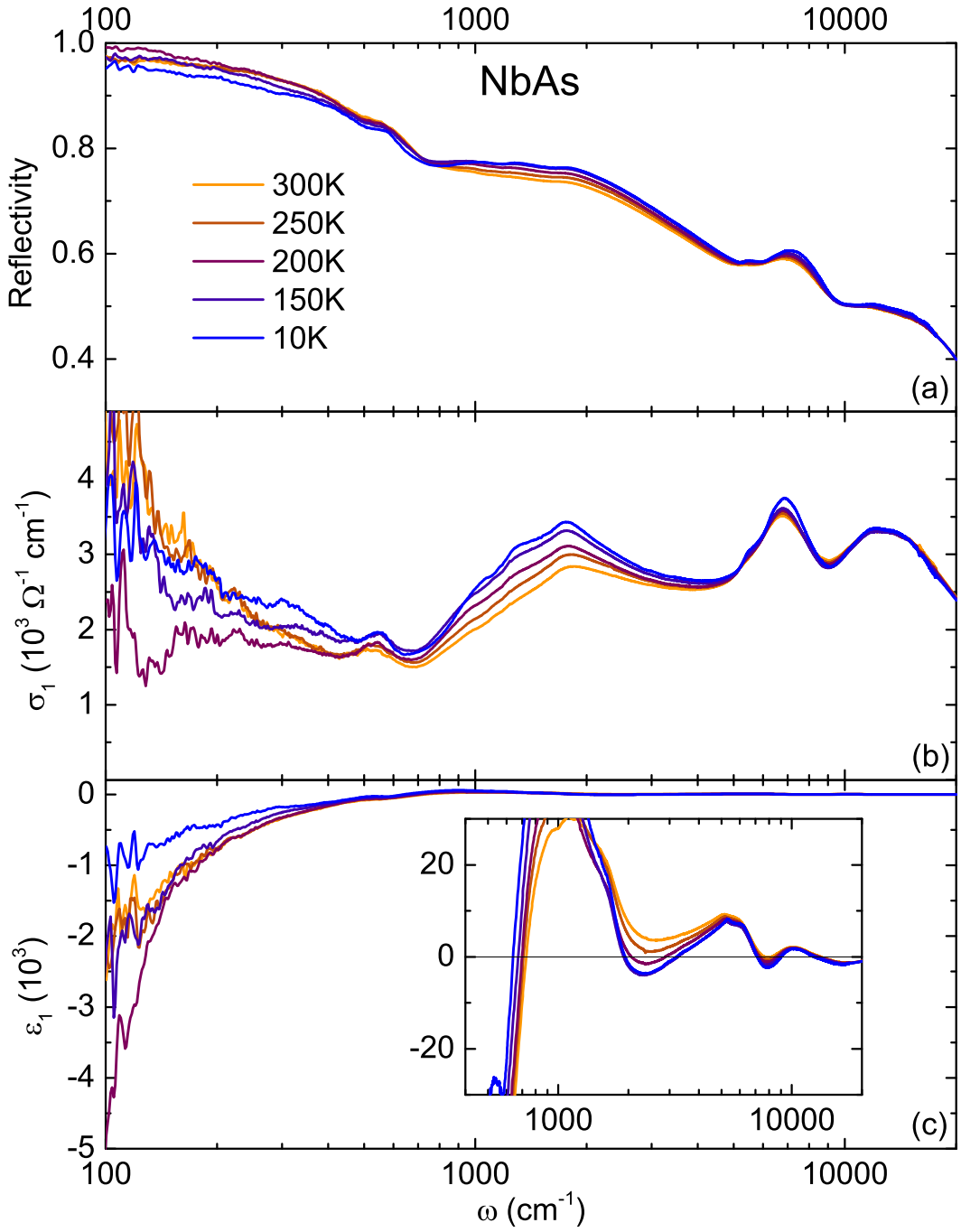

Figure B.3.: The frequency-dependent reflectivity (a), optical conductivity (b) and the dielectric function (c) of NbAs are shown for selected temperatures. The inset of panel (c) reveals several zero-crossings of $\varepsilon_1(\omega)$.

Above 700 cm^{-1}, $\sigma_1(\omega)$ increases quasi-linear with frequency, which is expected for three dimensional Weyl bands. At lower temperatures, however, the deviation from

a linear conductivity is larger, which is contradicting the picture of 3D Weyl cones.

During the measurement, two facts arise doubts about the final quality of the obtained optical response: On the one hand, the humps around $1000\,\mathrm{cm}^{-1}$, which are blurring the quasi-linear conductivity at lower temperatures, seem to be a problem of the measurement setup. They are also present in some high temperature measurements, but could be eliminated by repeating the measurement several times. At low temperatures, this, however, did not help. On the other hand, the metallic response at low frequencies is rather noisy, preventing a clear picture for the optical data. This frequency range is, however, important due to the flat response between 200 and $700\,\mathrm{cm}^{-1}$. Thus, the FIR as well as the MIR measurements should be repeated. Maybe crystals with a better surface are essential to obtain better results.

Nevertheless, magneto-optical measurements were performed in the FIR range and the results are depicted in Figure B.4. Panel (a) shows the relative reflectivity $R(B)/R(0\,\mathrm{T})$ for magnetic fields B between 0 and 7 T obtained at 10 K. The spectra are stacked for clarity and the dashed black lines are the base lines for each curve. Upon increasing the magnetic field, the reflectivity below $200\,\mathrm{cm}^{-1}$ decreases for fields above 4 T. At higher frequencies, the magnetic field induces an increase of the reflectivity. By plotting the absolute reflectivity in panel (b), this increase can be seen more clearly.
In panel (c), a contour plot of the reflectivity $R(B,\omega)$ is given. With this, the dispersion of the observed features can be traced easily. The feature between 300 and $400\,\mathrm{cm}^{-1}$ shows a square root dependence, as indicated by the black line. Such a $\sqrt{B}$-dependence is expected for Landau level transitions of Dirac/Weyl bands [24]. With the relation given in section B.1, the dispersion can be used to calculate the Fermi velocity of the involved bands. Here, a value of $v_F = 4.85 \times 10^5\,\mathrm{m/s}$ is obtained, assuming the transition between the zeroth and the first Landau level, i.e., $n = 0$ and $n = 1$.
The reduction of the reflectivity at lowest frequencies can be seen by the blue/violet colored area. A possible interpretation is the opening of an energy gap induced by the magnetic field. This requires, however, further investigation. Furthermore, a B-field-independent feature can nicely be seen in the contour plot. It is located at $220\,\mathrm{cm}^{-1}$ and appears for fields larger 3 T. The field-independent behavior suggests

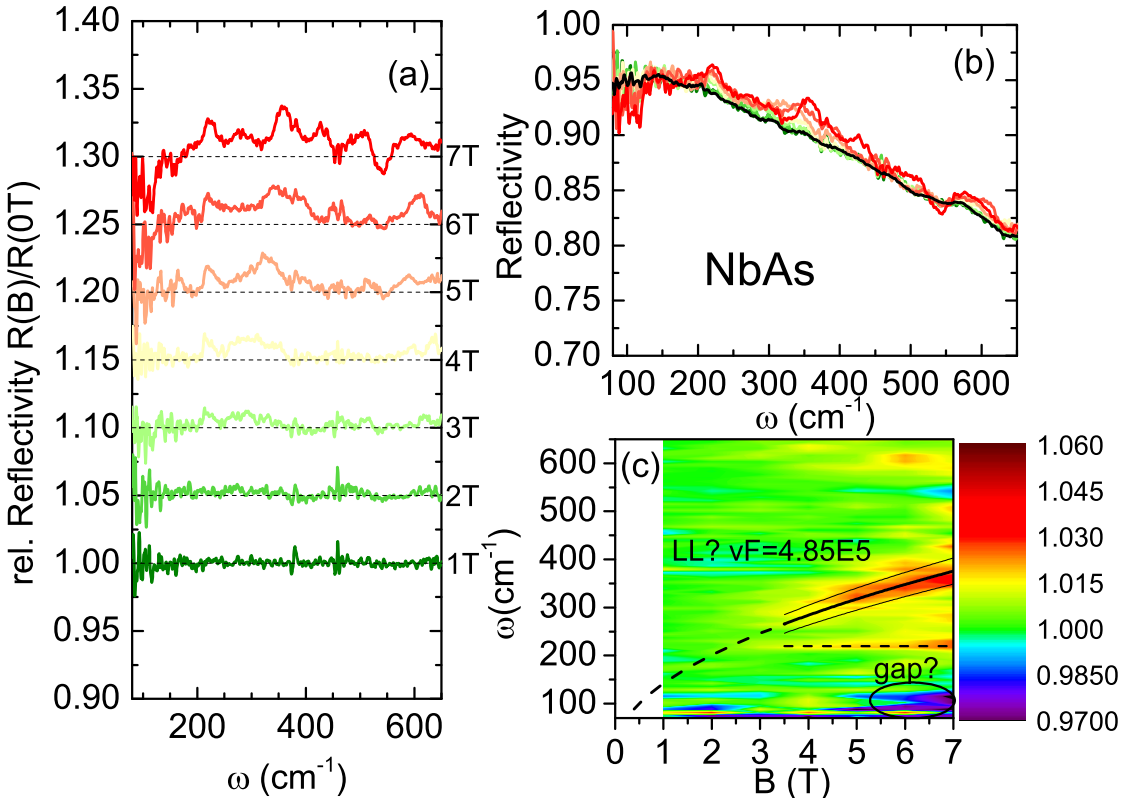

Figure B.4.: The magneto-optical results of NbAs obtained at 10 K. *Panel (a) shows the relative reflectivity for all fields. The spectra are stacked for clarity. The absolute values of the reflectivity $R(\omega)$ are given in panel (b). The contour plot of $R(B, \omega)$ in panel (c) provides a better access to the dispersion of features upon increasing the magnetic field.*

a connection to the zeroth Landau level [24], indicating also that NbAs is in the quantum limit, i.e., the Fermi level lies between the $n = -1$ and $n = 1$ Landau level and only the zeroth one is crossing it.

A more detailed interpretation of above shown results will be given elsewhere.

C. Acknowledgments

Here, I want to thank all the people who supported me during my PhD time at the 1. Physikalisches Institut in many different ways.

- First of all, I would like to thank my supervisor Prof. Dressel. There was always enough space for scientific creativity and an open door to ask for advise when required. Thank you for offering me this PhD position.

- I also would like to thank Dr. Smet for kindly accepting to co-referee this thesis.

- Additionally, I would like to thank Artem Pronin for supervising me in terms of Dirac physics. Thank you for organizing such interesting materials, sharing your knowledge and network and additionally supporting the publications a lot.

- Special thanks to David Neubauer, Sina Fella, and Tomislav Ivek for introducing me to the 1. Physikalisches Institut, the different setups, and arousing my interest for solid state research. I learned many things from you guys which made my experimental work possible. Accompanying with thanks to Andrej Pustogow and Weiwu Li for fruitful thoughts during our group meetings or personal discussions.

- Most of my measurements would not be possible without the outstanding technical support by Gabi Untereiner. Thank you for all you have done and the lean periods at the glovebox. Furthermore, I would like to thank Agni Schmidt, the low temperature department and the mechanics/electronics workshops for all the support in your special fields.

I also want to acknowledge all collaborators, people who provided some samples and supported my work:

- I would like to thank Leslie Schoop and her team for the astonishingly large single crystals of ZrSiS and the (theoretical) support towards a nice publications in PRL.

- I am grateful for the collaboration with Claudia Felser, C Shekhar, and Binghai Yan from Dresden. Thank you for the many crystals (YbPtBi, GdPtBi, WTe_2, NbAs, ...) you provided us, but also the nice theoretical support and many fruitful discussions.

- I thank Y. G. Shi and his group for providing many $CaMnBi_2$ and $SrMnBi_2$ crystals, which made several measurements possible. This gave me the opportunity to develop a technique measuring air sensitive samples.

- Hiro Nakamura, thank you for growing all the films of Sr_3SnO and Sr_3PbO. Thank you for sharing your glovebox knowledge and many inspiring thoughts in the field of Dirac physics. Hopefully, successful infrared measurements on your compounds will be performed soon.

- I also would like to thank Hongbin Zhang for the theoretical support, fruitful discussions and the nice calculations on YbPtBi, which provided access to the interband physics in this compound.

- Thank you Anja Löhle for providing such nice magneto-transport measurements on YbPtBi, which helped a lot understanding the underlying physics and made the publication possible. Furthermore, I thank Claudia Kamella for the EDX measurements on some of my samples.

I want to thank all the people who supported and accompanied me over the years:

- I would like to thank all people who were involved in the IR-team, for many fruitful discussions, nice breakfasts during group meetings and very familiar and friendly atmosphere.

- Special thanks to Andrea Rohwer, for being such a friend-like colleague when times were hard. Thank you for motivating me and making me focus on the right things. Thanks for many pleasant conversations.

- Billiard-Team! Thank you guys for nice evenings whenever we could not attend a nice colloquium.

- I also would like to thank my Bachelor and Master students André Haug and Felix Hütt. Thank you for all your questions which made me think and for your contributions to this work. I hope I could inspire you for your future carriers.

- Thanks also to all other people from the institute for all your on- and off-topic conversations, for a nice working atmosphere, nice lunch times, barbecues, ice time and many other refreshing distractions.

- Special acknowledgments to Andrea, Andreas, and Felix for proofreading this thesis and many fruitful suggestions.

Finally, I would like to thank my parents and family for supporting me already since my early days on my journey through life. Thank you for the possibility of such a long way of education. Thanks to all my friends for balancing my life, especially during hard times. Last but not least, thank you Joana for being my home and my family. Thank you for enduring me, regardless the mood I brought home. Thank you for all your support in daily life which strengthen me whenever it was necessary. Thank you a lot!

Bibliography

[1] M. B. Schilling, L. M. Schoop, B. V. Lotsch, M. Dressel, and A. V. Pronin, „Flat optical conductivity in ZrSiS due to two-dimensional Dirac bands“, Physical Review Letters **119**, 187401 (2017).

[2] J. P. Carbotte, „Optical response of a line node semimetal“, Journal of Physics: Condensed Matter **29**, 045301 (2017).

[3] L. M. Schoop, M. N. Ali, C. Straßer, A. Topp, A. Varykhalov, D. Marchenko, V. Duppel, S. S. P. Parkin, B. V. Lotsch, and C. R. Ast, „Dirac cone protected by non-symmorphic symmetry and three-dimensional Dirac line node in ZrSiS“, Nature Communications **7**, 11696 (2016).

[4] T. Habe and M. Koshino, „Dynamical conductivity in topological nodal-line semimetal ZrSiS“, arXiv, 1806.04283 (2018).

[5] M. B. Schilling, A. Löhle, D. Neubauer, C. Shekhar, C. Felser, M. Dressel, and A. V. Pronin, „Two-channel conduction in YbPtBi“, Physical Review B **95**, 155201 (2017).

[6] M. N. Ali, J. Xiong, S. Flynn, J. Tao, Q. D. Gibson, L. M. Schoop, T. Liang, N. Haldolaarachchige, M. Hirschberger, N. P. Ong, and R. J. Cava, „Large, non-saturating magnetoresistance in WTe2“, Nature **514**, 205–208 (2014).

[7] T. Liang, Q. Gibson, M. N. Ali, M. Liu, R. J. Cava, and N. P. Ong, „Ultrahigh mobility and giant magnetoresistance in the Dirac semimetal Cd3As2“, Nature Materials **14**, 280–284 (2014).

[8] H. Yang, J. Yu, S. S. P. Parkin, C. Felser, C.-X. Liu, and B. Yan, „Prediction of triple point fermions in simple half-Heusler topological insulators“, Physical Review Letters **119**, 136401 (2017).

[9] P. Hosur, S. A. Parameswaran, and A. Vishwanath, „Charge transport in Weyl semimetals“, Physical Review Letters **108**, 046602 (2012).

[10] Á. Bácsi and A. Virosztek, „Low-frequency optical conductivity in graphene and in other scale-invariant two-band systems“, Physical Review B **87**, 125425 (2013).

[11] Y. Feng, Z. Wang, C. Chen, Y. Shi, Z. Xie, H. Yi, A. Liang, S. He, J. He, Y. Peng, X. Liu, Y. Liu, L. Zhao, G. Liu, X. Dong, J. Zhang, C. Chen, Z. Xu, X. Dai, Z. Fang, and X. J. Zhou, „Strong anisotropy of Dirac cones in SrMnBi2 and CaMnBi2 revealed by angle-resolved photoemission spectroscopy.“, Scientific Reports **4**, 5385 (2014).

[12] Y. J. Jo, J. Park, G. Lee, M. J. Eom, E. S. Choi, J. H. Shim, W. Kang, and J. S. Kim, „Valley-polarized interlayer conduction of anisotropic Dirac fermions in SrMnBi2“, Physical Review Letters **113**, 156602 (2014).

[13] P. A. M. Dirac, „The Quantum Theory of the Electron“, Proceedings of the Royal Society of London A **117**, 610–624 (1928).

[14] H. Weyl, „Elektron und Gravitation. I“, Zeitschrift für Physik **56**, 330–352 (1929).

[15] T. O. Wehling, A. M. Black-Schaffer, and A. V. Balatsky, „Dirac materials“, Advances in Physics **63**, 1–76 (2014).

[16] H. B. Nielsen and M. Ninomiya, „The Adler-Bell-Jackiw anomaly and Weyl fermions in a crystal“, Physics Letters B **130**, 389–396 (1983).

[17] A. A. Burkov, „Negative longitudinal magnetoresistance in Dirac and Weyl metals“, Physical Review B **91**, 245157 (2015).

[18] P. E. C. Ashby and J. P. Carbotte, „Chiral anomaly and optical absorption in Weyl semimetals“, Physical Review B **89**, 245121 (2014).

[19] C. J. Tabert, J. P. Carbotte, and E. J. Nicol, „Optical and transport properties in three-dimensional Dirac and Weyl semimetals“, Physical Review B **93**, 085426 (2016).

[20] J. D. Bjorken and S. D. Drell, *Relativistic Quantum Mechanics* (McGraw-Hill Inc.,US, 1964).

[21] M. Dressel and G. Grüner, *Electrodynamics of Solids* (Cambridge University Press, 2002).

[22] C. G. Böhmer and L. Corpe, „Helicity - From Clifford to graphene“, Journal of Physics A **45**, 205206 (2012).

[23] A. H. C. Neto, F. Guinea, N. M. R. Peres, K. S. Novoselov, and A. K. Geim, „The electronic properties of graphene“, Reviews of Modern Physics **81**, 109 (2009).

[24] P. E. C. Ashby and J. P. Carbotte, „Magneto-optical conductivity of Weyl semimetals“, Physical Review B **87**, 245131 (2013).

[25] R. R. Bruner, „What is Topology?“, http://www.math.wayne.edu (2000).

[26] K. V. Klitzing, G. Dorda, and M. Pepper, „New method for high-accuracy determination of the fine-structure constant based on quantized hall resistance“, Physical Review Letters **45**, 494–497 (1980).

[27] E. Tiras, S. Ardali, T. Tiras, E. Arslan, S. Cakmakyapan, O. Kazar, J. Hassan, E. Janzén, and E. Ozbay, „Effective mass of electron in monolayer graphene: Electron-phonon interaction“, Journal of Applied Physics **113**, 043708 (2013).

[28] C. Hwang, D. A. Siegel, S. K. Mo, W. Regan, A. Ismach, Y. Zhang, A. Zettl, and A. Lanzara, „Fermi velocity engineering in graphene by substrate modification“, Scientific Reports **2**, 590 (2012).

[29] G. G. Guzmán-Verri and L. C. Lew Yan Voon, „Electronic structure of silicon-based nanostructures“, Physical Review B **76**, 075131 (2007).

[30] P. Vogt, P. De Padova, C. Quaresima, J. Avila, E. Frantzeskakis, M. C. Asensio, A. Resta, B. Ealet, and G. Le Lay, „Silicene: Compelling Experimental Evidence for Graphenelike Two-Dimensional Silicon“, Physical Review Letters **108**, 155501 (2012).

[31] M. Z. Hasan and C. L. Kane, „Colloquium: Topological insulators“, Reviews of Modern Physics **82**, 3045–3067 (2010).

[32] S. A. Parameswaran and Y. Wan, „Topological Insulators Turn a Corner“, Physics **10**, 132 (2017).

[33] M. Z. Hasan and J. E. Moore, „Three-Dimensional Topological Insulators“, Annual Review of Condensed Matter Physics **2**, 55–78 (2011).

[34] B. Yan, „Private communication“, Weizmann Institute of Science (2018).

[35] S. Jia, S. Y. Xu, and M. Z. Hasan, „Weyl semimetals, Fermi arcs and chiral anomalies“, Nature Materials **15**, 1140–1144 (2016).

[36] X. Wan, A. M. Turner, A. Vishwanath, and S. Y. Savrasov, „Topological semimetal and Fermi-arc surface states in the electronic structure of pyrochlore iridates“, Physical Review B **83**, 205101 (2011).

[37] M. Z. Hasan, S.-Y. Xu, I. Belopolski, and S.-M. Huang, „Discovery of Weyl fermion semimetals and topological Fermi arc states“, Annual Review of Condensed Matter Physics **8**, 289–309 (2017).

[38] A. M. Turner and A. Vishwanath, „Beyond band insulators: Topology of semimetals and interacting phases“, arXiv, 1301.0330 (2013).

[39] A. A. Zyuzin, S. Wu, and A. A. Burkov, „Weyl semimetal with broken time reversal and inversion symmetries“, Physical Review B **85**, 165110 (2012).

[40] J. S. Lamb and J. A. Roberts, „Time-reversal symmetry in dynamical systems: A survey“, Physica D: Nonlinear Phenomena **112**, 1–39 (1998).

[41] L. M. Schoop, F. Pielnhofer, and B. V. Lotsch, „Chemical Principles of Topological Semimetals“, Chemistry of Materials **(2018)**, 3155–3176.

[42] K. H. Ahn, K. W. Lee, and W. E. Pickett, „Spin-orbit interaction driven collective electron-hole excitations in a noncentrosymmetric nodal loop Weyl semimetal“, Physical Review B **92**, 115149 (2015).

[43] J. Klotz, S.-C. Wu, C. Shekhar, Y. Sun, M. Schmidt, M. Nicklas, M. Baenitz, M. Uhlarz, J. Wosnitza, C. Felser, and B. Yan, „Quantum oscillations and the Fermi surface topology of the Weyl semimetal NbP“, Physical Review B **93**, 121105 (2016).

[44] B. Yan and C. Felser, „Topological Materials: Weyl Semimetals“, Annual Review of Condensed Matter Physics, 1–18 (2016).

[45] H. Weng, C. Fang, Z. Fang, B. Andrei Bernevig, and X. Dai, „Weyl semimetal phase in noncentrosymmetric transition-metal monophosphides“, Physical Review X **5**, 011029 (2015).

[46] S. M. Huang, S. Y. Xu, I. Belopolski, C. C. Lee, G. Chang, B. Wang, N. Alidoust, G. Bian, M. Neupane, C. Zhang, S. Jia, A. Bansil, H. Lin, and M. Z. Hasan, „A Weyl Fermion semimetal with surface Fermi arcs in the transition metal monopnictide TaAs class“, Nature Communications **6**, 7373 (2015).

[47] S. Y. Xu, I. Belopolski, N. Alidoust, M. Neupane, G. Bian, C. Zhang, R. Sankar, G. Chang, Z. Yuan, C. C. Lee, S. M. Huang, H. Zheng, J. Ma, D. S. Sanchez, B. K. Wang, A. Bansil, F. Chou, P. P. Shibayev, H. Lin, S. Jia, and M. Z. Hasan, „Discovery of a Weyl fermion semimetal and topological Fermi arcs“, Science **349**, 613–617 (2015).

[48] X. Huang, L. Zhao, Y. Long, P. Wang, D. Chen, Z. Yang, H. Liang, M. Xue, H. Weng, Z. Fang, X. Dai, and G. Chen, „Observation of the chiral-anomaly-induced negative magnetoresistance: In 3D Weyl semimetal TaAs“, Physical Review X **5**, 031023 (2015).

[49] N. Xu, H. M. Weng, B. Q. Lv, C. E. Matt, J. Park, F. Bisti, V. N. Strocov, D. Gawryluk, E. Pomjakushina, K. Conder, N. C. Plumb, M. Radovic, G. Autès, O. V. Yazyev, Z. Fang, X. Dai, T. Qian, J. Mesot, H. Ding, and M. Shi, „Observation of Weyl nodes and Fermi arcs in tantalum phosphide“, Nature Communications **7**, 11006 (2016).

[50] C. L. Zhang, S. Y. Xu, I. Belopolski, Z. Yuan, Z. Lin, B. Tong, G. Bian, N. Alidoust, C. C. Lee, S. M. Huang, T. R. Chang, G. Chang, C. H. Hsu, H. T. Jeng, M. Neupane, D. S. Sanchez, H. Zheng, J. Wang, H. Lin, C. Zhang, H. Z. Lu, S. Q. Shen, T. Neupert, M. Z. Hasan, and S. Jia, „Signatures of the Adler-Bell-Jackiw chiral anomaly in a Weyl fermion semimetal“, Nature Communications **7**, 10735 (2016).

[51] D. J. Neubauer, „Optical and Magneto-Optical Investigations on 3D Dirac-and“, 1. Physikalisches Institut - Universität Stuttgart, PhD-thesis Stuttgart (2017) 10.18419/opus-9166.

[52] S. Souma, Z. Wang, H. Kotaka, T. Sato, K. Nakayama, Y. Tanaka, H. Kimizuka, T. Takahashi, K. Yamauchi, T. Oguchi, K. Segawa, and Y. Ando, „Direct observation of nonequivalent Fermi-arc states of opposite surfaces

in the noncentrosymmetric Weyl semimetal NbP“, Physical Review B **93**, 161112(R) (2016).

[53] N. Xu, G. Autès, C. E. Matt, B. Q. Lv, M. Y. Yao, F. Bisti, V. N. Strocov, D. Gawryluk, E. Pomjakushina, K. Conder, N. C. Plumb, M. Radovic, T. Qian, O. V. Yazyev, J. Mesot, H. Ding, and M. Shi, „Distinct Evolutions of Weyl Fermion Quasiparticles and Fermi Arcs with Bulk Band Topology in Weyl Semimetals“, Physical Review Letters **118**, 106406 (2017).

[54] C. Z. Li, L. X. Wang, H. Liu, J. Wang, Z. M. Liao, and D. P. Yu, „Giant negative magnetoresistance induced by the chiral anomaly in individual Cd3As2nanowires“, Nature Communications **6**, 10137 (2015).

[55] S.-Y. Xu, C. Liu, S. Kushwaha, R. Sankar, J. W. Krizan, I. Belopolski, M. Neupane, G. Bian, N. Alidoust, T.-R. Chang, H.-T. Jeng, C.-Y. Huang, W.-F. Tsai, H. Lin, P. P. Shibayev, F.-C. Chou, R. J. Cava, and M. Z. Hasan, „Observation of Fermi arc surface states in a topological metal“, Science **347**, 294–299 (2015).

[56] M. Neupane, S. Y. Xu, R. Sankar, N. Alidoust, G. Bian, C. Liu, I. Belopolski, T. R. Chang, H. T. Jeng, H. Lin, A. Bansil, F. Chou, and M. Z. Hasan, „Observation of a three-dimensional topological dirac semimetal phase in high-mobility cd3as2“, Nature Communications **5**, 4786 (2014).

[57] Z. Wang, Y. Sun, X. Q. Chen, C. Franchini, G. Xu, H. Weng, X. Dai, and Z. Fang, „Dirac semimetal and topological phase transitions in A 3Bi (A=Na, K, Rb)“, Physical Review B **85**, 195320 (2012).

[58] Z. K. Liu, B. Zhou, Y. Zhang, Z. J. Wang, H. M. Weng, D. Prabhakaran, S. Mo, Z. X. Shen, Z. Fang, X. Dai, Z. Hussain, and Y. L. Chen, „Discovery of a Three-Dimensional Topological Dirac Semimetal , Na 3 Bi“, Science **343**, 864–867 (2014).

[59] A. A. Soluyanov, D. Gresch, Z. Wang, Q. Wu, M. Troyer, X. Dai, and B. A. Bernevig, „Type-II Weyl semimetals“, Nature **527**, 495–498 (2015).

[60] Y. Yuan, X. Yang, L. Peng, Z.-J. Wang, J. Li, C.-J. Yi, J.-J. Xian, Y.-G. Shi, and Y.-S. Fu, „Quasiparticle interference of Fermi arc states in the type-II Weyl semimetal candidate WTe2“, Physical Review B **97**, 165435 (2018).

[61] S.-Y. Yang, H. Yang, E. Derunova, S. S. P. Parkin, B. Yan, and M. N. Ali, „Symmetry Demanded Topological Nodal-line Materials“, arXiv, 1707.04523 (2017).

[62] Z. Zhu, G. W. Winkler, Q. Wu, J. Li, and A. A. Soluyanov, „Triple Point Topological Metals“, Physical Review X **6**, 031003 (2016).

[63] S. Zaheer, S. M. Young, D. Cellucci, J. C. Y. Teo, C. L. Kane, E. J. Mele, and A. M. Rappe, „Spin texture on the Fermi surface of tensile-strained HgTe“, Physical Review B **87**, 045202 (2013).

[64] „Laser ARPES“, Shen Laboratory - Stanford University.

[65] D. Neubauer, J. P. Carbotte, A. A. Nateprov, A. Löhle, M. Dressel, and A. V. Pronin, „Interband optical conductivity of the [001]-oriented Dirac semimetal Cd3As2“, Physical Review B **93**, 121202(R) (2016).

[66] D. Shoenberg, *Magnetic Oscillations in Metals* (Cambridge University Press, 1984).

[67] A. Potter, I. Kimchi, and A. Vishwanath, „Quantum Oscillations from Surface Fermi-Arcs in Weyl and Dirac Semi-Metals“, Nature Communications **5**, 5161 (2014).

[68] Y. Zhang, D. Bulmash, P. Hosur, A. C. Potter, and A. Vishwanath, „Quantum oscillations from generic surface Fermi arcs and bulk chiral modes in Weyl semimetals“, Scientific Reports **6**, 23741 (2016).

[69] R. D. Reis, M. O. Ajeesh, N. Kumar, F. Arnold, C. Shekhar, M. Naumann, M. Schmidt, M. Nicklas, and E. Hassinger, „On the search for the chiral anomaly in Weyl semimetals: The negative longitudinal magnetoresistance“, New Journal of Physics **18**, 085006 (2016).

[70] H. Zheng and M. Zahid Hasan, „Quasiparticle interference on type-I and type-II Weyl semimetal surfaces: a review“, Advances in Physics: X **3**, 1466661 (2018).

[71] J. E. Hoffman, „A Search for Alternative Electronic Order in the High Temperature Superconductor Bi2Sr2CaCu2O8+δ by Scanning Tunneling Microscopy“, University of California, Berkeley, PhD-thesis (2003).

[72] „Quasiparticle interference“, https://ocw.tudelft.nl/ (2018).

[73] H. Inoue, A. Gyenis, Z. Wang, J. Li, S. W. Oh, S. Jiang, N. Ni, B. Andrei Bernevig, and A. Yazdani, „Quasiparticle interference of the Fermi arcs and surface-bulk connectivity of a Weyl semimetal“, Science **351**, 1184–1187 (2016).

[74] R. Batabyal, N. Morali, N. Avraham, Y. Sun, and M. Schmidt, „Visualizing weakly bound Fermi-arcs and their correspondence with Weyl fermions“, Science Advances **2**, 1600709 (2016).

[75] Z. Q. Li, E. a. Henriksen, Z. Jiang, Z. Hao, M. C. Martin, P. Kim, H. L. Stormer, and D. N. Basov, „Dirac charge dynamics in graphene by infrared spectroscopy“, Nature Physics **4**, 6–9 (2008).

[76] R. Y. Chen, S. J. Zhang, J. A. Schneeloch, C. Zhang, Q. Li, G. D. Gu, and N. L. Wang, „Optical spectroscopy study of the three-dimensional Dirac semimetal ZrTe5“, Physical Review B **92**, 075107 (2015).

[77] Z.-G. Chen, R. Y. Chen, R. D. Zhong, J. Schneeloch, C. Zhang, Y. Huang, F. Qu, and R. Yu, „Spectroscopic evidence for bulk-band inversion and three-dimensional massive Dirac fermions in ZrTe 5“, Proceedings of the National Academy of Sciences **114**, 816–821 (2017).

[78] B. Xu, Y. M. Dai, L. X. Zhao, K. Wang, R. Yang, W. Zhang, J. Y. Liu, H. Xiao, G. F. Chen, A. J. Taylor, D. A. Yarotski, R. P. Prasankumar, and X. G. Qiu, „Optical spectroscopy of the Weyl semimetal TaAs“, Physical Review B **93**, 121110(R) (2016).

[79] D. Neubauer, A. Yaresko, W. Li, A. Löhle, R. Hübner, M. B. Schilling, C. Shekhar, C. Felser, M. Dressel, and A. V. Pronin, „Optical conductivity of the Weyl semimetal NbP“, arXiv, 1803.09708v1 (2018).

[80] T. Timusk, J. P. Carbotte, C. C. Homes, D. N. Basov, and S. G. Sharapov, „Three-dimensional Dirac fermions in quasicrystals as seen via optical conductivity“, Physical Review B **87**, 235121 (2013).

[81] Z. Li and J. P. Carbotte, „Conductivity of Dirac fermions with phonon-induced topological crossover“, Physical Review B **88**, 195133 (2013).

[82] Z. Li and J. P. Carbotte, „Magneto-optical conductivity in a topological insulator“, Physical Review B **88**, 045414 (2013).

[83] P. E. C. Ashby and J. P. Carbotte, „Theory of magnetic oscillations in Weyl semimetals“, European Physical Journal B **87**, 92 (2014).

[84] C. J. Tabert and J. P. Carbotte, „Anomalous behavior in the magneto-optics of a gapped topological insulator“, Physical Review B **92**, 245414 (2015).

[85] C. J. Tabert and J. P. Carbotte, „Particle-hole asymmetry in gapped topological insulator surface states“, Physical Review B **91**, 235405 (2015).

[86] Z. Li and J. P. Carbotte, „Optical spectral weight: Comparison of weak and strong spin-orbit coupling“, Physical Review B **91**, 115421 (2015).

[87] C. J. Tabert, J. P. Carbotte, and E. J. Nicol, „Magnetic properties of Dirac fermions in a buckled honeycomb lattice“, Physical Review B **91**, 035423 (2015).

[88] Z. Li and J. P. Carbotte, „Electron-phonon correlations on spin texture of gapped helical Dirac fermions“, European Physical Journal B **88**, 87 (2015).

[89] J. P. Carbotte, „Dirac cone tilt on interband optical background of type-I and type-II Weyl semimetals“, Physical Review B **94**, 165111 (2016).

[90] C. J. Tabert and J. P. Carbotte, „Optical conductivity of Weyl semimetals and signatures of the gapped semimetal phase transition“, Physical Review B **93**, 085442 (2016).

[91] S. P. Mukherjee and J. P. Carbotte, „Absorption of circular polarized light in tilted type-I and type-II Weyl semimetals“, Physical Review B **96**, 085114 (2017).

[92] S. P. Mukherjee and J. P. Carbotte, „Transport and optics at the node in a nodal loop semimetal“, Physical Review B **95**, 214203 (2017).

[93] S. P. Mukherjee and J. P. Carbotte, „Optical response in Weyl semimetal in model with gapped Dirac phase“, Journal of Physics: Condensed Matter **29**, 425301 (2017).

[94] S. P. Mukherjee and J. P. Carbotte, „Doping and tilting on optics in noncentrosymmetric multi-Weyl semimetals“, Physical Review B **97**, 045150 (2018).

[95] S. Ahn, E. J. Mele, and H. Min, „Electrodynamics on Fermi Cyclides in Nodal Line Semimetals“, Physical Review Letters **119**, 147402 (2017).

[96] D. N. Basov, R. D. Averitt, D. Van Der Marel, M. Dressel, and K. Haule, „Electrodynamics of correlated electron materials“, Reviews of Modern Physics **83**, 471–541 (2011).

[97] A. Baumgartner, „FTIR Spectroscopy and Magnetization Measurements on Europium-based Iron Pnictides“, 1. Physikalisches Institut - Universität Stuttgart, Masterthesis (2015).

[98] C. C. Homes, M. Reedyk, D. A. Cradles, and T. Timusk, „Technique for measuring the reflectance of irregular, submillimeter-sized samples“, Applied Optics **32**, 2976 (1993).

[99] J. Merz, „Infrarotspektroskopie an Eisenpniktiden“, 1. Physikalisches Institut - Universität Stuttgart, Bachelorthesis (2014).

[100] S. Kaiser, „Interplay of Charge Order and Superconductivity - Optical Properties of Quarter-Filled Two-Dimensional Organic Conductors and Superconductors.“, 1. Physikalisches Institut - Universität Stuttgart, PhD-thesis Stuttgart (2010).

[101] „Argon 5.0“, http://www.linde-gas.de/de/index.html (2018).

[102] D. B. Tanner, „Use of x-ray scattering functions in Kramers-Kronig analysis of reflectance“, Physical Review B **91**, 1–12 (2015).

[103] R. E. Hummel, *Electronic Properties of Materials* (Springer-Verlag New York, 1985).

[104] R. P. Prasankumar and A. J. Taylor, *Optical Techniques for Solid-State Materials Characterization* (CRC Press, 2011).

[105] A. Löhle, „High Pressure Magneto-Transport Studies: Tuning the Properties of Layered Correlated Materials“, 1. Physikalisches Institut - Universität Stuttgart, PhD-thesis Stuttgart (to be published).

[106] M. Geiger, „Dielektrische Messungen an quasi-eindimensionalen organischen Leitern“, 1. Physikalisches Institut - Universität Stuttgart, Bachelorthesis (2013).

[107] H. Freyhardt, F. U. Hillebrecht, E. Kisker, H. Kronmüller, M. Lambeck, P. Luger, H. Nelkowski, U. Scherz, W. Schilling, L. Thomas, H.-G. Wagemann, and R. Wördenweber, *Lehrbuch der Experimentalphysik - Festkörper*, edited by L. Bergmann and C. Schaefer (1992).

[108] M. McElfresh, „Fundamentals of magnetism and magnetic measurements featuring Quantum Design's magnetic property measurement system“, Quantum Design (1994).

[109] C. Wang and T. Hughbanks, „Main Group Element Size and Substitution Effects on the Structural Dimensionality of Zirconium Tellurides of the ZrSiS Type“, Inorganic Chemistry **34**, 5524–5529 (1995).

[110] Q. Xu, Z. Song, S. Nie, H. Weng, Z. Fang, and X. Dai, „Two-dimensional oxide topological insulator with iron-pnictide superconductor LiFeAs structure“, Physical Review B **92**, 205310 (2015).

[111] Y.-Y. Lv, B.-B. Zhang, X. Li, S.-H. Yao, Y. B. Chen, J. Zhou, S.-T. Zhang, M.-H. Lu, and Y.-F. Chen, „Extremely large and significantly anisotropic magnetoresistance in ZrSiS single crystals“, Applied Physics Letters **18**, 244101 (2016).

[112] X. Wang, X. Pan, M. Gao, J. Yu, J. Jiang, J. Zhang, H. Zuo, M. Zhang, Z. Wei, W. Niu, Z. Xia, X. Wan, Y. Chen, F. Song, Y. Xu, B. Wang, G. Wang, and R. Zhang, „Evidence of Both Surface and Bulk Dirac Bands and Anisotropic Nonsaturating Magnetoresistance in ZrSiS“, Advanced Electronic Materials **2**, 1600228 (2016).

[113] M. N. Ali, L. M. Schoop, C. Garg, J. M. Lippmann, E. Lara, B. Lotsch, and S. S. Parkin, „Butterfly magnetoresistance, quasi-2D Dirac fermi surface and topological phase transition in ZrSiS“, Science Advances **2**, 1–8 (2016).

[114] J. Hu, Z. Tang, J. Liu, X. Liu, Y. Zhu, D. Graf, K. Myhro, S. Tran, C. N. Lau, J. Wei, and Z. Mao, „Evidence of Topological Nodal-Line Fermions in ZrSiSe and ZrSiTe“, Physical Review Letters **117**, 016602 (2016).

[115] M. Neupane, I. Belopolski, M. M. Hosen, D. S. Sanchez, R. Sankar, M. Szlawska, S.-Y. Xu, K. Dimitri, N. Dhakal, P. Maldonado, P. M. Oppeneer, D. Kaczorowski, F. Chou, M. Z. Hasan, and T. Durakiewicz, „Observation

of Topological Nodal Fermion Semimetal Phase in ZrSiS“, Physical Review B **93**, 201104(R) (2016).

[116] S. M. Young and C. L. Kane, „Dirac Semimetals in Two Dimensions“, Physical Review Letters **115**, 126803 (2015).

[117] A. Topp, J. M. Lippmann, A. Varykhalov, V. Duppel, B. V. Lotsch, C. R. Ast, and L. M. Schoop, „Non-symmorphic band degeneracy at the Fermi level in ZrSiTe“, New Journal of Physics **18**, 125014 (2016).

[118] K. Momma and F. Izumi, „VESTA 3 for three-dimensional visualization of crystal, volumetric and morphology data“, Journal of Applied Crystallography **44**, 1272–1276 (2011).

[119] A. Topp, R. Queiroz, A. Grüneis, L. Müchler, A. Rost, A. Varykhalov, D. Marchenko, M. Krivenkov, F. Rodolakis, J. McChesney, B. V. Lotsch, L. M. Schoop, and C. R. Ast, „Surface floating 2D bands in layered nonsymmorphic semimetals: ZrSiS and related compounds“, Physical Review X **7**, 041073 (2017).

[120] R. Sankar, P. Ganesan, I. P. Muthuselvam, C. Butler, N. Rao, K. Dimitri, M. Neupane, M.-T. Lin, and F. C. Chou, „Crystal growth of Dirac semimetal ZrSiS with large magnetoresistance and high mobility“, Scientific Reports **7**, 40603 (2016).

[121] J. Hu, Z. Tang, J. Liu, Y. Zhu, J. Wei, and Z. Mao, „Nearly massless Dirac fermions and strong Zeeman splitting in the nodal-line semimetal ZrSiS probed by de Haas–van Alphen quantum oscillations“, Physical Review B **96**, 045127 (2017).

[122] R. Singha, A. Pariari, B. Satpati, and P. Mandal, „Large nonsaturating magnetoresistance and signature of non-degenerate Dirac nodes in ZrSiS“, Proceedings of the National Academy of Sciences **114**, 2468–2473 (2017).

[123] S. Pezzini, M. R. van Delft, L. M. Schoop, B. V. Lotsch, A. Carrington, M. I. Katsnelson, N. E. Hussey, and S. Wiedmann, „Unconventional mass enhancement around the Dirac nodal loop in ZrSiS“, Nature Physics **14**, 178–183 (2018).

[124] M. Matusiak, J. R. Cooper, and D. Kaczorowski, „Thermoelectric quantum oscillations in ZrSiS“, Nature Communications **8**, 15219 (2017).

[125] M. S. Lodge, G. Chang, C. Y. Huang, B. Singh, J. Hellerstedt, M. T. Edmonds, D. Kaczorowski, M. M. Hosen, M. Neupane, H. Lin, M. S. Fuhrer, B. Weber, and M. Ishigami, „Observation of Effective Pseudospin Scattering in ZrSiS“, Nano Letters **17**, 7213–7217 (2017).

[126] L. Aggarwal, C. K. Singh, M. Aslam, R. Singha, A. Pariari, S. Gayen, M. Kabir, P. Mandal, and G. Sheet, „Tip-induced Superconductivity Coexisting with Preserved Topological Properties in Line-nodal Semimetal ZrSiS“, arXiv, 1802.07993 (2018).

[127] R. Singha, S. Samanta, S. Chatterjee, A. Pariari, D. Majumdar, B. Satpati, L. Wang, A. Singha, and P. Mandal, „Probing lattice dynamics and electron-phonon coupling in topological nodal-line semimetal ZrSiS“, Physical Review B **97**, 094112 (2018).

[128] A. J. Klein Haneveld and F. Jellinek, „Zirconium silicide and germanide chalcogenides preparation and crystal structures“, Recueil des Travaux Chimiques des Pays-Bas **83**, 776–783 (1964).

[129] G. S. Jenkins, C. Lane, B. Barbiellini, A. B. Sushkov, R. L. Carey, F. Liu, J. W. Krizan, S. K. Kushwaha, Q. Gibson, T. R. Chang, H. T. Jeng, H. Lin, R. J. Cava, A. Bansil, and H. D. Drew, „Three-dimensional Dirac cone carrier dynamics in Na3Bi and Cd3As2“, Physical Review B **94**, 085121 (2016).

[130] M. M. Hosen, K. Dimitri, I. Belopolski, P. Maldonado, R. Sankar, N. Dhakal, G. Dhakal, T. Cole, P. M. Oppeneer, D. Kaczorowski, F. Chou, M. Z. Hasan, T. Durakiewicz, and M. Neupane, „Tunability of the topological nodal-line semimetal phase in ZrSiX -type materials (X=S,Se,Te)“, Physical Review B **95**, 161101(R) (2017).

[131] D. A. Bandurin, I. Torre, R. Krishna Kumar, M. Ben Shalom, A. Tomadin, A. Principi, G. H. Auton, E. Khestanova, K. S. Novoselov, I. V. Grigorieva, L. A. Ponomarenko, A. K. Geim, and M. Polini, „Negative local resistance caused by viscous electron backflow in graphene“, Science **351**, 1055–1058 (2016).

[132] J. Crossno, J. K. Shi, K. Wang, X. Liu, A. Harzheim, A. Lucas, S. Sachdev, P. Kim, T. Taniguchi, K. Watanabe, T. A. Ohki, and K. C. Fong, „Obser-

vation of the Dirac fluid and the breakdown of the Wiedemann-Franz law in graphene“, Science **351**, 1058–1061 (2016).

[133] J. Gooth, F. Menges, N. Kumar, V. Sü, C. Shekhar, Y. Sun, U. Drechsler, and R. Zierold, „Thermal and electrical signatures of a hydrodynamic electron fluid in WP 2“, arXiv, 1706.05925 (2017).

[134] P. Yu and M. Cardona, *Fundamentals of semiconductors: physics and materials properties*, Vol. 1 (2005), pp. 1829–1841.

[135] V. P. Gusynin, S. G. Sharapov, and J. P. Carbotte, „Ac Conductivity of Graphene: From Tight-Binding Model To 2 + 1-Dimensional Quantum Electrodynamics“, International Journal of Modern Physics B **21**, 4611–4658 (2007).

[136] O. V. Kotov and Y. E. Lozovik, „The dielectric response and novel electromagnetic modes in 3D Dirac semimetal films“, Physical Review B **93**, 235417 (2016).

[137] L. M. Schoop, „Private communication“, Princeton University (2017).

[138] W. Zhou, H. Gao, J. Zhang, R. Fang, H. Song, T. Hu, A. Stroppa, L. Li, X. Wang, S. Ruan, and W. Ren, „Lattice dynamics of Dirac node-line semimetal ZrSiS“, Physical Review B **96**, 064103 (2017).

[139] S. Wiedmann, N. E. Hussey, and L. M. Schoop, „No Title“, (to be published).

[140] C. Klingshirn, *Semiconductor Optics* (Springer, Berlin, 2007).

[141] A. N. Rudenko, E. A. Stepanov, A. I. Lichtenstein, and M. I. Katsnelson, „Excitonic instability and pseudogap formation in nodal line semimetal ZrSiS“, Physical Review Letters **120**, 216401 (2018).

[142] F. Hütt, M. B. Schilling, C. Shekhar, C. Felser, M. Dressel, and A. V. Pronin, „Strong optical evidence of 3D linear electronic bands in GdPtBi in zero magnetic field“, arXiv, 1803.00840 (2018).

[143] Z. Fisk, P. C. Canfield, W. P. Beyermann, J. D. Thompson, M. F. Hundley, H. R. Ott, E. Felder, M. B. Maple, M. A. Lopez De La Torre, P. Visani, and C. L. Seaman, „Massive electron state in YbBiPt“, Physical Review Letters **67**, 3310–3313 (1991).

[144] P. C. Canfield, J. D. Thompson, W. P. Beyermann, A. Lacerda, M. F. Hundley, E. Peterson, Z. Fisk, and H. R. Ott, „Magnetism and heavy fermion-like behavior in the RBiPt series“, Journal of Applied Physics **70**, 5800–5802 (1991).

[145] R. Movshovich, A. Lacerda, P. C. Canfield, J. D. Thompson, and Z. Fisk, „Fermi Surface Instability and Symmetry Breaking in Heavy-Fermion Compound YbBiPt“, Physical Review Letters **73**, 492–495 (1994).

[146] P. M. Oppeneer, V. N. Antonov, A. N. Yaresko, A. Y. Perlov, and H. Eschrig, „Fermi Level Pinning of a Massive Electron State in YbBiPt“, Physical Review Letters **104**, 4079–4082 (1997).

[147] E. D. Mun, S. L. Bud'Ko, C. Martin, H. Kim, M. A. Tanatar, J. H. Park, T. Murphy, G. M. Schmiedeshoff, N. Dilley, R. Prozorov, and P. C. Canfield, „Magnetic-field-tuned quantum criticality of the heavy-fermion system YbPtBi“, Physical Review B **87**, 075120 (2013).

[148] B. G. Ueland, A. Kreyssig, K. Prokeš, J. W. Lynn, L. W. Harriger, D. K. Pratt, D. K. Singh, T. W. Heitmann, S. Sauerbrei, S. M. Saunders, E. D. Mun, S. L. Bud'ko, R. J. McQueeney, P. C. Canfield, and A. I. Goldman, „Fragile antiferromagnetism in the heavy-fermion compound YbBiPt“, Physical Review B **89**, 180403 (2014).

[149] E. D. Mun, S. L. Bud'ko, Y. Lee, C. Martin, M. A. Tanatar, R. Prozorov, and P. C. Canfield, „Quantum oscillations in the heavy-fermion compound YbPtBi“, Physical Review B **92**, 085135 (2015).

[150] T. Graf, C. Felser, and S. S. P. Parkin, „Simple rules for the understanding of Heusler compounds“, Progress in Solid State Chemistry **39**, 1–50 (2011).

[151] O. Eriksson, J. M. Wills, and A. M. Boring, „Electronic structure of the RBiPt compounds (R = Y and Yb)“, Journal of Alloys and Compounds **185**, 145–149 (1992).

[152] K. H. Weyrich, „Full-potential linear muffin-tin-ornital method“, Physical Review B **37**, 10269 (1988).

[153] C. Shekhar, A. K. Nayak, S. Singh, N. Kumar, S.-C. Wu, Y. Zhang, A. C. Komarek, E. Kampert, Y. Skourski, J. Wosnitza, W. Schnelle, A. McCollam, U. Zeitler, J. Kubler, S. S. P. Parkin, B. Yan, and C. Felser, „Observation of chiral magneto-transport in RPtBi topological Heusler compounds“, arXiv, 1604.01641 (2016).

[154] W. Al-Sawai, H. Lin, R. S. Markiewicz, L. A. Wray, Y. Xia, S.-Y. Xu, M. Z. Hasan, and A. Bansil, „Topological electronic structure in half-Heusler topological insulators“, Physical Review B **82**, 125208 (2010).

[155] S. Chadov, X. Qi, J. Kübler, G. H. Fecher, C. Felser, and S. C. Zhang, „Tunable multifunctional topological insulators in ternary Heusler compounds“, Nature Materials **9**, 541–545 (2010).

[156] H. Lin, L. A. Wray, Y. Xia, S. Xu, S. Jia, R. J. Cava, A. Bansil, and M. Z. Hasan, „Half-Heusler ternary compounds as new multifunctional experimental platforms for topological quantum phenomena“, Nature Materials **9**, 546–549 (2010).

[157] M. Dzero, J. Xia, V. Galitski, and P. Coleman, „Topological Kondo Insulators“, Physical Review Letters **104**, 106408 (2010).

[158] J. Ruan, S.-K. Jian, H. Yao, H. Zhang, S.-C. Zhang, and D. Xing, „Symmetry-protected ideal Weyl semimetal in HgTe-class materials“, Nature Communications **7**, 11136 (2016).

[159] L. Peters, I. Di Marco, P. Thunström, M. I. Katsnelson, A. Kirilyuk, and O. Eriksson, „Treatment of 4f states of the rare earths: The case study of TbN“, Physical Review B **89**, 205109 (2014).

[160] G. J. McMullan and M. P. Ray, „The electronic band structure and Fermi surface of YbBiPt“, Journal of Physics: Condensed Matter **4**, 7095 (1992).

[161] R. A. Robinson, A. Purwanto, M. Kohgi, P. C. Canfield, T. Kamiyama, T. Ishigaki, J. W. Lynn, R. Erwin, E. Peterson, and R. Movshovich, „Crystallography and magnetism of the heavy-fermion compound YbBiPt“, Physical Review B **50**, 9595 (1994).

[162] B. G. Ueland, S. M. Saunders, S. L. Bud'ko, G. M. Schmiedeshoff, P. C. Canfield, A. Kreyssig, and A. I. Goldman, „High-resolution x-ray diffraction study of the heavy-fermion compound YbBiPt“, Physical Review B **92**, 184111 (2015).

[163] H. Nowotny and W. Siebert, „Ternäre Valenzverbindungen in den Systemen Cu(Ag)-As(Sb, Bi)-Mg“, Z.Metallkd. **33**, 391 (1941).

[164] C. Shekhar, A. K. Nayak, Y. Sun, M. Schmidt, M. Nicklas, I. Leermakers, U. Zeitler, Y. Skourski, J. Wosnitza, Z. Liu, Y. Chen, W. Schnelle, H. Borrmann, Y. Grin, C. Felser, and B. Yan, „Extremely large magnetoresistance and ultrahigh mobility in the topological Weyl semimetal candidate NbP“, Nature Physics **11**, 645 (2015).

[165] C. Y. Guo, F. Wu, M. Smidman, F. Steglich, and H. Q. Yuan, „Weyl fermions in a canonical heavy-fermion semimetal YbPtBi“, arXiv, 1710.05522 (2017).

[166] Z. Hou, Y. Wang, E. Liu, H. Zhang, W. Wang, and G. Wu, „Large low-field positive magnetoresistance in nonmagnetic half-Heusler ScPtBi single crystal“, Applied Physics Letters **107**, 202103 (2015).

[167] O. Pavlosiuk, D. Kaczorowski, X. Fabreges, A. Gukasov, and P. Wiśniewski, „Antiferromagnetism and superconductivity in the half-Heusler semimetal HoPdBi“, Scientific Reports **6**, 18797 (2016).

[168] F. Hütt, „Optical and magneto-optical spectroscopy on topologically non-trivial half-heusler compounds“, 1. Physikalisches Institut - Universität Stuttgart, Masterthesis (2018).

[169] M. Hirschberger, S. Kushwaha, Z. Wang, Q. Gibson, S. Liang, C. A. Belvin, B. A. Bernevig, R. J. Cava, and N. P. Ong, „The chiral anomaly and thermopower of Weyl fermions in the half-Heusler GdPtBi“, Nature Materials **15**, 1161–1165 (2016).

[170] N. Kumar, C. Felser, and C. Shekhar, „Planar Hall effect in Weyl semimetal GdPtBi“, arXiv, 1711.04133 (2017).

[171] S. Liang, J. Lin, S. Kushwaha, J. Xing, N. Ni, R. J. Cava, and N. P. Ong, „Experimental Tests of the Chiral Anomaly Magnetoresistance in the Dirac-Weyl Semimetals Na3Bi and GdPtBi“, Physical Review X **8**, 031002 (2018).

[172] C. Liu, Y. Lee, T. Kondo, E. D. Mun, M. Caudle, B. N. Harmon, S. L. Bud'Ko, P. C. Canfield, and A. Kaminski, „Metallic surface electronic state in half-Heusler compounds RPtBi (R= Lu, Dy, Gd)“, Physical Review B **83**, 205133 (2011).

[173] R. Resel and P. Hadley, „The first Brillouin zone of a face centered cubic lattice“, http://lampx.tugraz.at (2018).

[174] J. Park, G. Lee, F. Wolff-Fabris, Y. Y. Koh, M. J. Eom, Y. K. Kim, M. A. Farhan, Y. J. Jo, C. Kim, J. H. Shim, and J. S. Kim, „Anisotropic dirac fermions in a Bi square net of SrMnBi2“, Physical Review Letters **107**, 126402 (2011).

[175] J. K. Wang, L. L. Zhao, Q. Yin, G. Kotliar, M. S. Kim, M. C. Aronson, and E. Morosan, „Layered transition-metal pnictide SrMnBi2 with metallic blocking layer“, Physical Review B - Condensed Matter and Materials Physics **84**, 064428 (2011).

[176] K. Wang, L. Wang, and C. Petrovic, „Large magnetothermopower effect in Dirac materials (Sr/Ca)MnBi2“, Applied Physics Letters **100**, 112111 (2012).

[177] J. B. He, D. M. Wang, and G. F. Chen, „Giant magnetoresistance in layered manganese pnictide CaMnBi2“, Applied Physics Letters **100**, 112405 (2012).

[178] K. Wang, D. Graf, L. Wang, H. Lei, S. W. Tozer, and C. Petrovic, „Two-dimensional Dirac fermions and quantum magnetoresistance in CaMnBi2“, Physical Review B **85**, 041101(R) (2012).

[179] G. Lee, M. A. Farhan, J. S. Kim, and J. H. Shim, „Anisotropic Dirac electronic structures of AMnBi2 (A=Sr,Ca)“, Physical Review B **87**, 245104 (2013).

[180] A. Wang, E. Bozin, Y. Zhu, and C. Petrovic, „Interlayer electronic transport in CaMnBi2 antiferromagnet“, Physical Review B **94**, 125118 (2016).

[181] Y. F. Guo, A. J. Princep, X. Zhang, P. Manuel, D. Khalyavin, I. I. Mazin, Y. G. Shi, and A. T. Boothroyd, „Coupling of magnetic order to planar Bi electrons in the anisotropic Dirac metals AMnBi2 (A = Sr, Ca)“, Physical Review B **90**, 075120 (2014).

[182] A. Zhang, C. Liu, C. Yi, G. Zhao, T.-I. Xia, J. Ji, Y. Shi, R. Yu, X. Wang, C. Chen, and Q. Zhang, „Interplay of Dirac electrons and magnetism in CaMnBi2 and SrMnBi2“, Nature Communications **7**, 13833 (2016).

[183] K. Wang, D. Graf, H. Lei, S. W. Tozer, and C. Petrovic, „Quantum transport of two-dimensional Dirac fermions in SrMnBi2“, Physical Review B **84**, 220401(R) (2011).

[184] L. L. Jia, Z. H. Liu, Y. P. Cai, T. Qian, X. P. Wang, H. Miao, P. Richard, Y. G. Zhao, Y. Li, D. M. Wang, J. B. He, M. Shi, G. F. Chen, H. Ding, and S. C. Wang, „Observation of well-defined quasiparticles at a wide energy range in a quasi-two-dimensional system“, Physical Review B **90**, 035133 (2014).

[185] X. Yan, C. Zhang, S.-S. Liu, Y.-W. Liu, D. W. Zhang, F.-X. Xiu, and P. Zhou, „Two-carrier transport in SrMnBi2 thin films“, Frontiers of Physics **12**, 127209 (2017).

[186] M. Chinotti, A. Pal, W. J. Ren, C. Petrovic, and L. Degiorgi, „Electrodynamic response of the type-II Weyl semimetal YbMnBi2“, Physical Review B **94**, 245101 (2016).

[187] H. J. Park, B. C. Park, M.-C. Lee, D. W. Jeong, J. Park, J. S. Kim, H. S. Ji, J. H. Shim, K. W. Kim, S. J. Moon, H.-D. Kim, D.-Y. Cho, and T. W. Noh, „Electrodynamic properties of the semimetallic Dirac material SrMnB2 : Two-carrier-model analysis“, Physical Review B **96**, 155139 (2017).

[188] W. Z. Hu, J. Dong, G. Li, Z. Li, P. Zheng, G. F. Chen, J. L. Luo, and N. L. Wang, „Origin of the spin density wave instability in AFe2As2 (A=Ba,Sr) as revealed by optical spectroscopy“, Physical Review Letters **101**, 257005 (2008).

[189] J. Wooldridge, D. Mck Paul, G. Balakrishnan, and M. R. Lees, „Investigation of the spin density wave in NaxCoO2“, Journal of Physics Condensed Matter **17**, 707–718 (2005).

[190] S. J. Ray and L. Alff, „Superconductivity and Dirac fermions in 112-phase pnictides“, Physica Status Solidi (B) Basic Research **254**, 1–17 (2017).

[191] H. Nakamura, J. Merz, E. Khalaf, P. Ostrovsky, A. Yaresko, D. Samal, and H. Takagi, „Robust weak antilocalization due to spin-orbital entanglement in Dirac material Sr$_3$SnO“, arXiv, 1806.08712 (2018).

[192] T. Kariyado and M. Ogata, „Evolution of Band Topology by Competing Band Overlap and Spin-Orbit Coupling: Twin Dirac Cones in Ba$_3$SnO as a Prototype“, Physical Review Materials **1**, 061201(R) (2017).

[193] H. Nakamura, „Private communication“, Max Planck Institute for Solid State Research (Stuttgart) (2018).

[194] C. C. Homes, M. N. Ali, and R. J. Cava, „Optical properties of the perfectly compensated semimetal WTe2“, Physical Review B **92**, 161109(R) (2015).

[195] A. J. Frenzel, C. C. Homes, Q. D. Gibson, Y. M. Shao, K. W. Post, A. Charnukha, R. J. Cava, and D. N. Basov, „Anisotropic electrodynamics of type-II Weyl semimetal candidate WTe 2“, Physical Review B **95**, 245140 (2017).

[196] C. C. Lee, S. Y. Xu, S. M. Huang, D. S. Sanchez, I. Belopolski, G. Chang, G. Bian, N. Alidoust, H. Zheng, M. Neupane, B. Wang, A. Bansil, M. Z. Hasan, and H. Lin, „Fermi surface interconnectivity and topology in Weyl fermion semimetals TaAs, TaP, NbAs, and NbP“, Physical Review B **92**, 235104 (2015).

Declaration of Originality

I hereby declare that this thesis and the work reported herein was composed by and originated entirely from me. Information derived from the published and unpublished work of others has been acknowledged in the text and references.

Micha Benjamin Schilling